A Method for Quantifying Wind Turbine Leading Edge Roughness and its Influence on Energy Production: LER2AEP

Kruse, Emil Krog

Publication date:
2019

Document Version
Publisher's PDF, also known as Version of record

DTU Wind Energy
Department of Wind Energy

Ph.D. Thesis

A Method for Quantifying Wind Turbine Leading Edge Roughness and its Influence on Energy Production

LER2AEP

Emil Krog Kruse

Risø campus, Roskilde, 2019

DTU

Power Curve ApS
Emil Krog Kruse

Stationsmestervej 81
9200 Aalborg SV, Denmark
P: +45 96 600 300
E: eko@powercurve.dk
W: www.powercurve.dk

Technical University of Denmark
DTU Wind Energy
Department of Wind Energy

Supervisor: Christian Bak, *chba@dtu.dk*
Co-Supervisor: Niels N. Sørensen, *nsqr@dtu.dk*
Co-Supervisor: Mac Gaunaa, *macg@dtu.dk*

DTU Risø Campus
Frederiksborgvej 399 Building 125
4000 Roskilde, Denmark
P: +45 4677 5085
W: www.vindenergi.dtu.dk

Aalborg University
Department of Civil Engineering

Co-Supervisor: Thomas R. Bentzen, *trb@civil.aau.dk*

Department of Civil Engineering
Thomas Manns Vej 23
9220 Aalborg Ø, Danmark
P: +45 9940 9940
W: www.civil.aau.dk

Summary

This work propose a method for calculating the Annual Energy Production (AEP) of wind turbine generators that suffers from blade contamination and/or erosion. The calculations are based on 3D reconstructions of the blade surface acquired by an autonomous drone and post processed by a combination of commercial software and algorithms developed in this project. This Ph.D. work has been part of a project where several partners have taken part in providing the knowledge to obtain the chain from measuring the Leading Edge Roughness (LER) to predicting the Annual Energy Production (AEP) to establish the elements for the Leading Edge Roughness to Annual Energy Production (LER2AEP) method as shown in the title of this thesis.

The primary objectives of this Ph.D. was to collect information from the different project parties and research and develop a method for estimating the aerodynamics of contaminated and/or eroded wind turbine blades. This thesis will give an overview of the ideas, processes and findings within measurements, 3D reconstruction and the autonomous drone system as well as more in depth descriptions of the methods for estimating the aerodynamic penalty for contaminated and/or eroded wind turbine blades followed by a method for transferring these penalties to changes in the energy production of the wind turbine.

Most resources in the Ph.D. has been put into research of methods to simulate and measure the aerodynamic performance of airfoils subjected to contamination and/or erosion. The NACA 63_3-418 airfoil has been used as a baseline throughout the research. Validation of simulation models was based on measurements from two wind tunnels with a series of different disturbances on the surface emulating the presence of contamination or erosion. Two methods for computer aided simulation of these disturbances were presented. A study of which disturbance parameters had the most influence on aerodynamics was made with both simulations and by measurements in the Poul la Cour Tunnel at DTU Wind Energy.

The aerodynamic studies on 2D airfoils showed how protrusions and cavities influenced the aerodynamic performance and showed how the drag increased and the lift decreased dependent on how the surface damages/contamination appeared. Three examples of a 2 MW wind turbine with erosion was given to illustrate the method and process of the algorithms. The erosion was partially measured with the techniques developed in the project and applied to the three wind turbines to different extends.

Resumé

En metode til beregning af den årlige energiproduktion for en vindmølle med vingekontamination og/eller -erosion foreslås gennem dette arbejde. Beregningerne er baseret på 3D genskabninger af vingeoverfladen opmålt med en autonom drone og efterprocesseret af en kombination af kommerciel software og algoritmer udviklet i dette projekt. Dette Ph.D. arbejde har været en del af et projekt hvor flere partnere har deltaget i frembringelse af viden til at opnå en sammenhæng mellem måling af forkantsruhed til forudsigelse af energiproduktion, og som titlen på denne afhandling angiver, ender ud i en "Forkantsruhed til Energiproduktion" ("LER2AEP") metode.

De primære formål med denne Ph.D. var dels at samle al relevant viden fra de forskellige projektpartnere og dels at forske i og udvikle metoder til at estimere de aerodynamiske egenskaber for kontaminerede og/eller eroderede vindmøllevinger. Denne afhandling giver et overblik over idéer, processer og videnskabelige fund inden for målinger, 3D genskabning og det autonome drone system samt en mere detaljeret beskrivelse af metoderne brugt til at estimere den aerodynamiske degradering for kontaminerede og/eller eroderede vindmøllevinger. Efterfølgende beskrives en metode til at overføre den aerodynamiske degradering til ændringer i den årlige energiproduktion for vindmøllen.

De fleste ressourcer i Ph.D.'en er blevet lagt i forskning indenfor metoder til at simulere og måle den aerodynamiske ydeevne for vingeprofiler udsat for kontamination og/eller erosion. NACA 63_3-418 vingeprofilet er blevet brugt som basis igennem forskningen og simuleringsmodellerne blev valideret ud fra en række målinger foretaget i to forskellige vindtunneller hvor forskellige typer forstyrrelser af overfladen er blevet brugt til emulering af vingekontamination eller -erosion. To metoder til simulering af vingeprofiler med forstyrrelse af overfladen blev præsenteret. Derudover er der blevet lavet et studie gennem både simulering og målinger i Poul la Cour Tunnellen på DTU Vind Energi over hvilke parametre af en forstyrrelse som har mest indflydelse på aerodynamikken.

De aerodynamiske studier på 2D vingeprofiler viste hvordan forhøjninger og fordybninger i profilets overflade har inflydelse på den aerodynamiske ydeevne og derudover hvordan modstanden øges og opdriften forringes afhængig af overfladens beskaffenhed. Der blev givet tre eksempler på en 2 MW vindmølle med erosion for at illustrere metoden og fremgangsmåden for algoritmerne. Erosionen var delvist målt med teknikker udviklet i dette projekt og derefter anvendt på de tre vindmøller i forskellig udstrækning.

Preface

This thesis was prepared at the department of Wind Energy at the Technical University of Denmark in fulfillment of the requirements for acquiring a Ph.D. degree from the Ph.D School DTU Wind Energy. It was an External Ph.D. facilitated by Power Curve ApS to further strengthen their technical development of aerodynamic upgrades. I have primarily been located at Power Curve ApS offices in Aalborg in the Northern Denmark. The Ph.D. position was a part of a larger project named *Leading Edge Roughness on Wind Turbine Blades* financed by Energy Technology Development and Demonstration Program (EUDP) under project number 64015-0046. The project consortium included Power Curve ApS, Technical University of Denmark (DTU) Wind Energy, Aalborg University (AAU) Medialogy and Danish Fundamental Metrology (DFM).

This thesis is split into two parts: A synopsis giving an overview of the project and Ph.D. work and an appendix containing relevant articles and documents. The project started October 2015 and was scheduled to end September 2018. Due to unforeseen delays in the construction of the DTU Wind Tunnel, a key element in the project, the end date was postponed 6 months. Later during the construction, the DTU Wind Tunnel caught fire in the roof which resulted in an additional setback of several months. It was decided to end the project as intended the 31$^{\text{st}}$ of March 2019 and postpone only the Ph.D. submission deadline an additional 5 months. The construction and start up of the wind tunnel has been delayed a total of almost 3 years, complicating the process and natural development in the project in general. The first experimental results from the DTU Wind Tunnel came in hand in the middle of June 2019, leaving little time to process and publish the results. The submission was pushed one month and the final submission deadline was the 30^{th} of September 2019.

Risø campus, Roskilde, September 23, 2019

Emil Krog Kruse

List of Dissemination

Publications

- [Article 1] Emil Krog Kruse, Niels N. Sørensen, Christian Bak, **Predicting the Influence of Surface Protuberance on the Aerodynamic Characteristics of a NACA 63_3-418**, *The Science of Making Torque from Wind (TORQUE 2018) IOP Conf. Series: Journal of Physics: Conf. Series 1037 (2018) 022008 doi :10.1088/1742-6596/1037/2/022008*, Milan, Italy, 2018 [1].

- [Article 2] Emil Krog Kruse, Niels N. Sørensen, Christian Bak, Mikkel Schou Nielsen, **CFD Simulations and Validation of a Wall Roughness Model Applied on a NACA 63_3-418 Airfoil**, *Submitted to Wileys Wind Energy Journal, September 2019* [2].

- [Article 3] Emil Krog Kruse, Niels N. Sørensen, Christian Bak, **A 2-Dimensional Quantitative Parametric Investigation of Simplified Surface Imperfections on the Aerodynamic Characteristics of a NACA 63_3-418 Airfoil**, *Submitted to Wileys Wind Energy Journal, September 2019* [3].

- [Article 4] Emil Krog Kruse, Christian Bak, Anders Smærup Olsen, **Wind Tunnel Experiments on a NACA 63_3-418 Airfoil with Different Types of Leading Edge Roughness**, *Submitted to Wileys Wind Energy Journal, September 2019* [4].

- [Article 5] Mikkel Schou Nielsen, Ivan Nikolov, Emil Krog Kruse, Jørgen Garnæs, Claus Madsen, **The influence of surface texture on Structure-from-Motion reconstructions**, *DRAFT VERSION. Submission delayed due to main author maternity leave. In agreement with the Ph.D. office, it will be submitted before this thesis is published.* [Appendix G].

- [Article 6] Christian Bak, Mac Gaunaa, Anders Smærup Olsen, Emil Krog Kruse **What is the Critical Height of Leading Edge Roughness for Aerodynamics?**, *The Science of Making Torque from Wind (TORQUE 2016) Journal of Physics: Conference Series 753 (2016) 022023 doi:10.1088/1742-6596/753/2/022023*, Munich, Germany, 2016 [5].

Presentations

- [Oral Presentation] Emil Krog Kruse **Quantifying Leading Edge Roughness on Wind Turbine Blades**, *Erosion Day*, DTU Risø, 2017

- [Oral Presentation] Emil Krog Kruse **Competitiveness through innovation cooperation between industry and research**, *Wind Energy Denmark*, Messecenter Herning, 2017

- [Oral Presentation] Emil Krog Kruse **Predicting the Influence of Surface Protuberance on the Aerodynamic Characteristics of a NACA 63_3-418**, *The Science of Making Torque from Wind (TORQUE 2018)*, Milan, Italy, 2018

Acknowledgements

My gratitude goes to EUDP for funding and believing in this project. Without the EUDP support, the project would not have been carried out. Thanks to E.ON and Vattenfall for supporting the project proposal and taking part in the advisory board and contributing with valuable insights. I would like to thank AAU, DFM and DTU as the partners in the project consortium and their employees relevant to the project as well as the key persons involved, Claus B. Madsen (AAU), Jørgen Garnæs (DFM) and Christian Bak (DTU) for a good cooperation and effort in the project.

I would like to thank my supervisor Niels N. Sørensen from DTU for supporting me in my journey into CFD simulations. I know it has not been easy because I started CFD from scratch and because I have been located far away from DTU. On the same note, I would like to thank my co-supervisor Thomas R. Bentzen from AAU for supporting me in the beginning of the project. Thanks to Anders S. Olsen and Mac Gaunaa from DTU and Mikkel S. Nielsen from DFM and especially Ivan Nikolov from AAU for participating in research activities, reviews and publications. Thanks to Jimmie Beckerlee for his work on the DTU wind tunnel measurements.

Thanks to my colleagues Nicholas Gaudern and Lone B. Brønnum for support and assistance in the project. I would also like to thank Power Curve ApS and the board for providing me the opportunity of making a Ph.D. A special thanks goes to Niels B. Brønnum, Power Curve ApS CEO, for believing in me from the very beginning, supporting me professionally and personally both as a colleague and as a friend. I appreciate my time in Power Curve. My colleague Nicklas Koldkjær has been by my side almost every day for the last half of the project period. Thank you for your support and friendship.

My main supervisor Christian Bak from DTU has been indispensable throughout the project. Thank you Christian for being there all the time for both large and small, during day, night and weekend if needed.

Thanks to my family for the moral support and especially my mom and dad for their boundless believing in me. I appreciate how you never hesitate to help in harsh times.

Lastly and most importantly, I would like to thank my wife and our two sons for supporting me and being there every day, even days where I might not have been mentally present, especially in the final months of the Ph.D. Thank you Camilla for standing by my side through all my crazy ideas. I owe you everything.

Glossary

AAU Aalborg University. v, 17, 25

AEP Annual Energy Production. i, 1, 2, 7, 9, 12, 47, 49, 55, 61, 63–71

AoA Angle of Attack. 35–41, 43, 44, 47–50, 56, 60

BEM Blade Element Momentum. 16, 55, 56, 59–61, 63, 70, 76

CapEx Capital Expenditures. 1

CFD Computational Fluid Dynamics. 11, 12, 31, 32, 38, 43–47, 50, 55, 56, 69–71

CM Confocal Microscope. 26–29

CoE Cost of Energy. 1

DFM Danish Fundamental Metrology. v, 26

DTU Technical University of Denmark. v, 31, 50, 59, 70

EUDP Energy Technology Development and Demonstration Program. v, 2, 7, 22, 26

GF Gurney Flap. 2

GPS Global Positioning System. 22–24

GSD Ground Sample Distance. 17, 18

HAWC2 Horizontal Axis Wind turbine simulation Code 2$^{\text{nd}}$ generation. 59

IAG Institute of Aerodynamics and Gas Dynamics. 31, 35, 38, 52

LEP Leading Edge Protection. 2, 3, 6

LER Leading Edge Roughness. 1–3, 7, 8, 11–13, 16, 21, 26, 29, 32–34, 36, 41, 42, 47, 50, 52, 53, 55, 56, 60, 61, 63–67, 69–71, 76

LER2AEP Leading Edge Roughness to Annual Energy Production. i, 2, 8, 12, 13, 15, 16, 29, 49, 55, 57, 63, 69, 71

LiDAR Light Detection and Ranging. 24, 25

MP megapixels. 17

NACA National Advisory Committee for Aeronautics. 10, 11

NDA Non-disclosure agreement. 4

OEM Original Equipment Manufacturer. 1, 4, 71

OpEx Operational Expenditures. 1

PLC Programmable Logic Controller. 24

PLCT Poul la Cour Wind Tunnel. 50

PS pressure side. 32, 42, 47, 48, 50, 52, 53

RTK Real-Time Kinematic. 23–25

SDK Software Development Kit. 22–24

SfM Structure from Motion. 7, 9, 16–20, 22, 25–29, 57, 69

SS suction side. 32, 42, 47, 48, 50–53

UAV Unmanned Aerial Vehicle. 7, 9, 15

UN United Nations. 1

VG Vortex Generator. 2, 11

WP Work Package. 2

Contents

CHAPTER 1

Introduction

In the Paris Agreement of 2015, the United Nations (UN) agreed to put an empasis on "*pursuing efforts to limit the temperature increase to 1.5°C above pre-industrial levels...*" [6]. To reach this goal, emission of greenhouse gasses must be reduced by lowering the global energy consumption and/or by increasing the share of sustainable energy [7]. Wind turbines are one of the major contributors to sustainable energy, with an installed capacity of 540 GW worldwide in 2017 [8]. To increase the global wind power share further, the Cost of Energy (CoE) from wind turbines must be reduced. The CoE can be reduced in two ways: By reducing wind turbine Capital Expenditures (CapEx) and Operational Expenditures (OpEx) or by generating more power from the wind turbine. To bring down CapEx, many research institutes and Original Equipment Manufacturers (OEMs) have investigated the development and design of larger and more efficient wind turbines. In recent years, the global fleet of large wind turbines with over 10 years in operation has increased. This results in increased OpEx and hence a higher demand for research in cost-effective solutions.

Degradation of mechanical parts such as gearboxes, generators, bearings and blades contributed significantly to OpEx. Blade damages can be divided into two main areas: *Structural* and *Aerodynamic* damages. Some research has investigated structural damages as these jeopardize blade durability and may result in a critical breakdown of the blade or the whole wind turbine. Aerodynamic damages pose a threat to the wind turbine's loads and may decrease performance. Both types can prove expensive over time by reducing the lifetime of components and decreasing the revenue of the wind turbine, which both contribute to increasing CoE. Furthermore, aerodynamic damages can also jeopardize the structure, resulting in both aerodynamic and structural damages.

Aerodynamic damages are characterized by altering the shape or the surface texture of the blade. Manufacturing imperfections, bugs, dirt, ice or missing surface material are examples that can disturb the designed airflow and are described in detail in Section 2.1. These damages are often small compared to the size of the blade, and due to blade design and nature of the airflow, they tend to accumulate near the leading edge of the blade. Leading Edge Roughness (LER) has become the de facto term for these aerodynamic damages.

At the time of writing, neither academia nor the industry has reached a consensus on the impact of Leading Edge Roughness (LER) on aerodynamic performance of wind turbine blades and the wind turbine Annual Energy Production (AEP). Anecdotal accounts argue that AEP is reduced by less than 0.5%, whereas other references claims up

to 20% reduction in AEP, described in Section 2.3. This large gap in the understanding of LER highlights the need for more research and serves as the basis of this project. Funded by Energy Technology Development and Demonstration Program (EUDP), the goal of the project is to develop a method for estimating the changes in AEP based on the condition of a specific blade, named the Leading Edge Roughness to Annual Energy Production (LER2AEP) method. This method is the focal point of the work in this thesis, which is primarily concerned with aerodynamic predictions.

The results of LER2AEP can serve as a basis for wind turbine owners to decide *if*, *when* and *how* to invest in mitigaion of the damages. A common repair is to add new Leading Edge Protection (LEP). While this can prevent the area of missing material from growing until the protection wears off, it can also introduce other aerodynamic penalties. Aerodynamic upgrades such as Vortex Generators (VGs) and Gurney Flaps (GFs) have proven to be efficient and cost effective ways to compensate for lost performance and regain AEP.

As stated in Appendix B - Research Appendix to the EUDP application, the tasks of the Ph.D. address two major parts:

1) Linking together the different Work Packages (WPs) from each project party and incorporating the knowledge from these into Power Curve ApS.

2) Research and development of the aerodynamic methods and algorithms.

To understand the process, a brief description of the work done in each WP will be presented in Chapter 3. The structure of the thesis is illustrated in Figure 1.1:

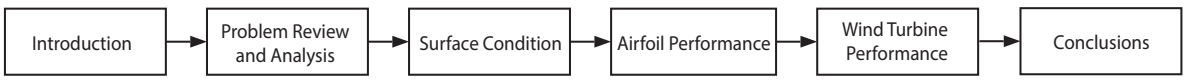

Figure 1.1: Flow diagram illustrating the thesis structure.

Chapter 2 presents an analysis of different types of LER as well as here and when they can occur, followed by a description of the proposed solution approach for LER2AEP. As most of the academic work for the Ph.D. concerns aerodynamics, the research overview is given from the aerodynamics perspective, and the chapter ends with an overview of the current research in the field. Chapter 3 describes methods used to scan the blade surface and obtain a satisfying result for the surface condition. The Ph.D. research results are described in Chapter 4, and a method for calculating the aerodynamic performance of a wind turbine is presented in Chapter 5. Chapter 6 rounds up the project and gives three examples of wind turbines with LER. Finally, Chapter 7 holds the governing project conclusions and suggestions for future work.

CHAPTER 2
Problem Review and Analysis

This chapter gives an overview of LER, the solution approach and finally a research overview including state of the art research.

2.1 Leading Edge Roughness

As mentioned in the Introduction, Leading Edge Roughness (LER) comes in many forms. By studying the literature, as done in Section 2.3, by confidential inspection reports and from experience, it is known that LER at least can be:

- Production imperfections e.g. from grinding, molding or fillings
- Dirt/mud/bugs on the blade
- Moss or similar organisms
- Ice accretion in cold areas
- Delamination of paint
- Erosion from rain, hail etc.
- Leading Edge Protection (LEP) add on

These different types of LER can have different severities and extends. Some of will evolve over time, some come and go and some are stationary in nature. Take the production imperfections, which are expected not to change. They will be the same from cradle to grave. Dirt/mud/bugs, moss and ice accretion come and goes with the weather. In moist areas, the mud can build up and reduce the power production by up to 80% in short periods, until the next rainy day, where the mud is washed away and power production is regained. An example on this is illustrated in Figure 2.1.

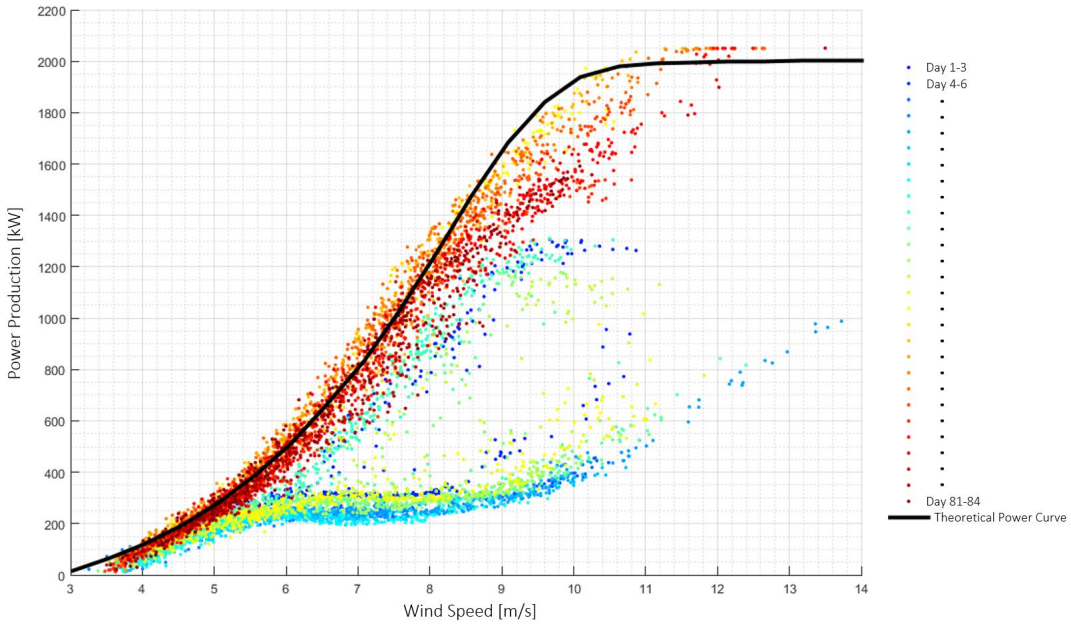

Figure 2.1: Power as a function of wind speed of a 2MW Wind Turbine over 84 days. The blades were highly contaminated by mud which was washed away by rain in the middle of the period.

Figure 2.1 shows a vast degradation in power of up to 80% in the mid and high wind speed region. The blades were covered in mud as a result of a combination of high humidity and dirt in the air. The mud was washed away by rain after 40-50 days and the power went back up, slowly starting to reduce again after 70-80 days. The data was provided by the OEM but masked due to a Non-disclosure agreement (NDA). Figure 2.1 has been approved for use in this Ph.D. thesis by the OEM.

Less severe are the dirt, bugs and moss, however the impact on performance is not insignificant. Ice accretion might change the shape of the profile and extend the chord length to a state where it no longer resembles the design shape. Delamination and erosion share the property of being missing material. Examples of dirt and moss can be seen in Figure 2.2.

Figure 2.2: 1) Example of a blade with dirt and bugs. 2) Example of blade with moss and dirt from [9].

Delamination occurs when the airflow starts peeling off the surface bit by bit. It is often concentrated close to joints and where the airflow speed is highest e.g. around the leading edge. It can also be seen further down the airfoil if the surface has been damaged from e.g. transporting or handling the blade during installation.

Erosion occurs when the surface is damaged by rain, hail or other particles. It peels of in small bits and exposes the fibers underneath. Eventually, the airflow will remove the remaining protuberation and the damage will become more like delamination. An example of erosion and some delaminations can be seen in Figures 2.3 and 2.4 .

Figure 2.3: 1) Example of erosion from a rain erosion test. 2) Example of delamination on blade tip from [10].

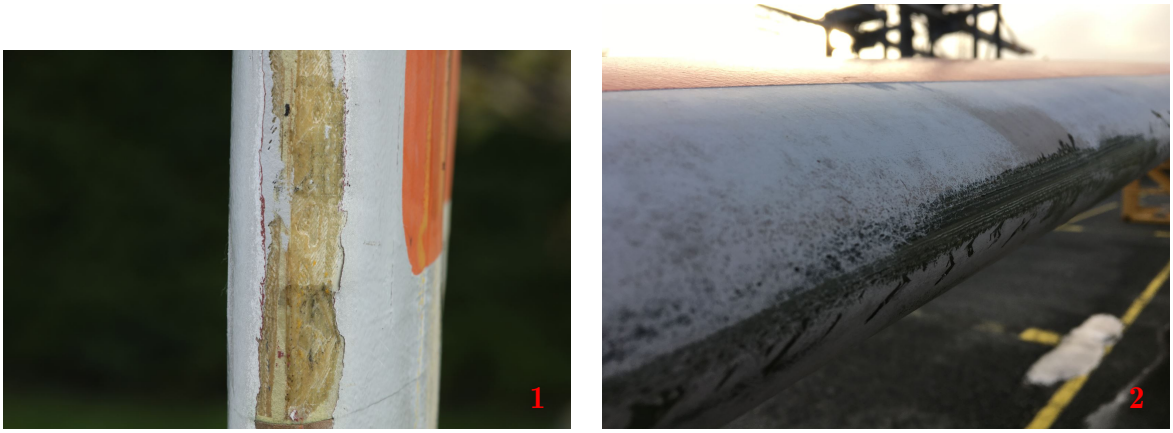

Figure 2.4: 1) Example of delamination on test specimen. 2) Example of both erosion and delamination on a 3 year old blade decommissioned due to structural manufacturing defects.

Some attempts to repair delamination and erosion with LEP can introduce a surface that deviates from the designed one, with an example given in Figure 2.5. Furthermore, LEP can also introduce a step down in surface height and thereby trigger the transition from laminar to turbulent flow in the airfoils boundary layer. Thus, preferable to delamination and erosion, the LEP might also change the aerodynamic properties of an airfoil.

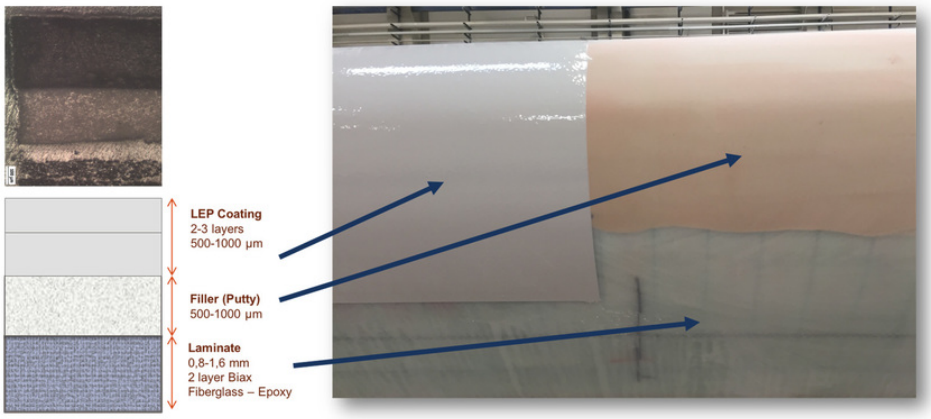

Figure 2.5: Example of LEP, showing several millimeter added material, possibly resulting in backwards facing bumps where it ends [11].

2.2 Solution Approach

The application for the EUDP project that this Ph.D. is a part of contained an initial study of methods, relevant technology and state of the art research. Based on this, a suggested approach was formed for quantifying LER and its impact on the AEP. The relevant part of the application can be found in Appendix B. The project work has been based on this solution approach and its requirements in order to research and develop a functional and acceptable solution.

A governing initial requirement was the ability to scan and detect **sub millimeter** roughness, in order to estimate the decrease in AEP at an acceptable level, based on the work by Bak et al. [5]. Another goal was to develop a cost effective and automated scanning method. At the time of the application writing, no technology were able to scan sub millimeter differences in surfaces at a ground-to-blade distance, which typically ranges from 50 meters to several hundreds of meters. Typical methods for inspecting wind turbine blades are personal hanging in ropes on the blade or some kind of lifting equipment, e.g. a basket from a "boom truck".

These methods are not cost effective nor automated. However, in recent years, the use of Unmanned Aerial Vehicle (UAV)/drones for inspections has grown. Some companies offers third party drone inspections both manually and semi-automated [12, 13]. These inspections focuses on the structural state of the blades, and so far, no company is known to estimate the aerodynamic state of the blades.

In current years, the UAV research, industry and market are developing and growing at a rapid pace, giving new opportunities to carry scanning equipment in a controlled environment in a sufficient time [14]. On this basis, the initial solution approach includes an UAV to carry scan equipment and perform an automated scan.

Several technologies for 3D scanning of surfaces exists, e.g. different kinds of light or laser scanners in various sizes or tactile scanning devices that touches the surface [15, 16]. Another method is a 3D object from images. In short, an object is photographed from different positions, where the images have some overlap in between. Computer vision is used to detect features in the images and stitch together a 3D reconstruction. The process is also known as Structure from Motion (SfM). Recent advances in the technology, software and hardware, both cost and performance wise, founds the basis for selecting SfM as the scanning technique.

With the assumptions in place, the process is for the LER2AEP is outlined and illustrated in the flow diagram in Figure 2.6.

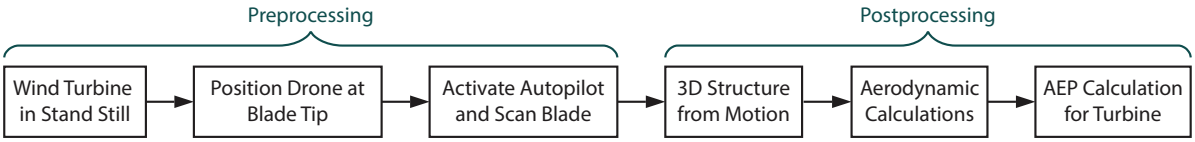

Figure 2.6: Flow diagram illustrating the general LER2AEP solution approach.

As described in Figure 2.6, the general solution consist of a pre- and postprocess. The preprocessing starts with a wind turbine in stand still and locked to avoid unintended rotation. The drone is positioned at the blade and the automated scanning is initiated. An animated demonstration video was developed in the first year of the project. Figure 2.7 shows 8 still images from the video, where a hyperlink to the video can be found at [17].

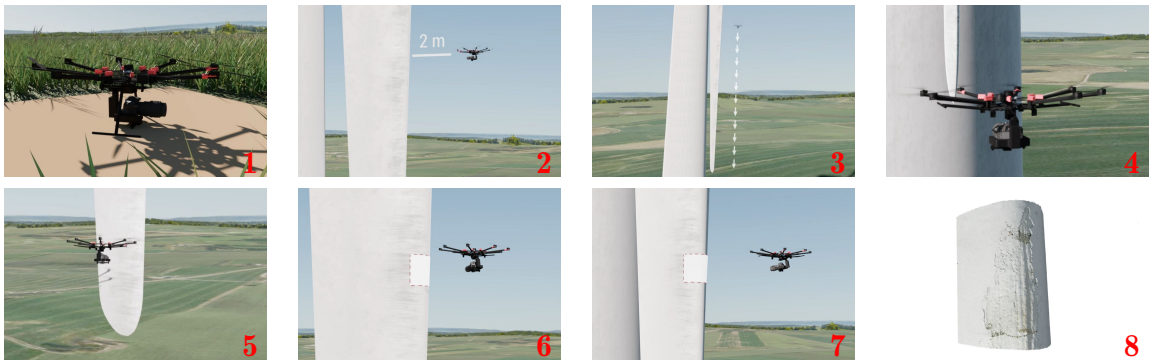

Figure 2.7: Pictures from the demonstration video available at [17], describing the scanning process from the project application.

In this demonstration video, the turbine is stopped in a so called bunny-ear position, where one blade is pointing down and two blades each pointing 30 degrees upwards from horizontal. All blades has the leading edge pointing opposite of the tower. 1) The drone is started from the ground. 2) The operator, or possibly autonomously at a later point, will fly the drone to the blade leading edge. The automated scanning is activated, and it starts to seek for the blade hub as a reference point. When positioned at the blade hub, the drone will do an initial scan of the blade leading edge from the hub to the tip. 3,4,5) When positioned at the tip, the drone will scan both sides of the blade, and finally return to the tip and hereafter land automatically on the takeoff location. 6,7) Critical areas with LER are detected by computer vision, and a more detailed scan of important areas will be carried out, by acquiring images from multiple positions, focusing the same area. 8) An example of a 3D reconstruction is seen, which is the first step in the postprocessing.

As a key part of the postprocessing, relevant aerodynamic calculations will be applied to the 3D reconstructed areas and turbine AEP decrease will be evaluated and reported to the user.

The solution approach had immature or non existing processes in most aspects of the workflow before the project started. These processes are among many:

- SfM
  - Camera and lens
  - Physical constraints (distances, amount of photos, etc.)
  - Commercial software for reconstruction
  - Postprocessing algorithms
- UAV
  - Drone model (size, payload, flight time)
  - Camera stabilizer
  - Position tracking (GPS)
  - Autopilot sensors, programming, on-board and ground station computer and communication
- Validation of SfM measurements
  - Absolute scale
  - Relative differences in height
  - Detection if it is roughness or just noise
- Aerodynamic performance calculation methods
  - Computational method
  - Validation of computations in wind tunnel experiments
  - Translation of aerodynamic changes to turbine AEP loss

In this Ph.D. these processes have been investigated, however with the main focus on the fourth and last item "Aerodynamic performance calculation methods". The processes will be described in the following chapters 3, 4, 5 and 6 to a relevant extend.

2.3 Research Overview

The study of ancient ship designs such as the canoes reveals that the attention paid to hydrodynamic design is not new. A design that had a lower resistance in the water lead to faster travel for the same effort. The largest contribution comes from the actual shape of the hull. However, poor surface quality of the hull surface will lead to a higher resistance. Some of the first English written research on the friction between a fluid and a solid can be traced back to the early 18^{th} century, with the example *"On the friction and resistance of fluids"* from 1831 by G. Rennie [18]. Rennie refers back to research by G. Amontons on friction between solids to 1699, which are all written in French.

The first research directly relevant to this work is found in the beginning of the 1930s where a series of experimental investigations were conducted at the National Advisory Committee for Aeronautics (NACA) with the focus on changes in the lift and drag properties of airfoils. In 1932 J. Eastman and A. Sherman conducted a series of wind tunnel experiments on an airfoil with different kinds of protuberances [19, 20]. A year later in 1933, R. W. Hooker conducted a series of wind tunnel experiments on an airfoil with distributed surface roughness [21]. One of the major findings was that roughness with a height of as little as 0.02% of the chord length had a negative impact on the performance. Although not directly on the topic of aerodynamics, J. Nikuradse was the author of some widely used publications concerning flows in pipes, which are often used as references for flow solvers [22, 23].

Two books are referred to especially throughout most of the relevant research. The first one is *"Theory of wing sections"* by I. H. Abbott and A. E. Von Doenhoff and was published in 1959 [24]. Among other things, it provides a wide catalogue of airfoil wind tunnel data with and without roughness, often used as a baseline in scientific articles. The second one is *"Fluid-Dynamic Drag"* by S. F. Hoerner, which was published in 1965 and gives an extensive overview of drag from different airfoils, basic geometries and different flat plate cases with cavities or protuberances.

Up until the 1990s the focus in aerodynamics has mainly been on aircrafts. The prediction of aerodynamic changes of an airfoil has been focused on ice accretion on the aircraft wings during flight, as the wings could be cleaned or repaired for smaller roughness in between flights. A large amount of work has been focused on predicting the geometry of ice accretion and its aerodynamic impact. Some examples of research in the aircrafts field are K. Sermeus and H. Yang [25], Bragg et al. [26], Broeren et al. [27–29] and T. Cebeci [30].

Wind turbines located in cold climates are prone to ice accretion and unlike an aircraft, the turbines might run for long periods with no de-icing. Ice on the blades has an impact on both the aerodynamics of the blades and the loads on the turbine. Efforts to simulate the ice accretion on wind turbine blades and/or simulate the impact on aerodynamics and loads can among others be found in L. Makkonen et al. [31], K.

Mortensen [32], E. Sagol [33], V. Turkia et al. [34], P. Blasco et al. [35], M. C. Pedersen et al. [36, 37] and M. Etemaddar et al. [38].

Public wind tunnel experimental data on airfoils with erosion are quite limited, however, a few good articles and reports are available. P. Fuglsang et al. published a report with wind tunnel measurements for the FFA-W3-241, FFA-W3-301 and NACA 63-430 airfoil with and without roughness in the form of zigzag- or bulge tape serving as turbulators combined with passive add-ons such as VG's to mitigate the effect from the turbulators [39]. A similar study on the NACA 63-415 and a modified NACA 63-415 were conducted by C. Bak et al. [40]. W. A. Timmer and R.P.J.O.M van Rooij published an overview of four DU-airfoils: DU 91-W2-250, DU 95-W-180, DU 97-W-300 and DU 93-W-210. These four were also equipped with turbulators and different passive aerodynamic add-ons [41]. In the same year the authors also published an overview of different 24%-30% thickness airfoils and their sensitivity to roughness [42]. W. A. Timmer published a similar overview of the NACA 6-Digit airfoil series with and without roughness [43]. Common for these four references is the focus on mitigating the aerodynamic penalty from LER, either by passive add-ons or by directly changing the airfoil geometry.

Until recent years, LER has often been represented in wind tunnel experiments by turbulators such as the aforementioned zigzag- or bulge tape. The need for predicting the influence of LER, and thereby the power production of the turbine with high precision, has grown. One way to achieve this could be by equipping wind tunnel airfoil models with a leading edge resembling real leading edges with erosion. N. Gaudern made an analysis of LER and decided on five erosion patterns in different stages which were tested on different airfoils [44]. A study with a modified leading edge on a NACA 63_3-418 were made by E. B. White et al. where different 3D printed leading edges were equipped on a modular test wing [45]. One of the purposes with the modular test wing was to develop a database that could be used for calibrating Computational Fluid Dynamics (CFD) simulations and designing airfoils.

A study analyzing the critical height of LER, i.e. the lower threshold for neglecting a disturbance, was conducted by C. Bak et al. [5], and is a part of a preliminary study to this project. They found that the critical height was around 0.01% of the chord which is in good agreement with the findings described in the NACA report by Hooker [21]. To back up the analysis of airfoils with LER, boundary-layer measurements could be valuable. However, public research with boundary-layer measurements are rare, but a study by M. F. Kerho and M. B. Bragg was found on a NACA 0012 with LER [46].

Two of the major computer aided tools to predict aerodynamics are panel codes and CFD. Even though panel codes are not simple and can pose a big challenge to implement, they can be programmed within a reasonable time due to the relatively low complexity. More sophisticated open source panel codes exist, such as XFOIL by Mark Drela [47] or the TU Delft modified version, RFOIL [48]. These are powerful tools in predicting simple 2D airfoil geometries. When it comes to more advanced simulations where e.g.

surface changes can be resolved, CFD is often seen as the preferred tool. However, for many years CFD simulations with free transition from laminar to turbulent flow have been interpreted as a "clean" surface and simulations with the assumption of turbulent flow from the very leading edge have been interpreted as the performance with surface roughness. Thus, no de facto standards exist when simulating surface roughness in CFD. A roughness extension to Menters SST-kω model [49] presented in *"Turbulence Modeling for CFD"* by D.C. Wilcox [50] has been used in some simulations. The Wilcox extension requires a very fine computational mesh close to the airfoil surface, which limits the practical use of the model in anything but 2D flows due to high computational time. An effort to make a roughness extension with moderate requirements to the boundary layer mesh resolution was made by Knopp et al. [51]. Knopps roughness extension was implemented in the DTU Wind Energy in-house CFD code EllipSys and tested within this project, although Knopps own application of their model showed questionable results [52].

2.3.1 State of the Art

Since the beginning of this project in 2015 and till 2017, similar work has been carried out at Texas A&M University and the University of California with help from Sandia National Laboratories. A vast amount of work has been put into wind tunnel measurements on airfoils with different kinds of LER. The same authors appear on most publications: C. M. Langel, R. Chow, C. P. van Dam, D. C. Maniaci, R. S. Ehrmann, B. Wilcox, E. B. White and O. F. Hurley [53–59]. The models used in this project (LER2AEP) are either a transition model or a roughness model. One of the new promising approaches presented in these publications is to simulate LER as a combination of both a roughness model and a transition model.

Hard conclusions on the impact of LER on AEP are difficult to come by. However, A. Sareen et al. reports possible AEP losses of up to 25% in heavy erosion situation [60], whereas K. Standish et al. show AEP losses of up to 10% in cases noted as *"highly unlikely"* ([61] p. 12). A recent Masters thesis conducted by M. L. W. Veraart with TU Delft, DTU Wind Energy and LM Wind Power estimates an AEP loss of 1% from rain erosion tests and simulations [62]. It is stated that *"When heavier erosion is observed, a repair is a necessity due to structural degradation of the blade."* ([62], p. 61), which could, in the Ph.D. thesis writer's opinion, be interpreted as an acknowledgement of a possible higher AEP loss with heavier erosion. However, the lower percentage loss estimates are backed up by R. S. Ehrmann et at. in [59] for large wind turbines of 5 MW and above, where the two digit losses are observed on smaller turbines. The inconsistent conclusions concerning the AEP penalty of wind turbines prone to LER within academia and the industry makes this project and its research even more relevant.

One of the major challenges in the project was to find data describing the condition of wind turbine blades in operation. One of the collaboration partners in the project provided blade inspection reports from a wind farm with turbines in the 2-3 MW range. A

typical blade inspection report, including these ones, only contains 2D photographs where it is very difficult, if not impossible, to estimate the surface topology with the necessary resolution. Another challenge is validating the LER2AEP method as a collected system, and only the sub parts of the system can be validated one at a time, e.g. measurements on airfoils with LER in a wind tunnel. The project did not have access to a wind turbine where it is known exactly what the power production should be compared to what is actually within the resolution range needed to validate the LER2AEP method.

CHAPTER 3
Surface Condition

This chapter describes how damages on blades are measured, starting with an overview of the Leading Edge Roughness to Annual Energy Production (LER2AEP) algorithm in Section 3.1 followed by a description of the selected equipment in Section 3.2 and 3.4, based on the initial requirements described in Section 2.2. In order to obtain the measurements with the selected equipment, an autopilot was developed for the Unmanned Aerial Vehicle (UAV)/drone (hereafter referred to as drone), including hardware, software and tests of these, briefly described in Section 3.4.2. Postprocessing of the measurements can be divided into multiple steps, where conversion from photographs to 3D structures is the first step and described in Section 3.3. The final section of this chapter, Section 3.5, contains validations of the reconstructed 3D surfaces.

The Ph.D. has participated in all activities to different extends, as a part of the task for incorporating knowledge into the company described in Appendix B. Thousands of research hours has gone into these topics in this project, but the sections are compressed to a minimum as the main focus of the academic work by the Ph.D. is on the aerodynamics.

3.1 Overview of the LER2AEP Algorithm

Figure 3.1 shows the steps involved in the postprocessing of the LER2AEP software. The images and geotagging in 1) are acquired by the drone as described in Section 2.2, 3.2, 3.4, 3.4.1 and 3.4.2. Structure from Motion (SfM) in 2) and 3) are described in Section 3.3 and validated in Section 3.5. The 3D models obtained in 2) are stored and sliced by scripts in step 3) and 4), resulting in a series of 2D slices in 5). The polars in the airfoil database is calculated by geometrical changes in the mesh as described in Section 4.2, 4.4 and backed up by Section 4.3 and 4.5. The airfoil and wind turbine databases are described in Section 5.1. The airfoil matching between the slices in 5) and the Clean and LER Airfoils database is done by the algorithm described in Section 5.2. The resulting LER polars are stored as 7) whereafter the special wrapped Blade Element Momentum (BEM) code described in Section 5.3 is utilized in 8). Lastly, 9) holds the results presented in Chapter 6.

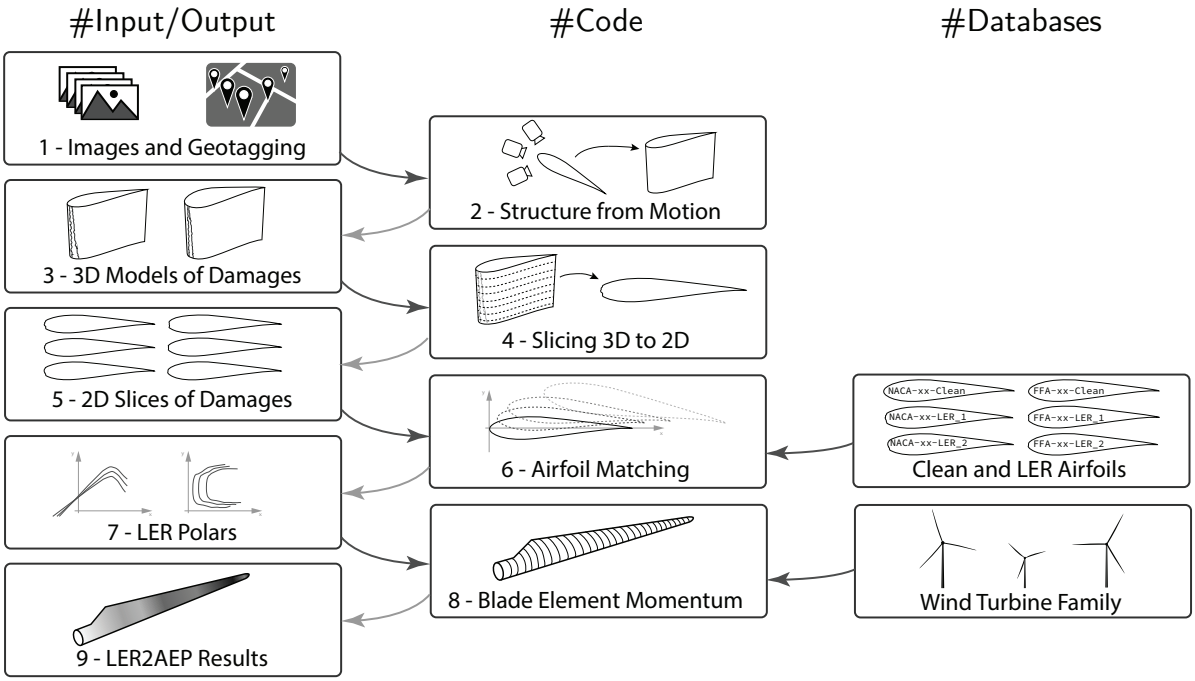

Figure 3.1: Step by step process of the LER2AEP Method.

3.2 Selection of Camera and Lens

A series of laboratory tests were carried out at Aalborg University (AAU) Medialogy in order to select a camera and a lens. As described in Section 2.2, it was decided to aim for a 3D reconstruction where surface imperfections of sub millimeter scale were detectable at a measuring distance of 2-3 m.

When making a high precision 3D reconstruction with the SfM technology, one of the most important parameters is the Ground Sample Distance (GSD), adopted from orthophotography. GSD can be used because the difference between minimum and maximum distance from the camera to the object is low. GSD is the pixel center distances on the surface of the photographed object. A low GSD is one of the components in a more detailed 3D reconstruction. The quality of the 3D reconstruction also depends on light conditions, focus and object material and texture. The light conditions, object material and texture may be difficult to change on an in situ blade scan, but the robustness to changes in light, focus and GSD highly depends on the specifications of the camera. Including the parameters for getting a 3D reconstruction with sufficient accuracy and precision, the most important parameters to consider for the camera and the lens are:

- Resolution
- Sensor size
- ISO sensitivity
- Shutter speed
- Aperture
- Lens
- Weight and size
- Price
- Digital interface (Remote access to taking a photo)

Extensive research has been put into determining some of the parameters, whereas others has been chosen based on laboratory tests or requirements from different equipment such as the drone described in Section 3.4 and the on-board computer described in Section 3.4.2. The GSD is a function of camera resolution, sensor size, lens zoom and distance to the object. A high resolution, large sensor, high zoom and low distance all contributes to a low GSD.

Based on all requirements, it was chosen to base the system on a Canon EOS 5DS with a Canon 70-300 mm EF f4-5.6 L IS USM lens. The 5DS has a maximum resolution of 8688×5792 pixels (50.6 megapixels (MP)). The sensor is a "Full-frame" with dimensions of 36×24 mm. The ISO settings ranges from 50 to 12800. Shutter speed can be as short as 1/8000 seconds and up to 30 seconds. The Canon lens has a variable focal length of 70-300 mm and an aperture of f4-5.6. The aperture range is quite low, but the choice

of lens is mainly based on the desired GSD and a distance of 2-3 m to the blade. The camera and lens were at the time of buying in 2015 in the price range of 4000 Euro. The GSD can be calculated to be 0.041 mm/pixel on a 3 m distance with a 300 mm focal length on the lens. The camera with lens can be seen in Figure 3.2. The total weight of the camera and lens is 1.6 kg.

Figure 3.2: The Canon EOS 5DS equipped with the EF f4-5.6 L IS USM lens.

Other cameras and lenses fulfilling the same requirements could substitute the selected one and still be a functional scanning system.

3.3 Structure from Motion

In short, Structure from Motion (SfM), is a technique for converting 2D images such as a photograph to a 3D computer model/structure, also denoted as a 3D reconstruction. The idea was first presented by H. C. Longuet-Higgins in 1981 [63]. 3D geometries such as buildings or nature requires more photos with a higher detail than more simple geometries such as a bottle or a cup. More photos and higher detail sets high demand for computing power. With recent years rapid enhancement in available computing power, the method has matured resulting in commercial softwares such as *ContextCapture* by Bentley [64] or *Metashape* (previously *PhotoScan*) by Agisoft [65]. Among others, these softwares provides fairly good 3D reconstructions on consumer grade computers. A good overview and more in detail description of SfM is given by O. Özyesil et al. in [63].

The principle in SfM is to collect a series of 2D images from different positions (hence the "Motion") with overlaps of the object in each image. The more overlap, the easier it is for the SfM algorithms to find equalities in the images. Obviously, too much overlap does exist, as almost identical images will mainly contribute to increased computational

effort without any benefit. Exactly how many images needed for a 3D reconstruction is difficult to define and depends on the object. A typical number of images is between 10 and 50 if most of the object is captured in the photos, i.e. 50 images of a building part will not reconstruct the building. Typically, less than 10 images will fail to reconstruct anything.

The major advantage of the SfM is the low requirement for hardware. It requires a consumer grade camera to get decent results. However, as all technologies, SfM in its current state also has shortcomings. The most critical challenges to this project, as they are difficult to solve in general, are:

1) The need for recognizable features on the object. A clean and white wind turbine blade has very few features that the SfM can merge together. A leading edge without any damages has not until the current state of the project, been able to successfully reconstruct without severe noise issues. The problem was temporary put to rest by the statement that clean parts of the blade with no damages has no relevance to the project. A statement that is not entirely true, since imperfections in the production might be hidden by a clean and white surface.

2) The lighting conditions highly affects the outcome. A wind turbine parked in a position where the images will be backlit will either ruin the image or change the settings in the camera and hence changing the shadings and colors, resulting in problems with merging the images.

Other but solvable difficulties are that the number of photos needed for a successful 3D reconstruction might be challenging to get with the current available drone flight time. Having the object in focus while flying has also proven difficult due to the high focal length, yielding a very low depth of focus, highly sensitive to even small movements. Even though the drone might be steady, oscillations of the wind turbine blade can make the image out of focus.

The last of the major difficulties is the scale of the object. The photos contains no usable information about size, i.e. the 3D reconstruction could be the size of a golf ball or the moon. One way to solve this is by knowing the location/position of the image, also known as geotagging. I. Nikolov and C. Madsen published an article with a solution approach for defining the absolute scale of the 3D reconstructed object [66].

An example of a 3D reconstruction can be seen in Figure 3.3. The left picture shows camera positions for 52 photos of a test specimen. The middle picture is a close-up of the test specimen. The right picture is a 3D reconstruction result from *ContextCapture*.

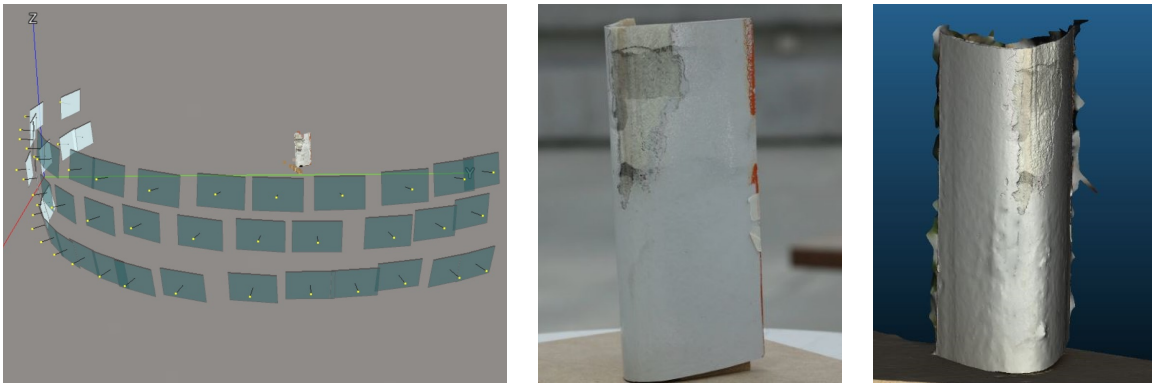

Figure 3.3: Left: Illustration of 52 camera positions. Middle: Close up of test specimen. Right: 3D reconstructed test specimen.

A series of experimental campaigns were formed through the project. Some of them are briefly described in the following paragraphs.

The first campaign important to mention was conducted as in the example above with 52 images. Different softwares were tested and benchmarked. The most promising software were the prementioned *ContextCapture* and *Metashape*. These findings were published by I. Nikolov and C. Madsen [67]. As *Metashape* was free for testing purposes and offered a good python scripting interface, the choice was made to continue with that. The experiment with the 52 images was also used to find the lower limit for the number of images needed for a satisfying 3D reconstruction. As illustrated in the left picture in Figure 3.3, the positions were repeated in three different heights: One slightly below (10 degrees to horizontal) one in the center and one slightly above. The main findings from the study was two heights with 9 images in each were sufficient, reducing the images from 52 to 18. 3D reconstructions from less than 18 images would either fail or be dominated by noise.

Other experimental campaigns were conducted in order to investigate the accuracy of the SfM method for different objects. A test specimen with steps of height 10 mm, 5 mm, 2.5 mm, 1.25 mm and 0.675 mm was developed and is depicted in the left of Figure 3.4. A 3D reconstruction of the step test specimen can be seen in the right picture of Figure 3.4. The 3D reconstruction shows reconstruction difficulties on the edges of the 10 mm step, even though the specimen is well represented by photos in the reconstruction software. It should be noted that the test specimen was painted with blue dots just to even get a successfully reconstruction. Pictures of the white edition did not reconstruct well, which illustrates the mentioned requirements for features to merge.

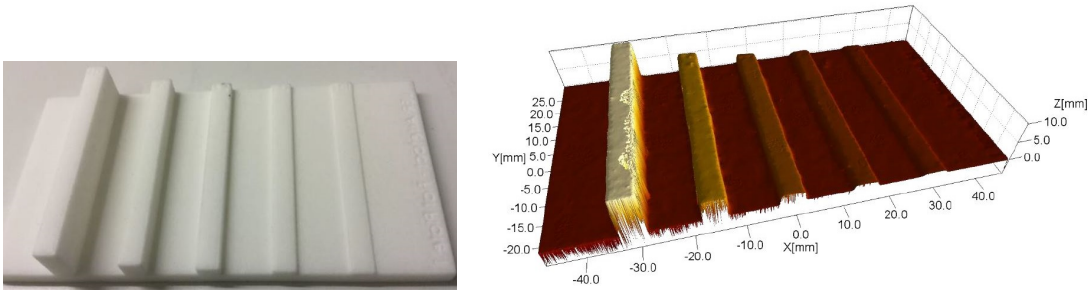

Figure 3.4: Left: 3D printed test specimen with step heights of 10, 5, 2.5, 1.25 and 0.675 mm. Right: Height map of 3D reconstruction step test specimen.

Another laboratory experimental campaign was conducted on a selection of sand grain papers/sandpapers. Sandpaper has been used in wind tunnel experiments to emulate a distributed surface roughness/LER. Sandpaper is well defined from standards [68] and even though the pattern of which the sand grain lies is random, it is still far less stochastic compared to erosion on a wind turbine blade. The order of magnitudes are similar on erosion and sandpaper which is why it was chosen as test specimens. The results for for 3D reconstructions and measurements of both the step height test speciment and the sandpapers can be seen in Article 5 found in Appendix G with reference [61].

An example of a realistic experimental campaign was the *Vindeby campaign*. *Vindeby* was the first offshore wind turbine farm in the world. The wind farm was fully decommissioned in 2017. One of the wind turbine blades ended at Risø for research purposes. The blade had some damages from transporting. The left picture in Figure 3.5 shows a photograph of a damage and the right picture shows the textureless 3D reconstruction of the same damage.

Figure 3.5: Left: Close up photograph of a transport damage on a decomissioned wind turbine blade. Right: Textureless 3D reconstruction of the damage.

As mentioned, a 3D reconstruction is of arbitrary size. Geotagging combined with the scaling algorithm by I. Nikolov [69] has provided dimensions for the experiments

conducted later in the project. The above results was used for calibration of the final method. The experiments used to test the final method and a validation of these will be shown in Section 3.5.

As a final note on SfM, setup of a test environment and acquisition of images proved to be time consuming. I. Nikolov and C. Madsen published a solution where 3D models are rendered to emulate 2D photographs and used as input to the SfM [69], which could come in very useful especially with wind turbine blades hard to reach. Unfortunately the solution was developed too late in the project to be utilized.

3.4 Drone

It is stated in the EUDP project application that acquisition of surface topology data should be done from a drone. In the recent ten years, the drone development has skyrocketed. The confidence on the continued development was high before the project. The first hope was that a commercial platform capable of doing what was needed would be available in reasonable time. This turned out not to be the case, and a drone system based on open source software was purchased early in the project. The system then turned out to be challenging to modify and make a stable platform for the camera. On top of that, it proved difficult to get the necessary personnel for the task. 18 month into the 36 month project, it was decided to go for a recent developed system by DJI. Although not solving all problems, the DJI Matrice 600 Pro had many of the features needed to develop an autopilot and acquiring the images.

The DJI Matrice 600 Pro had redundant hardware, minimizing the risk of failure and setbacks. It also had the option of a high precision Global Positioning System (GPS). The combination of payload and flight time was the highest at market at the current time, without building a drone from scratch. Lastly and most important, it had the new DJI Software Development Kit (SDK). The SDK allows some limited third party input to the flight controller, making it possible to control it with a small computer instead of the remote control.

The DJI Matrice 600 Pro can be seen partly equipped with accessories in Figure 3.6. The Canon EOS DS5 is mounted in the gimbal. The accessories are described in Section 3.4.1.

Figure 3.6: The DJI Matrice 600 Pro used in the project, equipped with the Canon EOS DS5 and the Ronin gimbal.

With a combined load of the gimbal and camera of 4 kg and a resulting takeoff weight of nearly 15 kg in total, the current drone regulations requires that the operators have a drone license. Four people in the project got the drone license, including the Ph.D.

One major shortcoming of the DJI Matrice 600 Pro is that it has no built in autopilot nor the sensors to accommodate an autopilot. Neither does it has a forward facing camera, which makes it difficult to operate it close to a wind turbine blade at high distances between the operator and the drone. Even though it allows third party inputs, it does not have a built in computer to execute the commands. Lastly, the SDK was in a beta state at the time, resulting in lack of documentation and quite a lot of bugs in the system. The solution approaches for these shortcomings can also be found in Section 3.4.2 and 3.4.1.

3.4.1 Selection of Drone Accessories

Besides the camera and lens described in Section 3.2, the drone was equipped with some extra hardware to solve the shortcomings described above. These are listed and briefly descrbied in the following.

3.4.1.1 GPS/RTK

The drone comes with an out-of-the-box GPS. The accuracy is within 1 m. The drone needed to fly within a few meters of the blade, so a 1 m accuracy was to low. The add on Real-Time Kinematic (RTK) system by DJI was purchased on the promise of 10 cm

accuracy in decent weather conditions. The RTK system provides a ground station that is used together with the GPS satellites.

3.4.1.2 Gimbal

A DJI Ronin MX gimbal was put on the drone to both stabilize the camera and allow it to tilt and rotate without moving the drone. The gimbal movement could be controlled through the SDK and hence moved by the autopilot algorithm. The tilting function is especially handy when acquiring images from below and above a damage, since tilting of the drone itself would result in propulsion.

3.4.1.3 Raspberry Pi 3

The Raspberry Pi 3 is a small Linux based computer. The Raspberry Pi handles the inputs from the sensors and sends instructions to the drone. One strong advantage of the Raspberry Pi is the Linux system, allowing different kinds of algorithms to be executed. Combined with the USB interface, this makes it powerful in a development state. A later replacement by a small Programmable Logic Controller (PLC) could make sense, as the Raspberry Pi is not particularly robust.

3.4.1.4 Xbee

The Xbee is a small wireless communication device allowing the ground station computer to communicate with the Raspberry Pi, as the drones communication channel is locked.

3.4.1.5 LiDAR

The Light Detection and Ranging (LiDAR) is used as a distance sensor on the drone. The LiDAR should work in sunlight in distances of 0-30 meters and with a sufficient high angular resolution and with a maximum weight of 0.5 kg. A Hokuyo UTM-30LX was found to be the only LiDAR meeting the requirements within reasonable pricing (below 7.000 Euro in 2016). It has an USB interface providing an easy setup for communication with the Raspberry Pi.

3.4.1.6 Front Facing Camera

The front facing camera selected was a small radio based 720p camera. It was chosen to be radio based in case of lag on the communication to the drone, as this was experienced through the development phase. A radio based transmission does not have lag but a bad signal is seen as noise on the display instead.

3.4.2 Development of Autopilot

From the beginning it was expected that some work had to be put into an autopilot. The final scale of the workload was unexpected. Not only was the tasks piling up, the necessary manpower and competences were unavailable. None of the personnel in the

project had prior experience with drones. However, the Ph.D., E. K. Kruse, has a background in mechatronics and control engineering and the key person from AAU, I. Nikolov, has a background in computer vision. Furthermore, a colleague from Power Curve ApS, N. Koldkjær also has a background in mechatronics and control engineering. Out of necessity of an autonomous flight when flying close to a wind turbine blade, it was decided to make a combined effort to develop an autopilot.

The hardware setup for the drone autopilot prototype is outlines in Figure 3.7. The desired flight pattern is described in Section 2.2.

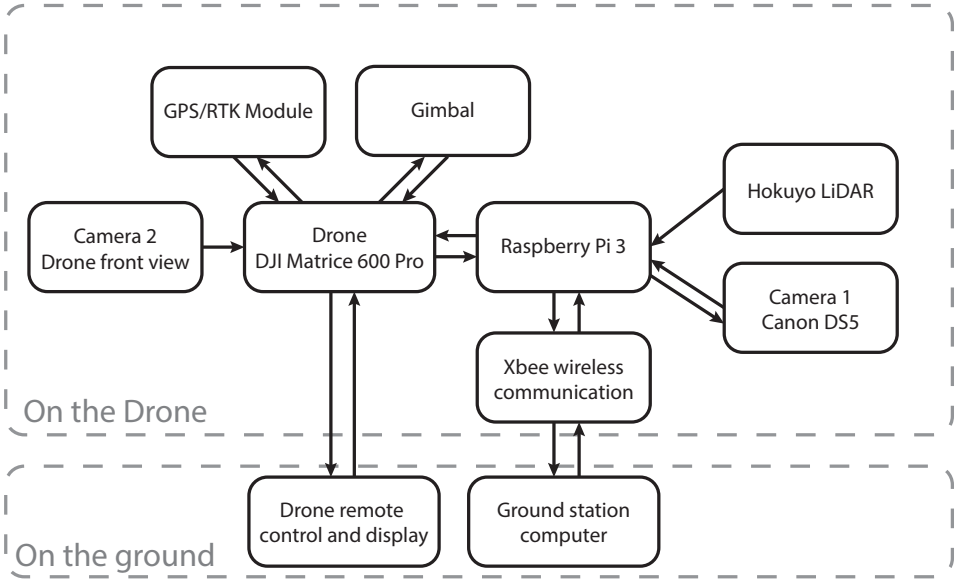

Figure 3.7: Overview of the drone and extra hardware used in the autopilot algorithms. The arrows shows the communication between hardware.

A series of algorithms were written in python and C++ and stored on the Raspberry Pi. They were activated from the ground station computer. Sadly, the autopilot development was never completed to a fully functional stage, as an error on the RTK system resulted in a crash of the drone and 6 months repair time of parts. Nevertheless, the autopilot was 90% functional with minor inputs from the ground station of when to initiate the semi circle flight patterns around the blade tip. A series of images were acquired by the drone shortly before the crash, but the images were a little out of focus which resulted in a failed 3D reconstruction. I. Nikolov published a method for calculating position references from the LiDAR measurements [70]. Therefore, the final tests of the SfM was made by hand from a lift. These images were utilized in Section 3.5.

Development of the autopilot required a vast amount of testing which, until the acquiring of the drone licenses, had to be carried out at a remote testing facility at Aalborg Model Airplane. Later in the project, most of the test flying would be at the mock-up described in Section 3.5.

3.5 Validation of Structure from Motion

Since Structure from Motion (SfM) is a technique mostly used for 3D reconstructions where the exact scale of the object is of little importance, the method had to be validated in the project. Based on the findings in Bak et al. [5], the initial objective was to achieve sub millimeter precision of the 3D reconstruction. Danish Fundamental Metrology (DFM) was included in the project as they have the means of high precision validation of measurements.

The validation of SfM has been an ongoing process since the beginning of the project starting with laboratory experiments and later field experiments, with some of them briefly described in Section 3.3. It was stated in the project application to EUDP, that the final validation of the SfM should be a field trial on a real wind turbine blade where the images should be acquired by a drone. The ambitions for the final test were reduced primarily due to three reasons: 1) Replicating damages would require access by rappelling down the wind turbine blade. Capabilities that were not within the project consortium at the moment. 2) Access to wind turbines with sufficient LER. 3) Immature drone autopilot technology. The drone system was not thoroughly tested and risk of failure during flight was deemed too high.

It was decided to simplify the validation test but still keepign it realistic. A mock-up was constructed and placed in the backyard of Power Curve ApS. The outer two meters of a decommissioned Vestas V80 blade was put in the mock-up. It served as testing platform for both drone autopilot development and SfM. The mock-up with blade tip can be seen on the left picture in Figure 3.8. Furthermore, the images were acquired manually with the Canon EOS DS5 from a lift instead of the drone, as the drone was still not ready at the time of the test. The lift was placed in the same positions as intended for the drone described in Section 3.4, and since the lift was quite shaky, the accuracy of camera positions was within the expected range as for the final drone system.

The validation by DFM was done by replicating small areas/patches with an epoxy based adhesive and later taking it to the laboratory where the surface topology was measured on a Confocal Microscope (CM). Three areas were selected for the replication. These areas can be seen on the right picture in Figure 3.8.

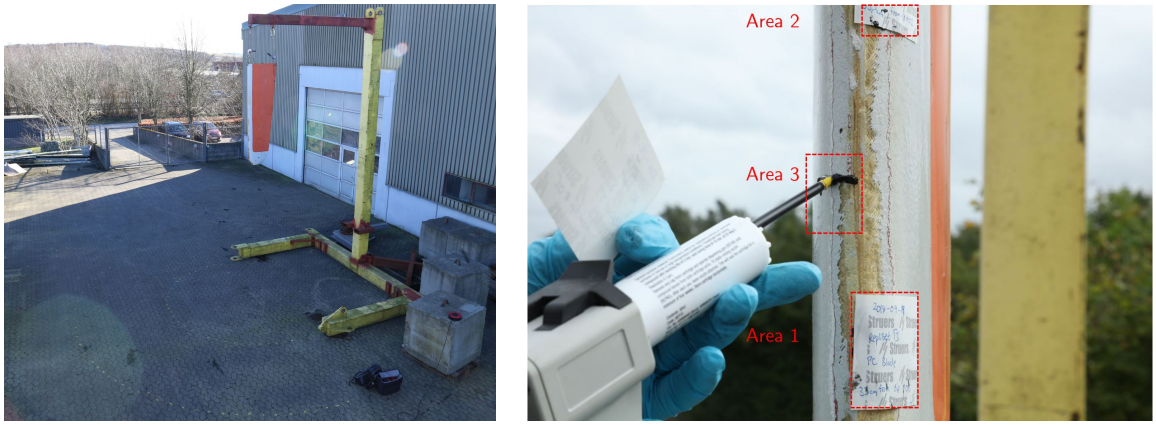

Figure 3.8: Left: Mock-up for testing purposes of drone autopilot and SfM. Right: Close-up of the blade tip leading edge with three areas selected for replication and validation in the laboratory.

This overview is of qualitative character and does not go into much detail on numerical values, as it is outside the scope of this thesis. It merely serves as an overview of the processes. Detailed analysis of the SfM validation is still in writing by M. S. Nielsen, I. Nikolov and E. K. Kruse, but a draft version of Article 5 can be found in Appendix G with reference [61].

Area 1 can be seen in Figure 3.9 with the CM laboratory measurement to the left and the SfM to the right. The lower resolution of the SfM method can be seen from the blurriness. The glass fibers from the blade appears in the CM measurement whereas the SfM measurements show less detail. The Z ranges, being the difference between minimum and maximum height, are 1.550 mm and 1.446 mm and thereby deviating with ≈0.1 mm (≈7%). The deviation might be a result of the scaling algorithm described in Section 3.3 that needs further calibration. A step from the glass fiber to the surface coating is clearly seen in both experiments.

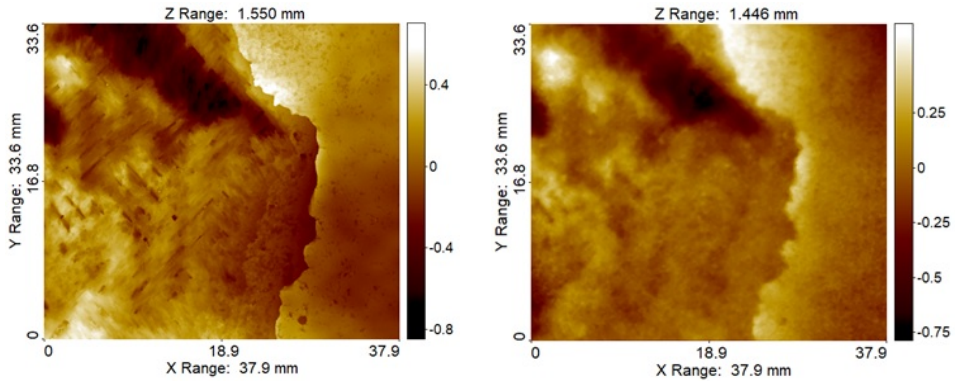

Figure 3.9: Area 1 comparison of CM to the left and SfM to the right. The glass fibers clearly show in the CM and less clear in the SfM. However, the lower frequency changes are well caught by SfM.

Area 2, shown in Figure 3.10, has similar tendencies to the results for Area 1. The Z ranges are 2.853 mm and 2.651 mm, and hence deviates ≈0.2 mm (≈7%). The edge between the glass fiber layer and the coating can be seen going down the center of the depicted surface topology.

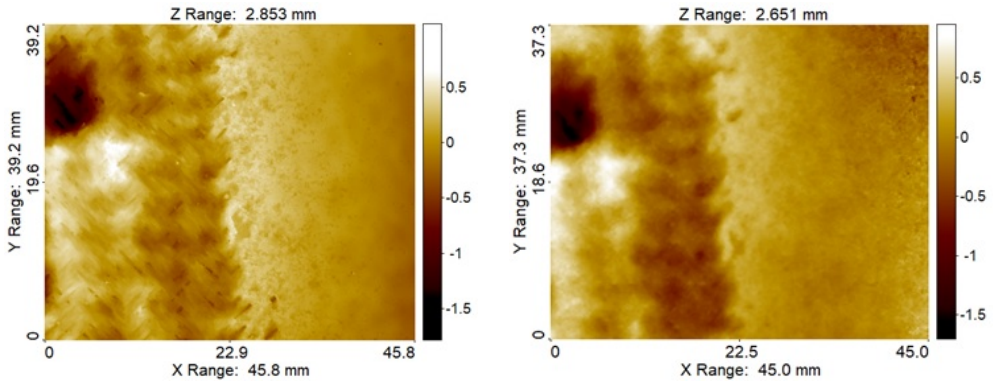

Figure 3.10: Area 2 comparison of CM to the left and SfM to the right. Again, the lower frequency changes are caught by SfM.

Area 3 is located on the other side of the leading edge. The dark area in both the CM and SfM in Figure 3.11 show a step in height as in Area 1 and 2. The Z ranges are 2.396 mm and 2.717 mm, with a deviation of -0.3 mm (≈12-13%). The deviation is negative compared to Area 1 and 2 and suggests that either the conditions for the SfM on this side of the blade are different or the postprocessing algorithms needs more work.

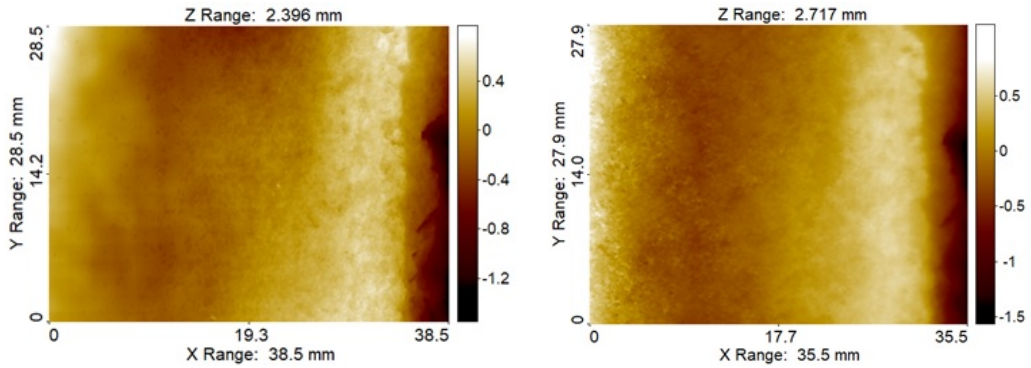

Figure 3.11: Area 3 comparison of CM to the left and SfM to the right. The glass fibers does not show as the damage might not be deep enough. As in the Area 1 and 2 patches, the lower frequency changes are caught by SfM.

Despite the inconsistencies, the differences are considered to be minor and acceptable at the current state of the technology. Several iterations of testing and calibration of the SfM method needs to be done. However, the resolution is sub millimeter as inconsistencies in deviation are below 0.5 mm in total. The larger steps in height are caught in all three areas.

Obviously, three areas on one wind turbine blade tip does not validate the method. At best, it verifies some intermediate step in the process. It does however give comfort in the technique, the developed methods and the processes. It allows for further work to be continues in parallel to improving the SfM. The surface height topology measurements of this particular blade will be utilized as the basis for three examples of blades with LER illustrating the LER2AEP method in Chapter 6.

CHAPTER 4
Simulating Aerodynamic Performance of Airfoils with LER

The aerodynamic performance of an airfoil can be found based on measurements or based on calculations using different kinds of mathematical models. Accurate measurements on an airfoil is not straight forward and often requires a vast amount of sensors, a confined space and high wind speeds. This can be achieved in a wind tunnel. Accurate calculations requires a code that has been validated extensively against measurements and experience in how to make the setup of the code, i.e. generation of mesh, choice of boundary conditions and choice of turbulence model.

In this project it was decided to carry out wind tunnel measurements partly to investigate how complex surface topologies influence the aerodynamic performance and partly to validate the simulations. Also, it was decided to carry out simulations to be able to carry out parameter studies including hundreds of realizations of surface configurations.

Tests from two wind tunnels were used in this project. One was the open return Laminar Wind Tunnel of the Institute of Aerodynamics and Gas Dynamics (IAG), University of Stuttgart (hereafter noted as "IAG Wind Tunnel"), and the Poul la Cour Tunnel at the Technical University of Denmark (DTU) (hereafter noted as "DTU Wind Tunnel").

Two methods for prediction of the aerodynamic properties of an airfoil were used in this project: A panel code and Computational Fluid Dynamics (CFD). The panel code XFOIL [71], mentioned in Section 2.3, is particularly efficient in engineering applications due to the low calculation time and low hardware requirement. A full set of airfoil polars can be calculated within a few seconds on any consumer grade computer. The downside of a panel code is that it is limited to 2D airfoil analysis and can be difficult to use if the surface is not smooth, i.e. if sudden jumps in curvature of the airfoil are observed. Where panel codes are developed for estimating aerodynamic performance of airfoils, CFD is a general purpose model. CFD can simulate most fluid flows if the proper models are utilized. CFD models consist of two parts: The mesh and the solver. The mesh describes the geometry and the solver describes the physics. There are many ways to simulate airfoils in CFD which often depends on the software used to simulate. In this project, the DTU Wind Energy in-house CFD code, EllipSys, is used in both the 2D and the 3D version [72–74].

As described in Section 2.3, attempts to simulate Leading Edge Roughness (LER) on wind turbine blades and airfoils have been published and tested. So far, none of the methods has become a de facto standard, and the way to simulate and test LER is still being discussed.

In the past, aerodynamic performance of airfoils with LER was evaluated by assuming fully turbulent flow, i.e. transition from laminar to turbulent flow appeared at the very leading edge and no part of the boundary layer was laminar. However, apart from this very simple assumption, LER can be applied to a CFD simulation of an airfoil in at least three different ways: 1) By changing the mesh, 2) by adding certain boundary conditions or 3) a combination of both. Figure 4.1 illustrates the three methods. The top picture is an example of the mesh around a NACA 63_3-418. The pictures below show a zoom in on the leading edges where the left picture shows changes in the geometry with a cavity of 0.3%c depth going from 3%c on the pressure side (PS) to 3%c on the suction side (SS) and where LER is represented by the edges. The right picture is unchanged compared to the upper picture but with LER is represented through boundary conditions on the airfoil.

A further zoom in is shown at the lower pictures, where LER at the left picture is simulated through the edge of the cavity that is orthogonal to the original surface. At the mid picture a combination of geometry changes (the edges) and introduction of boundary conditions are illustrated by the red curve in the middle and at the right picture only a change in the boundary condition is introduced. A boundary condition was suggested by Knopp et al. [51] and was implemented in EllipSys and this model was tested in this project.

In wind tunnels the performance of airfoils for wind turbines with LER was evaluated in many tests by adding zigzag tape at the suction side 2%c from the leading edge and at the pressure side 10%c from the leading edge. This has been and still is the common way of evaluation LER. However, because the aerodynamic wind turbine performance is significantly influenced by the drag increase at low angles of attack and the decrease in maximum lift it is important to understand the impact of LER on drag and maximum lift in combination. An increase in drag at low angles of attach will result in a decrease of the power curve at low wind speeds and especially when the wind turbine operates at variable speed. A decrease in maximum lift will influence the power curve close to rated power, where a significant part of the potential energy production can be lost due to LER. Thus, in this project the common way of evaluating LER in wind tunnels is tested to investigate whether this is a good way of testing or if other ways of simulating LER should be considered. Thus, apart from testing LER using the common way with zigzag tape, also zigzag tape in different positions and different heights were tested. Furthermore, sandpaper with different grain sizes and a cavity was tested.

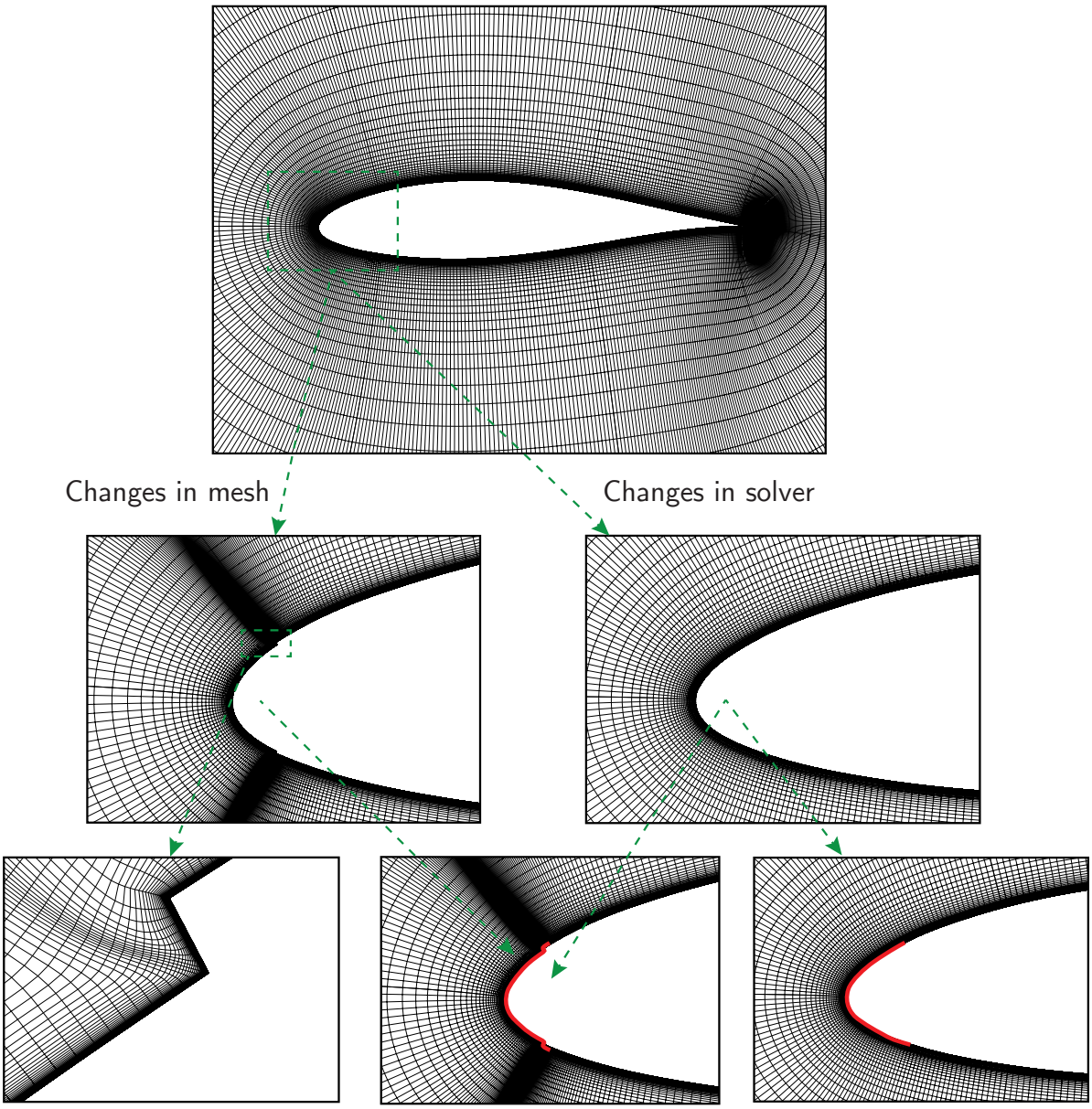

Figure 4.1: Illustration of a NACA 63_3-418 airfoil with LER as geometrical changes and solver changes or as a combination are illustrated by the red curve.

All investigations of the impact of LER on airfoil performance was carried out on the NACA 63_3-418 airfoil. This is chosen partly because this airfoil geometry is known and open and partly because this airfoil was frequently used for wind turbines until a decade ago. In this chapter a more fundamental validation of the simulation of the performance of the NACA 63_3-418 is described in Section 4.1. Whether changes in the surface geometry like e.g. edges can be simulated correctly is investigated in Section 4.2. This is followed in Section 4.3 by an investigation of how well an addition of surface roughness through a boundary condition can simulate the performance of an airfoil with LER. Because the investigations in Section 4.2 showed that changes in the surface geometry can be simulated in a trustworthy way, Section 4.4 describes a parameter study that was carried out to investigate how changes in the geometry of different sizes and at different positions affected the airfoil performance. Finally, Section 4.5 describes wind tunnel tests of the airfoil that was carried out using different ways of emulating LER.

4.1 Aerodynamic Predictions of a Clean NACA 63_3-418 Airfoil

The NACA 63_3-418 airfoil that was tested in the IAG Wind Tunnel founds the basis for most simulations presented in this thesis and the related publications. The airfoil used in the experiments was a NACA 63_3-418 airfoil with a chord length of 0.60 m and a span width of 0.73 m mounted vertically from floor to ceiling in the 0.73 m high and 2.73 m wide test section. The clean airfoil has been simulated with EllipSys2D, and this section gives an overview of the results. The results shown are the ones denoted as "Clean" throughout the thesis and used in the articles [1–3].

The mesh is constructed as an o-mesh with the DTU in-house code HypGrid2D [75]. The chord length of the simulated airfoil is 1.0 meter. The mesh has a radius of 45 times the chord length and can be seen in the left picture of Figure 4.2. A closeup of the airfoil can be seen in the middle picture of Figure 4.2. The mesh is divided into blocks each with the same amount of cells on both sides and with the same amount of cells in each of the blocks. The blocks with the inlet and outlet can be seen in the right picture of Figure 4.2. The outlet is marked with small lines outside the domain. The flow direction is left to right.

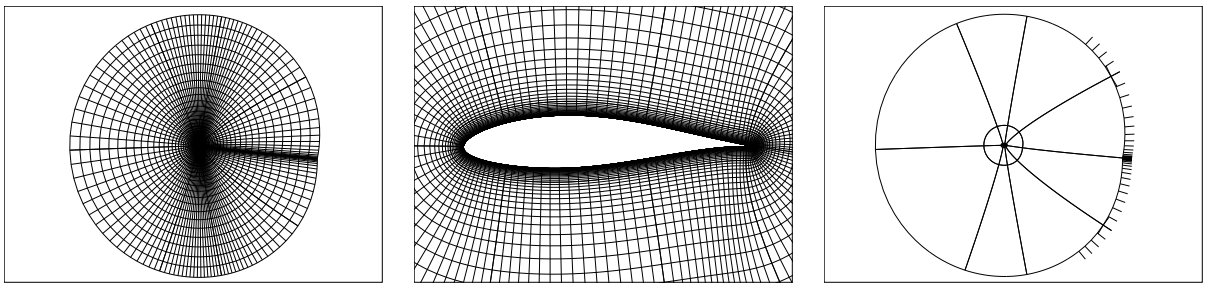

Figure 4.2: Left: 1/16 cells in the total domain. Middle: 1/16 cells around the airfoil. Right: Cell blocks with inlet and outlet.

The simulations are made with laminar inflow and free transition. The transition is simulated by the e^N model. The N factor is set to 9, as this corresponds to the turbulence intensity of the IAG Wind Tunnel. The same setup is used in all simulations with laminar inflow. Simulations with turbulent inflow does not use the transition model. The Reynolds number is Re = 3 million.

Figure 4.3 shows the experimental lift and drag coefficients C_l and C_d for -5 to 15 degrees Angle of Attack (AoA). The lift coefficient shows good correspondence within 1% from -5 to 9 degrees AoA. The stall occurs at higher AoAs in the simulations and it is less severe. The drag coefficient is slightly underestimated with around 5% in the linear lift region.

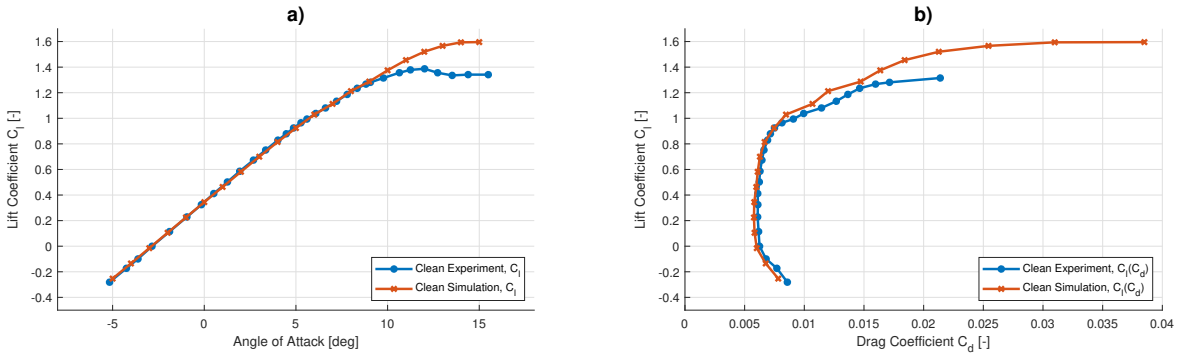

Figure 4.3: Experimental and simulated a) lift coefficient C_l as a function of AoA and b) lift coefficient C_l as a function of drag coefficient C_d.

The pressure coefficients C_p for -10, -5, 0, 5, 10 and 15 degrees AoAs can be seen in Figure 4.4. The simulated pressure coefficients agree in general well with experiments. However, the pressure coefficients deviates slightly at 10 degrees AoA and significantly at 15 degrees AoA. This deviation is seen at 80%c for 10 degrees AoA, where an adverse pressure gradient starts to form. The 15 degrees AoA shows and adverse pressure gradient from 40%c till the trailing edge, revealing an early separation. The simulations has the same tendencies although it separates in 60%c instead of 80%c. The suction peak is overestimated in the simulation as well, resulting in a higher lift coefficient. The deviation of the predictions in the stall region could origin from wall effects in the wind tunnel and/or from the turbulence model in the EllipSys2D code not estimating the development of the turbulent boundary layer correctly.

The simulations were considered acceptable within the scope of the application described in Chapter 2, 3 and 5. However, since the simulations showed an expected overprediction of $C_{l,max}$ the expected reduction in $C_{l,max}$ due to LER should be evaluated as a relative decrease compared to the simulated Clean conditions in contrast to an absolute comparison.

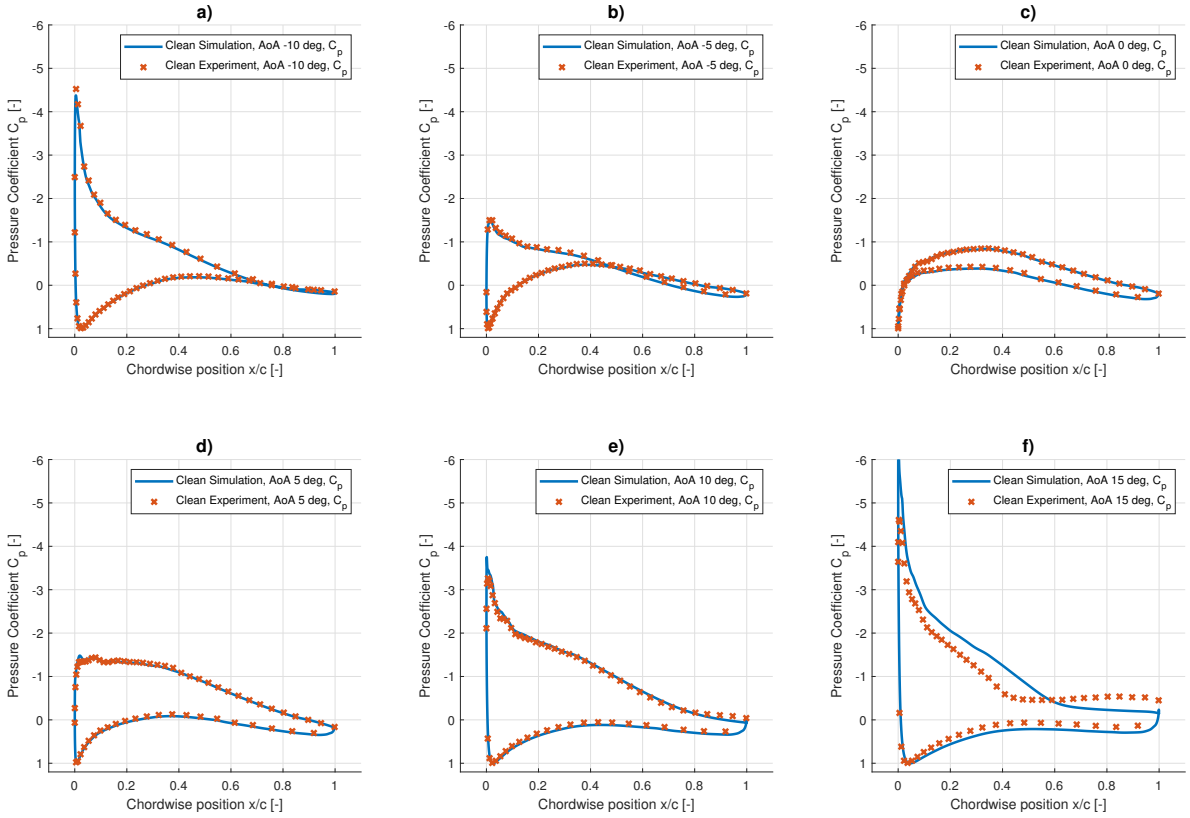

Figure 4.4: Pressure coefficient C_p comparison between simulations and experiments for -10, -5, 0, 5, 10 and 15 degrees AoA.

4.2 Aerodynamic Predictions by Geometrical Representation

In the beginning of the project, it was still unclear if the CFD code was able to predict the aerodynamics of airfoils with small protuberances modelled directly into the mesh. In effort to determine how well EllipSys did this, the experimental data with zigzag tape from the IAG Wind Tunnel were used. The airfoil used in the experiments was the NACA 63_3-418 airfoil as described in the section above. Due to the lower complexity and computational time, it is desired to run CFD simulations in 2D. However, zigzag tape is in itself a three-dimensional shape and varies in chord position throughout the span of the 2D airfoil. This might introduce crossflows unpredictable by a 2D CFD simulation. Based on this, it was chosen to make 3D simulations as well and analyze the differences. The zigzag tape has heights of 0.4 mm and 0.8 mm. The chord was 600 mm resulting in protuberance heights of 0.067%c and 0.13%c, respectively.

This work resulted in *Article 1*, found in Appendix C, containing the submitted article, reference [1]. Description of the experimental setup, the meshing and the flow solvers can be found in this reference. This section brings the most important findings and conclusions.

Figure 4.5 and 4.6 shows the changes in lift and drag coefficients compared to the clean simulations. **Note** that in the original article found in Appendix C, the axes are shown differently in the figures. In the c) and d) plots, the lift decrease is calculated as $(100 \cdot (C_{l,Clean} - C_{l,Rough})/C_{l,Clean})$ and the drag increase is calculated as $(100 \cdot (C_{d,Rough} - C_{d,Clean})/C_{d,Clean})$. The simulated clean has been added for reference in the plots, however, the rough and clean values used in the increase/decrease calculations are either from experiments or simulations, respectively. The results are identical to those presented in [1], but Figure 4.5 and 4.6 has been plotted as percentage increase and decrease rather than a ratio in order to streamline with the other articles in the following sections. Simulations are denoted by CFD and experiments by WT. 2D denotes a 2D simulation, 3D denotes a 3D simulation and the pseudo-2D denotes a simulation where the airfoil with a 2D representation of the zigzag tape is extruded to 3D, i.e. the zigzag tape is simulated as a strip/normal tape.

Figure 4.5 shows the results for the 0.4 mm zigzag tape. Good correspondence between the experiments and all simulations are seen from 0 to 8 degrees AoA. In plot c) the percentage changes becomes high for negative AoA. This is due to small lift coefficients where the differences are in the order of the lift coefficients. The stall starts introducing above 8 degrees AoA, where the 2D simulations predict the lift changes better than the 3D simulations. Similar to the lift, the drag is predicted best by the 2D simulations in the linear region. In the stall region, the 3D simulations seems to do a better drag prediction, based on the trend of the last two drag measurement. There are no drag measurements above 9 degrees AoA, as the wake rake was removed from the IAG Wind

Tunnel in the stall region to protect it from high and dynamic loads. In general, all simulations predicts the relative drag quite well in the linear lift region, with values of around 80% drag increase.

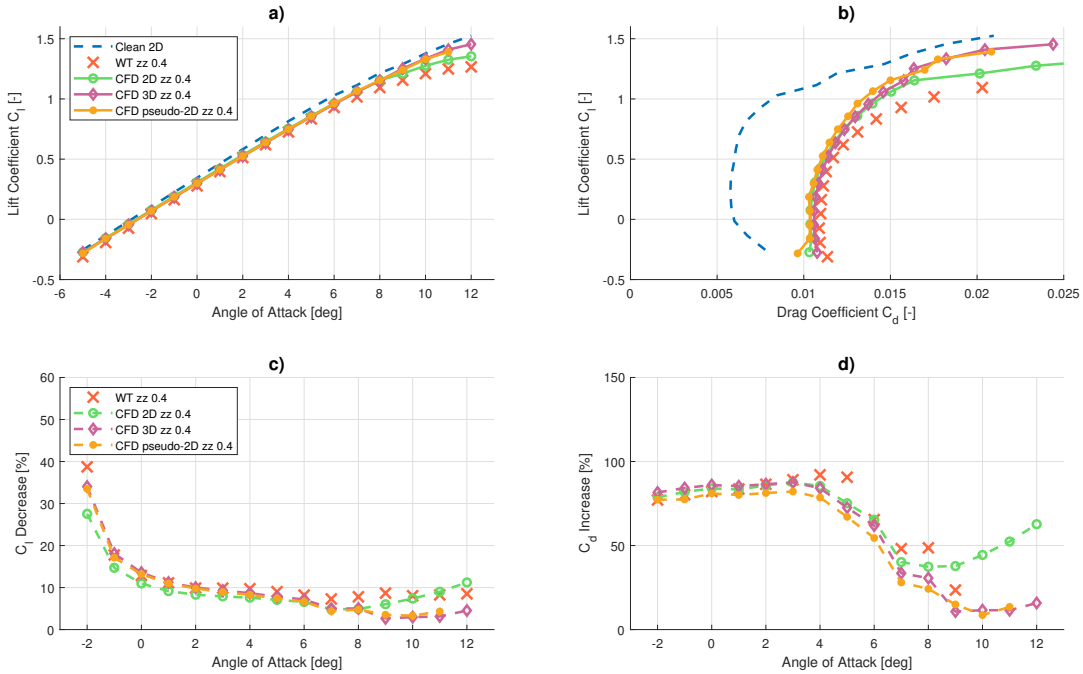

Figure 4.5: Wind tunnel experimental results and simulations for a NACA 63_3-418 airfoil with 0.4 mm zigzag tape for: a) Lift coefficient C_l. b) Drag coefficient C_d. c) C_l decrease relative to the clean airfoil. d) C_d increase relative to the clean airfoil. Experimental data has been interpolated from -5 to 12 with steps of 1 degree AoA for calculation purposes [1].

Figure 4.6 shows the results for the 0.8 mm zigzag tape. The penalty on the lift is higher, especially in the stall region, and the 3D simulations starts to show better predictions than the 2D simulations. The 2D simulations show a small overprediction of the lift coefficient. The drag is higher for all AoAs. At first glance, the absolute drag prediction for the 3D simulations are in very good agreement with the measurements, however, when calculating it as a change relative to the clean, the 2D predicts better at low AoAs from -2 to 3 degrees whereafter the 3D seems to predict better. The relative drag penalties are less concise than for the 0.4 mm zigzag tape.

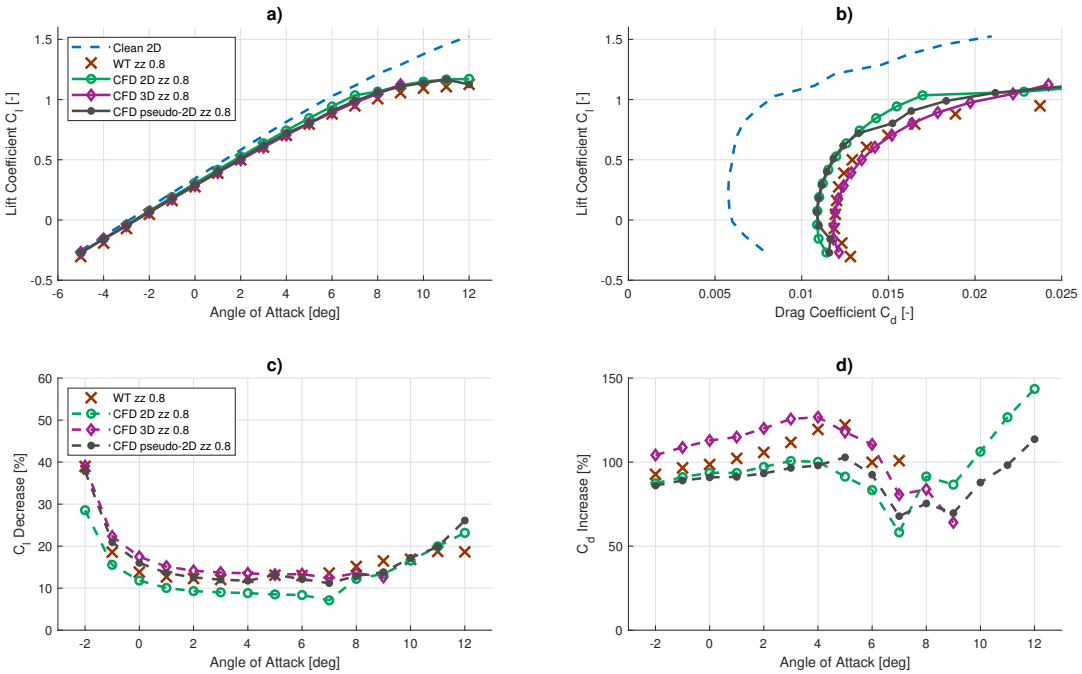

Figure 4.6: Wind tunnel experimental results and simulations for a NACA 63_3-418 airfoil with 0.8 mm zigzag tape for: a) Lift coefficient C_l. b) Drag coefficient C_d. c) C_l decrease relative to the clean airfoil. d) C_d increase relative to the clean airfoil. Experimental data has been interpolated from -5 to 12 with steps of 1 degree AoA for calculation purposes [1].

Based on the above simulations and observations, the governing conclusions are that it is possible to predict the aerodynamics of an airfoil with relatively small protuberances within reasonable accuracy and with the purpose described in Section 2.2 in mind. The integral entities like the lift coefficient and drag coefficient is with the 3D simulations in general not in better agreement with the measurements than the 2D simulations. Furthermore, most of the 3D simulations above 8 degrees AoA had to be solved with unsteady flow to converge, resulting in a much higher computational time. The 10, 11 and 12 degrees AoA of the 0.8 mm zigzag tape simulation did never successfully converge, even with the unsteady solver and high relaxation parameters and has been left out of the plots. Despite the minor inconsistencies in the 2D simulations, it was chosen to continue the work with the geometrical changes in the mesh for non-distributed roughness using the EllipSys2D solver.

4.3 Aerodynamic Predictions by Mathematical Representation

As mentioned in this chapter's introduction, a distributed roughness model introduced through a boundary condition by Knopp et al. [51], has been implemented into EllipSys2D in the beginning of the project. In this section the LER introduced by this boundary condition is investigated where simulations are compared to wind tunnel measurements.

This work resulted in *Article 2*, found in Appendix D containing reference [2]. Description of the experimental setup, the meshing and the flow solvers can be found in this reference. This section brings the most important findings and conclusions.

Some inconsistencies were observed during the simulations of airfoils with rough surfaces, where the lift was decreasing and drag increasing until a certain roughness height k_r, whereafter a further increase in roughness height would result in lift and drag returning to the values corresponding to a clean surface. An analysis seeking the limitations of the roughness model was conducted.

Figure 4.7 shows the lift decrease and drag increase as a function of roughness height for 0, 4 and 8 degrees AoA. The roughness is applied to all wall cells on the airfoil. The figure shows that roughness heights above $k_r \approx 2 \cdot 10^{-2}$ resulted in a break down of the model. However, a roughness height of that magnitude corresponds to sandpaper grains with the size of 5.6 mm in diameter on a 1 meter chord airfoil. Based on experiments from samples of LER on full scale wind turbines, a 1 meter chord can have damages of this magnitude. However, the protuberances investigated in Section 4.2 seems to be more suitable for these order of magnitudes. The 0 and 4 degrees AoAs show a drop in drag increase around $k_r = 3 \cdot 10^{-4}$. Figure 4.7 c) shows the pressure and viscous components of the drag for 0 degrees AoA, where it can be seen that the drop in drag is because the pressure drag continuously increases whereas the viscous drag starts to decrease.

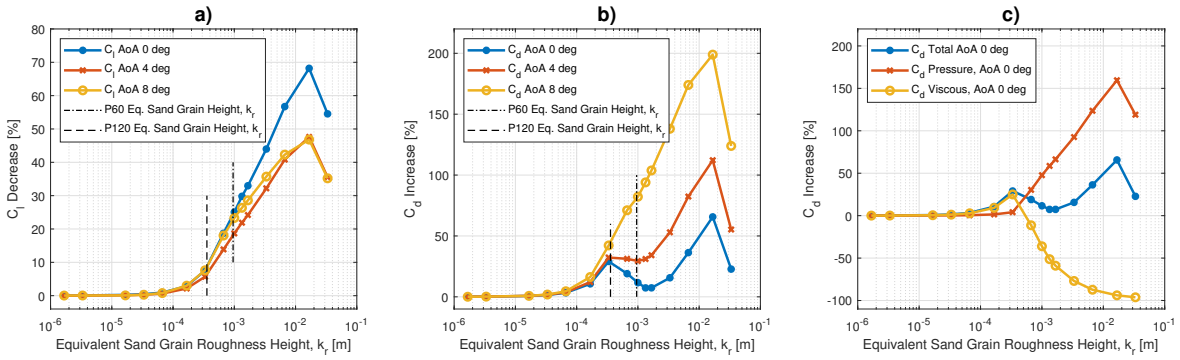

Figure 4.7: Roughness model applied to all airfoil wall cells for different equivalent sand grain roughness heights k_r for 0, 4 and 8 degrees AoA, with k_r for P60 and P120 sandpaper marked by dashed lines. a) Decrease in C_l as a function of k_r. b) Increase in C_d as a function of k_r. c) Pressure and viscous components of C_d as a function of k_r at 0 degrees AoA [2].

The simulations were compared to data collected in the same experimental campaign on a NACA 63_3-418 as in Section 4.2. The measurements of the airfoil equipped with zigzag tape are the ones used in Section 4.2. In contrary to the simulations in 4.2, the distributed roughness model requires turbulent flow to work, hence no transition model is used, and the inflow is fully turbulent. Additional details can be found in [2]. The different cases has been denoted either Exp denoting experimental data or Sim denoting simulation data. Both are given a number, No, where the corresponding LER can be found in Table 4.1.

Table 4.1: Experiments with a designated Experiment Number (ExpNo) or Simulation Number (SimNo) [2].

ExpNo/SimNo	LER Type	Location
1	Clean	-
2	P120	3%c SS to 3%c PS
3	P120	8%c SS to 8%c PS
4	P60	8%c SS to 8%c PS
5	Zigzag 0.4 mm	2%c SS & 10%c PS
6	Zigzag 0.8 mm	2%c SS & 10%c PS
7 (Sim Only)	P20	8%c SS to 8%c PS

Figure 4.8 shows the lift and drag of the airfoil equipped with sandpaper. The difference between lift for the three sandpaper types is very small in the experiments. Zooming in reveals a very small difference, where the ExpNo 4 P60 has the most impact on lift. However, the drag penalty is higher for the ExpNo 2 and 3 P120 sandpaper cases. Furthermore, it can be seen that in the simulations, the most rough sandpaper, the SimNo 2 P60, gives the highest lift penalty. The SimNo 3 P120 with the largest extension gives the second largest and the SimNo 2 P120 with the least extension has the least impact. Regarding drag, the SimNo 3 P120 gives the most drag.

A clean simulation with zero input to the roughness model results in a drag very close to the ones with an active roughness model, suggesting that the main contribution to the drag is from the inflow being turbulent rather than laminar, which suggests that the roughness model has little impact on the simulation results. Another observation is that all experiments with sandpaper gives very similar results, which is unexpected based on the assumption that a rougher surface (P60) would give more drag and lesser lift than a smoother surface (P120), which was seen in Section 4.5 and Article 4 [4].

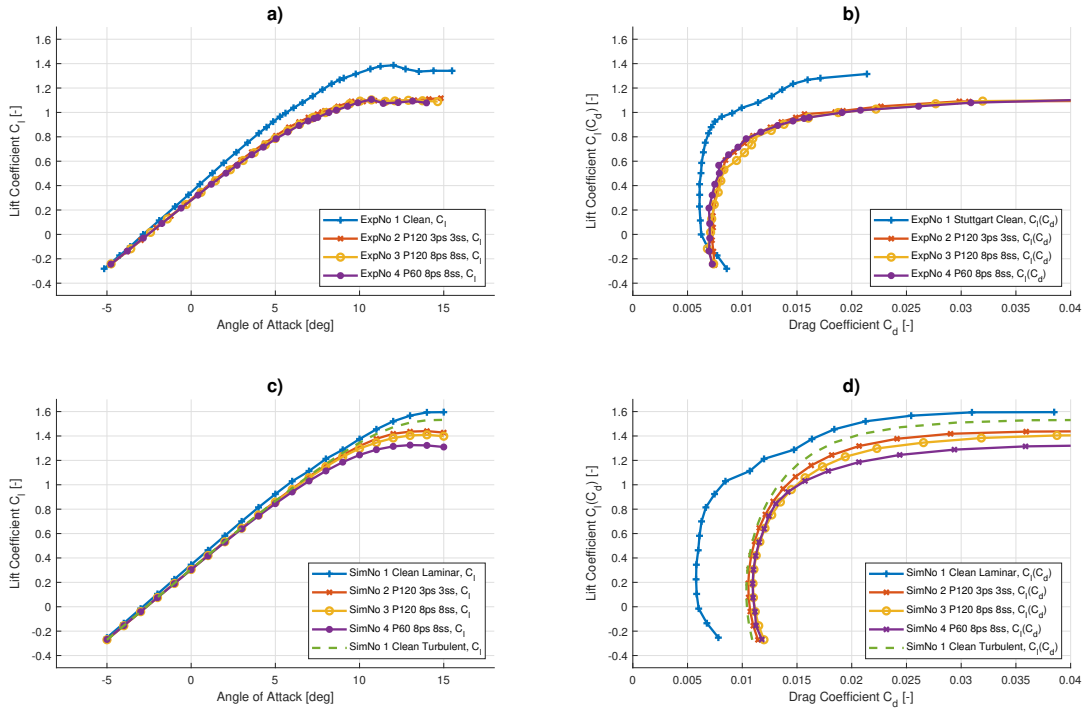

Figure 4.8: Results for ExpNo and SimNo 1, 2, 3 and 4 in Table 4.1. a) C_l as a function of AoA from wind tunnel experiments, b) C_l as a function of C_d from wind tunnel experiment, c) C_l as a function of AoA from CFD simulations and d) C_l as a function of C_d from CFD simulations. The Reynolds number is Re = 3 million in all cases [2].

Figure 4.9 shows the data from Figure 4.8 compared individually and as a lift percentage decrease and drag percentage increase. The percentages are calculated as described in Section 4.2. a), c) and e) shows that the lift is underpredicted by around 50% for most AoA. b), d) and f) shows that the drag is overpredicted by between 50-100% in the linear lift region. The drag prediction is good at 8-10 degrees AoA, but that might be due to the drag being dominated by pressure drag as illustrated in Figure 4.7.

Figure 4.9 e) and f) shows the data from a minor test simulating a P20 sandpaper, which has a roughness on the brink of the limitations in the distributed roughness model. This was done to ensure that the roughness height was not just calculated as too low a value. But, even with the P20 roughness, the lift was underpredicted and drag was overpredicted, which suggests that the model is not able to accurately simulate the influence from sandpaper on an airfoil.

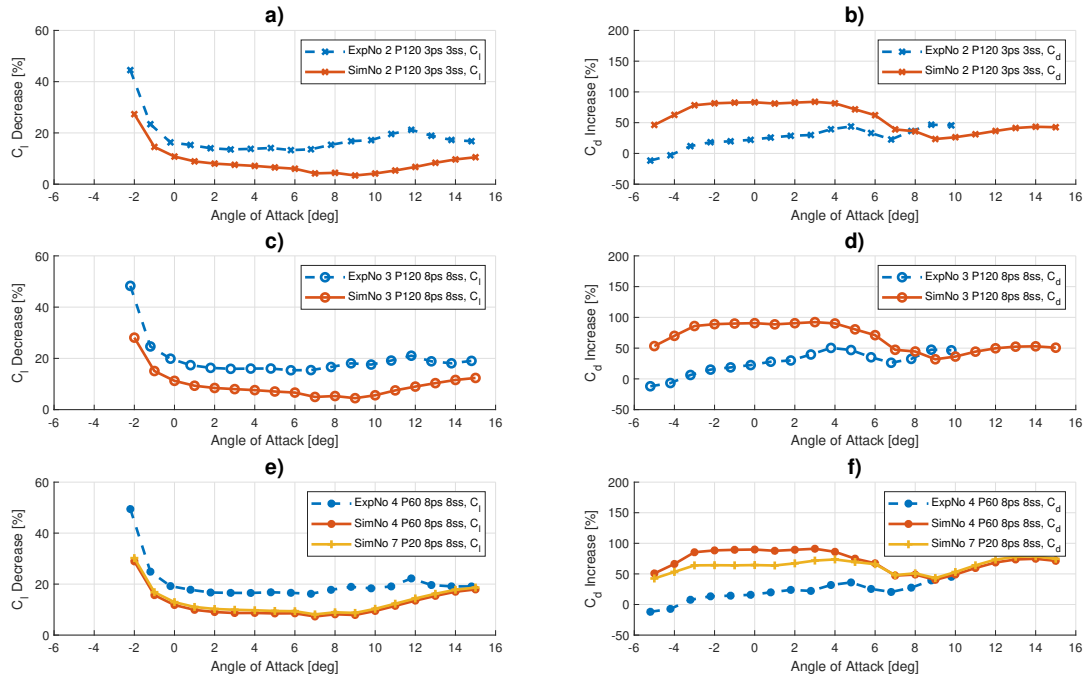

Figure 4.9: Changes in lift and drag for experiments and CFD simulations shown in Figure 4.8. a), c) and e) shows C_l *Decrease*. b), d) and f) shows C_d *Increase*. Experimental data has been interpolated from -5 to 15 with steps of 1 degree AoA for calculation purposes [2].

Since the results from the simulations with the roughness model did not agree well with the wind tunnel experiments, it was decided to test if the model was capable of simulating the impact from zigzag tape. Figure 4.10 shows the lift and drag for the airfoil equipped with zigzag tape. The zigzag tape in ExpNo 5 and 6 results in a significant lift decrease and drag increase. The simulations SimNo 5 and 6 also shows a decrease in drag and increase in lift, but the difference between SimNo 5 and 6 is very small.

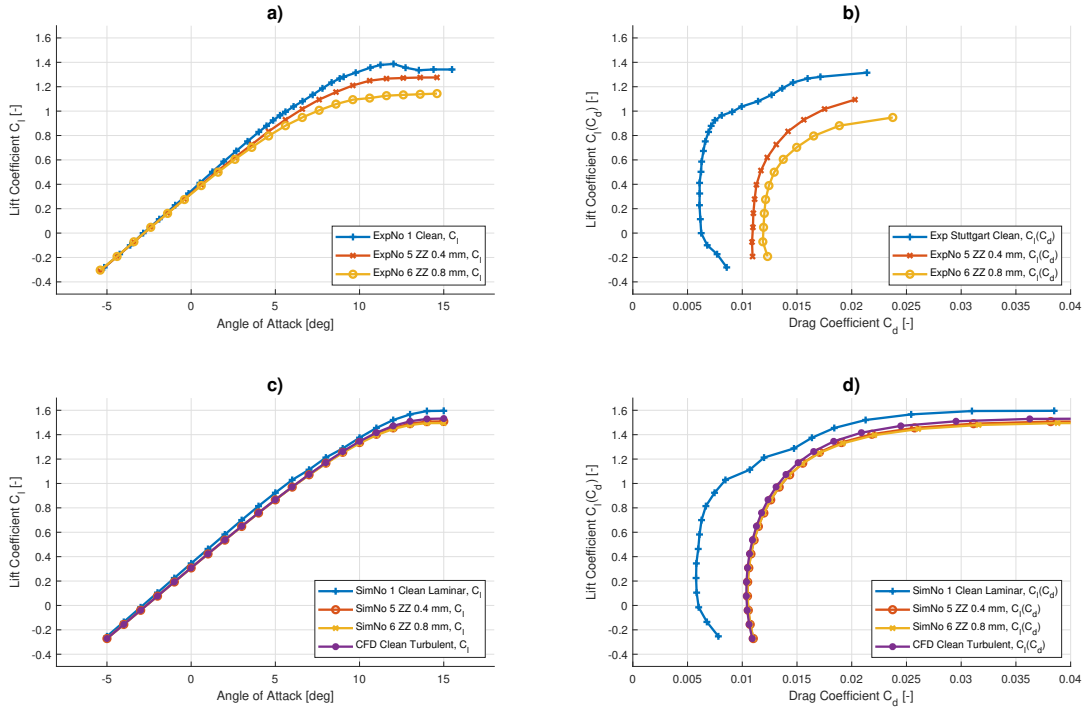

Figure 4.10: Results for ExpNo 1, 5 and 6 in Table 4.1. a) C_l as a function of AoA from wind tunnel experiments, b) C_l as a function of C_d from wind tunnel experiment, c) C_l as a function of AoA from CFD simulations and d) C_l as a function of C_d from CFD simulations. The Reynolds number is Re = 3 million in all cases [2].

By looking at the percentage changes in Figure 4.11 similar tendencies for the experiments and simulations are seen. Both the lift decrease and drag increase are of similar percentage magnitudes, especially for the SimNo 5, the 0.4 mm zigzag tape. The deviation increases when the zigzag tape height is increased to 0.8 mm. In plot e) and f), the 0.4 mm zigzag tape results are compared to the clean SimNo 1 with a turbulent inflow in the simulations. The results are very similar to a) and b), which suggests that the main contribution to the aerodynamic changes in the simulations are due to the inflow being turbulent and not due to the roughness model.

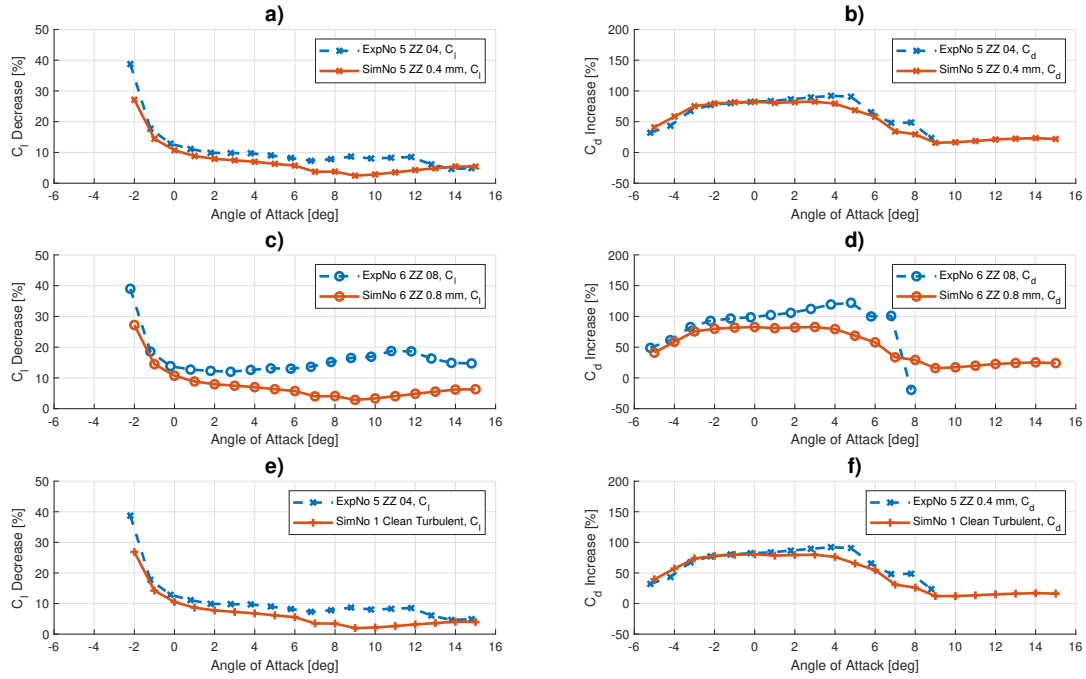

Figure 4.11: Changes in lift and drag for experiments and CFD simulations shown in Figure 4.10. a), c) and e) shows C_l *Decrease*. b), d) and f) shows C_d *Increase*. Experimental data has been interpolated from -5 to 15 with steps of 1 degree AoA for calculation purpose [2].

The conclusion is that the distributed roughness model does not predict the aerodynamic changes of a NACA 63_3-418 to an extend useful in this project. It is questionable if tweaking of the roughness model for use on airfoils can be carried out because the increase in drag is significantly overestimated compared to the decrease in lift. Another conclusion that could be useful is that zigzag tape of 0.4 mm (0.067%c) or a slightly less, resembles a fully turbulent inflow, at least for the NACA 63_3-418 airfoil.

4.4 Geometric Parameter Analysis

After investigating methods for simulating LER in CFD, it was decided to conduct a study of where parameters of a 2D surface imperfection had the most impact on the aerodynamics. This work resulted in *Article 3*, found in Appendix E, reference [3]. Description of the meshing and the flow solvers can be found in this reference. This section brings the most important findings and conclusions.

It was decided to analyze five parameters: Position, extension (parallel to the surface), edge angle and depth/height. The position and extension is defined by the location of the two edges denoted Edge 1 and Edge 2, see [3] for elaboration. A depth occurs for a cavity where a height occurs in protuberances such as zigzag tape in [1]. The analysis is carried out on the same NACA 63_3-418 airfoil as in the other publications.

The top plots in Figure 4.12 and 4.13 show the lift decrease in percent and the lower plots show the lift/drag decrease in percent, both for 6, 8 and 10 degrees AoA. It was chosen to show the lift/drag at 6, 8 and 10 degrees AoA because it has direct impact on the AEP of a wind turbine. The first results shown in Figure 4.12 are combinations of positions and widths of a cavity located on the SS of the airfoil. It reveals that a position of the cavity closest to the leading edge results in the highest loss in lift and lift/drag for all three AoAs. It also shows that a wide cavity is worse than a narrow cavity. A narrow cavity with sufficient distance to the leading edge has almost no impact on aerodynamics at 10 degrees AoA, but might reduce the lift/drag with ≈25% at 6 degrees AoA. Another observation is that for a small cavity of the size in this study and three AoAs relatively close to each other, the decrease in lift/drag can vary between 0 and 40%, which also shows that a prediction based on intuition is very difficult to make.

Figure 4.13 shows the lift and lift/drag decrease for a leading edge cavity growing in chordwise direction and depth. It shows that the airfoil performance is highly sensitive to the depth of the cavity. A 1% depth in cavity might be a stretching of reality, but also lower depths show significant performance reductions. Even a 0.1%c cavity from 1%c PS to 1%c SS gives a ≈40% lift/drag reduction for 6 degrees and less for higher AoAs. Even though the lift/drag at 10 degrees AoA suffers the least from a 0.1%c cavity, it suffers the most when the cavity exceeds ≈0.2%c. Here a loss of more than 80% is seen which means that with a starting point in clean and undamaged conditions lift/drag might be around 100 and in damaged condition lift/drag is only 20. Using the formula $1.5 \cdot \lambda_{local}/(\text{lift/drag})$, by Bak [76], the loss in performance with $\lambda_{local} = 7$ and with lift/drag of 100 compared to no losses (inviscid flow) shows a loss of 10.5% in local power coefficient C_p. With lift/drag of 20 this loss becomes 52.5% in C_p and thereby the loss between clean and damaged condition is 42%. The chordwise position also highly influence the penalty where a cavity that extends farther down the airfoil gives less penalty. The last conclusion could be different if the cavity was rough on the surface as seen in wind tunnel tests and described in Section 4.5 and [4].

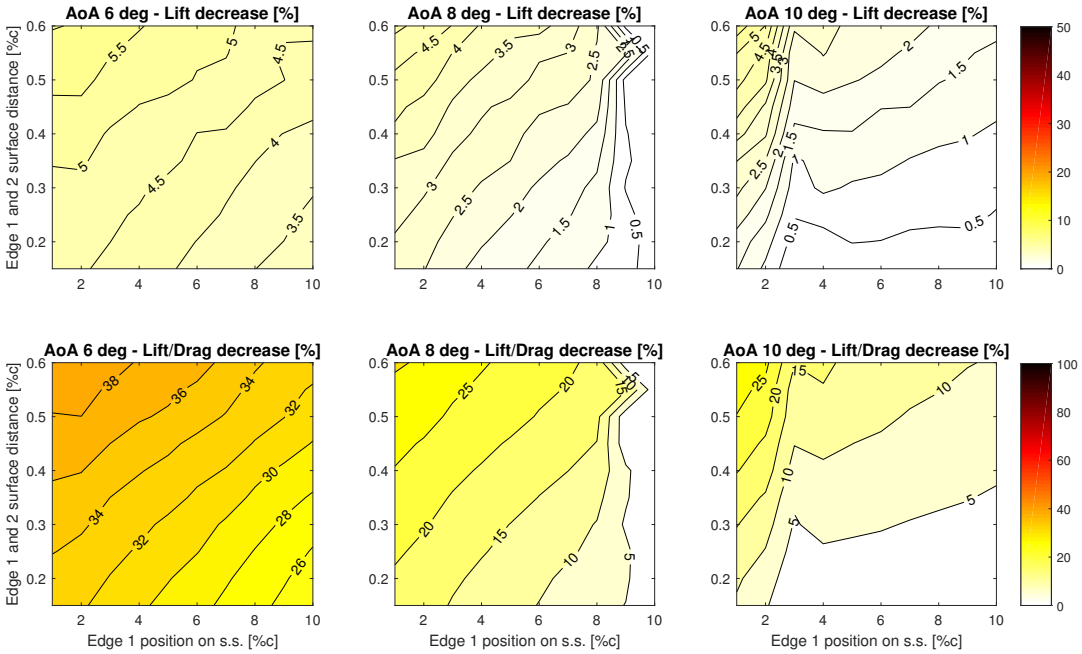

Figure 4.12: Lift and lift/drag decrease for 6, 8 and 10 degrees AoA for changes in Edge 1 position on the SS and distance between Edge 1 and Edge 2. [3].

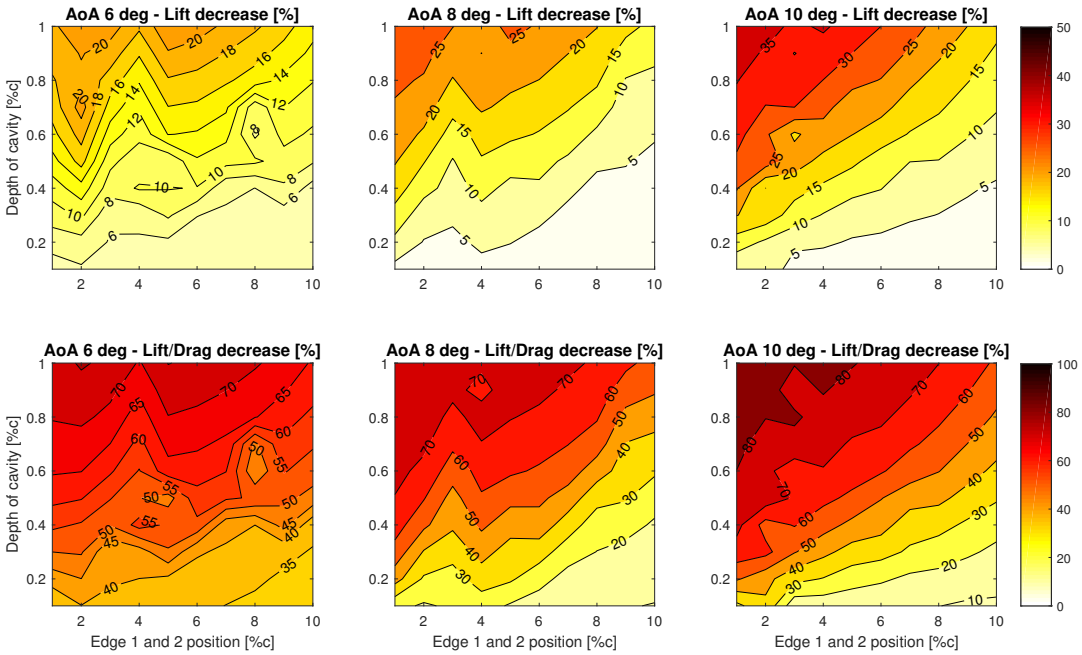

Figure 4.13: Lift and lift/drag decrease for 6, 8 and 10 degrees AoA for a combined change in Edge 1 and Edge 2 position on the PS and SS, respectively and the depth of the cavity. [3].

In general, the study showed that a protuberance/bump has more impact on the aerodynamics of an airfoil than a cavity of the same size and position. The deeper a cavity or the higher a bump is, the worse is the penalty. The study is limited to one damage on the airfoil at a time. Multiple damages would most likely give different results, however the observation from miscellaneous simulations not presented suggests that the largest damages located closest to the leading edge dominates the impact on aerodynamic aerodynamic performance.

Besides the observations described above, the tendency was that the angle of the cavity or bump had little impact on the lift and lift/drag changes for the 6, 8 and 10 degrees AoA. However, wind tunnel tests in [4] showed that the maximum lift might suffer less with 45 degree edges compared to 90 degree edges. The results in general are very sensitive to AoAs, which suggests that a full set of polars, e.g. -30 to 30 degrees AoAs, is desirable when evaluating AEP of a wind turbine rather than just one or two polar scaling parameters. This conclusion is used in the design process of the method to determine how the surface topology influences the AEP, which is also called LER2AEP and described in Chapter 5 and 6.

The governing conclusion of the study is that one should focus on the depth/height and location of a damage rather than the actual in-detail geometrical shape of it, i.e. details of a damage well distanced from the leading edge is not where the focus should be when estimating AEP.

4.5 Wind Tunnel Measurements

In this section results from wind tunnel tests of the NACA 63_3-418 airfoil in clean and LER configurations are presented. This work resulted in *Article 4*, found in Appendix F reference [4]. Description of the experimental setup can be found in this reference. This section describes the experimental results of damages similar to those investigated with CFD. As mentioned earlier, the construction of the DTU Poul la Cour Wind Tunnel (PLCT) has been a key element in the project from the very beginning. The wind tunnel experiments were supposed to form the basis for CFD calibration and the general understanding of LER and its impact on aerodynamics of airfoils. However, the first experimental campaign in the PLCT and postprocessing of results were finished in July 2019, leaving no time for CFD simulations based on these results. Even though the wind tunnel tests were carried out very late in the project, the results are still of high value and has been published as a paper solely with wind tunnel measurements.

The NACA 63_3-418 airfoil used in the experiments had an exchangeable leading edge. Three different leading edges were produced: The first one was a clean and smooth one, the second one had a cavity at the leading edge designed to be equipped with different kinds of leading edges with distributed roughness, e.g. 3D printed leading edges, and lastly a leading edge with cavities on the SS and PS, close to the leading edge. The first two mentioned leading edges were utilized in this paper. The chord length of the airfoil was 1.0 m and the Reynolds numbers were either Re = 3 million or Re = 5 million (The Re = 3 million cases are not shown here but can be found in [4]). In this work the last leading edge with cavities on the SS and PS was not used because several practical issues occurred in the wind tunnel when forming the cavities. These practicalities could not be solved within the time frame of this project. Also, the second leading edge with a cavity at the very leading edge was not used to the extent as intended because the 3D printed pieces with the distributed roughness could not be properly mounted.

Figure 4.14 shows a comparison of the clean airfoil and the airfoil equipped with three heights of zigzag tape. The zigzag tape heights were 0.2, 0.4 and 0.8 mm and the Reynolds number was Re = 5 million. All results show a significant increase in drag for higher AoAs. The lift decrease in the stall region is highly dependant on the zigzag tape height, with the 0.8 mm zigzag tape resulting in the most decrease in lift.

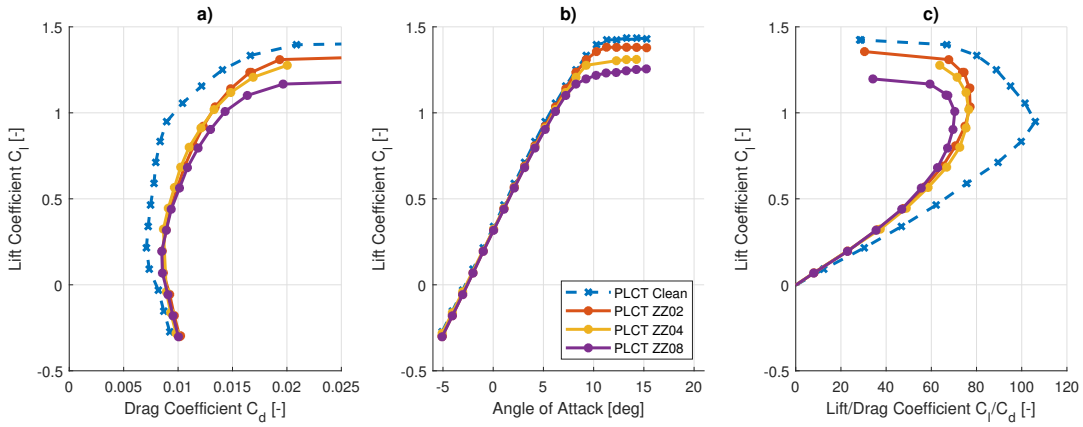

Figure 4.14: a) Comparisons of C_l as a function of C_d, b) C_l as a function of AoA and c) C_l as a function of C_l/C_d for the NACA 63_3-418 with zigzag tape at Re = 5 million tested in the PLCT. The zigzag tape is located only in SS = 2%c. Three different heights of zigzag tape are shown and compared to the clean case [4].

Figure 4.15 shows a comparison of two strips: The 0.8 mm zigzag tape and a 2D strip in the same location but with a height of 0.962 mm. The results are very close and the difference might be due to the different heights of the strips. This is well in line with the findings by Kruse et al. in [1], that a 3D protuberance might be substituted by 2D simulations.

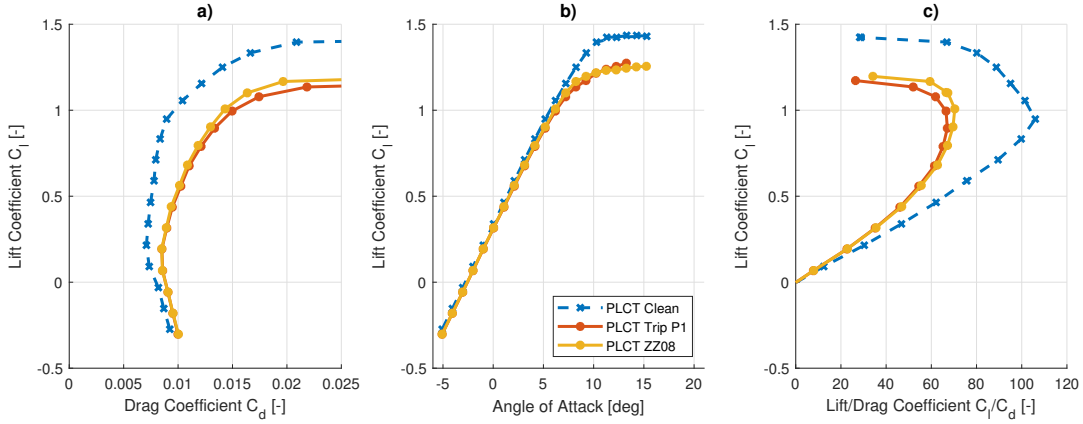

Figure 4.15: a) Comparisons of C_l as a function of C_d, b) C_l as a function of AoA and c) C_l as a function of C_l/C_d for the NACA 63_3-418 with a 0.962 mm protuberance at the LE at 2%c at the SS at Re = 5 million tested in the PLCT compared to the clean and 0.8 mm zigzag tape cases [4].

Figure 4.16 shows a comparison of the airfoil equipped with P40, P120 and P400 sandpaper, where the P40 is the one with the biggest grains and thereby with the biggest roughness height. Opposite to the zigzag tape, an increase in sandpaper grain size does not change lift particularly much, however, the drag seems to increase with grain size. The wind tunnel experiments used in Section 4.2 and 4.3 show different tendencies. They have similar lift and drag for both P120 and P60. This might be due to the fact that the average grain diameter of a P40 is almost twice the one for P60 sandpaper, and then might have a higher influence on the drag. Furthermore, the Reynolds number in the Stuttgart IAG Wind Tunnel was Re = 3 million where these results are at Re = 5 million. The drag for higher Reynolds numbers might be more sensitive to distributed roughness.

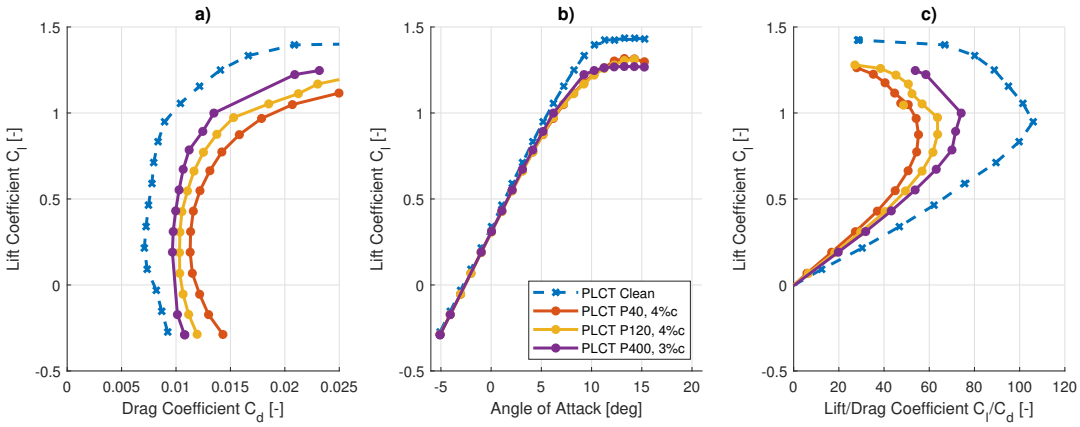

Figure 4.16: a) Comparisons of C_l as a function of C_d, b) C_l as a function of AoA and c) C_l as a function of C_l/C_d for the NACA 63_3-418 with sandpaper at Re = 5 million tested in the PLCT. Three different types of sandpaper are shown and compared to the clean case [4].

Figure 4.17 shows the results for the leading edge with a cavity from 3%c PS to 3%c SS with a depth of 0.3%c and a Reynolds number of Re = 5 million. One case is clean, one case with P40 sandpaper in the cavity, one with P120 sandpaper in the cavity and one with tape on the edges of the cavity, forming slopes of 45 degrees instead of 90 degrees as in the clean case. The drag is very similar in the linear lift region where it starts to deviate in the stall region. The cavity with the P40 sandpaper gives the highest drag and lowest lift, where the P120 case show similar but less severe tendencies. Mounting tape on the edges of the clean cavity does reduce the aerodynamic penalty in drag an almost removes the penalty in lift.

Lastly, the different types of LER is compared in Figure 4.18. It shows that changes to the airfoils aerodynamics can be tailored by using sandpaper, cavities and protuberances. In general, a very rough surface like the P40 sandpaper does increase drag significantly, especially at higher Reynolds numbers, where as steps in the surface like the cavity or protuberances such as strips and zigzag tape has a higher impact on lift. Whether a P40 sandpaper is a realistic representation of real erosion is still in question.

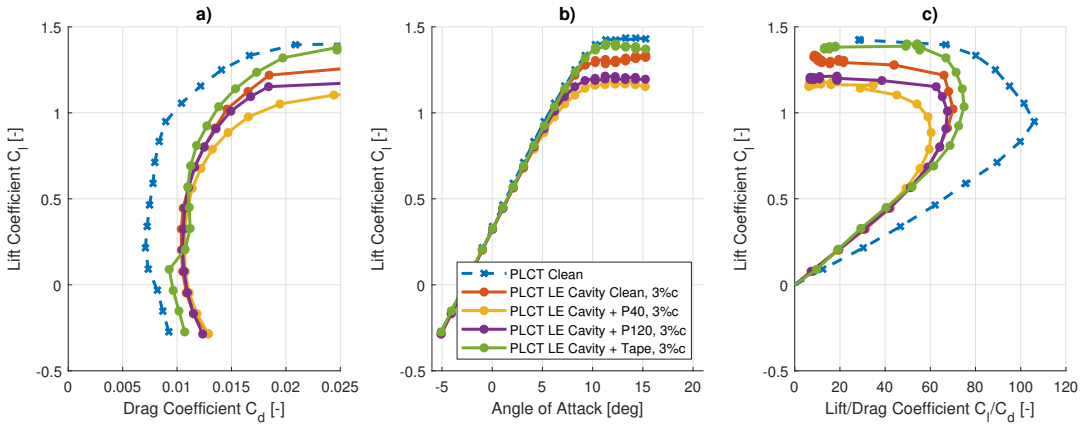

Figure 4.17: a) Comparisons of C_l as a function of C_d, b) C_l as a function of AoA and c) C_l as a function of C_l/C_d for the NACA 63_3-418 with a cavity at the LE (LE Cavity) from 3%c at the PS to 3%c at the SS with and without sandpaper in the cavity at Re = 5 million tested in the PLCT. Two different types of sandpaper are shown and compared to the clean case, the case with no sandpaper in the cavity and with no sandpaper in the cavity and tape reducing the slopes at the edges of the cavity [4].

A direct comparison is difficult because the P40 sandpaper case extends to 4%c and the cavity including P40 only extends to 3%c which probably gives less drag. Furthermore, by mounting P40 sandpaper in the cavity, the depth is no longer 0.3%c but closer to ≈0.2%c. Nevertheless, the public available data for airfoils with LER is significantly expanded with these results and will hopefully help in future calibration of simulation models.

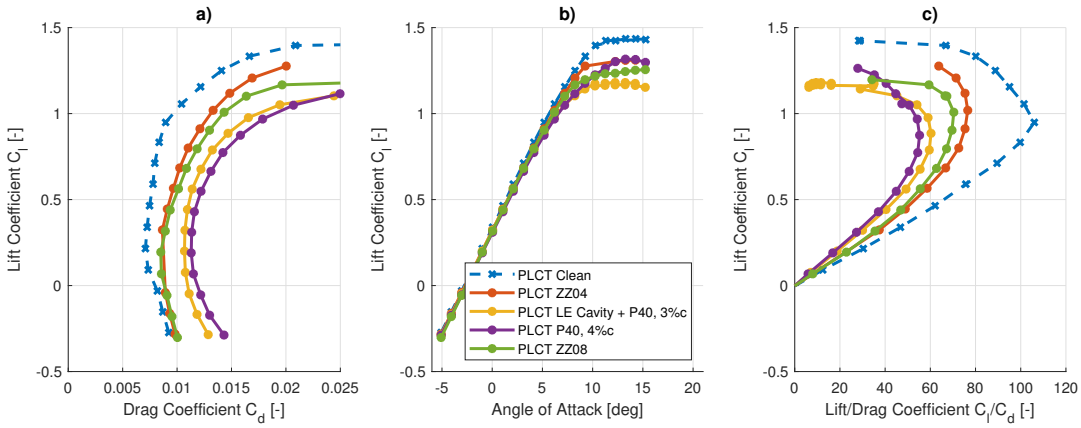

Figure 4.18: a) Comparisons of C_l as a function of C_d, b) C_l as a function of AoA and c) C_l as a function of C_l/C_d for the NACA 63_3-418 with different types of LE roughness at Re = 5 million tested in PLCT: Zigzag tape 0.4 mm at 5% SS 10% PS, zigzag tape 0.8 mm at 2%c, sandpaper P40 from 3%c PS to 3%c SS and LE cavity with sandpaper P40 in the cavity [4].

CHAPTER 5
Estimating AEP on Wind Turbines with LER

This chapter describes how the airfoil polars influenced by LER, calculated as described in Chapter 4, are utilized in an AEP estimation. Section 5.1 describes how and why it was chosen to form a database with simulated airfoil polars. Section 5.2 describes how a match between the scanned airfoils described in Chapter 3 are matched with this database. Lastly, Section 5.3 describes how a DTU in-house BEM code was wrapped to accommodate the LER2AEP purpose.

5.1 Degraded Airfoil and Wind Turbine Database

The LER2AEP software system was intended for use by many independent drone operators who would either buy a hardware and software bundle system or just buy a software solution. Either way requires a reasonable postprocessing time and high system robustness. As many damages/LERs seem to have similar nature, it was chosen to develop a system with pre-simulated airfoils in a database. For each airfoil with an individual LER, the database contains a file with the shape and a file with the polars. Running a new CFD simulation for each airfoil section from the scan process would be time consuming, costly and a higher risk of failure either from the meshing or a non convergent solution.

It was decided that the software should contain predefined information about the wind turbines. There should be information for the wind turbine blades about blade length and chord, twist and thickness as a function of radius, which is also a common input to BEM codes. Furthermore, information about the airfoil families used on the blades would improve the results, however, it is not a requirement. The position of the drone is known, and by pairing this position to the blade information, the chord, twist and thickness is known within a reasonable resolution.

A folder containing all damages and radial position of these starts at the blade tip and works towards the blade root. If a radial position has a damage, a best match in the database is found and if it does not have a damage, the polars for the clean airfoil is used. The scanned airfoils are compared to the database by the algorithm described in Section 5.2. The polars for best match is calculated as a ratio to the clean airfoil and copied to a folder used by the BEM code. The reason for using the polars as a ratio between the clean and LER case is to reduce the risk of error, because the clean polars used for a specific turbine might be experimental, and as described in Chapter

4, the simulated and experimental polars might deviate, especially in the stall region, whereas the relative changes/ratios are of similar magnitude. In other words, the ratio calculated from simulations can be applied to experimental polars. When the code has worked through all damages for blade 1, it will continue to blade 2 and 3. It is possible to scan only one blade and assume the same damages on blade 2 and 3. This is done in the examples given in Chapter 6. A database with an insufficient amount of LER airfoils will give inaccurate results. It is expected that a database should contain tens of thousands airfoils with different thicknesses, e.g. 18%, 21% etc, families e.g. NACA, FFA, DU, etc. and different damages on these. The setup seems vast, but it is possible and quite simple to obtain through CFD simulations combined with scripting.

Figure 5.1 shows examples of polars from the database with similar but slightly different damages. The case number notation is used to identify the parameters describing the damage are simply identifiers.

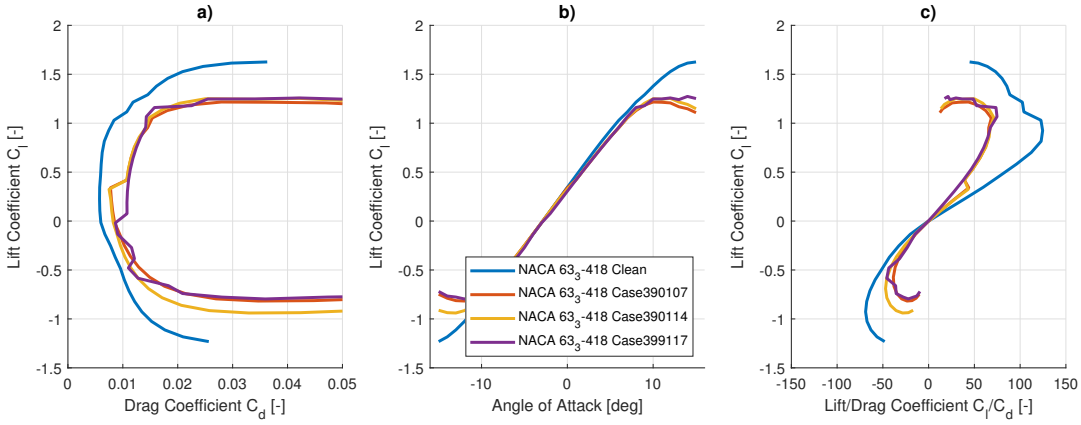

Figure 5.1: The NACA 63_3-418 clean and three LER cases for a) Lift coefficient C_l as a function of drag coefficient C_d. b) C_l as a function of AoA. c) C_l as a function of C_l/C_d.

Information about a specific wind turbine's control scheme, used by the BEM code as well, is also stored in the database as default settings. Two identical wind turbines on different wind turbine sites might have different controllers, and therefore, the control schemes can be defined individually.

5.2 Scanned Airfoil Matching Algorithm

An essential part of the LER2AEP method is to scan the surfaces of wind turbine blades and quantify the surface damages. These scans are made in 3D, but in order to predict the aerodynamics, the coordinates are needed in 2D, and an algorithm was developed to find a match between the scanned set of 2D coordinates and the aerodynamic catalogue, described in Section 5.1.

When designing the matching algorithm, it should be kept in mind that the scanned airfoil has an arbitrary number of coordinates, typically in the range of 10.000-20.000 coordinate sets, whereas the airfoil from the aerodynamic catalogue typically contains between 100 and 1000 coordinate sets. The scanned airfoil is compared to the catalogue, described in Chapter 5.1, containing predefined airfoils. The airfoils in the database, hereafter denoted as the theoretical airfoil, are compared one by one to the scanned airfoil.

The theoretical airfoils are positioned with the leading edge in $x = 0$ and $y = 0$ with the trailing edge located in $x = 1$ and $y = 0$. The minimum thickness is expected to be 10%c and the maximum thickness is 100%c.

Details about the formulation of the matching algorithm can be found in Appendix A.1, but in the following a more general description is made. The Structure from Motion (SfM) described in Section 3.3 outputs a series of coordinates somewhere in space. The orientation is assumed to be within 45 degrees of the theoretical airfoil to match from the postprocessing algorithms of the SfM. The chord is known from the blade planform either obtained by a scan of the blade type, from the manufacturer or the owner/operator. It is expected to be within 20% of the true value. These boundaries can be seen in Equation A.3. The coordinates from the SfM method are moved so that $min(x) = 0$ and $avg(y) = 0$, see Equation A.7 and A.8.

The algorithm is inspired by the branch and bound method [77]. In short, the branch and bound method is an optimization method that starts with a given domain defined by some boundaries and resolution. A temporary solution is found based on an objective function and the input variables. The solution founds the basis for the next branch which in this case is a smaller domain with the same resolution and the method repeat. The optimization problem is non-linear and multidimensional and convergence to the global minimum can not be guaranteed. The solution highly depends on the constraints. For example, as in this case of matching two sets of coordinates, if the scaling is not constrained, the algorithms might scale all coordinates to resemble one point and hence satisfy the objective function and go in a non desirable direction. Figure 5.2 illustrates the functionality of the algorithm. It is greatly simplified as it illustrates only one point with two variables.

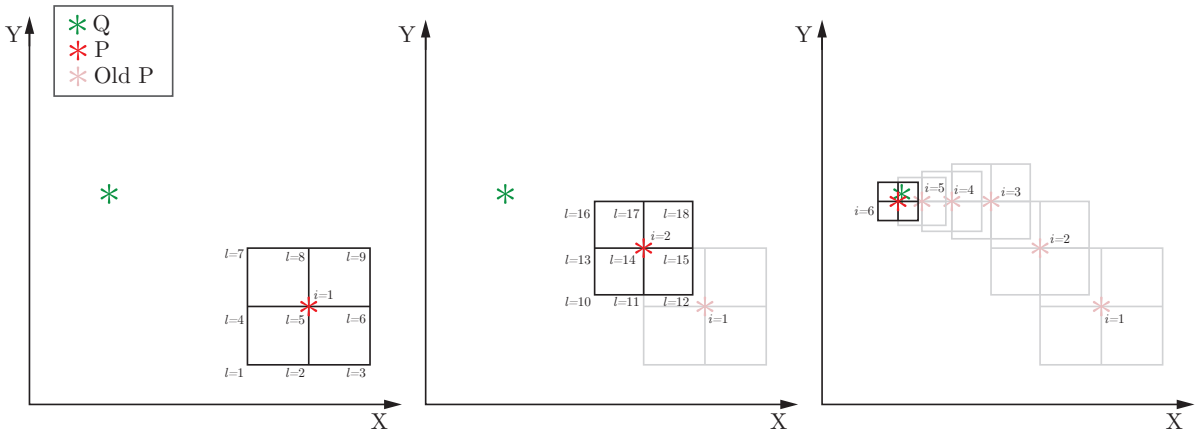

Figure 5.2: Illustration of the algorithm in two dimensions with only one point with P being the point that needs to be moved and Q is the target. Left: First iteration. Middle: Second iteration. Right: Last iteration.

The objective is to move the original point and get the lowest distance to the target. Figure 5.2 shows how in the first iteration, the $l = 7$ has the minimum distance to the target. The next iteration is a branch of the first iteration and starts in $l = 7$ with reduced boundaries $V = 0.8$ in the example in Figure 5.2. The last iteration skips to $i = 6$ where the convergence criteria is met. The algorithm can be found in Appendix A.1.

The execution time of Algorithm 1 highly depends on the settings of L, I and V. The total domain reduction can be calculated as $TotalReduction = V^I$ which in the example in Figure 5.3 results in a domain size of 0.013% of the initial size defined by the boundaries in Equation A.3. Figure 5.3 a) shows the scanned airfoil before and after application of Algorithm 1 compared to the theoretical airfoil as the objective. The main contributor to the execution time is the domain resolution L. A higher resolution increases the total calculations by the power of 4. Computational wise, it is more efficient to reduce the domain just a little and keep the resolution low. This is illustrated in b) in Figure 5.3, where the same convergence criteria is met with different inputs, with 1.01 seconds being the fastest calculation time and 16.21 seconds being the longest.

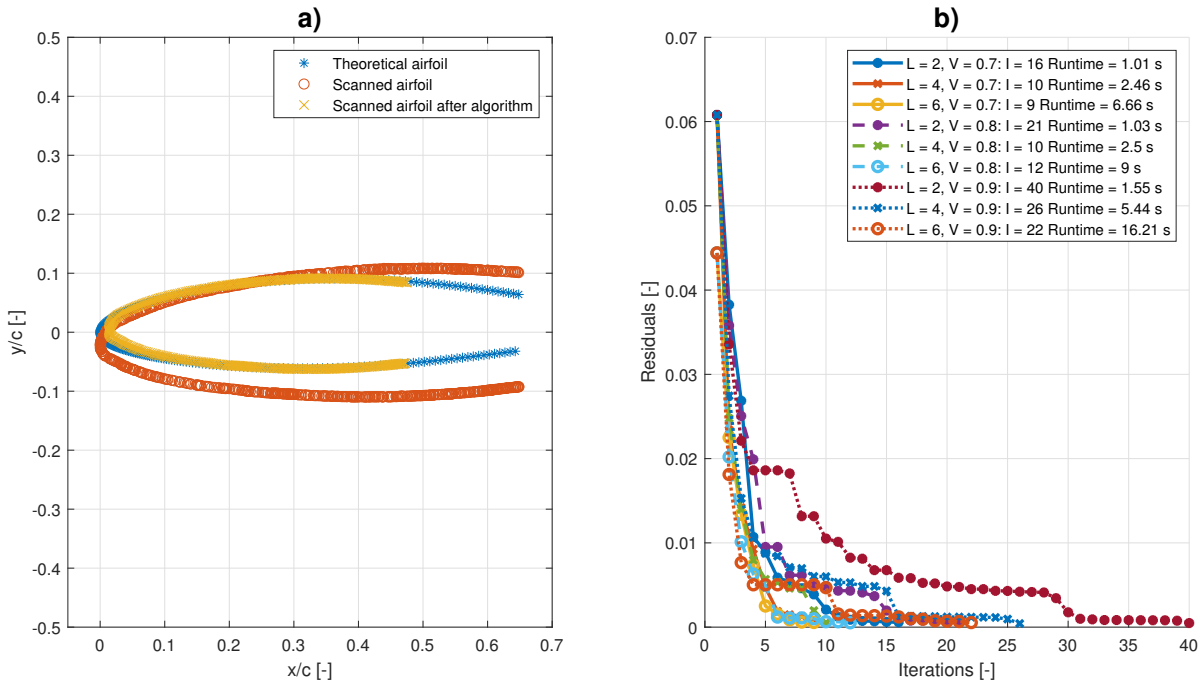

Figure 5.3: a) Example of the baseline theoretical airfoil $\mathbf{Q}$, the initial scanned coordinates $\mathbf{P}$ and the matched scanned coordinates $\mathbf{P}^I$. b) Examples of how the branch and bound settings affect the runtime. Using a coarse resolution L but increasing the total iterations I gives the fastest runtime. A low reduction factor V seems to reduce the runtime as well, but a low reduction factor might result in missing the minimum..

5.3 Special Blade Element Momentum Wrapper

The process of moving from 2D airfoil polars to power production of a wind turbine can be done by using a Blade Element Momentum (BEM) code. DTU has created an in-house BEM code based on the Horizontal Axis Wind turbine simulation Code 2$^{\text{nd}}$ generation (HAWC2) aeroelastic software. The BEM code is a purely aerodynamic code and need no information about the structure, but needs information about the wind turbine control scheme, i.e. the blade pitch and rotor rotational speed as a function of wind speed. This information can be estimated or obtained from the turbine manufacturer. The BEM also needs blade planform information, i.e. the chord length, twist and thickness as a function of blade length/radius. Lastly, the BEM code needs information about the aerodynamics of the airfoils used on the blade, i.e. the polars. It is typical to use between 20 and 50 blade sections in the BEM code, where the polars and blade planform are interpolated. It is often seen that the aerodynamics of a blade is represented by only 5-6 sets of polars.

The strategy for running a BEM code on wind turbines with LER was to make a blade section for each blade part with a damage. If the damage is continuous along e.g. the leading edge, the damage is chopped into small elements. It was found that a blade element should be around 20 cm, each with its own set of polars. If an element has more than one set of polars, the resulting polar are calculated as an average of the polars in the element. The LER polars are calculated from -30 to 30 degrees AoA with increments of 1 degree AoA, assuming that the degraded polars outside this range has no importance to the BEM.

Figure 5.4 shows the power curve for a 2 MW wind turbine with clean blades. It is simulated using the wrapper, expanding from 40 to 100 and further to 500 blade elements serving as examples for the higher resolution BEM code. It can be seen that the results are identical for the three resolutions, which it needs to be in order to function properly.

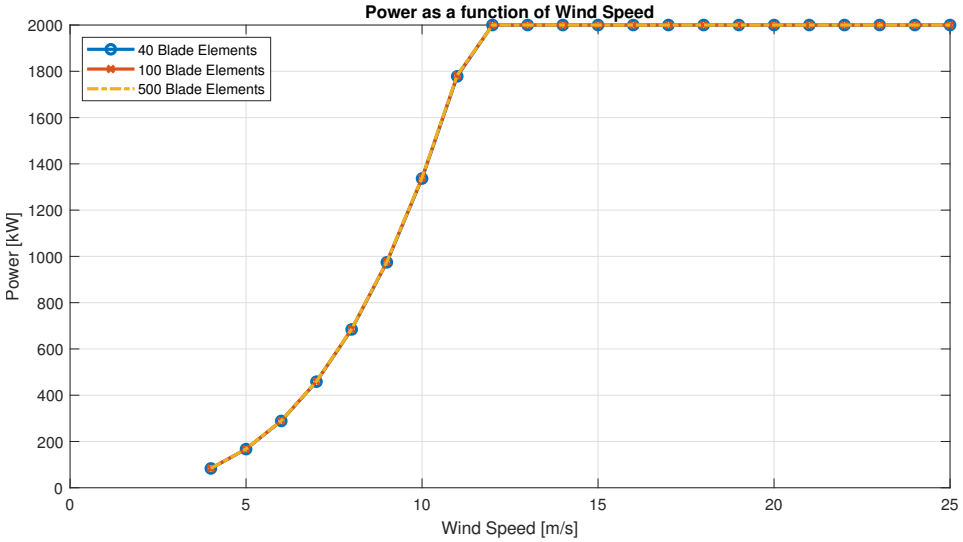

Figure 5.4: Power as a function of wind speed (Power curves) for a clean 2 MW wind turbine calculated from a BEM code with 40, 100 and 500 blade elements.

The left graph in Figure 5.5 shows the power per blade element for 10 m/s wind speed for 40, 100 and 500 blade elements. The middle graph shows the power per blade element for 100 blade elements for the wind speeds from cut in to rated. The results are as expected for utilization in a high resolution LER setup. The last sanity check of the BEM wrapper is the AEP per blade element for 40, 100 and 500 blade elements shown in the right plot. It shows that each element of the 40 element case produces more AEP than the 100 and 500 cases, which also is in line with the expectations. The utilization of the special BEM wrapper can be seen in Chapter 6.

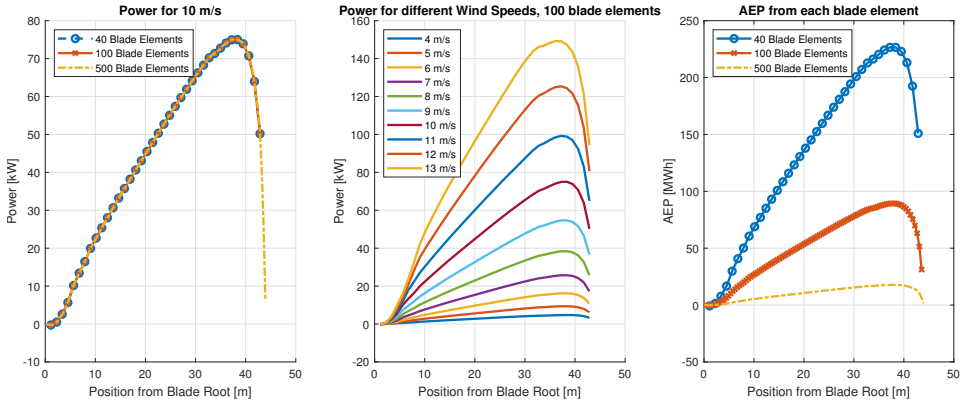

Figure 5.5: Left: Power as a function of blade radius for a clean 2 MW wind turbine calculated from a BEM code with 40, 100 and 500 blade elements at 10 m/s. Middle: Power as a function of blade radius for a clean 2 MW wind turbine calculated from a BEM code with 100 blade elements at 4 to 13 m/s. Right: AEP for each blade element as a function of blade length/radius for a clean 2 MW wind turbine for 40, 100 and 500 blade elemenets.

CHAPTER 6
Results of the LER2AEP Method

This chapter presents three examples of wind turbines with LER. A light, medium and heavily eroded wind turbine. The erosion utilized is the one presented in Section 3.5 in the right of Figure 3.8 repeatedly applied on the wind turbine blade. The difference between the cases is how much of the blade that suffers from LER. Besides the extend of the LER, the blades/wind turbines are identical in the three examples. The rotor radius is 45 meters and the blade length is 44 meters. It is a 2 MW pitch regulated wind turbine. The wind climate is represented by a Weibull distribution with the parameters $\lambda = 7.00$ and $k = 2.00$. The wind climate of a site influences the losses from LER, and some examples on how much the wind climate affects the AEP change are given in Table A.1. The efficiency of the wind turbine drivetrain is set to 0.9. The AEP from the clean wind turbine blades is according to the BEM code 5405.9 MWh, corresponding to a capacity factor $C_f = 0.309$.

Based on the results from the LER2AEP method it is the intention to get an overview of the conditions of the wind turbine blade based on quantifiable measures. With this as a basis the wind turbine service organization can judge whether maintenance is needed and if it is needed where the maintenance is best paid off. All three cases has been calculated with 200 blade elements resulting in an element width of 0.22 m.

6.1 Lightly Eroded Wind Turbine

The first example is given for a wind turbine with LER on the outer 6 meters of the blade, i.e. from 38 m to 44 m, which means that 13.6% of the blade length has a damage. The power as a function of wind speed, i.e. the power curve, can be seen in Figure 6.1. A small change in power can be seen up till rated wind speed. The AEP produced by each blade element can be seen in Figure 6.2. The AEP is seen to drop on the outer 6 m and unaffected on the rest of the blade.

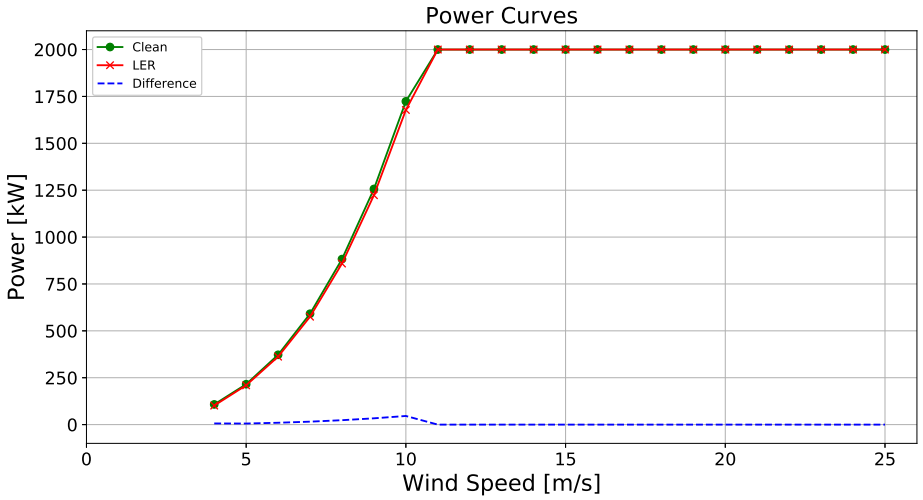

Figure 6.1: Power as a function of wind speed in the lightly eroded case for the clean and LER blade and the difference between these two.

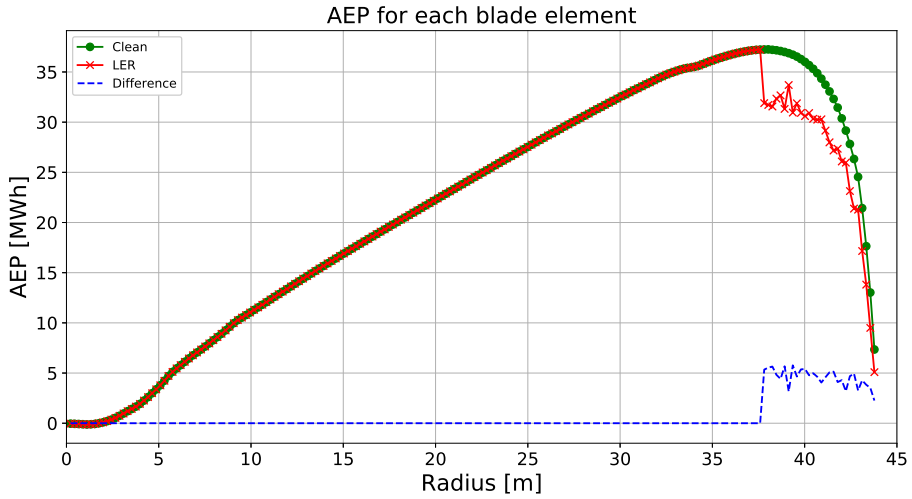

Figure 6.2: AEP per blade element in the lightly eroded case for the clean and LER blade and the difference between these two.

Figure 6.3 shows a graphical representation of the blade with light erosion at the tip. The color denotes the percentage loss in AEP for the blade element. Figure 6.2 and 6.3 only illustrates the blade elements AEP from cut in to rated power. In total, the wind turbine has an AEP change of -1.81% including wind speeds above rated.

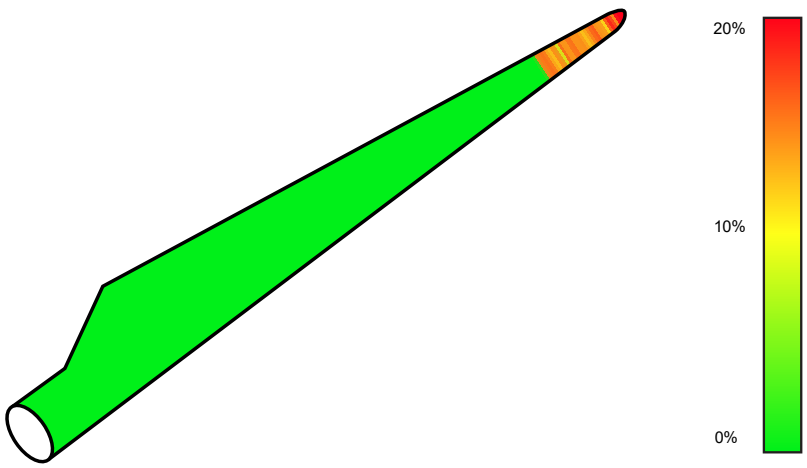

Figure 6.3: Graphical representation of the AEP reduction of each blade element in the lightly eroded case.

6.2 Medium Eroded Wind Turbine

The second example is given for a wind turbine with LER on the outer 14 meters of the blade, i.e. from 30 m to 44 m, which means that 31.8% of the blade length has a damage. The power as a function of wind speed, i.e. the power curve, can be seen in Figure 6.4. A larger change in power, than the lightly eroded case, can be seen up till rated wind speed.

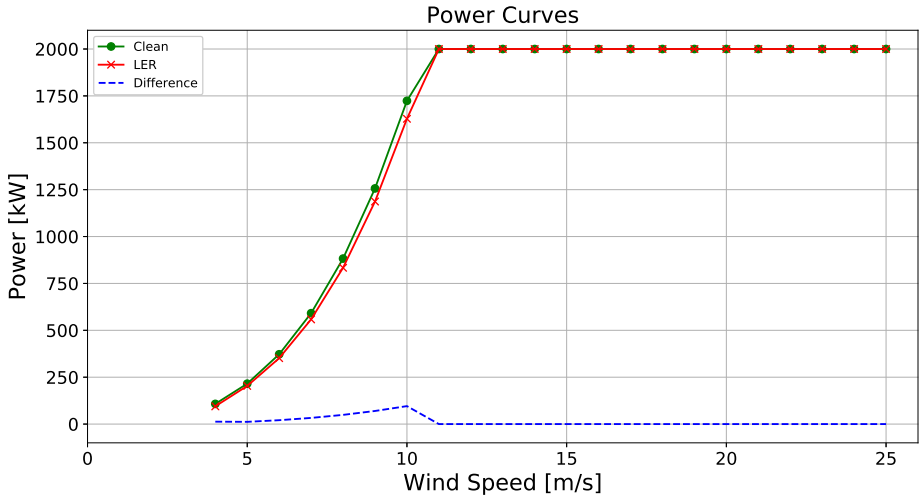

Figure 6.4: Power as a function of wind speed in the medium eroded case for the clean and LER blade and the difference between these two.

The AEP produced by each blade element can be seen in Figure 6.5. The AEP is seen to drop on the outer 14 m and unaffected on the rest of the blade.

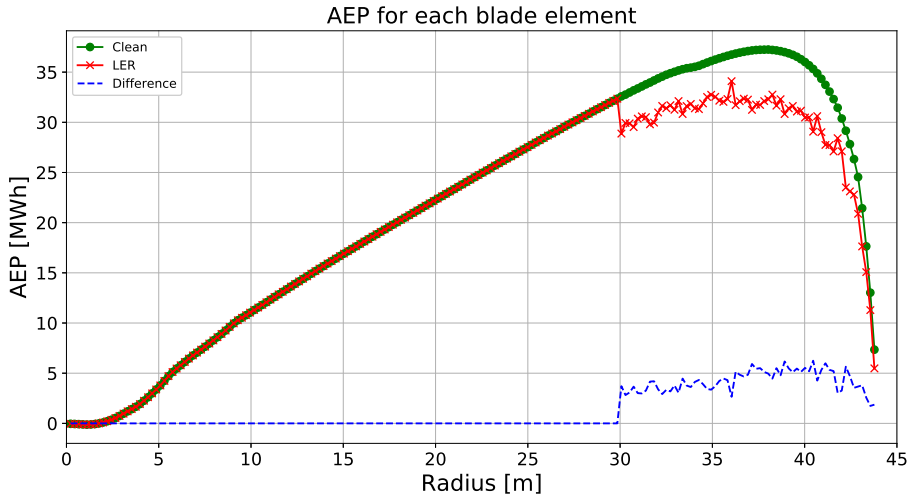

Figure 6.5: AEP per blade element in the medium eroded case for the clean and LER blade and the difference between these two.

Figure 6.6 shows a graphical representation of the blade with medium erosion in the outer part of the blade. In total, the wind turbine has an AEP change of -3.76% including wind speeds above rated.

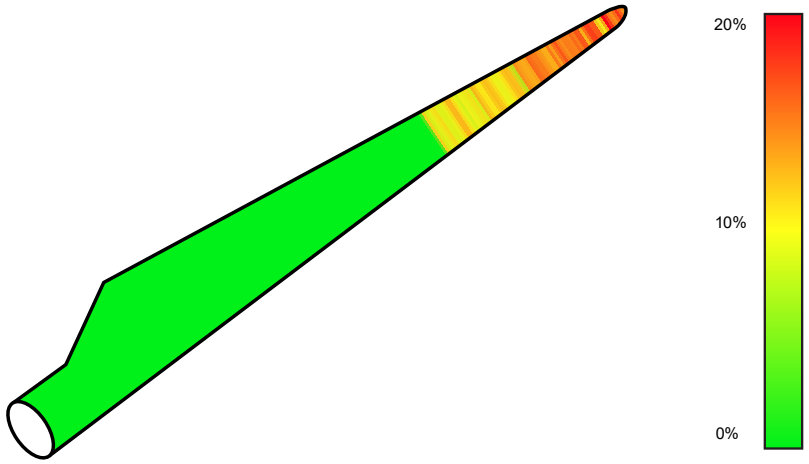

Figure 6.6: Graphical representation of the AEP per blade element in the medium eroded case.

6.3 Heavily Eroded Wind Turbine

The third and last example is given for a wind turbine with LER on the outer 32 meters of the blade, i.e. from 12 m to 44 m, which means that 72.7% of the blade length has a

damage. The power as a function of wind speed, i.e. the power curve, can be seen in Figure 6.7. A significant change in power can be seen up till rated wind speed.

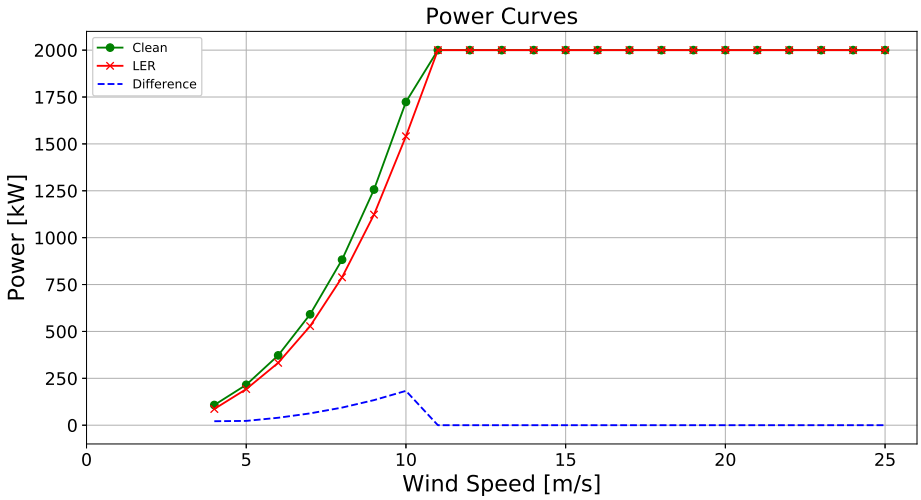

Figure 6.7: Power as a function of wind speed in the heavily eroded case for the clean and LER blade and the difference between these two.

The AEP produced by each blade element can be seen in Figure 6.8. The AEP is seen to drop on most of the blade, except for the inner 12 meters. Even though the blade is eroded with a similar damage on most of the blade, the most of the AEP change can be seen to come from the outer part of the blade, which is because the outer part generates the most power in general.

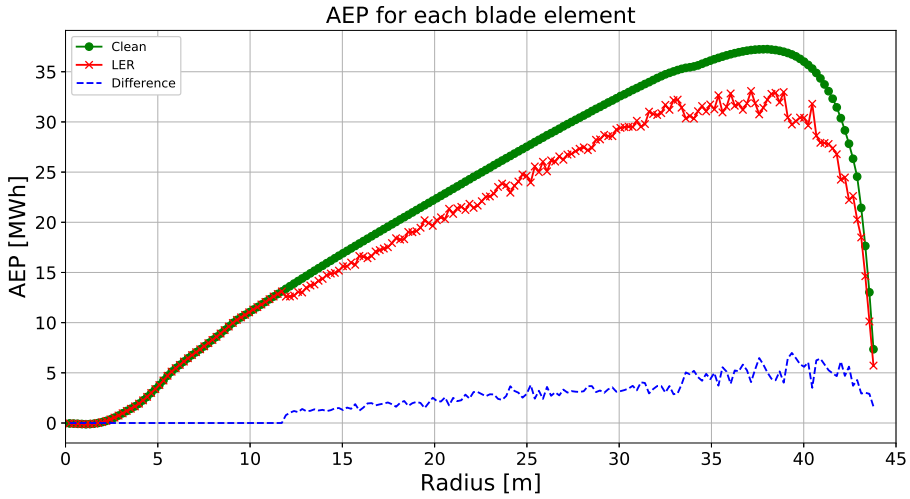

Figure 6.8: AEP per blade element in the heavily eroded case for the clean and LER blade and the difference between these two.

Figure 6.9 shows a graphical representation of the blade with heavy erosion. In total, the wind turbine has an AEP change of -7.13% including wind speeds above rated wind speed.

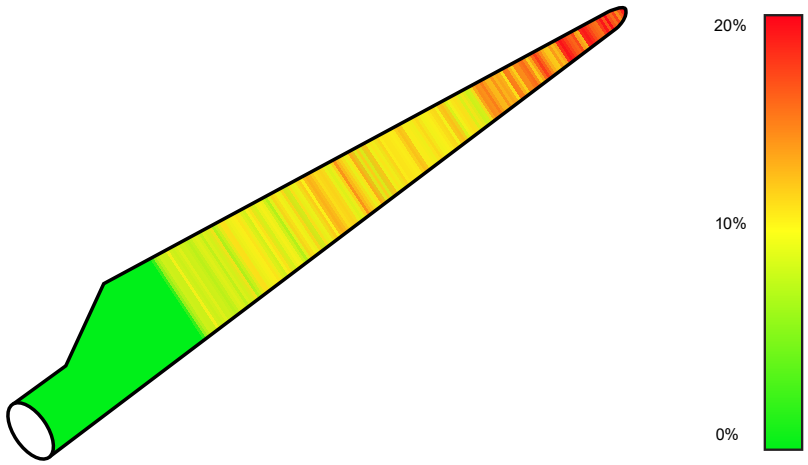

Figure 6.9: Graphical representation of the AEP per blade element in the heavily eroded case.

CHAPTER 7
Conclusion and Outlook

This work contributes to the first steps of a systematic approach for calculating the Annual Energy Production (AEP) of a wind turbine with blades that suffer from Leading Edge Roughness (LER). In the beginning of the project, the overall intention was to develop a categorization of LER. As the project progressed, it became evident that LER takes many more forms and shapes than it would be feasible to establish a useful system of categories for. Rather than the geometry of LER itself, it is suggested that a LER categorization is based on the aerodynamic changes to an airfoil or blade as a result of LER. This could be a percentage change in lift and drag. It was decided not to propose a final categorization in this project because the data foundation is still insufficient. Hopes are that this work will contribute to a future de facto standard categorization of LER.

Using a drone for acquiring measurements of the LER on wind turbine blades proved more challenging than anticipated. The chosen measurement technique was Structure from Motion (SfM) as early research suggested that it was the most promising technology for achieving measurements of wind turbine blade surfaces with sufficient detail. It was later concluded that SfM required more stable conditions than what was possible with the available drone technology. It required the drone to fly for a longer time than practically possible and very close to the wind turbine blades, down to distances of 2-3 meters between drone and blade. Furthermore, the distance between the operator and drone would be 50-100 meters. These distances required a drone with autonomous flight as well as a detection and anti-collision system. Neither of these were commercially available at the time of the project, and it was decided to develop a sufficient control system within the project based on the premise "no flight, no measurements". The development resulted in an autonomous drone capable of acquiring the necessary photographs of the blade. However, the system was not matured in time for the project to utilize it on a real wind turbine. Measurement with SfM of a real wind turbine blade tip with LER, mounted in a mock-up, showed promising preliminary results and was used to simulate LER in three test cases of the proposed Leading Edge Roughness to Annual Energy Production (LER2AEP) method.

Two methods for simulating aerodynamics of airfoils using Computational Fluid Dynamics (CFD) have been tested: 1) A method where the geometry of the airfoil was changed to resemble an airfoil with LER and 2) a method where the physics were changed through boundary conditions in the airfoil surface to resemble the expected behaviour of LER.

The first method was used to simulate the aerodynamic changes of airfoils with small steps in the surface such as a leading edge cavity or a tape strip. The simulation method was tested and compared to wind tunnel experiments in which a NACA 63_3-418 airfoil was equipped with zigzag tape with either 0.4 or 0.8 mm height. The simulations showed similar results in lift and drag prediction. This method was used to conduct a parameter study revealing which geometrical properties of LER that had the most impact on aerodynamics. The governing findings are that the location of the dominating steps in LER geometry together with their depth/height has the most impact on aerodynamics. The deeper/higher the step is and the closer to the leading edge, the higher is the penalty. The shape details of the LER has less importance when simulating the aerodynamics.

The other method was used to simulate the aerodynamic changes of airfoils with distributed surface roughness. Distributed roughness is simulated in wind tunnel experiments by putting sandpaper on the leading edge. The same NACA 63_3-418 was equipped with two types of sandpaper: A coarse P60 and a finer P120. A distributed roughness model was used in the CFD simulations, but the results did not show the expected behaviour. The lift penalty was underpredicted and the drag penalty was overpredicted. However, the changes in aerodynamics displayed similar tendencies, yet the project concluded this to be a result of a turbulent inflow condition rather than a result of the roughness model.

In the final months of the project, the Poul la Cour Tunnel at DTU Risø was functional and an airfoil with an exchangeable leading edge was mounted in the test section. A series of configurations similar to earlier wind tunnel tests were tested along with new configurations. It was concluded in early work that a 3D protuberance such as zigzag tape could be simulated in 2D simulations. This conclusion was supported by two experiments with first 3D zigzag tape and later a 2D metal strip in the same location and similar height, which showed similar results. It was also concluded that sandpaper of different grain sizes had comparable impact on lift but an increasing impact on drag, with the coarsest sandpaper generating most drag. In contrast, three different heights of zigzag tape generated similar drag but varying lift penalties, with the highest zigzag tape reducing lift the most. By combining sandpaper and cavities, the aerodynamic penalty of an airfoil can be designed in wind tunnel experiments.

Lastly, the thesis proposed a method for applying the polars from the 2D airfoils with LER to a wind turbine. A Blade Element Momentum (BEM) code was used where each section was exposed to individual LER from measurements of a real blade tip. Since the examples given were merely a proof of concept, it is difficult to draw any definitive conclusions on AEP changes. Nevertheless, the examples showed AEP losses between 1.8% and 7.1% depending on the LER extent, which is aligns acceptably with the expectations based on the literature.

7.1 Future Work

The work with LER has only just begun, leaving many areas unresearched. With only aerodynamics in mind, this work has focused on one airfoil, the NACA 63_3-418 at two Reynolds Numbers of 3 and 5 million. The suggested methods must still be tested on other airfoil families, thicknesses and Reynolds Numbers.

The CFD models used to predict aerodynamic changes from distributed roughness were unsatisfactory, and further development into such models would be of high value. One approach could be a model combining distributed roughness with geometrical changes in both a laminar and a turbulent inflow situation, to avoid using two separate models, as real LER is often a combination of the two.

Because of the stochastic nature of the wind, there are no sufficiently accurate methods available for calculating the AEP of a real wind turbine with LER based on a power curve. Therefore, it has not been possible for this project to actually validate the simulated AEP changes. Access to measurement equipment and a wind turbine with LER would increase the fidelity of the LER2AEP method.

Samples of LER on wind turbines in operation have been difficult to locate. These are prerequisite to build a database of airfoils with LER. Detailed representations of airfoils with realistic LER, e.g. coordinates of 2D cross sections where the topology is clear are essential for optimal scoping of resources.

Valuable strides could be made with a common effort between e.g. wind turbine owners and/or OEMs to quantify different stages of LER and thereby map the damages. A significant effort in establishing a database of airfoils at different stages of LER and its impact on aerodynamic performance would form an efficient basis for using the LER2AEP method.

APPENDIX A

Thesis Appendix

A.1 Appendix to Scanned Airfoil Matching Algorithm

Let $\mathbf{P}$ be denoted as the Scanned Airfoil xy coordinates and $\mathbf{Q}$ be denoted as the Theoretical Airfoil xy coordinates with the structure given in equation A.1:

$$\mathbf{P} = \begin{bmatrix} x_1 & y_1 \\ x_2 & y_2 \\ \vdots & \vdots \\ x_N & y_N \end{bmatrix} \qquad \mathbf{Q} = \begin{bmatrix} a_1 & b_1 \\ a_2 & b_2 \\ \vdots & \vdots \\ a_M & b_M \end{bmatrix} \tag{A.1}$$

Step 1: Definitions

The changes to the coordinates are described by:

$$\mathbf{\Psi} = \begin{bmatrix} X \\ Y \\ S \\ \theta \end{bmatrix} \tag{A.2}$$

Where X is the translation of all coordinates in the x direction, Y is the translation of all coordinates in the y direction, S is the scaling parameter of all coordinates and θ is the rotation of all coordinates. The variables might be arrays.

Let $\mathbf{\Psi} \in \chi \subset \mathbb{R}^4$
s.t.

$$\chi \equiv \begin{cases} -1.0 \leq X \leq 1.0 \\ -0.5 \leq Y \leq 0.5 \\ 0.8 \leq S \leq 1.2 \\ -\frac{\pi}{4} \leq \theta \leq \frac{\pi}{4} \end{cases} \tag{A.3}$$

$$\check{\mathbf{\Psi}} < \mathbf{\Psi} < \hat{\mathbf{\Psi}} \qquad \hat{\mathbf{\Psi}} = min\{\mathbf{\Psi}\} \qquad \check{\mathbf{\Psi}} = max\{\mathbf{\Psi}\} \tag{A.4}$$

$$L = 2k | k \in \mathbb{N} \tag{A.5}$$

The objective function J is given as:

$$J(\mathbf{P}(\mathbf{\Psi}), \mathbf{Q}) = \sum_{i=1}^{N} \left[\min_{j=1}^{M} \left(\sqrt{(x_i - a_j)^2 + (y_i - b_j)^2} \right) \right] \tag{A.6}$$

Step 2: Initial changes to coordinates

$$\mathbf{P}^* = \mathbf{P} - \mathbf{P}_{avg} = \begin{bmatrix} x_1 - \frac{1}{N}\sum_{i=1}^{N}(x_i) & y_1 - \frac{1}{N}\sum_{i=1}^{N}(y_i) \\ \vdots & \vdots \\ x_N - \frac{1}{N}\sum_{i=1}^{N}(x_i) & y_N - \frac{1}{N}\sum_{i=1}^{N}(y_i) \end{bmatrix} \tag{A.7}$$

$$\mathbf{P}^{**} = \mathbf{P}^* - \mathbf{P}^*_{min,x} = \begin{bmatrix} x_1 - \min_{i=1}^{N}(x_i) & 0 \\ \vdots & \vdots \\ x_N - \min_{i=1}^{N}(x_i) & 0 \end{bmatrix} \tag{A.8}$$

Step 3: Nested for loops

Algorithm 1 Scanned coordinate matching

$l = 1$ #Counter

$I = 40$ #Total iterations of the algorithm, alternatively a convergence criteria

$L = 4$ #Defines the resulting resolution

$V = 0.8$ #Branch domain reduction factor

$\mathbf{\Psi} = \chi$ #Initiate with the boundaries as search space

$\mathbf{P}^{l=1} = \mathbf{P}^{i=1} = \mathbf{P}^{**}$

$K^{i=1} = (\frac{\check{\mathbf{\Psi}}+\hat{\mathbf{\Psi}}}{2} \pm n \cdot \frac{\hat{\mathbf{\Psi}}-\check{\mathbf{\Psi}}}{L})$ for $n \in \{1, 2, 3...\frac{L}{2}\}$ #Defines X, Y, S and θ

for $i = 1$ to I **do**

for $k_1 = 1$ to K_X^i **do**

for $k_2 = 1$ to K_Y^i **do**

for $k_3 = 1$ to K_S^i **do**

for $k_4 = 1$ to K_θ^i **do**

$\mu^l = \min(J(\mathbf{P}^l, \mathbf{Q}))$ #Evaluate the objective function

if $\mu^l < \mu^*$ **then**

$\mu^* = \mu^l$ #Store the latest minimum

end if

$\mathbf{P}^{l+1} = \mathbf{P}^l(\mathbf{K}^i_{k_1,k_2,k_3,k_4})$ #Move the points to reevaluate in next iteration

$l = l + 1$

end for

end for

end for

end for

end for

$\mathbf{P}^{i+1} = \mathbf{P}^l|\mu^*$ #Store the i^{th} iteration optimum as P^{i+1}

$K^{i+1} = (\frac{\check{\mathbf{\Psi}}+\hat{\mathbf{\Psi}}}{2} \pm V \cdot n \cdot \frac{\hat{\mathbf{\Psi}}-\check{\mathbf{\Psi}}}{L})$ #Create new bounded branch and repeat with P^{i+1}

end for

A.2 Appendix to the Results

Table A.1: Alternative inputs to the BEM in the *Heavily eroded* case with 200 blade elements.

Weibull Parameters	**AEP, Clean**	**AEP, LER**	**AEP Change**	C_f**, Clean**
$\lambda = 9.00$, $k = 2.00$	8221.8 MWh	7819.6 MWh	-4.89 %	0.469
$\lambda = 9.00$, $k = 3.00$	8747.5 MWh	8197.1 MWh	-6.29 %	0.499
$\lambda = 8.00$, $k = 2.00$	6887.9 MWh	6482.3 MWh	-5.89 %	0.393
$\lambda = 8.00$, $k = 3.00$	6937.9 MWh	6392.5 MWh	-7.86 %	0.364
$\lambda = 7.00$, $k = 2.00$	5405.9 MWh	5020.2 MWh	-7.13 %	0.309
$\lambda = 7.00$, $k = 3.00$	5038.5 MWh	4543.8 MWh	-9.82 %	0.288
$\lambda = 6.00$, $k = 2.00$	3856.9 MWh	3524.6 MWh	-8.62 %	0.220
$\lambda = 6.00$, $k = 3.00$	3283.4 MWh	2929.2 MWh	-10.79 %	0.187

APPENDIX B

EUDP Project Application "Appendix 5"

Appendix B contains the research part for the initial EUDP project proposal, referred to as "Appendix 5". It describes the different work packages (WP) within the project, being the assumptions, responsible institutions and goals. The basis for the Ph.D. can be found in WP3, "Predicting the aerodynamic performance and influence on annual energy production from roughness".

“Appendix 5” for research application assessment, “LER wind turbine blades – quantifying leading edge roughness”

Background:

During their operational life span of around 20 years the wind turbine blades are exposed to extreme environmental influences and the impact is compounded by the high speed of the blade tip, which can exceed 90 m/s. These effects result in leading edge erosion which creates a larger surface roughness and mm scale surface imperfections which can include e.g. recessions, grooves, blowholes, shrinkage holes, dents, scales, inclusions and burr, [i]. The degradation is referred to as Leading Edge Roughness (LER) and leads to reduced aerodynamic performance, which in turn leads to reduced Annual Energy Production (AEP). The reduction can exceed 10% for turbines that are only a few years old.

Vision:

This project aims to develop a process for in situ measurement and objective quantification of LER. The process developed in this project will enable **exact quantification** of the state of LER for a given turbine, *and* provide an **estimate of the decrease in AEP** the turbine is suffering due to the measured state of leading edge erosion.

This will represent a giant leap forward compared to current methods, where LER is qualitatively judged by experts from visual inspection. A key component of the proposed LER quantification process is in situ leading edge 3D scanning performed from an Unmanned Aerial Vehicle (UAV, popularly referred to as a drone) using low cost photogrammetric methods.

The UAV will fly up along the leading edge of a parked turbine and photograph surface patches on the leading edge. These images will be used for 3D reconstruction of the surface patch with sub-millimeter precision; geometric analysis of these 3D reconstruction will produce a set of roughness descriptors which will be correlated to aero-dynamical performance as determined by wind-tunnel measurements and simulations.

During deployment of the developed techniques, blade scans will be automatically processed and quantitative characterizations of the state of LER for that turbine will be produced.

State-of-the-art:

Some literature deals with the roughness effect on the flow field and power generation and include discussions of contamination agents [ii,iii,iv]. Only a very few papers deal with the *erosion* of the blades. Almost no literature discusses the surface imperfections on the leading edge and the influence on the performance - in particular almost no quantitative results are given[v]. The reliability and equivalence between different approaches is not known. Additionally, there is no standardized test procedure for the evaluation of the durability and protective effect of the coating materials. The blade sections have for many years been tested aerodynamically in wind tunnels for leading edge roughness effects, but the concern has mainly been bugs and dust, which unavoidable will stick to the leading edge. In later years, however, the concern has also been on erosion [iii,iv], but a systematic study of how leading edge erosion looks like and how it can be categorized has not been carried out.

The scientific hypotheses

Three main scientific hypothesis form the basis of the research elements of the proposed project:

1. It is possible to perform sub-millimeter 3D leading edge surface reconstruction from uncalibrated sets of images acquired from a UAV (a drone)
2. It is possible to derive a set of surface roughness descriptors which can be computed from the 3D surface reconstructions, and which correlate to the aero-dynamical performance of the turbine blade
3. It is possible to map the surface roughness descriptors to an estimate in drop in Annual Energy Production (AEP)

The activities relating to each of these hypotheses will be described separately in the following.

Leading edge surface scanning using sets of uncalibrated images acquired from a UAV, WP1

The scientific objective is to:

- Develop visual structure from motion photogrammetry techniques which can perform 3D surface reconstruction in the sub-millimeter domain from sets of uncalibrated images.
- Develop techniques for determining the absolute scale of the reconstructions performed by photogrammetry

Research plan: AAU will lead this effort, with crucial contributions from DFM; it is part of WP1.

Method: With recent advanced in image feature detection and tracking (SIFT) and bundle adjustment on uncalibrated images it has become feasible to very high quality 3D reconstruction of surface from images. Typically 3 to 10 overlapping images from different directions of a surface area are sufficient for performing a 3D reconstruction. The technique is already in general use for land area reconstruction from aerial photography, and for 3D reconstruction of artifacts for cultural heritage preservation and mediation.

In this project we will take the technique into the sub-millimeter area by using images that are acquired of a relatively small leading edge surface patch using high quality telephoto optics that are zoomed in on the patch. The camera(s) will be mounted on an Unmanned Aerial Vehicle (UAV).

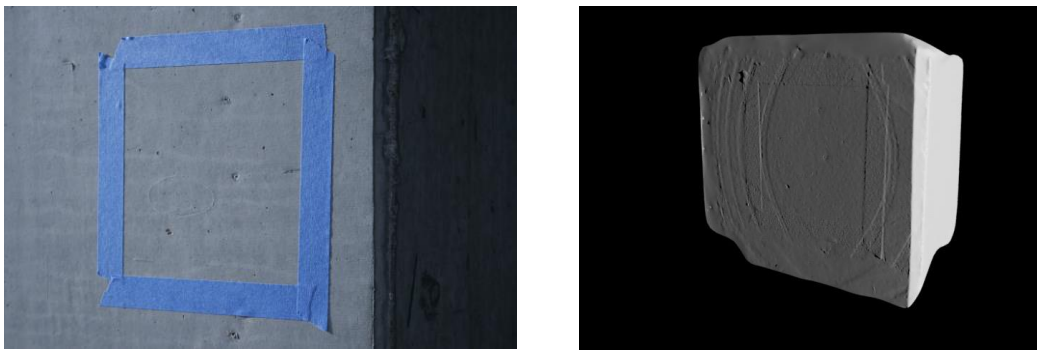

Figure 1. The left side is one of a small number of images acquired of a concrete pillar with masking tape. The right side is an initial 3D surface reconstruction showing surface structure and masking tape. The semi-circular surface features are artefacts due to insufficient image overlap.

3D reconstruction from uncalibrated images results in a reconstruction up to an unknown scale factor. For the purposes of this project it is essential to know the absolute scale of the reconstruction in order to map extracted surface parameters describing roughness to aerodynamic performance. Therefore, we will develop novel domain appropriate techniques for automatically fixing the scale of the reconstructions. Two different approaches to this are being considered for this effort: 1) using two cameras with a known, pre-determined relative external calibration (known translation and rotation), or 2) fixing the scale by performing an extra bundle adjustment based on projecting one or more laser beams on the turbine blade, such that these show up as clear dots in the images acquired.

The performance of the image-based 3D reconstruction will be benchmarked with ground truth surface measurements performed by DFM as part of WP4.

Milestones/deliverables:

- Initial leading edge surface patch reconstruction from real blade images acquired in controlled conditions on ground, with manually fixed absolute scale, milestone M1.1, month 3.
- Leading edge surface patch reconstruction from real blade images acquired in controlled conditions on ground, automatically fixed absolute scale, milestone M1.3, month 9.
- Leading edge surface patch reconstruction under real-life conditions from UAV imagery, milestone M1.4, month 18
- Software and workflow specification for performing surface patch reconstructions, versions to be iteratively refined throughout project life cycle, with deliverables every 6 months, starting month 12 (deliverables D1.2x).

Roughness analysis, part of WP1 and WP3

The scientific objective is to;

- Identify a few surface parameters which describe the combination of a homogeneous sub mm scale surface roughness and the possible mm scale imperfections from erosion on the leading edge. The surface parameters shall categorize the surface topography so it best predicts the effect on power efficiency in particular with respect to the mm scale surface imperfections.
- Identification of a set of leading edge surface models where each surface model have a measurement report giving the surface roughness and a reliable characterization of an overlaid of the mm scale surface imperfection.

Research plan: DFM will lead the task about roughness analysis with essential support from DTU Wind Energy and AAU. The task about roughness analysis will be part of WP1 and WP3 lead by DTU Wind Energy and AAU.

Method: A small number of “leading edge surface models” with different mm scale surface imperfections shall be assemble, manufactured by 3D printing or by replication. These leading edge surface models shall have mm scale imperfections resembling different types of surface imperfections found on samples from wind turbine blades with different age and different protection, such as varnishes and foils. These model surfaces shall be examined thoroughly by stereographic imaging, focus stacking images, perhaps supplied with confocal microscopy imaging. Combined with the knowledge about aerodynamic a few surface parameters shall be identified which describe the combination of the homogeneous sub mm scale surface topography and the possible mm scale imperfections from erosion on the leading edge.

The amplitude of the surface topography is probably one of the important factors that contribute to aerodynamic drag and thereby lower the wind energy capture. However, if mm scale imperfections

dominate the surface topography an aerodynamic relevant baseline from where the amplitude is best measured is not trivial and has to be discussed thoroughly. The amplitude of the surface topography shall be quantified with respect to the size of the amplitude, the degree of symmetry about the baseline, the number of peaks, orientation, correlation length etc. A challenge will be to identify and categorize the different types of mm scale imperfections and characterize them by a suitable height, width, area and number per unit area.

Milestones/deliverables:

- Five leading edge surface models with different mm scale surface imperfections suitable for final analysis is identified by sampling or manufactured with 3D printing. Contribute to Task 2.4 and M2.4
- A set of surface parameters characterizing the mm scale surface imperfection is *identified* which correlates strongly to the aerodynamic efficiency. Contribute to Task 1.2 and M1.2 and Task 3.1 to 3.3 and M3.1 to 3.3.
- A set of surface parameters predicting the influence on annual energy production from surface topography or roughness is *identified* and *implemented*. Contribute to Task 3.4 and M3.4.

Predicting the aerodynamic performance and influence on annual energy production from roughness, WP3

The scientific objective is to:

- Understand the mechanisms leading to reduced aerodynamic performance
- Quantify the aerodynamic performance under influence from different degrees of leading edge roughness on blade section scale.
- Quantify the loss in annual energy production under influence from different degrees of leading edge roughness.

Research plan: The task will be led by DTU Wind Energy, and AAU and DFM will contribute. It is part of WP3.

Method:
Computations using Computational Fluid Dynamics (the DTU in-house code EllipSys [vi],[vii], [viii]) will be used to investigate leading edge roughness. This will be done by investigations of different topographies of the leading edge and roughness models predicting the influence of leading edge roughness at 2D airfoils. Also, investigations will be carried out using panel codes like XFOIL.
Based on the computational investigations wind tunnel test on 2D airfoils are set up to validate the computations and to determine the influence of leading edge roughness on the aerodynamics.
Finally, the influence on the entire wind turbine, i.e. the annual energy production (AEP), is investigated. This is done based on the investigations on the 2D airfoils, where this information will be used in computations on the entire wind turbine. These investigations will if possible be compared to full scale measurements on wind turbines. An exact agreement is not expected, but since measurements on the turbines are carried out by comparing the performance of two neighboring wind turbines, a relative increase between two turbines will also be used for the computations. The ultimate goal in this work package is to determine a transfer function that can predict the decrease in AEP based on the level of degradation of the leading edge.

Milestones/deliverables

- A roughness model will be implemented in CFD and validated. Such a model is implemented and validated after 12 months delivering a report.

- A number of predictions on airfoils with different leading edge topography/roughness will be carried out. Such computations is carried out after 22 months delivering a report.
- Wind tunnel tests on two airfoils with different types of leading edge roughness will be carried out. The wind tunnel tests are carried out between month 22 and 30 delivering a report.
- Predictions of the loss in annual energy prediction as a function of surface degradation will be carried out. The predictions are carried out at the end of the project between month 30 and 36 delivering a report.

Ph.D. study

This part of the project will be focal point of a Ph.D. study within the project. The study will link the individual parts together interfacing with WP1 concerning reconstruction and associated workflow, extraction of roughness parameters, and mapping to aerodynamic performance and AEP loss. The Ph.D. supervisor will be Christian Bak, DTU Wind Energy.

Reference measurements of leading-edge surface topography, WP2 and part of WP4

Background: DFM has several state of the art microscopes including an atomic force microscope and a combined confocal and white light interference microscope. The combined measurement capability for these microscopes ranges from the nanometer to millimeter range in both lateral and height dimensions. DFM can thus provide traceable measurements in the same range. In this project also a larger length scale of up 10 cm for the lateral dimensions and 1 cm in the height is necessary for characterization of segments of wind mill blades. For this purpose DFM will build a microscope system with a measuring capability that overlaps the existing traceable microscopes and goes up to the centimeter scale.

Method: While many instruments exist for characterization of both macroscopic and microscopic structures, only a few instruments are available that bridges the gap (Image and Vision Computing 25 (2007) 1107–1116). One of the challenges is that high-resolution objectives have a shallow depth of field making stereography reconstruction challenging. DFM will build a microscope that obtain topographic information of surfaces using the shape from focus technique (Information Sciences 181 (2011) 1249–1263), but here the challenge is that the software algorithm should be able to recognize even very small variations in defocusing. For regular patterns in a laboratory environment this is routinely used. However, for field test where we are interested in studying small variations in a semi-transparent layer the resolution using standard algorithms are not sufficient. We will therefore also look into the possibility of projecting a regular pattern on the surface, which can be used to assist the reconstruction (Proc. SPIE 7432 (2009) 743210).

Research plan: DFM will lead WP2 and the task in WP4 with characterization of wind mill blades at the field site using the new microscope.

Milestones/deliverables:

- Building an optical microscope with focus stacking and develop software for analysis of a series of images. The microscope will be validated with a comparison to DFM's traceable confocal microscope (report). Task T2.1 and D2.1 after 12 months
- Fabricate and measure on a physical object that are inside the measurement range of both the drone based imaging system and the new microscope (report). Tasks T2.2 and D2.2 after 21 month.
- Replication of microstructures using a fast curing polymer. Investigation of humidity and reproducibility on structures with a height up to 1 cm. (report). Task T2.3 and D2.3 after 15 month.

- Measurements on 5 segments of wind mill blades using both the new microscope and the replication method in a laboratory environment. Each section shall have a lateral dimension of at least 5 cm x 1 cm. Task 2.4 and D2.4 after 24 month.

---

[i] A common vocabulary of terms with definitions relating to surface imperfections are given in ISO 8785 *Geometric product specifications (GPS) Surface imperfections – Terms, definitions and parameters*

[ii] *Issues concerning roughness on wind turbine blades* E. Sagol et al., Renewable and Sustainable Energy Reviews 23(2013) page 514–525 (and references here in)

[iii] Agrim Sareen,Chinmay A. Sapre, Michael S. Selig, "Effects of leading edge erosion on wind turbine blade performance", Wind Energy, Volume 17, Issue 10, pages 1531–1542, October 2014

[iv] N Gaudern, A practical study of the aerodynamic impact of wind turbine blade leading edge erosion, *J. Phys.: Conf. Ser.* **524** 012031, 2014

[v] *Investigation of the impact of rain and particle erosion on rotor blade aerodynamics with an erosion test facility to enhancing the rotor blade performance and durability* J Liersch1 et al., The Science of Making Torque from Wind 2014 (TORQUE 2014), Journal of Physics: Conference Series 524 (2014) 012023

[vi] J. A. Michelsen. Basis3D - a Platform for Development of Multiblock PDE Solvers. Technical Report AFM 92-05, Technical University of Denmark, 1992.

[vii] J. A. Michelsen. Block structured Multigrid solution of 2D and 3D elliptic PDE's. Technical Report AFM 94-06, Technical University of Denmark, 1994.

[viii] N. N. Sørensen. General Purpose Flow Solver Applied to Flow over Hills. Risø-R- 827- (EN), Risø National Laboratory, Roskilde, Denmark, June 1995.

APPENDIX C

Article 1: Predicting the Influence of Surface Protuberance on the Aerodynamic Characteristics of a NACA 63_3-418

IOP Conf. Series: Journal of Physics: Conf. Series **1037** (2018) 022008 doi:10.1088/1742-6596/1037/2/022008

Predicting the Influence of Surface Protuberance on the Aerodynamic Characteristics of a NACA 63_3-418

Emil Krog Kruse[1,2], Niels N. Sørensen[2] and Christian Bak[2]

[1]Power Curve ApS, Stationsmestervej 81, DK-9200 Aalborg SV, Denmark
[2]Technical University of Denmark, Department of Wind Energy, Frederiksborgvej 399, DK-4000 Roskilde, Denmark

E-mail: eko@powercurve.dk

Abstract. Leading Edge Roughness (LER) has become a critical challenge for wind turbine operators, often reducing the energy production of their turbines. LER has not yet been systematically categorized, and the transfer function between height/extent of roughness and the aerodynamic performance has not been established. A common method for emulating LER is to use zigzag tape or distributed sand grain roughness in a wind tunnel. This paper contains 2D and 3D CFD simulations and wind tunnel tests with zigzag tape on a NACA 63_3-418 airfoil, to evaluate the changes in aerodynamic characteristics. Because 3D CFD requires a vast amount of computing power, it is investigated if 2D simulation gives a sufficient level of accuracy.

1. Introduction

It is known that the flow behavior of a fluid is influenced by the shape and the conditions of the surfaces nearby where the fluid passes [1]. In aerodynamics, a rough surface is known to have a negative impact on the boundary layer properties resulting in a higher drag, and for airfoils also a decrease in lift. Wind turbine blades are known to suffer from contamination in the form of bugs, moss and dirt in general[2, 3]. Wear and tear of the wind turbine blades over time can also result in erosion that gives the surface a certain roughness height. These different disturbances are generally described as Leading Edge Roughness (LER). From experience, the LER often causes a 1-7% loss in annual energy production (AEP), but it can cause as high as 20% (estimated by PROPID based on Wind Tunnel Tests, see [4]) for some airfoil families in severe cases [5–7]. The loss in AEP dealt with in this paper is less severe.

Cleaning or repairing of wind turbine blades is difficult and expensive compared to airplane wings, due to their location and accessability, thus the loss in power has to be high before measures are taken by the turbine owner. The critical height of roughness scales proportionally with rotor diameter between $R^{0.5}$ and $R^{0.8}$ [8], i.e. larger blades generally suffer relatively more from the presence of LER than smaller blades, given the LER has the same relative size to the blade. This makes the prediction of aerodynamic changes due to LER important for wind turbines.

In the past, a series of devices attached to airfoil surfaces, known in the literature as protuberances, have been used to emulate LER, mainly in wind tunnel tests. [9] This includes stall strips, trip strips and zigzag (ZZ) tape. The devices all serve the same purpose: To trip the flow and provoke a premature turbulent boundary layer and possibly separation of the

flow. Descriptions of simulations of such protuberances have not been found by the authors. Simulations on airfoils with ice accretion have been made, but the extent of ice on airfoils is much higher than the described LER and mostly conducted for airplanes with higher mach numbers than wind turbines, see [10–17]. Some simulations have also been conducted on sandpaper as LER using roughness models for simulations, see [18, 19]. The present studies are the reasons for this investigation.

The computational code used to predict the aerodynamic characteristics of a common NACA 63_3-418 is the Danish Technical University (DTU) Wind Energy in-house Computational Fluid Dynamic (CFD) software Ellipsys2D and Ellipsys3D. The NACA 63_3-418 airfoil is well known and has previously been simulated in Ellipsys2D [20–22]. The objective of this paper is to investigate the possibility of simulating the flow on the NACA 63_3-418 with protuberances modeled in the grid in 2D and predict the aerodynamic characteristics.

2. Methods

This section describes the experiments with protuberances in the form of wind tunnel tests and general CFD setup.

2.1. Experiments

A series of experiments have been conducted in the Laminar Wind Tunnel (LWT) at the Institute for Aerodynamics and Gas Dynamics, University of Stuttgart, in 2015. [23] The Stuttgart LWT has a test section of 0.73 m x 2.73 m with a length of 3.15 m. Lift was determined by integration of pressure distribution along the tunnel walls, and drag was determined by an integrating wake rake. The chord c of the NACA 63_3-418 test airfoil was 600 mm. The experiments used in this article are all conducted at a Reynolds number of Re = 3 million. The test section can be seen in Figure 1.

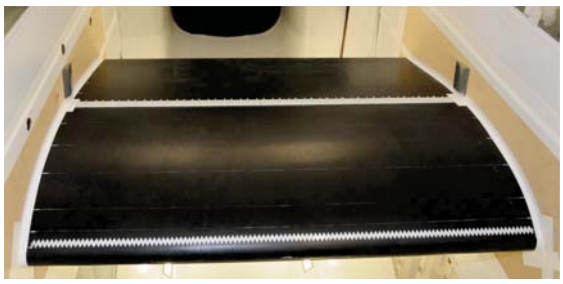

Figure 1. Wind turbine blade model in Stuttgart LWT seen with ZZ tape on the leading edge and Vortex Generators around x/c = 0.5 suction side.

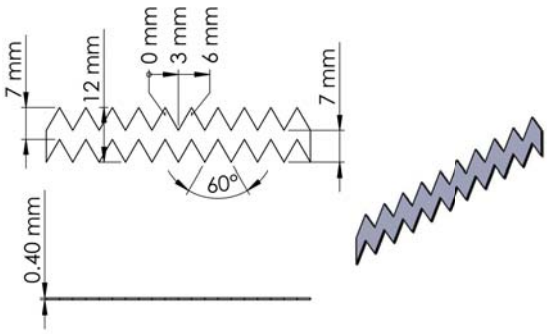

Figure 2. Dimensions of the ZZ tape used as LER in the experimental setup. Two pieces were put on top of each other to give the ZZ tape height of 0.8 mm.

To emulate LER, the wind turbine blade model is equipped with ZZ tape at x/c = 0.02 suction side and x/c = 0.1 pressure side. The zigzag (ZZ) tape has a height of 0.4 mm and measures 7 mm in width as illustrated in Figure 2.

2.2. Simulations

The simulations are based on the same notations as the wind tunnel tests. In text and figures, the different results will be presented with the following notation: Wind tunnel test results is "WT". Simulated results are denoted "CFD". Cases with no LER is "Clean", the 0.4 mm ZZ

tape is "0.4", and the 0.8 mm ZZ tape is "0.8". Likewise, it will be noted if it is 2D or 3D simulations. The 0.8 mm ZZ tape is obtained by using two 0.4 mm strips layered on top of each other.

2.2.1. Grid The grid is constructed using the geometry of the measured airfoil from the wind tunnel test. Some deviation between the theoretical and measured NACA 63_3-418 test airfoil was evident, especially at the leading edge. It was chosen to simulate on the measured airfoil to get the most accurate results. Smoothing was applied to the measured points within reasonable limits. It is constructed using the DTU Wind in-house HypGrid2D, a 2-D Mesh Generator [24]. An overview of combinations and notations are given in table 2.2.1:

Notation	**Description**
s.s.	Suction Side of the airfoil
p.s.	Pressure Side of the airfoil
Clean 2D	NACA $63_3$418 2D simulations without protuberance ("Clean")
Clean 3D	NACA $63_3$418 3D simulations without protuberance ("Clean")
0.4 mm 2D	0.4 mm zigzag tape in 2%c s.s. and 10%c p.s. in 2D simulation
0.6 mm 2D	0.6 mm zigzag tape in 2%c s.s. and 10%c p.s. in 2D simulation
0.8 mm 2D	0.8 mm zigzag tape in 2%c s.s. and 10%c p.s. in 2D simulation
0.4 mm pseudo 2D	0.4 mm 2D extruded spanwise and simulated in 3D
0.6 mm pseudo 2D	0.6 mm 2D extruded spanwise and simulated in 3D
0.8 mm pseudo 2D	0.8 mm 2D extruded spanwise and simulated in 3D
0.4 mm 3D	0.4 mm zigzag tape in 2%c s.s. and 10%c p.s. in 3D simulation
0.6 mm 3D	0.6 mm zigzag tape in 2%c s.s. and 10%c p.s. in 3D simulation
0.8 mm 3D	0.8 mm zigzag tape in 2%c s.s. and 10%c p.s. in 3D simulation
WT	WT is noted for coefficients measured in a Wind Tunnel
CFD	CFD is noted for CFD simulated coefficients
Grid-A	Profile grid used in 2D simulations, 0.4, 0.6 or 0.8 mm zigzag tape
Grid-B	Profile grid used with grid-A to form a 3D grid

The grid of the clean airfoil can be seen in Figure 3. A structured O-mesh with a domain radius of 45 times the chord has been used. The simulated airfoil chord is 1 m.

The zigzag tape height and width is scaled accordingly with 1000mm/600mm. Figure 3 shows the total 2D grid domain of the clean airfoil. Figure 4 shows a close up of the grid of the clean airfoil. Only every 4th grid line is shown. The total number of cells in the circumferential direction is 512 and 384 in the normal direction, a total of 196,608 cells in the 2D grids. The high number of cells was necessary to get grid-independent results in 3D simulations with the 0.8 mm ZZ protuberance, described in section 3. The boundary layer consist of approximatly 60 cells where the boundary layer is thinnest, which also applies for the boundary layer on top of the ZZ tape. All wall cells on the airfoil are $\approx 1 \cdot 10^{-6}$ chord length, which results in a y+ of 0.1-0.2 for all wall cells. To achieve uniformity, the same grid settings were used for all simulations. The outlet is around 45° and can be seen together with the grid blocks in Figure 5. The grid blocks make it possible to run on multiple CPU's [24].

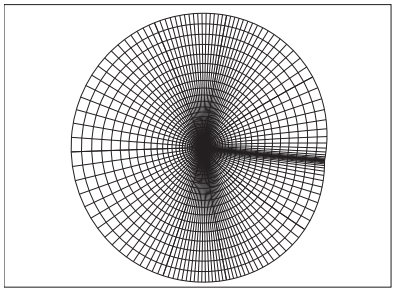

Figure 3. Grid lines in the total domain, shown is coarser level 3 grid

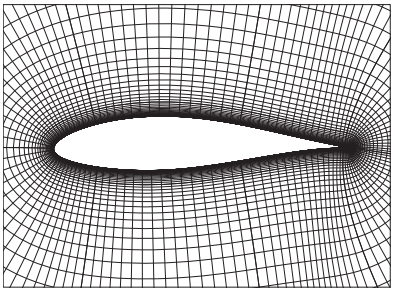

Figure 4. Grid lines around the airfoil, shown is coarser level 3 grid

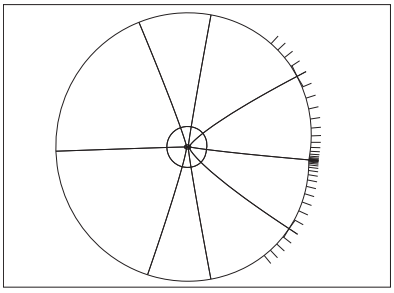

Figure 5. Grid blocks with inlet and outlet, shown is coarser level 3 grid

The grid used for 3D simulations has the same amount of cells and cell distribution as in 2D. The 3D grid is made from two grids, grid-A and grid-B. Grid-A is identical to the corresponding 2D grids, whereas grid-B has the ZZ tape shifted towards the trailing edge, see Figure 7. Naturally, there is a grid-A and grid-B for both 0.4, 0.6 and 0.8 mm ZZ tape and the clean airfoil. The spanwise length is 0.02 m. The unscaled ZZ tape has a tip-to-tip distance of 6 mm, which results in 10 mm when scaled by 1000mm/600mm, hence the 0.02 m span contains two periods of ZZ tape form as depicted in Figure 6-8. It could be limited to a span of 0.01 m, but for illustration purposes it was chosen to use 0.02 m. Each of the two ZZ tape instances is divided into 8 cells each with the same spanwise length, resulting in a total of 32 cells in the spanwise direction, resulting in a total of 6,291,456 cells in the 3D cases. The ZZ tape height was also simulated with 12 and 16 cells, but gave results similar to 8 cells. A periodic condition is applied to the spanwise boundaries. Grid-A blends into grid-B in the farfield using a tanh function over the first 150 cells, resulting in stable 3D simulations. All coefficients calculated for 3D cases are spanwise averages.

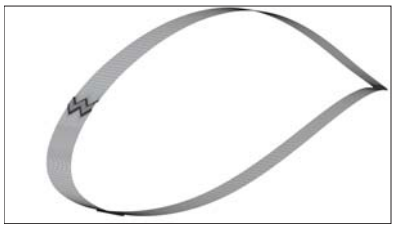

Figure 6. Perspective view of ZZ on airfoil. The entire span wise domain is shown

Figure 7. Closeup of ZZ tape grid. The entire span wise domain is shown

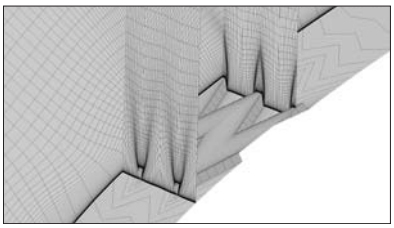

Figure 8. Closeup of ZZ tape grid with three planes showing the grid normal to the airfoil

2.2.2. Numerical Setup One goal of the project was to investigate if the in-house DTU CFD software EllipSys was capable of simulating protuberances or if optimisation was needed. EllipSys is an incompressible finite volume RANS flow solver, which uses the SIMPLE algorithm to solve the Navier-Stokes equations [25–28]. The QUICK scheme is used to discretize the convective terms, see [29]. A relaxation of 0.6 is used on all velocities, and a relaxation of 0.1 on the pressure in all simulations. The density of the fluid is 1 kg/m^3, the chord is 1 m, and the dynamic viscosity is $3.333{\cdot}10^{-7}$ m^2/s. The inlet is laminar flow with a velocity of $[u;\ v;\ w] = [1;\ 0;\ 0]$ m/s for an Angle of Attack (AoA) of 0 deg. These inputs result in a Reynolds number

of 3 mio. All simulations run untill convergence with the limit of $1{\cdot}10^{-6}$ of the error in the first iteration.

Menter's k-ω with SST is used as turbulence model [30]. The e^N by Drela-Giles is used to simulate transition and separation of the flow. [31] The N factor was tested with values from 3 to 9 with an increment of 1 and found to give the best fit with N = 9 in the clean case, hence this factor is used in all simulations. The calibration of the N factor was mainly based on lift and drag fits between the experimental results and the CFD simulations for the clean situation.

The simulations are done on coarser level 2 and 3 to assure grid-independent results. All simulations are run from -5 to 12 deg AoA as no steady solution was found in the 3D simulations above 12 deg AoA. Furthermore, no wind tunnel drag measurements are present above 10 deg AoA.

3. Results and Discussion

A first glance at the simulation results in Figure 9 for the clean airfoil shows good correspondence between grid levels. A reduction in cells causes changes in lift and drag for AoA above 9 deg. The results are in close agreement and the grid resolution is acceptable.

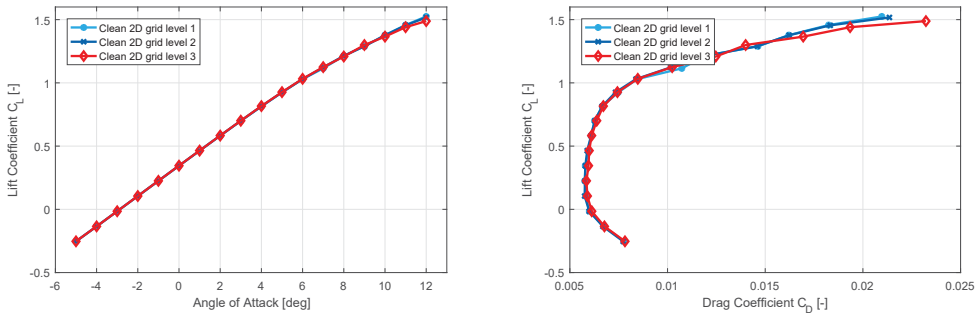

Figure 9. Comparison of Coarser grid level 1, 2 and 3 lift and lift/drag

3.1. Wind Tunnel vs. CFD: Clean Airfoil

The next natural step is to compare the clean simulations for both 2D and 3D simulations to the WT Clean results. The 3D grid is constructed using the same grid file in each spanwise position. The results can be seen in Figure 10.

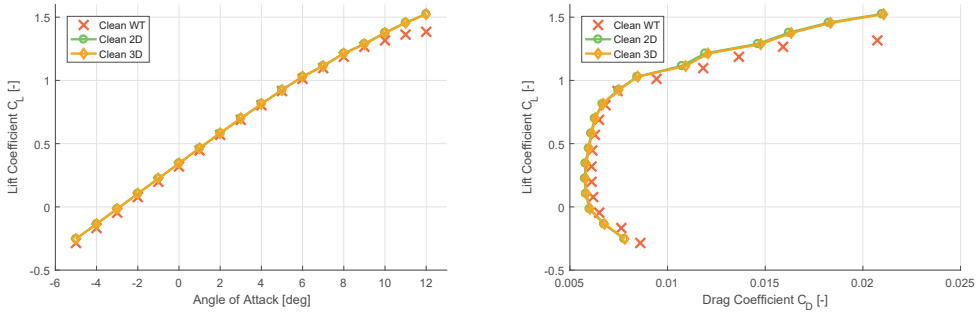

Figure 10. Comparison of Clean 2D, Clean 3D and Clean Wind Tunnel test results lift and lift/drag

The 2D and 3D results are similar. The drag is slightly higher in 3D, probably from the cross flows induced by the turbulence model, which has been examined in streamline plots, although

the cross flows are small. The WT Clean test data is slightly lower in lift for negative AoA. Stall is not predicted to be as severe in simulations as in the WT test. There will be differences between the implementation methods of the simulation models in 2D and 3D. The lift/drag ratio correspondence is as good as can be expected.

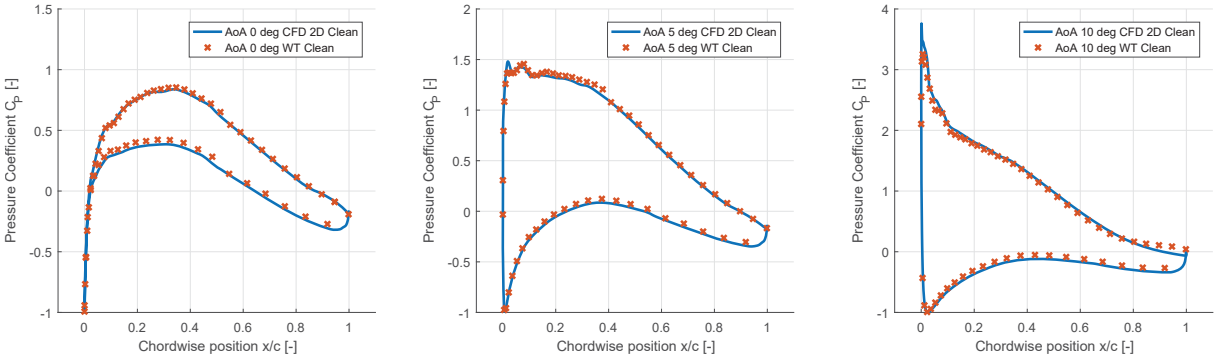

Figure 11. Pressure coefficients C_P for CFD simulation and wind tunnel tests for 0, 5 and 10 deg AoA.

A comparison of the pressure coefficients (C_P) is done at 0, 5 and 10 deg AoA. Figure 11 shows the 2D CFD Clean against the WT Clean test. In all cases the pressure is predicted to be slightly lower than measurements, which might explain the small deviation in drag. No tunnel correction has been applied to the measured C_P which will introduce some deviation between simulation and test data.

3.2. Wind Tunnel vs. CFD: Protuberance Airfoil

As partly described in section 2.2.1, the grid is made in both 2D and 3D. An intermediate step has been introduced, which is called "pseudo-2D". In this step grid-A is used also as grid-B, to see the effect of 2D LER in 3D. This is done because zigzag tape cannot be modeled in 2D CFD. Here it turns into a bump with no geometrical changes in the spanwise direction.

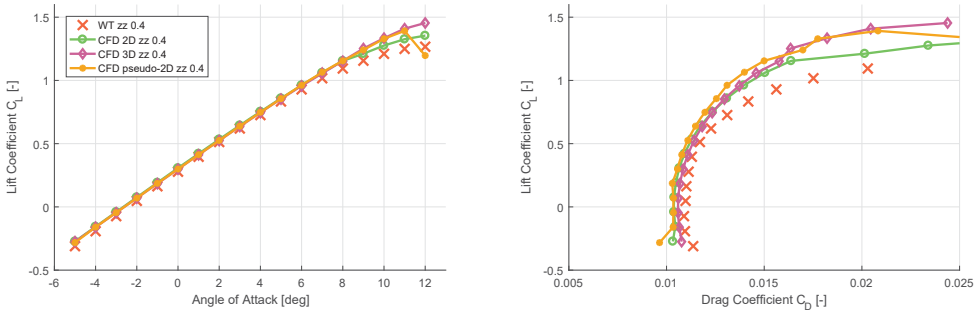

Figure 12. Comparison of lift and lift/drag for simulations and WT test with 0.4 mm ZZ tape

Figure 12 shows the simulated and measured lift as a function of AoA (left) and as a function of drag (right) for the 0.4 mm ZZ tape case. As in the clean case, the 3D computations predict the drag better at low AoA. The lift is still over-predicted, especially in the stall region. Figure 13 shows the simulated and measured lift and lift/drag for the 0.8 mm ZZ tape case.

A difference between 2D and 3D can be seen, with a much higher drag and better correspondence in the 3D case. The pseudo-2D simulations predict the flow just as 2D from -5 to 4 deg AoA and slightly better above that, but not as well as the real 3D simulation.

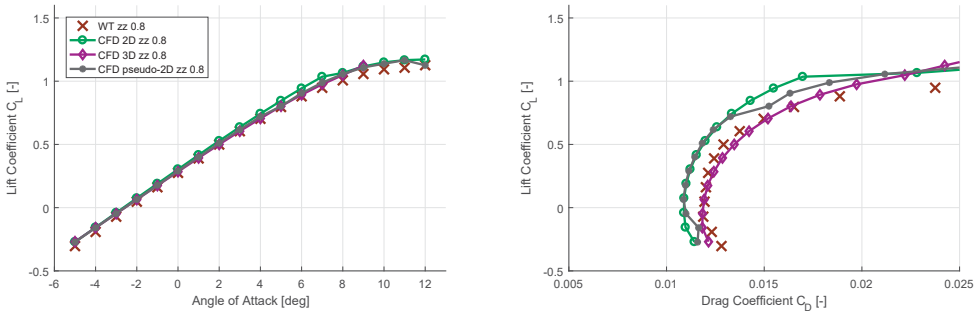

Figure 13. Comparison of lift and lift/drag for simulations and WT test with 0.8 mm ZZ tape

It can be difficult to see how well the simulation predicts the WT tests solely from lift and drag values. A relation between the Clean and ZZ tape cases is introduced as $(X_{Clean} - X_{Rough})/X_{Clean}$ where X is C_L or C_L/C_D for either CFD or WT test. The ratios are plotted in Figure 14 and 15. The best-case correspondence is a CFD ratio equal to the WT ratio.

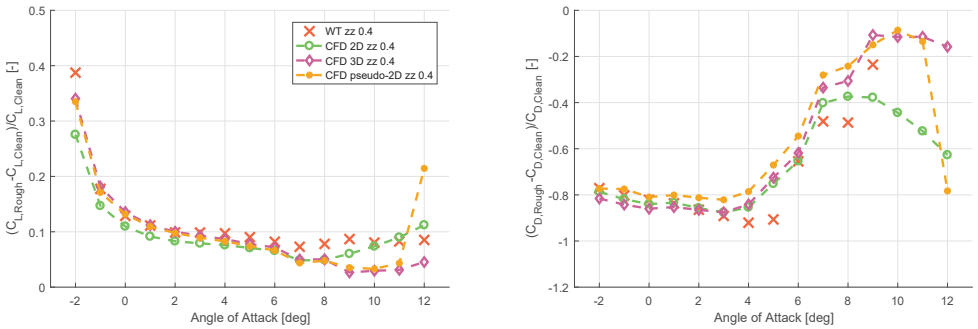

Figure 14. Comparison of lift and lift/drag ratios for simulations and WT test with 0.4 mm ZZ tape

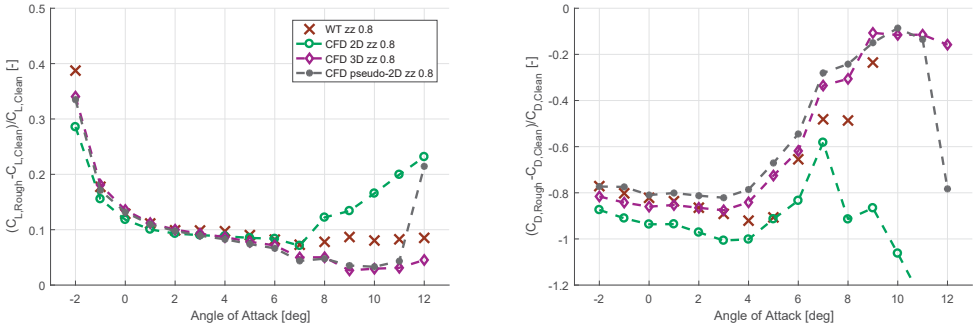

Figure 15. Comparison of lift and lift/drag ratios for simulations and WT test with 0.8 mm ZZ tape

From Figure 14 and 15 it is easier to see that the simulations show high deviation from 7 deg AoA and up. The best match is still 3D, even though the deviation at AoA above 7 deg increases, but the trends remain.

A relation between 2D and 3D simulation with ZZ tape is difficult to establish based on two cases. Therefore, a third case is introduced, being 0.6 mm ZZ tape. However, no WT tests are available for this. Based on the results described above, it is concluded that EllipSys2D and EllipSys3D are both capable of simulating this kind of geometry, and the 0.6 mm case relies solely on the CFD simulations. The simulation results for Clean, 0.4, 0.6 and 0.8 mm ZZ tape are collected in Figure 16.

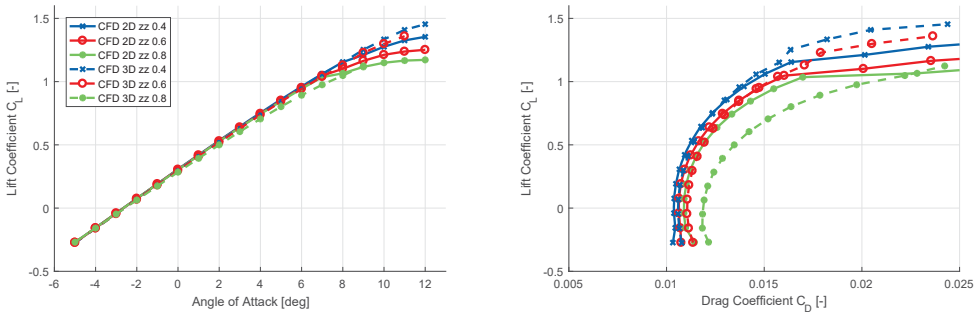

Figure 16. Comparison of lift and lift/drag ratios for simulations and WT test with 0.8 mm ZZ tape

From Figure 16, a linear relation between ZZ tape height and drag coefficient C_D in 2D is observed. The 3D simulations have a non-linear relation. It would be possible to estimate a correction factor when going from 2D to 3D, but the data basis for this is not present. There are too many unknown parameters such as the chord-wise location of the protuberance, the angle in the protuberance (being 60 deg here), edge angles on the protuberance and the fact that the shape will never be as clearly defined and periodic in real LER cases. In the case of 60 deg ZZ tape, the third dimension of the ZZ tape has very little impact on 0.4 mm, medium impact on 0.6 mm and quite a high impact on 0.8 mm.

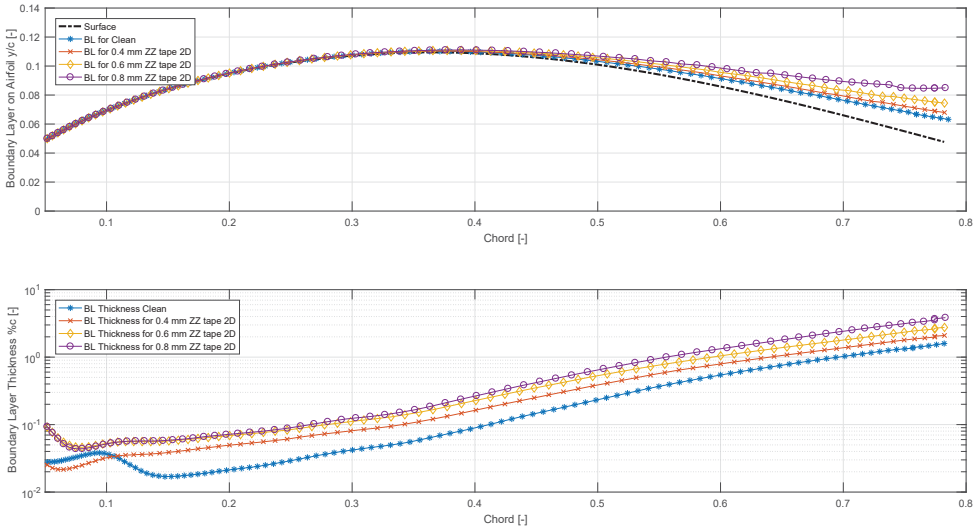

Figure 17. Quantitative comparison of the boundary layer for 2D situations with Clean from both CFD, 0.4 mm, 0.6 mm and 0.8 mm ZZ tape for AoA 8 deg.

Figure 17 shows the boundary layer of the s.s. for 2D simulations of 0.4, 0.6 and 0.8 mm ZZ tape compared to the clean airfoil in AoA 8 deg. The boundary layer is found to be in cells where the absolute velocity is 99% of the free stream velocity. The upper figure shows the airfoil surface and the boundary layer. It is clear that higher ZZ tape results in a thicker boundary layer, leading to earlier separation of flow. The lower figure shows the height of the boundary layer on a Y log scale. Again, the boundary layer thickness is thicker for higher ZZ tape, especially after 0.5 chord length.

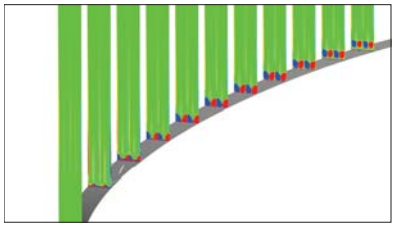

Figure 18. Vorticities for 0.4 mm 3D ZZ tape

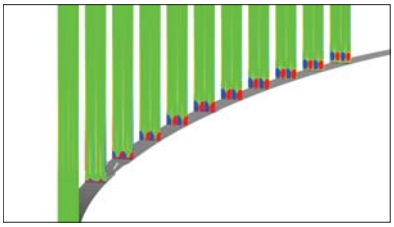

Figure 19. Vorticities for 0.6 mm 3D ZZ tape

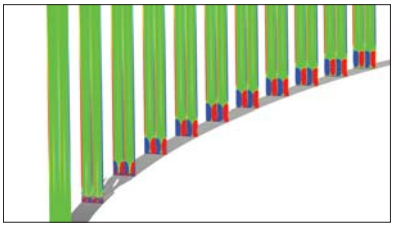

Figure 20. Vorticities for 0.8 mm 3D ZZ tape

Figure 18-20 show the vorticities in the flow along the airfoil. The colorbar is set to be from -5 to 5 for all three ZZ heights. It is clear how the cases with 0.6 and 0.8 mm ZZ tape are subjected to stronger vorticities both close to the airfoil and in the normal direction. The 3D effect in the 0.4 mm ZZ case is present but low. It can also be seen that double ZZ tape height results in more than double the vorticity size.

One of the conclusions of the investigations above is that 2D simulations can be used to predict the flow for a 3D situation up until a certain height of the protuberance. Since the computational time is longer compared to 2D and the complexity of making the grid for 3D is much higher, the accuracy is deemed acceptable for 2D simulations.

4. Conclusion

As stated in section 1, existing literature deals with the simulations of LER as being either ice accretion, simulated by implementing the ice structure directly in the grid or smaller LER like sandpaper or particles simulated by a roughness model. The possibility of simulating small LER with a size (height or depth) of 0.1%c and above, has been investigated in this paper.

Both EllipSys2D and EllipSys3D are able to predict the transient solution for the angles in the range -5 to 12 deg AoA. EllipSys3D struggles with solutions for steady simulations in the range from 9 to 12 deg AoA when the protuberance/LER becomes larger than approximately 1%c. For the EllipSys2D simulations no such problems are experienced. Simulations have been compared to wind tunnel tests and generally good agreement is found. As often seen, the maximum lift is over predicted simulations as well as an underrated drag. Differences between 2D and 3D simulations is found where the drag in particular is predicted better in 3D, however, the significantly lower calculation time and grid complexity justifies simulations done in 2D.

The final conclusion states that it is indeed possible to simulate small LER by direct implementation in the grid, and it is to some extent sufficient to do simulations in 2D rather than 3D.

References

[1] Hoerner S F 1965 *Fluid-Dynamic Drag* (USA) Hoerner
[2] Corten G P and Veldkamp H F 2001 *Aerodynamics: Insects can halve wind-turbine power* vol 412, 4142
[3] Bak C, Andersen P B, Madsen H A, Gaunaa M, Fuglsang P and Bove S 2008 *Design and verification of airfoils resistant to surface contamination and turbulence intensity* vol AIAA 2008-7050 (Reston, VA (US)) American Institute of Aeronautics & Astronautics

[4] Sareen A, Sapre C A and Selig M S 2014 *Effects of leading edge erosion on wind turbine blade performance* Department of Aerospace Engineering, University of Illinois at Urbana-Champaign, Urbana, IL 61801, USA
[5] van Rooij R and Timmer W A 2003 *Roughness Sensitivity Considerations for Thick Rotor Blade Airfoils* vol 125
[6] Hooker R W 1933 *The aerodynamic characteristics of airfoils as affected by surface roughness* (Washington) NACA-TN-457 Langley Memorial Aeronautical Laboratory
[7] Gaudern N 2014 *A practical study of the aerodynamic impact of wind turbine blade leading edge erosion* Vestas Technology UK Ltd.
[8] Bak C, Gaunaa M, Olsen A S and Kruse E K 2016 *What is the critical height of leading edge roughness for aerodynamics?* vol 753
[9] Bak C, Fuglsang P, Johansen J and Antoniou I 2000 *Wind Tunnel Tests of the NACA 63-415 and a Modified NACA 63-415 Airfoil* (Risø National Laboratory)
[10] Bragg M, Broeren A, Addy H, Potapczuk M, Guffond D and Montreuil E 2007 *Airfoil ice-accretion aerodynamic simulation*
[11] Sermeus K and Yang H 2015 *CFD Simulation of Aircraft Icing Effects using Roughness Modeling*
[12] Broeren A P, Addy H E, Bragg M B, Busch G T, Guffond D and Montreuil E 2011 *Aerodynamic Simulation of Ice Accretion on Airfoils* NASA
[13] Cebeci T 1987 *Effect of Intercycle Ice Accretions on Airfoil Performance* California State University (NASA)
[14] Broeren A P, Bragg M B and Addy H E 2004 *Effects of Environmentally Imposed Roughness on Airfoil Performance*
[15] Turkia V, Huttunen S and Wallenius T 2013 *Method for estimating wind turbine production losses due to icing* VTT Technology)
[16] Mortensen K 2008 *CFD simulations of an airfoil with leading edge ice accretion* Technical university of Denmark
[17] Langel C M, Chow R, Hurley O F, van Dam C P, Ehrmann R S and White E B 2015 *Analysis of the Impact of Leading Edge Surface Degradation on Wind Turbine Performance* AIAA
[18] Standish K, Rimmington P, Laursen J and Paulsen H N 2010 *Computational Prediction of Airfoil Roughness Sensitivity*
[19] Ehrmann R S, White E B, Maniaci D C, Chow R, Langel C M and van Dam C P 2013 *Realistic Leading-Edge Roughness Effects on Airfoil Performance*
[20] Bertagnolio F, Sørensen N, Johansen J and Fuglsang P 2001 *Wind Turbine Airfoil Catalogue* (DK-4000 Roskilde) Risø National Laboratory
[21] White E B, Kutz D, Freels J, Hidore J P, Grife R, Sun Y and Chao D 2011 *Leading-Edge Roughness Effects on 63_3-418 Airfoil Performance*
[22] Timmer W A 2009 *An Overview of NACA 6-Digit Airfoil Series Characteristics with Reference to Airfoils for Large Wind Turbine Blades*
[23] Würz W and C Vetter M L K 2015 *Wind Tunnel Measurements of the NACA 63_3-418 Airfoil with Vortex Generators (Confidential)* IAG, Universität Stuttgart
[24] Sørensen N 1998 *HypGrid2D, a 2-D Mest Generator* Risø National Laboratory
[25] Ceyhan O, , Pires O, Munduate X, Sorensen N N, Schaffarczyk A P, Reichstein T, Diakakis K, Papadakis G, Daniele E and Schwarz M 2017 *Summary of the Blind Test Campaign to predict the High Reynolds number performance of DU00-W-210 airfoil*
[26] Michelsen J 1992 *Basis3D - a Platform for Development of Multiblock PDE Solvers*
[27] Michelsen J 1994 *Block structured Multigrid solution of 2D and 3D elliptic PDE's*
[28] Sørensen N 1995 *General Purpose Flow Solver Applied to Flow over Hills* Risø National Laboratory
[29] Leonard B P 1979 *A stable and accurate convective modelling procedure based on quadratic upstream interpolation* Comput. Meths. Appl. Mech. Eng
[30] Menter F R 1993 *Zonal Two Equation k-omega Turbulence Models for Aerodynamic Flows*
[31] Drela M and Giles M B 1987 *Viscous-Inviscid Analysis of Transonic and Low Reynolds Number Airfoils*

APPENDIX D

Article 2: CFD Simulations and Validation of a Wall Roughness Model Applied on a NACA 63_3-418 Airfoil

CFD Simulations and Validation of a Wall Roughness Model Applied on a NACA 63_3-418 Airfoil

Emil Krog Kruse[1,2], Niels N. Sørensen[2], Christian Bak[2] and Mikkel Schou Nielsen[3]

[1]Power Curve ApS, Stationsmestervej 81, DK-9200 Aalborg SV, Denmark
[2]Technical University of Denmark, Department of Wind Energy, Frederiksborgvej 399, DK-4000 Roskilde, Denmark
[3]Dansk Fundamental Metrologi A/S, Kogle All 5, DK-2970 Hoersholm, Denmark

E-mail: ekk@powercurve.dk

Abstract. The implementation of a model to simulate distributed surface roughness, which is the *New k-ω extension* by Knopp et al. into the DTU Wind Energy in-house CFD Reynolds-Average Naviar Stokes solver EllipSys, was validated against wind tunnel experiments conducted in the Laminar Wind Tunnel of the Institute of Aerodynamics and Gas Dynamics, University of Stuttgart. The effort was to predict the aerodynamic penalty of five cases of leading edge roughness applied to a NACA 63_3-418. Three cases were sandpaper and two cases were turbulators/zigzag tape. Simulation of the sandpaper cases showed some agreement in the tendencies of decreased lift and increased drag as a function of angle of attack. However, the magnitudes of the penalties were predicted and underestimated the lift changes and over predicted the drag changes. Modeling the zigzag tape using the roughness model was not successful, because the influence from the model was too small. The simulated zigzag tape hardly deviated from the fully turbulent simulation so when using the model in its current form, one should be aware of its limitations.

1. Introduction

The performance of wind turbines, both new and old models, has become of great interest for wind turbine owners as their profit depends on this. Among other parameters, the surface condition of the wind turbine blades is crucial to the performance [1, 2, 3, 4, 5]. The surface condition around the leading edge of a turbine blade plays a critical role in the aerodynamic properties and thereby the turbine performance. Contamination on the leading edge can take many forms and has over time been reduced to the term Leading Edge Roughness (LER) [6, 7]. All surfaces have some roughness, but the question is how much an airflow over an airfoil suffers from a given roughness. When the roughness of a surface is lower than the laminar sub layer of the flow, it is said to be hydrodynamically smooth, and the aerodynamic changes are negligible [8].

Predicting the aerodynamic properties of an airfoil with non-smooth walls has proven to be challenging in both experiments and simulations. Since the LER on wind turbine blades in the field is closer to stochastic than deterministic, some simplification of the LER has been needed. There are at least two governing methods for emulating LER in a wind tunnel experiment: Boundary layer tripping and distributed roughness. The boundary layer tripping is done with

a trip strip or turbulator such as zigzag tape. The distributed roughness causes the boundary layer thickness to increase over the rough surface and might, as the trip strip, eventually cause a separation of the airflow. The impact for both methods is often decreased lift, increased drag and premature stall.

In reality, the impact of LER is often a a result of the combination of the airflow tripping over an edge and losing energy from distributed roughness. Determining the main contributor to aerodynamic changes on a given LER situation might be challenging, especially for a wind turbine blade, as LER will likely vary along the radial span. Even though LER can be realized in many ways the performance of LER on airfoils has been modeled simply by forcing transition either from the very leading edge or e.g. from where a zigzag tape is mounted on a wind tunnel model. Previous work has been carried out by the authors on predicting the influence on the aerodynamics by turbulators such as zigzag tape, see [9]. The method utilized in this work is not suitable for simulating distributed roughness, as the simulation grid would have to completely resolve the roughness, resulting in a vast number of cells in the grid. Effort has been made to simulate the influence of distributed roughness by modifying the criteria for transition from laminar to turbulent flow [10, 11, 12, 13, 14, 15]. Since simulation of LER by simply forcing transition in many cases do not result in sufficiently big losses in aerodynamic performance, there is a need to model this roughness and the performance loss in a simple way. As an alternative approach, this work is based on a wall roughness model developed by Knopp et al. [16] modifying the k-ω turbulence model on rough surfaces which was tested later in Knopp et al. [17]. Even though this model simulate the impact of distributed surface roughness, studies are also carried out to determine whether this roughness model can be used to represent a turbulator in simulations.

2. Methods

A series of wind tunnel experiments were carried out in 2015 by the Technical University of Denmark, Department of Wind Energy (DTU Wind) in the Stuttgart Laminar Wind Tunnel. One of the main objectives with this experimental campaign was to test different kinds of LER. The LER was emulated by either zigzag tape or by sand grain paper on the leading edge. The experiments are described in Section 2.1. The flow fields are predicted by Computational Fluid Dynamics (CFD) Simulations. The CFD consists of a grid and a solver, which are described in more detail in Section 2.2 and 2.3. The results are presented in Section 3.

2.1. Experimental Setup

In 2015 a series of wind tunnel experiments were conducted in the Laminar Wind Tunnel (LWT) of the Institute of Aerodynamics and Gas Dynamics, University of Stuttgart. The objectives were to test the performance of different Vortex Generator (VG) add on solutions. Vortex Generators are typically applied to a turbine blade as a measure to mitigate the performance losses from LER. In an effort to create realistic results, some LER had to be applied to the test airfoil. It was chosen to use one of the standard methods, zigzag tape, as a turbulator, but some experiments were done with sand grain paper that corresponds to sandpaper on the leading edge as well. The LER types were tested with and without VGs. The VGs are of no interest to this work, which focuses on simulating LER. This results in the following experimental data with LER:

The zigzag tape has a 60 degrees pattern and the height is denoted in the overview above. For the sand grain paper, the chordwise end position is denoted in *Location* whereas the chordwise start of the zigzag tape is denoted. Pressure side is denoted by p.s. and suction side by s.s. The same profile was used in all experiments at a Reynolds Number of 3 million The chord length was 0.6 m and the span is 0.73 m. The lift coefficient C_l was calculated as an integration of the measured pressure distribution along the tunnel walls. The drag coefficient

Table 1: Experiments with a designated Experiment Number (ExpNo) or Simulation Number (SimNo).

ExpNo/SimNo	LER Type	Location
1	Clean	-
2	P120	3%c s.s., 3%c p.s.
3	P120	8%c s.s., 8%c p.s.
4	P60	8%c s.s., 8%c p.s.
5	Zigzag 0.4 mm	2%c s.s., 10%c p.s.
6	Zigzag 0.8 mm	2%c s.s., 10%c p.s.
7 (Sim Only)	P20	8%c s.s., 8%c p.s.

C_d is calculated by integration of the wake rake. The pressure coefficient C_p is measured by 62 pressure taps distributed on the profile surface with a higher concentration around the leading edge. Standard tunnel corrections are applied to C_l and C_d as $K_{C_l} = 0.9841$ and $K_{C_d} = 0.9939$. C_p is uncorrected. An angle of attack (AoA) offset of 0.2 degrees is observed in the experiments and are compensated for in the simulations, such that 4 degrees AoA is simulated with 3.8 degrees AoA. The profile equipped with sand grain paper and zigzag tape can be seen in Figure 1.

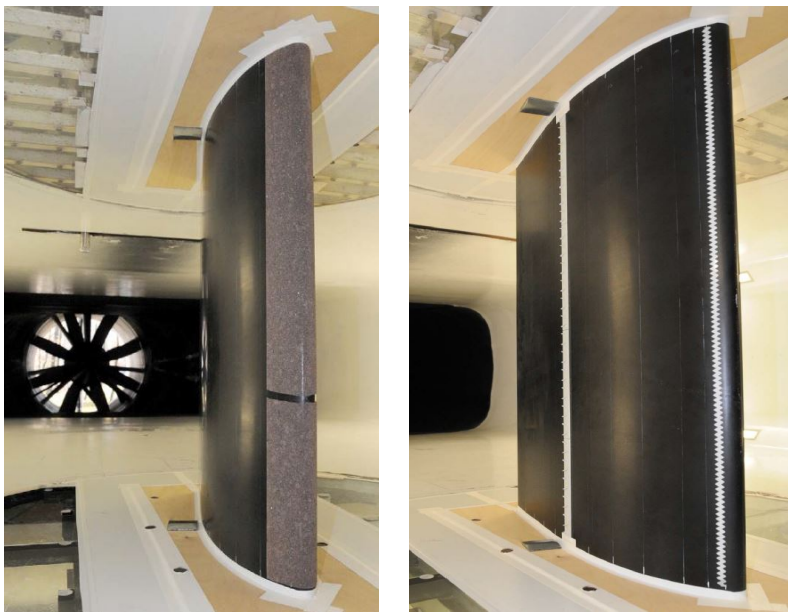

Figure 1: 1) P60 sand grain paper on the leading edge with pressure taps uncovered. 2) Example of zigzag tape in 2% chord and VGs on the suction side.

2.2. Numerical Setup for CFD Simulations

In an effort to simulate the airflow measured in the experiments described in Section 2.1, the CFD code EllipSys from DTU Wind Energy was chosen, which comes in a 1D, 2D and 3D version. As the experimental profile is an extruded NACA 63_3-418 and as the wind tunnel tests simulate 2D conditions, the code chosen is EllipSys2D. EllipSys is an incompressible finite volume RANS flow solver. The Navier-Stokes equations are solved with the SIMPLE algorithm [18, 19, 20]. The convective terms are discretized with the QUICK scheme [21]. The relaxation

parameters are of typical magnitude 0.7 for velocities and 0.2 for pressures. The simulation input parameters are normalized to obtain a Reynolds Number of 3 million determined by the dynamic viscosity $\mu = 3.333 \cdot 10^{-7}$, hence an inflow velocity of $u = 1$ m/s and a chord length of $c = 1$ m. No convergence problems have been observed in any simulation, with a convergence criteria of reducing the residuals of velocity and pressure to $1{\cdot}10^{-6}$ of the residuals in the first iteration.

Grid independent solutions are ensured by running the simulation on two coarser grid levels with 1/4 cells in the second level and 1/16 cells in the third level, and only observing minor changes between the levels. For each AoA the grid is divided into 64 blocks and typically split to 16 cores. The focus of the study is the typical operational region for a wind turbine in the part of the power curve where power is maximized, and also the first part of the stall region, hence it has been chosen to simulate -5 to 15 degrees AoA.

The model used for simulating turbulence is Menter's SST k-ω model with a *New* k-ω *extension* by Knopp et al. to account for wall roughness [22, 16]. The usual rule of thumb for wall cell height is to have a $y^+(1) \approx 1$. Older roughness extensions of the k-ω turbulence model exist, see [23], first presented in 1998, with reportedly good agreement between simulations and experimental results. The Wilcox extension requires $y^+(1) < 0.003$ which in most cases results in a vast amount of cells in the normal direction. One of the major strengths of using the *New* k-ω *extension* is the requirement that $y^+(1) < 0.3$, which is a less strict constraint on the wall cell height. One disadvantage of using the *New* k-ω *extension* to simulate wall roughness is that it only works in turbulent flow. Since the roughness both in experiments and simulations is applied to the leading edge, the simulated inflow must be turbulent, which might not represent reality. The *New* k-ω *extension* is applied to the relevant wall cells of the airfoil together with an equivalent sand grain roughness height k_r.

2.3. Grid Setup for CFD Simulations

As in previous work [9], the NACA 63_3-418 airfoil used in the experimental setup was measured and used in the CFD simulations. The measured coordinates were smoothed to reduce small fluctuations in curvature. The trailing edge was represented by one set of coordinates, and was substituted by more coordinates with a smoother shape and a thickness of approximately 0.1% chord length. The grid has 512 cells in both the circumferential and the normal direction, with the total of 262,144 cells. In order to satisfy the $y^+(1) < 0.3$ constraint described in Section 2.2, the wall cell has a height of $\approx 1 \cdot 10^{-7}$, resulting in a maximum $y^+(1) \approx 0.03$ in the simulation with the clean airfoil, providing sufficient $y^+(1)$ margin for possibly different local conditions in other simulations.

An o-mesh forms the basis of the grid with the airfoil at the center. The grid is made with the DTU Wind Energy in-house grid generator *HypGrid2D*. The radius is 45 times the chord length with the outer cells having a height of 3 times the chord length. The outlet boundary condition is put on 72 cells on each side of the trailing edge, in this grid corresponding to between 40-50 degrees on each side, whereas the inlet covers the remaining outer boundary. The grid is divided into 64 blocks each of 4,096 cells, allowing parallel processing to be performed. A simulation is run on 16 parallel cores and the calculation time is between 4 and 12 minutes depending on AoA. The full domain, blocks, in- and outlet are illustrated in Figure 2 and a zoom on the grid close to the profile in Figure 3, where only 1 of 4 lines are shown, hence only 1 in 16 cells are shown. The concentration of cells follows the curvature with more cells in regions with high curvature.

2.4. Determining the Equivalent Grain Roughness Height

In the *New* k-ω *extension* turbulence model, the equivalent sand-grain height k_r is used to include the effect of surface roughness. However, as already noted by Schlichting [24], the definition of

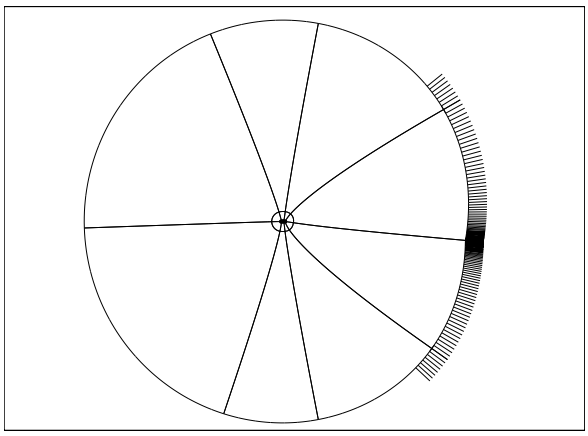

Figure 2: Grid domain showing blocks, inlet and outlet. Domain radius is 45 times the chord length.

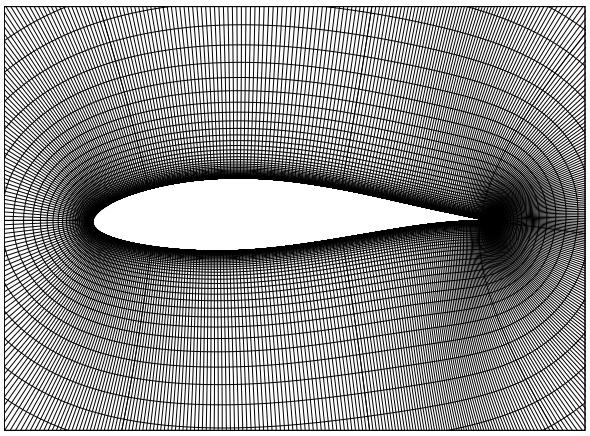

Figure 3: Coarser grid lines near the profile with 1/4 lines shown in each direction.

k_r is not directly linked to the geometric surface roughness. Thus, several correlations have been proposed to predict k_r from the geometric characteristics of the surface as discussed in reviews by Bons [25] and Flack and Schultz [26]. Nonetheless, no single type of correlation seems to predict all surface topographies [27].

For distributed roughness, Flack and Schultz [26] investigated the correlation between observed k_r and the surface topography of several surface types including sandpaper. They proposed the following empirical relation between k_r and two surface roughness parameters; the RMS roughness Sq and skewness Ssk.

$$k_r = 4.43 \cdot Sq(1 + Ssk)^{1.37} \tag{1}$$

To establish values of k_r, the surface topography of sandpaper of grits P40, P60, P80, P100, P120, P180 and P240 was measured using a calibrated PLU NEOX confocal microscope by Sensofar. A x5 magnication objective with spatial pixel size of 3.32 μm, a vertical step size of 12 μm, and a field of view of 9 mm x 9 mm were used. The estimated relative uncertainty of the microscope in the vertical direction was 1%. The 3D surface reconstruction was done using the SensoSCAN software as illustrated in Figure 4 for grits P60 and P120.

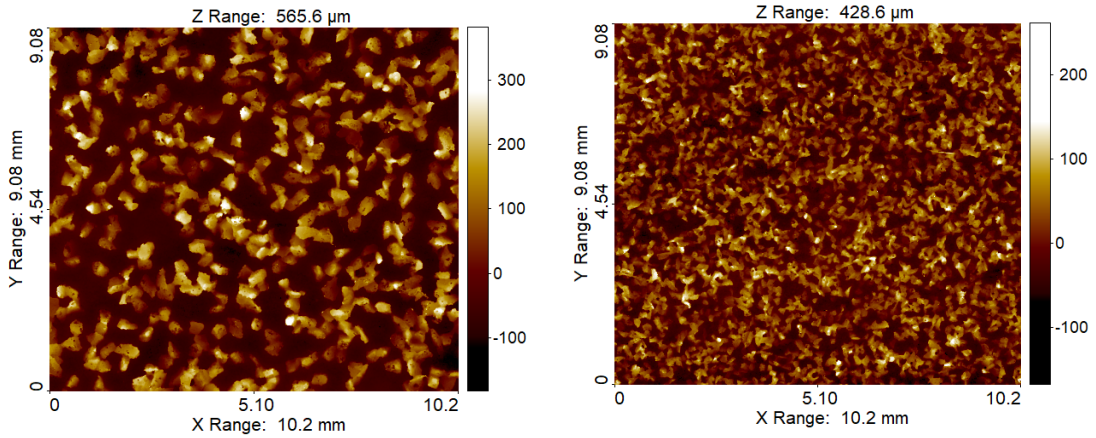

Figure 4: Confocal microscopy height-maps of sandpaper of grit P60 (left) and P120 (right).

The Sq and Ssk parameters were calculated using the SPIP application software from Image metrology. A leveling was applied prior to a roughness analysis using a S-filter of 10 μm and a L-filter of 10 mm as described in ISO 25178-3 [28]. From the measured Sq and Ssk, values of k_r were calculated using Equation 1 as shown in Table 2. Also shown is the average grain diameter associated with each grit size in accordance to ISO 6344 [29]. As seen in Figure 5, the value of k_r is approximately proportional to the average grain diameter. Using a linear least-squares fit, the scaling factor was found to be 3.56 with a R^2 value of 0.997. The reported values from [26] were included in the fit.

Table 2: Sandpaper topography values. Average grain diameter according to [26]. Measured values for Sq and Ssk. Calculated values for k_r using Equation 1.

Grit Size [-]	P40	**P60**	P80	P100	**P120**	P180	P240
Average Grain Diameter [μm]	425	269	201	162	125	82	53
RMS Roughness, Sq [μm]	142	88	62	53	42	28	23
Skewness Ssk [-]	1.01	0.92	1.07	0.71	0.62	0.51	0.34
Eq. Sand Grain Roughness, k_r [μm]	1637	955	741	492	357	216	152

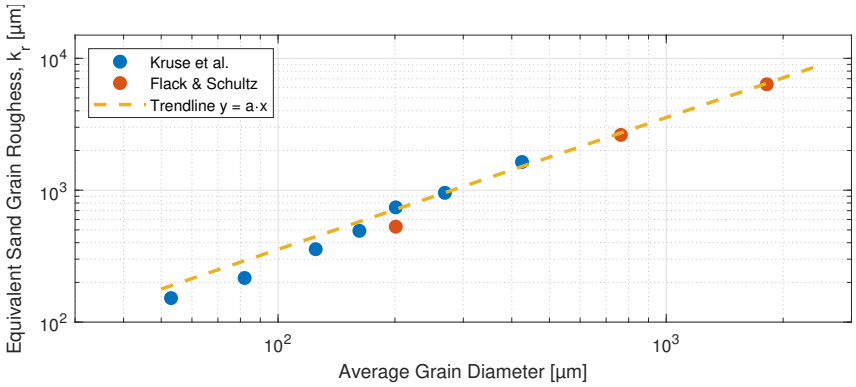

Figure 5: The average sand grain diameter from [26] versus k_r calculated from Equation 1 on a loglog plot. The trendline is a linear fit with crossing in (0,0) and a slope of 3.56. The R^2 value is 0.997.

As the EllipSys CFD simulation is done on a profile with a chord different from the experimental profile, the roughness height k_r is scaled as accordingly with $c_{exp}/c_{cfd} \cdot k_r = 1/0.6 \cdot k_r$. However, one should be aware of how to scale the roughness height if Reynolds numbers are varied [30].

2.5. Roughness Model Limitations

As the purpose of this study is to test a method for applying distributed roughness to CFD simulations, a study of the model limitations has been conducted. Roughness is applied to all wall cells of the profile. Roughness heights are applied ranging from hydrodynamically smooth values to fully rough conditions and then further in to practically infeasible values. The maximum realistic roughness height is difficult to determine, but roughness higher than a few percent of the chord seems unrealistic. For testing purposes, the study is limited to an over exaggerated value $k_r = 0.333$ m, corresponding to a hydrodynamic roughness length of $1 \cdot 10^{-2}$ m. Simulations are done at 0, 4 and 8 degrees AoA.

Figure 6 shows the ratio between the rough and clean lift coefficient C_l in a) and drag coefficient C_d in b). A tendency change of C_d is observed around $k_r \approx 4 \cdot 10^{-4}$ m. Investigation of the skin friction and pressure distributions reveals that around this roughness height, there is a shift in balance between pressure drag and friction drag. The pressure drag is lowered for low angles of attack, but increased for higher angles of attack. The reason for this is the separation of the flow, which moves towards the leading edge as the roughness height is increased. The lower angles of attack do not show any separation. As illustrated in c), a shift in the balance of forces is observed again around $k_r = 2 \cdot 10^{-3}$ m, where the skin friction increase becomes dominant and the total drag increases. The model reaches its limits shortly below $k_r = 2 \cdot 10^{-2}$ m where the skin friction drops rapidly towards 0.

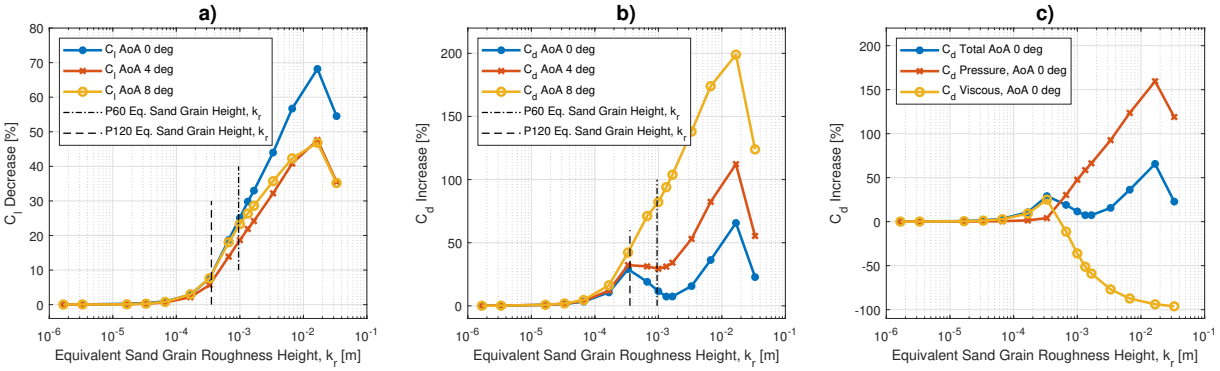

Figure 6: Roughness model applied to all airfoil wall cells for different equivalent sand grain roughness heights k_r for 0, 4 and 8 degrees AoA, with k_r for P60 and P120 sandpaper marked by dashed lines. a) shows the decrease in C_l as a function of k_r. b) shows the increase in C_d as a function of k_r. c) shows the pressure and viscous components of C_d as a function of k_r at 0 degrees AoA.

3. Results

Figure 7 shows the clean experiment ExpNo 1 compared to the CFD simulated clean airfoil, as this forms the basis for the rough simulations.

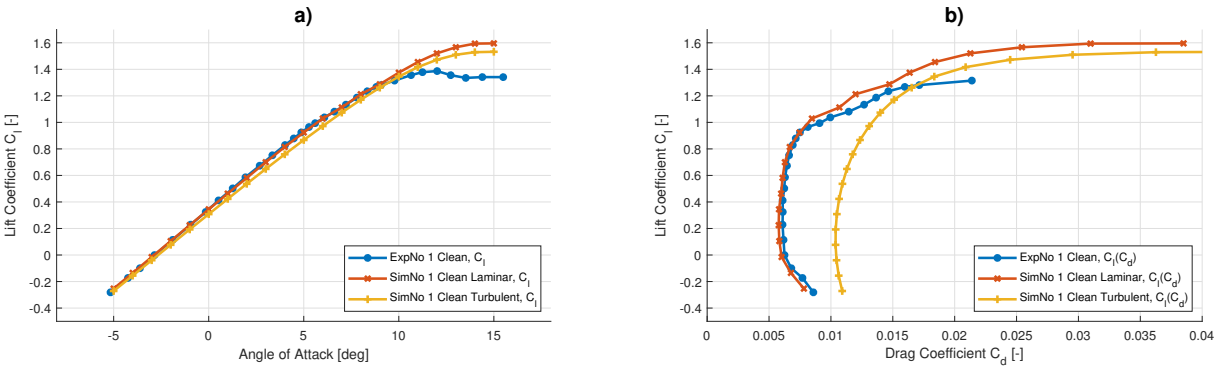

Figure 7: Results for ExpNo 1 compared to CFD simulations with laminar and turbulent inflow. The e^N transition model is used to predict transition in the laminar simulation with a N factor of 9, corresponding to the LWT turbulence intensity. All results are for a Reynolds Number of 3 million.

Figure 7 a) shows the lift as a function of AoA ranging from approximately -5 to 15 degrees and b) shows the lift as a function of drag. The experimental clean airfoil shows stall at a lower AoA than the simulation seen in a), probably due to tunnel effects and the simplification of the turbulence model. The lift has a small change in slope at 7 deg AoA which is also seen in the simulations. The geometric properties of the airfoil used in the wind tunnel are probably the root cause for this, as it is not observed on a theoretical NACA 63_3-418 airfoil. The maximum lift is over predicted in simulations. The experimental drag seen in b) is close to the drag predicted assuming laminar inflow and using modeling of free transition. The drag is under predicted in the simulations after the slope change at 7 deg AoA. The LWT has very low turbulence, and it makes sense that the laminar inflow gives the best result. Making the inflow turbulent gives a higher drag by a factor of two and a less accurate lift. There are no drag measurements present in experiments with separated flow. When comparing clean cases to rough cases in the following, it is chosen to use the laminar simulation as a baseline, as this is deemed the most realistic representation of the physics.

3.1. Results for Sandpaper

Figure 8 shows the lift and drag polars from the wind tunnel experiments and CFD simulations denoted ExpNo and SimNo 1, 2, 3 and 4 in Table 1, i.e. clean case and cases with sandpaper P120 to x/c=0.03 on both s.s. and p.s. and P120 and P60 to x/c=0.08 on both s.s and p.s., respectively.

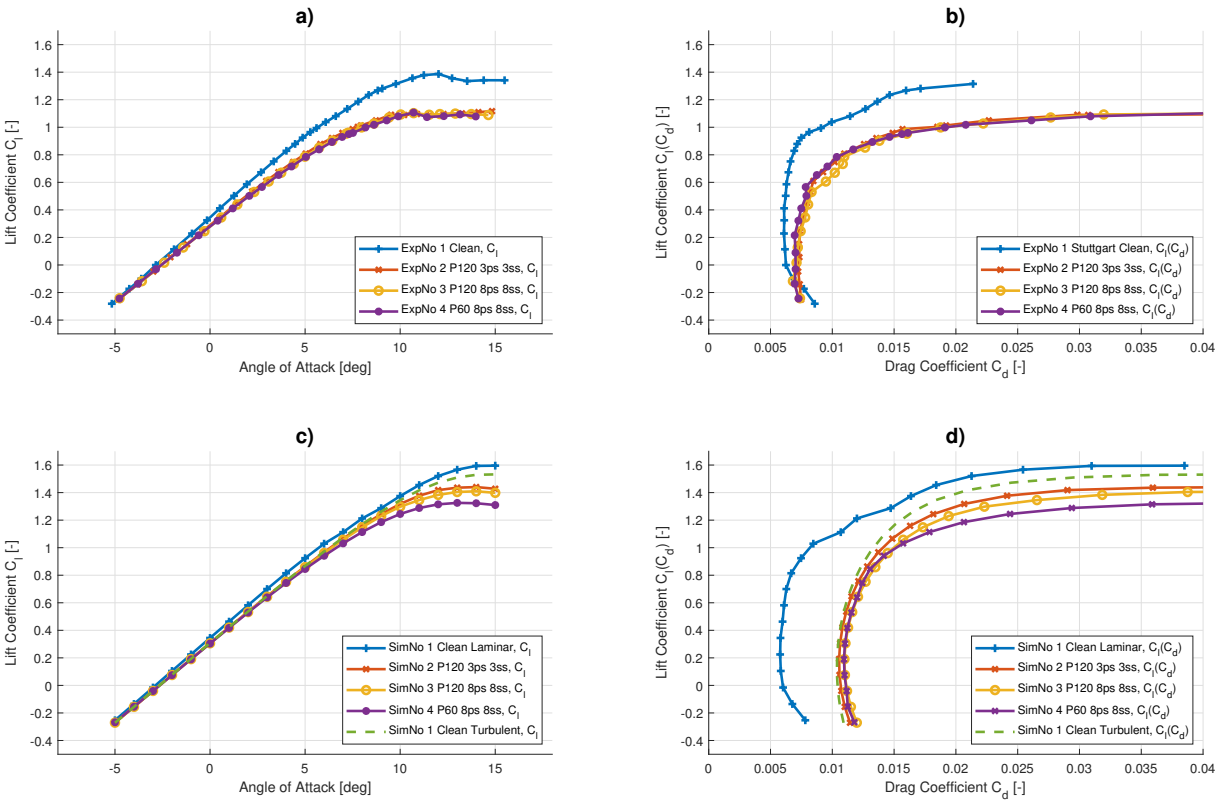

Figure 8: Results for ExpNo and SimNo 1, 2, 3 and 4 in Table 1. a) C_l as a function of AoA from wind tunnel experiments b) C_l as a function of C_d from wind tunnel experiment c) C_l as a function of AoA from CFD simulations d) C_l as a function of C_d from CFD simulations. The Reynolds Number is 3 million in all cases.

Figure 8 a) and c) shows the lift coefficient C_l as a function of AoA whereas b) and d) shows the lift coefficient C_l as a function of the drag coefficient C_d. Plots a) and b) are the experimental data and c) and d) are the CFD simulations.

One interesting phenomena is that the experiments with sandpaper show no significant differences in aerodynamic performance despite changing both the roughness and the extent of it. When zooming in, the difference can be seen with only marginal decrease in maximum C_l and increase in C_d with increase in grain size or extent of the sandpaper. Regarding the lift, ExpNo 2 shows the lowest penalty closely followed by ExpNo 3 and lastly ExpNo 4, which makes physical sense since a surface with a higher roughness coverage and severity is expected to suffer the most. The simulated results show more pronounced but similar tendencies. The lift penalty on SimNo 4 is almost twice that for SimNo 2 and 3.

Zooming in on the drag shows no significant tendencies as it seems the differences are lower than the accuracy of the experiments. The same applies for the simulated drag where the differences are small in the linear lift region. The drag increases in the stall region but the uncertainty of the experiments is higher and therefore hard to draw conclusions on. Comparing absolute values often proves to be infeasible, and it was chosen to compare the results from Figure 8 by the decrease in lift and increase in drag with the ExpNo and SimNo 1 as base. The changes can be seen in Figure 9.

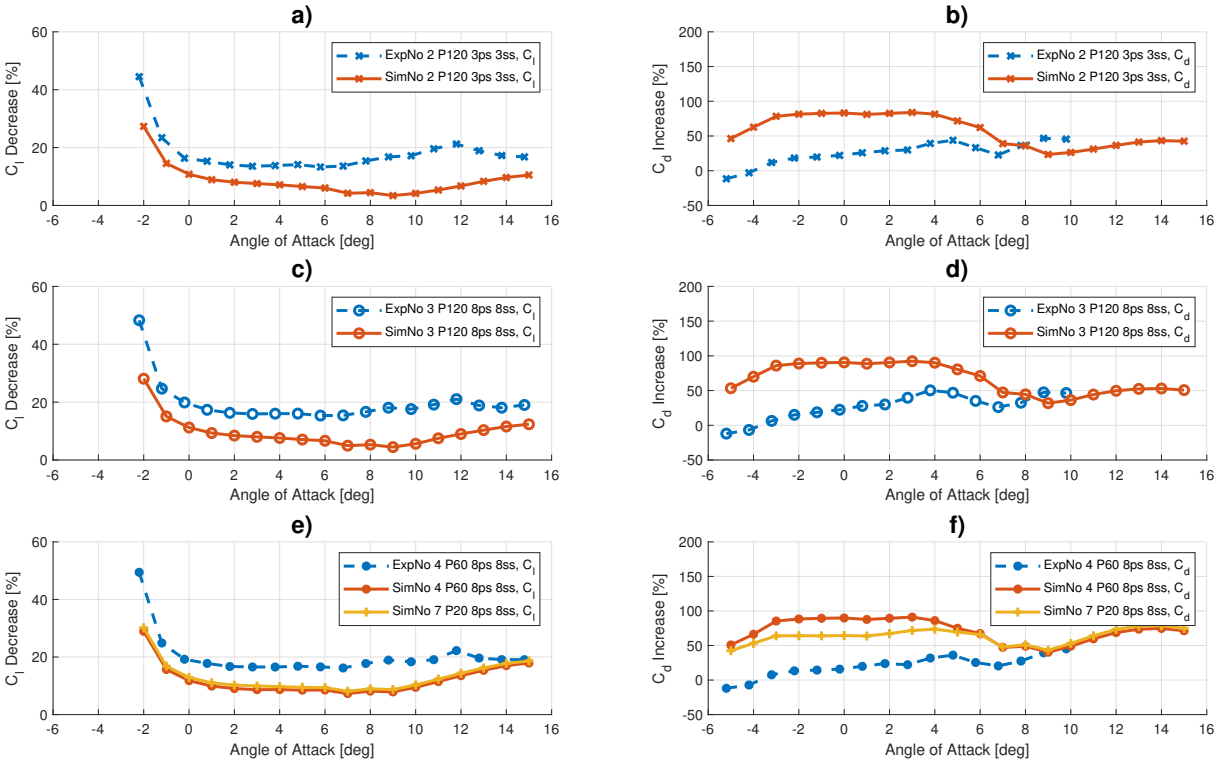

Figure 9: Changes in lift and drag for experiments and CFD simulations shown in Figure 8. a), c) and e) shows C_l *Decrease* which is calculated as $(C_{l,Clean}\text{-}C_{l,Rough})/C_{l,Clean}$. b), d) and f) shows C_d *Increase* which is calculated as $(C_{d,Rough}\text{-}C_{d,Clean})/C_{d,Clean}$. Experimental data has been interpolated from -5 to 15 with steps of 1 degree AoA for calculation purpose.

Figure 9 a), c) and d) shows the decrease in lift and b), d) and f) shows the increase in drag for the experiments compared to different rough cases. The tendencies in these results are clear: The simulations under predict the lift decrease and over predicts the drag increase. One might suspect that the roughness parameter k_r has been under estimated, as Figure 6 shows a region where the lift decrease continues as the drag increase is reduced. To test this, the SimNo 7 P20 simulation is introduced as an extrapolation of the values in Table 2. SimNo 7 has the same coverage as SimNo 3 and 4. The result can be seen in e) and f), where the lift decrease is changed but with no significant magnitude. The same goes for the drag. One should keep in mind that changing from P60 to P20 is a change in k_r of a factor 4.5. Running the P20 is also on the brink of the limitations described in Section 2.5.

Figure 10 shows three examples of the pressure coefficient C_p with one for 0, 4 and 8 degrees AoA for ExpNo/SimNo 2, 3 and 4. respectively.

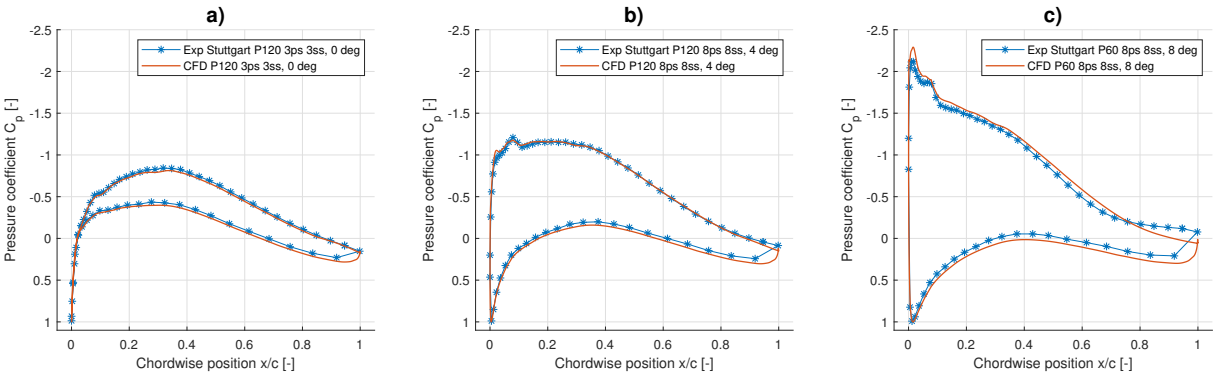

Figure 10: Each graph shows a pressure coefficient C_p from experiments compared to C_p from CFD simulation for different roughness and AoA.

The difference in C_p between ExpNo/SimNo 2, 3 and 4 is close to unnoticeable. Zooming on the pressure peak for 8 degrees AoA will show a little difference. The prediction of C_p is generally good, especially for lower AoA. Plot c) shows adverse pressure gradient from 70%c to the trailing edge in terms of almost constant pressure. This might be a sign of separation, and is less severe in the CFD simulation. This might account for some of the difference in the stall region illustrated in Figure 8.

Investigation of the skin friction C_f is only present in the CFD simulations, as there are no experimental data for skin friction. The skin friction is illustrated in Figure 11.

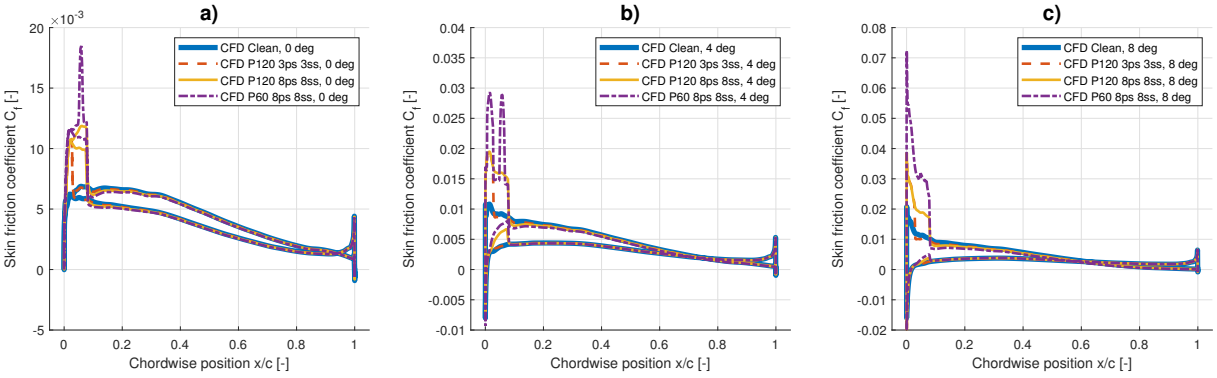

Figure 11: Simulated skin friction C_f for the situations illustrated in Figure 10. The friction for the rough case is close to the clean case in cells without modified boundary conditions.

The skin friction of the cells with no model applied has similar values to the clean simulation. The skin friction in cells with the model active is increased and the higher the roughness, the higher the skin friction. The skin friction also increases with the AoA due to the higher velocities around the leading edge, where the roughness is applied. It is difficult to conclude whether the magnitudes of the skin friction are realistic due to lack of experimental data. The polars in Figure 8 show no significant increase in drag in the linear region and based on this, the skin friction magnitude is probably within a realistic range. Increasing it further would lead to an increase in drag.

3.2. Results for Zigzag Tape

The next question is if the *New k-ω extension* is able to simulate the effect of turbulators. ExpNo 5 and 6 is conducted with zigzag tape, in the same location but two different heights. Figure 12

shows the polars from the experiments and the simulations.

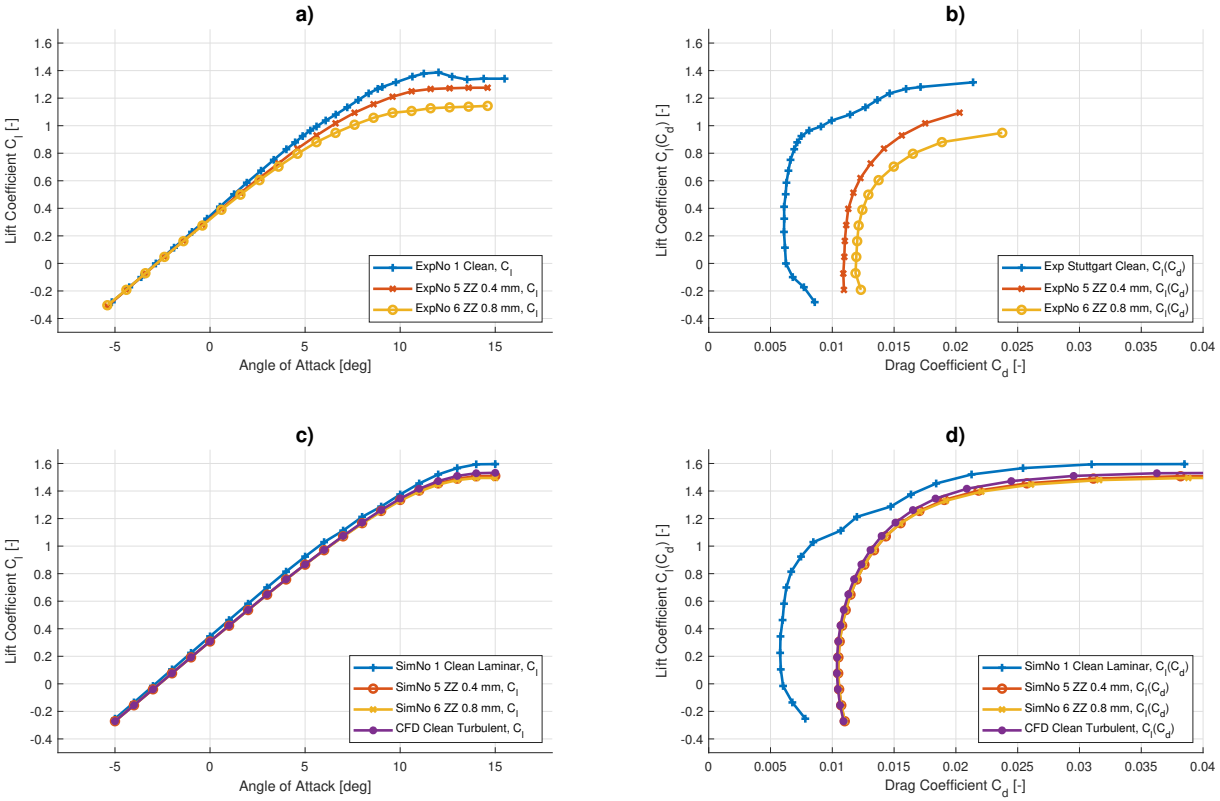

Figure 12: Results for ExpNo 1, 5 and 6 in Table 1. a) C_l as a function of AoA from wind tunnel experiments b) C_l as a function of C_d from wind tunnel experiment c) C_l as a function of AoA from CFD simulations d) C_l as a function of C_d from CFD simulations.. The Reynolds Number is 3 million in all cases.

In contrary to the distributed roughness/sandpaper in Section 3.1, the difference in lift is significant due to an increased height of the turbulator. The difference in drag is less significant, but more pronounced than the sandpaper. Simulation of the turbulator also requires a roughness height k_r. No correlation between zigzag tape and roughness height was found in the literature. The roughness height k_r is defined to be the height of the zigzag tape, 0.4 mm and 0.8 mm. From Figure 12 c) and d) it is clear that the difference is small between different zigzag tape heights. The physics is not captured by the model. Comparing to the fully turbulent simulation without any roughness model shows no significant difference. For consistency, the percentage difference between the clean and turbulated polars is illustrated in Figure 13.

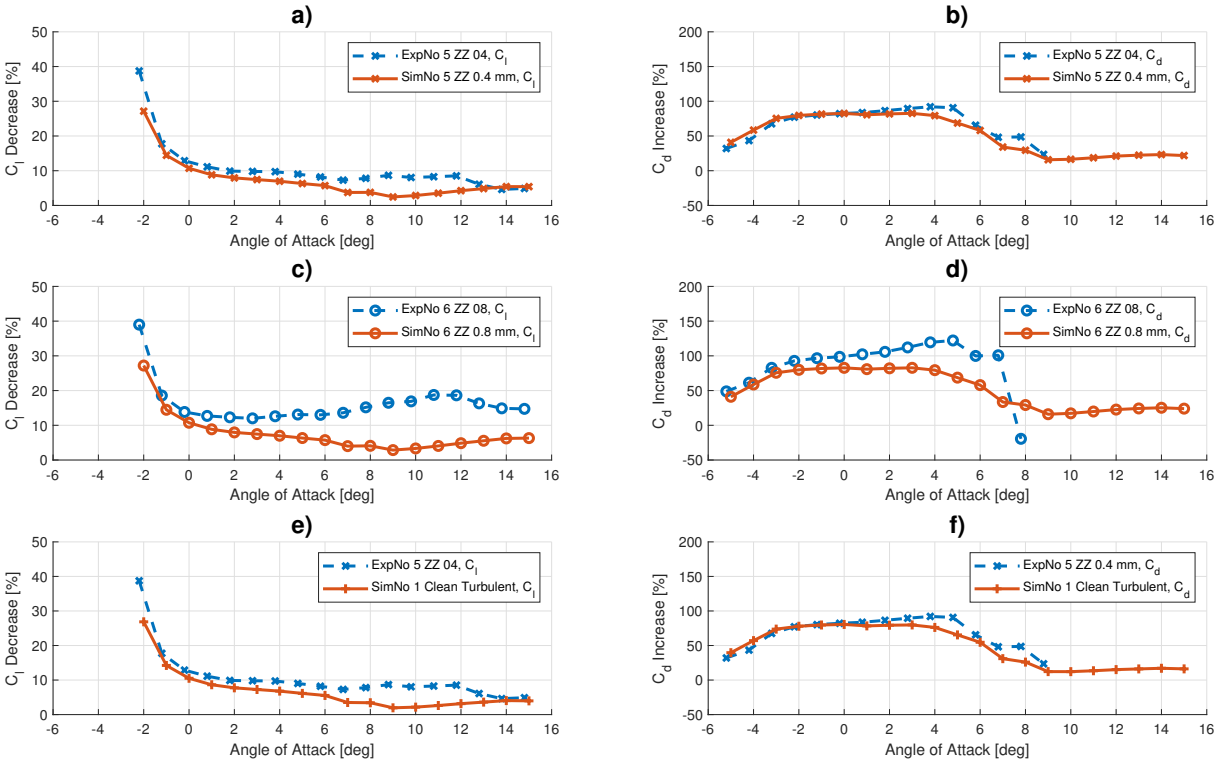

Figure 13: Changes in lift and drag for experiments and CFD simulations shown in Figure 12. a), c) and e) shows C_l *Decrease* which is calculated as $(C_{l,Clean}\text{-}C_{l,Rough})/C_{l,Clean}$. b), d) and f) shows C_d *Increase* which is calculated as $(C_{d,Rough}\text{-}C_{d,Clean})/C_{d,Clean}$. Experimental data has been interpolated from -5 to 15 with steps of 1 degree AoA for calculation purpose.

At first glance, Figure 13 a) and b) shows similar results for ExpNo and SimNo 5. The trends are similar as well as the percentage magnitudes. When increasing the zigzag tape height from 0.4 mm to 0.8 mm in c) and d), the difference increases. The simulation results are almost unchanged. As previously mentioned, the difference between the turbulent clean in the experiments and turbulated simulation is small. Plot e) and f) compares ExpNo 5 to SimNo 1 Turbulent. A good correspondence is observed as in SimNo 5. A conclusion can be that a profile with the transition triggered by turbulators might be simulated by a fully turbulent inflow as long as the turbulator has a height where its presence has low impact on the geometry of the airfoil. When the turbulator gets high, not only is the transition point triggered, but the boundary layer profile may be changed dramatically. To simulate higher turbulators, one approach could be geometrical changes of the simulation grid as in the work by Kruse et al. [9].

4. Conclusion

The implementation of the *New k-ω extension* by Knopp et al. into EllipSys was validated against wind tunnel experiments. The wind tunnel experiments showed that the lift was decreased with between 15-20% and the drag increased with 0-50% depending on AoA. At AoAs of -4 and -5, the wind tunnel experiments showed a small decrease in drag, which questions the accuracy of the drag measurements. The difference between the three sandpaper types and extension was significantly low. All three of sandpaper with different roughness height and extension types showed similar behaviour and magnitudes.

The simulation of the aerodynamic changes showed somewhat similar tendencies but did not

correspond well on the magnitudes of the decrease in lift and drag. The simulations showed that the lift was decreased with between 5-10% and the drag increased with 30-90% depending on AoA. Furthermore, the model predicted a different change in lift and drag penalty for the three sandpaper types. The differences in between seemed to have a somewhat linear development, but the physics might be highly non-linear and more complex than anticipated by the model.

When simulating the aerodynamic performance of cases with zigzag tape, the conclusion is different. The wind tunnel experiments showed a significant difference in results for the zigzag tape of 0.4 and 0.8 mm heights. The model predicted the same aerodynamic penalty for both the 0.4 and 0.8 mm zigzag tape heights. The full turbulent simulation without the roughness model activated showed results similar to the ones simulated with zigzag tape, which suggests that the model can not properly simulate the changes in the airflow for turbulators.

In general, the performance of the *New k-ω extension* did not perform well on the NACA 63_3-418 with the given leading edge roughness and more work needs to be put into the calibration of it. A combination of the *New k-ω extension* and a laminar to turbulent transition model might prove beneficial.

Acknowledgements
Our acknowledgement goes to the Danish Energy Agency for the support and funding for this project, the *"Leading Edge Roughness on Wind Turbine Blades", 64015-0046, the Technical University of Denmark and Power Curve ApS.*

References

[1] Sareen A, Sapre C A and Selig M S 2014 Effects of leading edge erosion on wind turbine blade performance *Wind Energy, 17:15311542* 17:15311542
[2] Langel C M, Chow R, Hurley O F, van Dam C P, Ehrmann R S and White E B 2015 Analysis of the Impact of Leading Edge Surface Degradation on Wind Turbine Performance *33rd Wind Energy Symposium* URL `https://doi.org/10.2514/6.2015-0489`
[3] van Rooij R and Timmer W A 2003 Roughness Sensitivity Considerations for Thick Rotor Blade Airfoils *Journal of Solar Energy Engineering-transactions of the ASME* **125** 468–478
[4] Hooker R W 1933 The aerodynamic characteristics of airfoils as affected by surface roughness *NACA-TN-457 Langley Memorial Aeronautical Laboratory* 468–478
[5] Gaudern N 2014 A practical study of the aerodynamic impact of wind turbine blade leading edge erosion *The Science of Making Torque from Wind 2014 (TORQUE 2014), Journal of Physics: Conference Series 524 (2014) 012031*
[6] Corten G P and Veldkamp H F 2001 Aerodynamics: Insects can halve wind-turbine power *Nature* **412, 4142**
[7] Bak C, Andersen P B, Madsen H A, Gaunaa M, Fuglsang P and Bove S 2008 Design and verification of airfoils resistant to surface contamination and turbulence intensity *In Collection of Technical Papers - AIAA Applied Aerodynamics Conference* **AIAA 2008-7050**
[8] Schlichting H 1979 Boundary-Layer Theory 7^{th} Edition *McGraw Hill*
[9] Krog Kruse E, Sørensen N and Bak C 2018 Predicting the Influence of Surface Protuberance on the Aerodynamic Characteristics of a NACA 63_3-418 *Journal of Physics: Conference Series, 1037(2), 2018 [022008]* URL `https://doi.org/10.1088/1742-6596/1037/2/022008`
[10] Standish K, Rimmington P, Laursen J and Paulsen H N 2010 Computational Prediction of Airfoil Roughness Sensitivity *48th AIAA Aerospace Sciences Meeting and Exhibit*
[11] Ehrmann R S, White E B, Maniaci D C, Chow R, Langel C M and van Dam C P 2013 Realistic Leading-Edge Roughness Effects on Airfoil Performance *31st AIAA Applied Aerodynamics Conference*
[12] White E B, Kutz D, Freels J, Hidore J P, Grife R, Sun Y and Chao D 2011 Leading-Edge Roughness Effects on 63_3-418 Airfoil Performance *49th AIAA Aerospace Sciences*
[13] Langel C M, Chow R, van Dam C P, Maniaci D, Ehrmann R and White E B 2014 A Computational Approach to Simulating the Effects of Realistic Surface Roughness on Boundary Layer Transition *American Institute of Aeronautics and Astronautics*

[14] Langel C M, Chow R and van Dam C P 2015 Further Developments to a Local Correlation Based Roughness Model for Boundary Layer Transition Prediction *American Institute of Aeronautics and Astronautics*
[15] Langel C M, Chow R and van Dam C P 2017 RANS Based Methodology for Predicting the Influence of Leading Edge Erosion on Airfoil Performance *Sandia National Laboratories*
[16] Knopp T, Eisfeld B and Calvo J B 2008 A new extension for the k-ω turbulence models to account for wall roughness *International Journal of Heat and Fluid Flow*
[17] Eisfeld B, Knopp T and Calvo J B 2010 Application of a New Roughness Extension for kω Turbulence Models *Springer Berlin Heidelberg* 43–50
[18] Sørensen N 1995 General Purpose Flow Solver Applied to Flow over Hills *Risø National Laboratory*
[19] Michelsen J 1992 Basis3D - a Platform for Development of Multiblock PDE Solvers *Technical Report AFM 92-05, Technical University of Denmark, Department of Fluid Mechanics*
[20] Michelsen J 1994 Block structured Multigrid solution of 2D and 3D elliptic PDE's *Technical Report AFM 94-06, Technical University of Denmark, Department of Fluid Mechanics*
[21] Leonard B P 1979 A stable and accurate convective modelling procedure based on quadratic upstream interpolation *Comput. Meths. Appl. Mech. Eng, 19:59–98* 19:59–98
[22] Menter F R 1993 Zonal Two Equation k-ω Turbulence Models for Aerodynamic Flows *AIAA 1993-2906*
[23] Wilcox D C 2006 Turbulence Modeling for CFD, 3^{rd} Edition *DWC Industries*
[24] Schlichting H 1937 Experimental Investigation of the Problem of Surface Roughness *National Advisory Committee for Aeronautics*
[25] Bons J P 2010 A Review of Surface Roughness Effects in Gas Turbines *J. Turbomach., vol. 132, no. 2, p. 21004*
[26] Flack K A and Schultz M P 2010 Review of Hydraulic Roughness Scales in the Fully Rough Regime *J. Fluids Eng., vol. 132, no. 4, p. 41203*
[27] Yuan J and Piomelli U 2014 Estimation and prediction of the roughness function on realistic surfaces *J. Turbul., vol. 15, no. 6, pp. 350365*
[28] ISO 25178-3(2012) Geometrical product specifications (GPS) – surface texture: Areal – part 3: Specification operators `https://www.iso.org/standard/42895.html` accessed: 2019-07-03
[29] ISO 1998 6344-1:1998 coated abrasives grain size analysis part 1: Grain size distribution test
[30] Bak C, Gaunaa M, Olsen A S and Kruse E K 2016 What is the critical height of leading edge roughness for aerodynamics? *Journal of Physics: Conference Series* **753**

APPENDIX E

Article 3: A 2-Dimensional Quantitative Parametric Investigation of Simplified Surface Imperfections on the Aerodynamic Characteristics of a NACA 63_3-418 Airfoil

A 2-Dimensional Quantitative Parametric Investigation of Simplified Surface Imperfections on the Aerodynamic Characteristics of a NACA 63_3-418 Airfoil

Emil Krog Kruse[1,2], Niels N. Sørensen[2] and Christian Bak[2]

[1]Power Curve ApS, Stationsmestervej 81, DK-9200 Aalborg SV, Denmark
[2]Technical University of Denmark, Department of Wind Energy, Frederiksborgvej 399, DK-4000 Roskilde, Denmark

E-mail: ekk@powercurve.dk

Abstract. The aerodynamic performance of a NACA 63_3-418 airfoil has been analyzed with disturbances in approximately 1,000 different configurations focused on the frontal 10% of the airfoil. The configuration parameters are based on field test samples and rain erosion test specimens. The most important trends are presented by 500 configurations each simulated for 6, 8 and 10 degrees angle of attack. The simulations are done in the DTU Wind Energy in-house 2D CFD Reynolds-Average Navier Stokes solver, EllipSys2D. The configurations are applied directly to the computational mesh that combined with the e^N transition model calculates the flow field. The results show that the most important parameters are the position and the depth/height of the disturbance, with up to 35% lift reduction and 90% lift/drag reduction within the specified angle of attacks and disturbance parameter ranges.

1. Introduction

The global ambition for increasing renewable energy has led to a high demand for wind turbines. As the wind turbines continue to grow in size and number, the focus on optimization and performance for every part of the wind turbine is essential.

With an objective of performance and optimization, one critical part of a wind turbine are the blades. If a wind turbine blade deviates from the design shape, the result might be reduced power production [1, 2]. A deviation in shape can origin from the production imperfections, wear and tear or surface contamination such as ice or dirt. These factors are often mentioned in the literature and industry as erosion or roughness, with roughness being a more general term. The performance of a wind turbine blade is most sensitive to roughness close to the leading edge of the airfoil [3, 4], giving basis for the general term Leading Edge Roughness (LER).

Prediction of the influence of LER on the airfoil characteristics is useful in both the design phase and cost-benefit analysis of a correction or repair. So far, no proven general method for calculating the influence from LER has been published. Some research has been conducted on ice accretion in the past, due to problems with ice on airplane wings. Ice accretion is often extensive and can extend the chord length with orders of magnitude compared to roughness from dirt, erosion or imperfections [5, 6, 7, 8, 9, 10]. To the authors knowledge, no public parametric

study exists for LER. However, an attempt to quantify how big imperfections need to be for the airfoil characteristics to deviate from clean conditions has been made in [11]. The LER in wind tunnel tests and simulations are often limited to a few erosion patterns, turbulators such as stall strips or zigzag tape or sand grain paper, with in depth studies of either boundary layers or general airfoil characteristics such as lift and drag. [12, 13, 14, 15, 16, 17, 18]

This paper is a part of the Danish Energy Agency (EUDP), the "LER Project" carried out by the Technical University of Denmark (DTU), Aalborg University (AAU), Danish Fundamental Metrology (DFM) and Power Curve ApS. One of the main tasks in the project is research on methods to simulate and predict the influence of LER on wind turbine blades. During this research, it has become clear that LER can be physically described by many factors such as shape, extension, airfoil family and -thickness and Reynolds number.

The focus of this paper is to investigate the important parameters of the shape and extension of LER. The Computational Fluid Dynamics (CFD) code EllipSys2D is used to calculate 2 dimensional airflow around an airfoil and estimate the changes in lift and drag. The calculations have been validated in previous work by the same authors in [19], and this paper is based on the same NACA 63_3-418 airfoil, given the same conditions, described in section 2.

2. Methods

To investigate the aerodynamic effect of shape and extension of the LER, a series of test subjects and photo samples have been collected. Common for most samples are that the LER can be divided into and area with sandpaper-like roughness and an edge between the LER and the undisturbed/clean surface (from here on noted by "Clean"). This is illustrated in Figure 1 and 2, where the rough parts is marked with a yellow curve and the edges are marked by arrows:

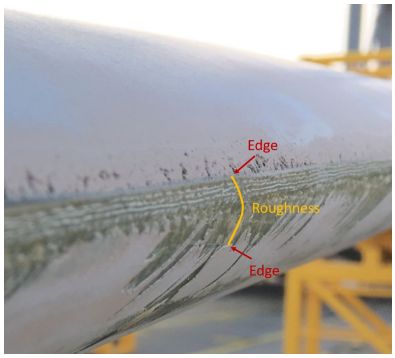

Figure 1. Decommissioned blade from 3 MW offshore wind turbine. The blade has been in service for 3 years.

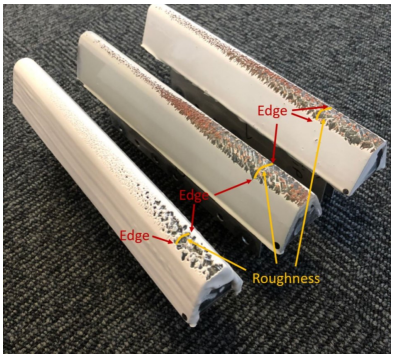

Figure 2. Rain erosion test specimens with different leading edge coating.

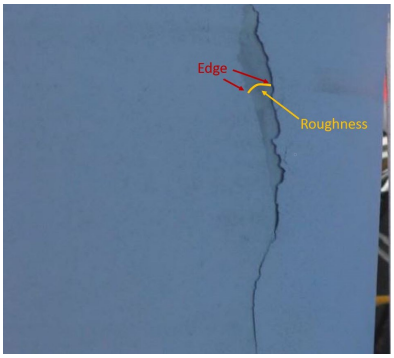

Figure 3. Missing surface material on the side of a blade.

It can also be seen from Figure 1, 2 and 3 that LER is highly three dimensional. Since the shape and extension varies with spanwise position of the blade, it has been decided to divide LER into 2D spanwise sections, based on the results from [19], that suggests that 2D polars are integrated over a small span to mimic the flow that basically is influenced by 3D flow because 2D computations are significantly less complex and requires a smaller computational effort.

This study is limited to the edges marked in Figure 1 and 2. Investigations suggests that the edges are the main contributor to changes in aerodynamic characteristics, when a combination of roughness and edges is seen. To achieve reasonable simplicity and amount of result the parameters for both edges are defined to be chordwise position, slope of edge and depth/height

of the section. In this definition, a case of LER can only have one height or one depth, which limits the parameters in this study to five parameters. The parameters are illustrated in Figure 4.

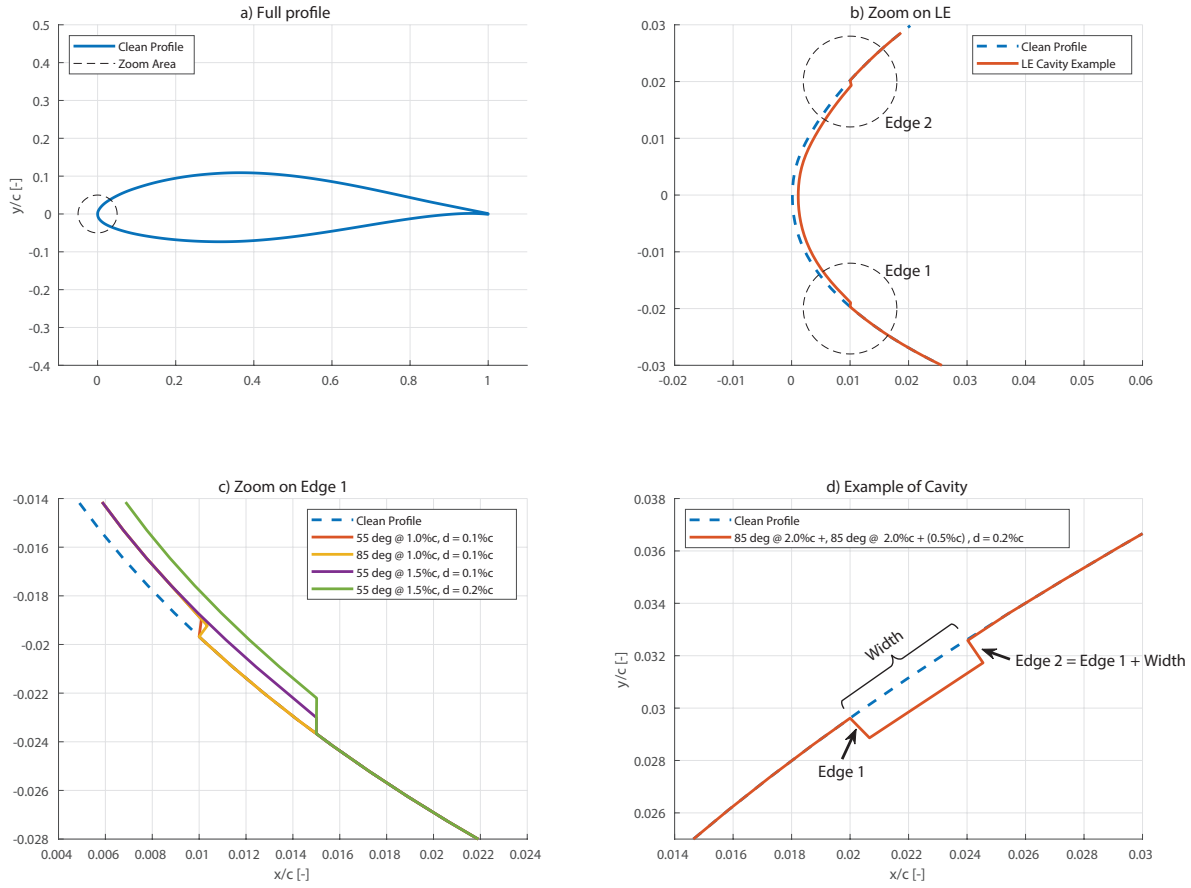

Figure 4. a) Shape of the NACA 63_3-418 airfoil with a zoom area for marked. b) The marked zoom area from a) with marks of Edge 1 and Edge 2. c) Zoom on Edge 1 showing the clean airfoil and 4 different cavities. d) Zoom on a cavity with Edge 2 described as Edge 1 plus a width measured on the surface.

The NACA 63_3-418 airfoil can be seen in Figure 4 a). A zoom on leading edge can be seen in b). When moving clockwise from the trailing edge, around the airfoil, the first edge encountered is defined to be "Edge 1" whereas the clockwise latter edge is defined as "Edge 2". A zoom on some Edge 1 examples can be seen in c) illustrated with four cases compared to the clean case. The cases are denoted in the legend with comma separated parameters, where the first one is the slope, the second one is the chordwise position and the latter one being the depth/height. Height is noted with a positive scalar where depth is noted with a negative scalar.

Figure 4 d) shows an example of a cavity. When the disturbance is either on the suction- or the pressure side, this notation is used. For example in Table 1. The position of Edge 1 is then noted plus a surface distance/width to Edge 2. Edge 2 thereby depends on the position of Edge 1. Similar to the examples in b) and c), a height is noted positive and a depth is negative. The

slope notation is identical as well.

It is chosen to run all parameters with 10 different values for each parameter. Having five parameters with 10 values each gives 100,000 cases. Presentation of a five dimensional simulation matrix is a significant effort and not practical, hence a series of simulations are made for 2 parameters at a time, yielding 100 sets of polars for each set of simulations. The selected inputs, combinations and results can be seen in section 4.

It is important to notice that the edges can be on the same side of the airfoil. Figure 4 is illustrating cavities where Edge 1 is on the pressure side (p.s.) and Edge 2 on the suction side (s.s.). Some of the simulations is made where both edges are on either the pressure- or suction side, illustrating for example a smashed bug on the blade or a small delamination from a transport damage.

3. Simulations

The simulation results are obtained by usage of Computational Fluid Dynamics (CFD), which consist of two major parts, the grid and the numerical setup, which is described in section 3.1 and 3.2. The output from the simulation used in the results is described in section 3.3.

3.1. Grid

The NACA 63_3-418 airfoil founds the basis for the grid used in the simulation. The simulations are validated in previous work [19], hence the airfoil used for simulation of an airfoil with a clean surface.

As mentioned in section 2, this article contains several hundred cases. Each case has an individual grid based on the same properties. Each grid has 512 cells in the circumferential direction and 384 cells in the normal direction.

The distribution of the 512 cells are done with a algorithm implemented in Matlab, satisfying a set of constraints, such as maximum difference in cell length of neighbouring cells of 10%, minimum number of cells in cavities depending on cavity dimensions and a higher concentration of cells in location of high pressure gradients.

The distribution of the 384 cells follows a hyperbolic tangens distribution function. The wall cells have a height of $\approx 1 \cdot 10^{-6}$ of the chord length. This results in a y+ value of $\approx$ 0.1-0.2. The cells most distant from the airfoil have a height of 3 chord lengths.

The grid is constructed using the DTU Wind in-house HypGrid2D grid generator [20]. It is set to generate an o-mesh with a radius of 45 times the chord length. The outlet is set to cover around 40-50 degrees on both sides of the trailing edge. If a case requires a lot of points in the cavities, the total distribution is changed slightly, and might change the outlet size. The grid is divided into blocks to allow parallel processing. The domain, blocks, inlet and outlet are illustrated in Figure 5.

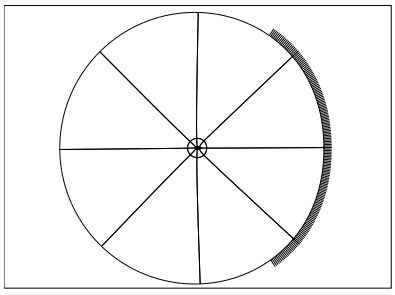

Figure 5. Full grid domain with blocks, inlet and outlet.

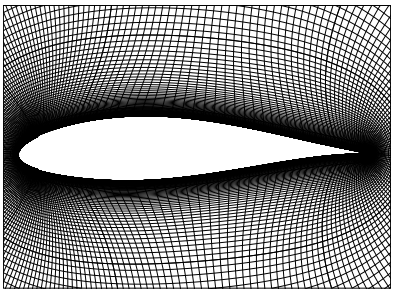

Figure 6. Coarser grid lines around the airfoil.

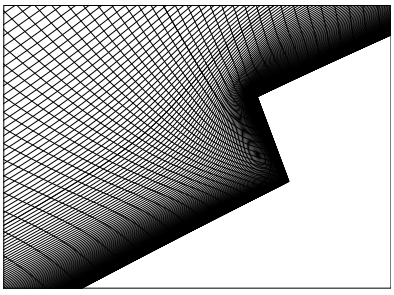

Figure 7. Full grid example with zoom on edge 2.

Figure 6 shows a close up of the airfoil. Only a coarser grid with every other gridline in both directions is shown. A higher concentration can be seen on the leading edge, the disturbances, the trailing edge and close to the wall.

Figure 7 shows an example of Edge 2, which is not a coarser grid, located in 6% chord and with a depth of 0.6 %c. The edge is in this case defined by 12 cells. The major parameter for distributing the number of cells is a scale of the 2.25'th root of the curve length. As an example, a depth of 0.3 %c will give 8 cells and 0.1 %c will give five cells.

3.2. Numerical Setup

The CFD solver used in this article is the in-house DTU software EllipSys2D. EllipSys2D is an incompressible finite volume RANS flow solver, which in this work uses the SIMPLE algorithm to solve the Navier-Stokes equations [21, 22, 23]. The QUICK scheme is used to discretize the convective terms, see [24]. A relaxation of 0.5 is used on all velocities, and a relaxation of 0.15 on the pressure in all simulations. The density of the fluid is 1 kg/m^3, the chord is 1 m, and the dynamic viscosity is $3.333{\cdot}10^{-7}$ m^2/s. The inlet is laminar flow with a velocity of 1 in the u direction for an Angle of Attack (AoA) of 0 deg. These inputs result in a Reynolds number of 3 million All simulations run until convergence with the limit of $1{\cdot}10^{-6}$ of the residuals from the initial conditions.

The solution is found from three simulations, the first two done on a coarser grid. The results from the coarser grid is used as initial conditions in the finer grid. The grid is divided into 48 blocks, hence 1 node with 16 cores is allocated for every AoA.

Menter's k-ω with SST extension is used as turbulence model [25]. The e^N model by Drela-Giles is used to simulate transition of the flow. [26] The e^{N}s has a N factor of 9, transition level of 3 and a relaxation of 0.5. The system is more relaxed than the default setup for EllipSys2D, as the disturbances often is seen to trigger the transition point resulting in more flow dynamics. This could be solved by using an unsteady solver, however, to keep calculation time low, higher relaxation is used with a steady solver.

The assumption of a steady solution holds in most cases, however, some cases showed behaviour as an unsteady solution, not being able to converge despite changing solver parameters and cell distribution. Three AoAs have been discarded from the plots due to this, and substituted with one of the neighbouring cases results. These are marked with an X. However, the governing tendencies, behaviour and conclusions remains unaffected.

3.3. Output

A typical method for analyzing the aerodynamics of an airfoil, is to investigate the lift and drag coefficients for 20 degrees around zero lift, which is a typical no-stall range. Using that method with this work would produce a vast amount of curves, making it impossible to analyze.

Wind turbines operate in various ways, but a typical rule of thumb is to design the controller such that the blade operates at an AoA corresponding to design lift (often around 0.7 to 0.8 times the maximum lift), which often is close to the maximum lift/drag. This is close to 8 degrees AoA for the clean airfoil. A blade with LER does not usually change pitch scheme, and since maximum lift becomes lower with LER the blade will operate closer to maximum lift. It is chosen to plot results for 6, 8 and 10 degrees AoA based on these premises. However, it should be noted that it is not straight forward whether it should be chosen to analyze for constant AoA or for constant lift, because LER will change the induction field around the rotor. With the lower lift caused by the LER both the lift value and the AoA will in general change.

Figure 8 a) and b) shows an example of lift and drag for the clean simulation and a simulation with LER. The 6, 8 and 10 degrees AoA are marked for clarity.

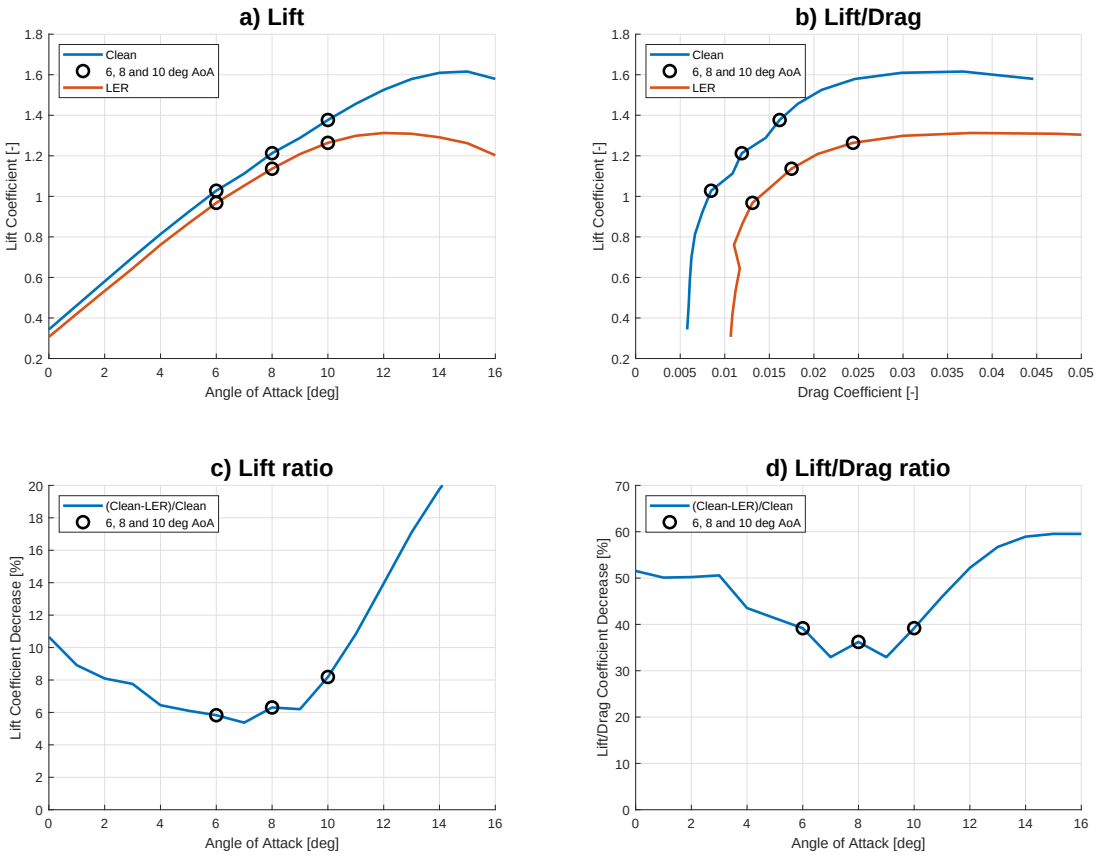

Figure 8. a) Example of lift curve with and without LER with marked AoAs. b) Example of lift/drag curve with and without LER with marked AoAs. c) Example of lift increase in percent. d) Example of lift/drag decrease in percent.

Plotting only three AoAs reduces the amount of data. In order to compare the three AoAs, the change in lift and drag are all normalized w.r.t. the clean simulation. This is shown in Figure 8 c) and d). It can be seen that the changes differs a lot when moving to lower or higher AoAs, however, it was chosen to omit these as a wind turbine rarely operates at these AoAs for wind speeds below rated power when maximizing the power coefficient.

All plots contain a normalized lift decrease and normalized lift/drag decrease. It is chosen to plot lift/drag instead of drag, because the lift/drag ratio directly affects the rotor performance. Furthermore, it is possible to have a similar range on the plots, as well as staying in "decreases", as drag is seen to increase. An increase in drag will result in a decrease in normalized lift/drag. The plot chosen is a 2D color map, as it allows for 2 parameters to change. Each plot has a related table and text describing the input and results. All figures contains 100 results, i.e. 300 lift and 300 drag values in total for each plot. The colorbar is fixed in all plots, ranging from 0-50% for normalized lift decrease and 0-100% for normalized lift/drag decrease. The fixed values makes it easier to compare plots with different inputs. White is minimum, going into yellow hence red, ending with black as maximum. No plot has a value above the color bar range. The increments are variable and set by the difference between minimum and maximum values in a plot.

4. Results

This section contains five sets of results, each set with two variables.

4.1. Cavities with widths up to 0.6%c at the pressure side

An example of how some variables affect the airfoil performance is illustrated by one common example, seen in Figure 9. The input can be seen in Table 1.

Table 1. Input values for variation in cavity position and width on the pressure side.

Figure 9 Total: 100	**Edge 1 Position**	**Edge 2 Position (Width)**	**Edge 1 Slope**	**Edge 2 Slope**	**Depth (-) Height (+)**
	1 %c p.s.	Edge 1 + (0.15 %c)	85°	85°	-0.1 %c
	2 %c p.s.	Edge 1 + (0.20 %c)			
	⋮	⋮			
	10 %c p.s.	Edge 1 + (0.60 %c)			

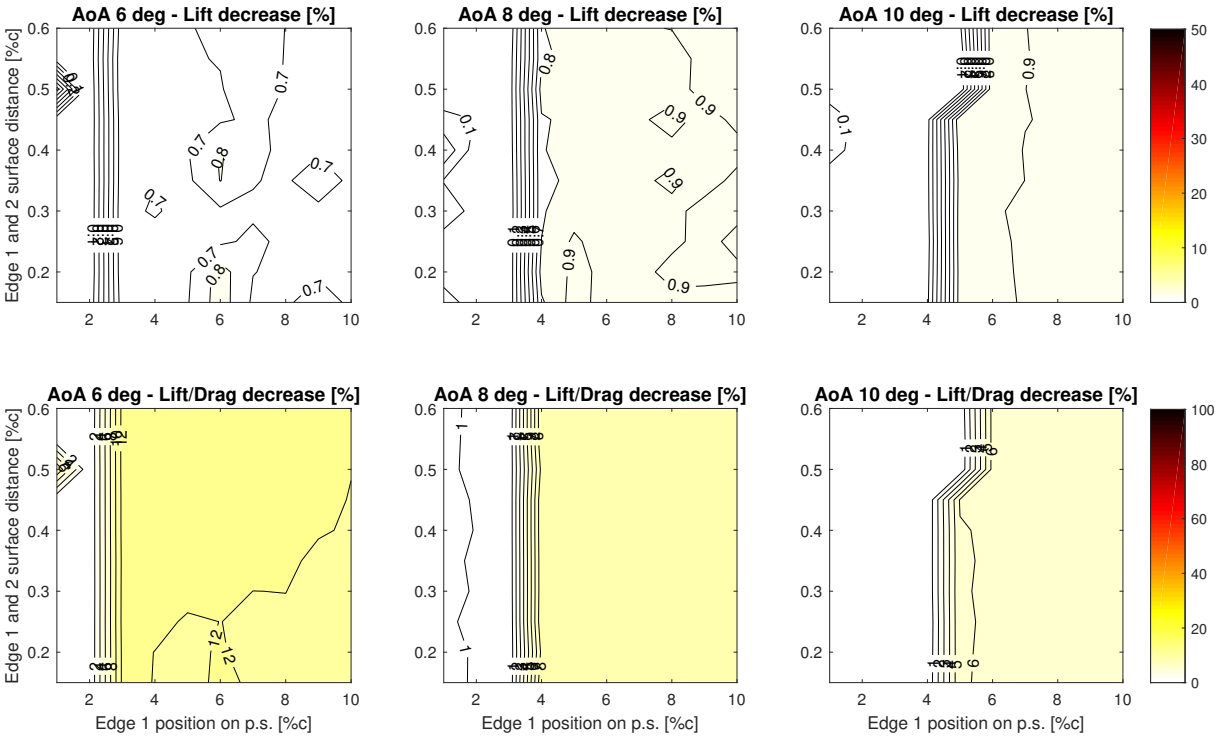

Figure 9. Results for variation in cavity position and width on the pressure side.

The first set of results illustrated in Figure 9 shows below 1% change in lift for all three AoAs. The lift/drag decreases around 12% for 6 degrees AoA and less for higher angles. Due to the high pressure on the pressure side of the airfoil, the disturbance has little effect despite changes in chordwise position and width. There is a small but noticeable plateau change on both the lift and lift/drag, when the disturbance is downstream of the stagnation point.

Surface imperfections that result in minor changes in performance are not unique. A bump with the same Edge 1 and 2 position gave similar results. All simulations have been carried out with 85 degrees slope on both edges. A study was made on the edge angles as well, ranging from 45° to 90° with increments of 5°. It was done on different types of cavities and bumps. Common for all was that the slope had little effect on the results, similar to the results shown in Figure 9. Even though the existence of the edges resulted in a significant reduction of lift and increase

in lift/drag, the maximum variation of the Edge 1 slope was ±0.5% in lift decrease and ±1% in lift/drag decrease compared to the surface without cavities and bumps. For the Edge 2 slope the variation was ±1% in lift decrease in ±2.5% in lift/drag decrease compared to the surface without cavities and bumps. A shallow slope, in general, did result in less drag, however, the results were all dominated by the depth and position.

It was chosen to simulate all other cases with slopes of 85° for consistency as well as good convergence of simulation for most results.

Presentation of results with minor changes, being Edge 1 and 2 slopes, have been omitted in this paper to focus on parameters that influences the aerodynamic performance the most. It was chosen to include them in the tables because it is describing the geometry and to inform that they have been analyzed.

4.2. Cavities with widths up to 0.6%c at the suction side

Figure 10 shows results of inputs similar to the inputs of the results in Figure 9. The difference is that the cavity is placed on the suction side of the airfoil instead of the pressure side. The inputs can be seen in Table 2.

Table 2. Input values for variation in cavity position and width on the suction side.

Figure 10 Total: 100	**Edge 1 Position**	**Edge 2 Position (Width)**	**Edge 1 Slope**	**Edge 2 Slope**	**Depth (-) Height (+)**
	1 %c s.s.	Edge 1 + (0.15 %c)	85°	85°	-0.1 %c
	2 %c s.s.	Edge 1 + (0.20 %c)			
	⋮	⋮			
	10 %c s.s.	Edge 1 + (0.60 %c)			

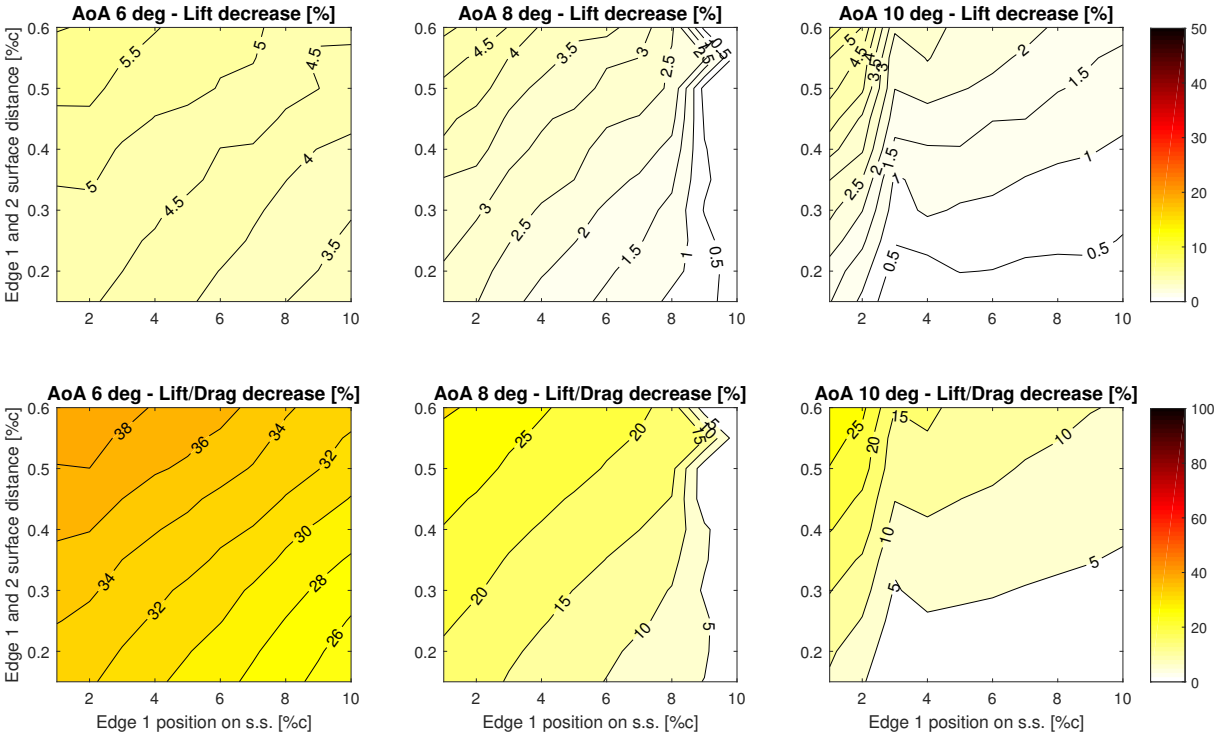

Figure 10. Results for variation in cavity position and width on the suction side.

A cavity located on the suction side results in a drop of around 5% in lift for 6 degrees AoA and a lower drop for higher AoAs. The lift/drag decreases more aggressively, resulting in a maximum change in lift/drag of 40% at 6 degrees AoA.

The changes are sensitive to both the position and the width (surface distance) of the cavity. The worst situation is it when the cavity is located close to the leading edge and is very wide.

4.3. Bumps with widths up to 0.6%c at the suction side

Figure 11 shows results for a bump with the same locations and dimensions as in Figure 10. The inputs can be seen in Table 3.

Table 3. Input values for variation in bump position and width on the suction side.

Figure 11 Total: 100	**Edge 1 Position**	**Edge 2 Width**	**Edge 1 Slope**	**Edge 2 Slope**	**Depth (-) Height (+)**
	1 %c s.s.	Edge 1 + (0.15 %c)	85°	85°	0.1 %c
	2 %c s.s.	Edge 1 + (0.20 %c)			
	⋮	⋮			
	10 %c s.s.	Edge 1 + (0.60 %c)			

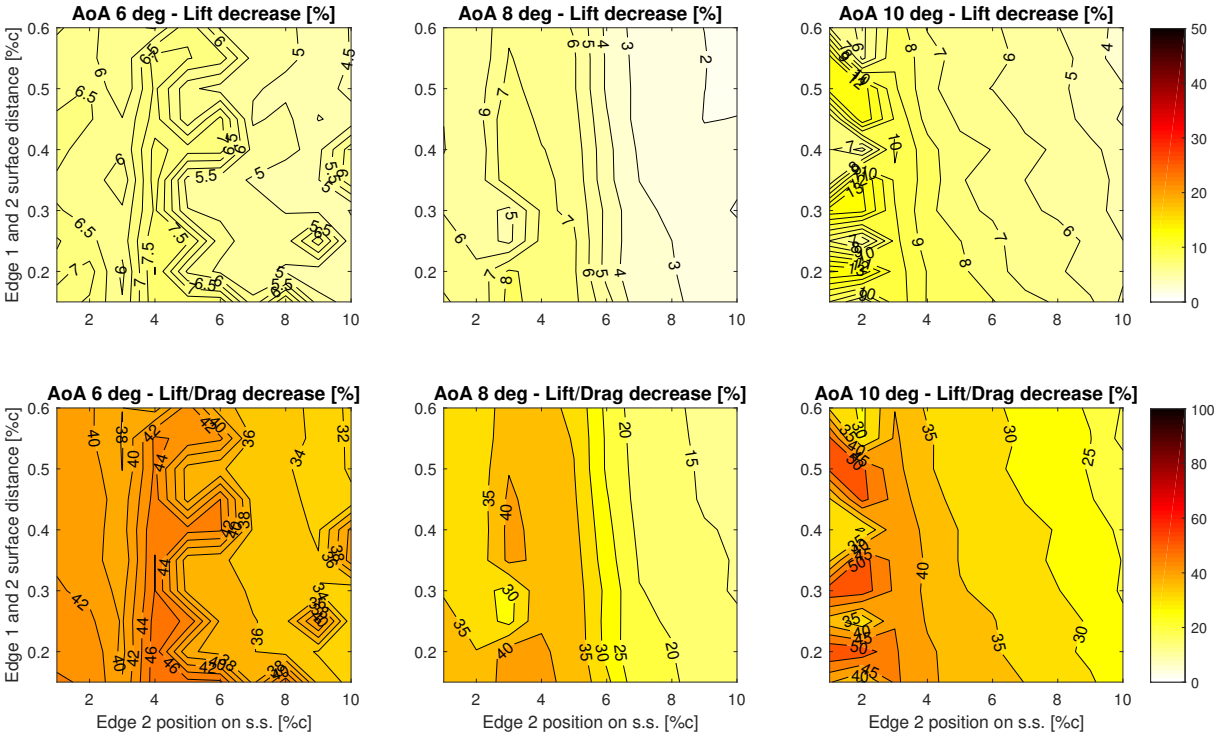

Figure 11. Results for variation in bump position and width on the suction side.

The bump introduced in the results in Figure 11 shows a higher lift penalty compared to voids of the same dimensions as shown in Figure 10. The cavity had less effect on higher AoAs, where the bump shows a higher effect of up to 12% lift reduction for 10 degrees AoA. The highest aerodynamic influence can be seen for the same Edge 2 position for all distances. For the 6 degrees AoA, the Edge 2 position of 4%c is the worst, for 8 degrees AoA it is 3%c and for

10 degrees AoA it can be found at 2%c. These positions are where Edge 2 is perpendicular to the flow direction, resulting in the highest form drag.

4.4. Wide cavities covering the leading edge

The next step is to move to situations where the cavity covers the leading edge as in the example seen in Figure 1, 2, 3 and 4. The positions of Edge 1 and 2 are varied in combinations described in Table 4 with the results plotted in Figure 12.

Table 4. Input values for variation in leading edge cavity position for Edge 1 and 2.

Figure 12 Total: 100	**Edge 1 Position**	**Edge 2 Position**	**Edge 1 Slope**	**Edge 2 Slope**	**Depth (-) Height (+)**
	0.5 %c p.s.	0.5 %c s.s.	85°	85°	-0.1 %c
	1.0 %c p.s.	1.0 %c s.s.			
	⋮	⋮			
	5.0 %c p.s.	5.0 %c s.s.			

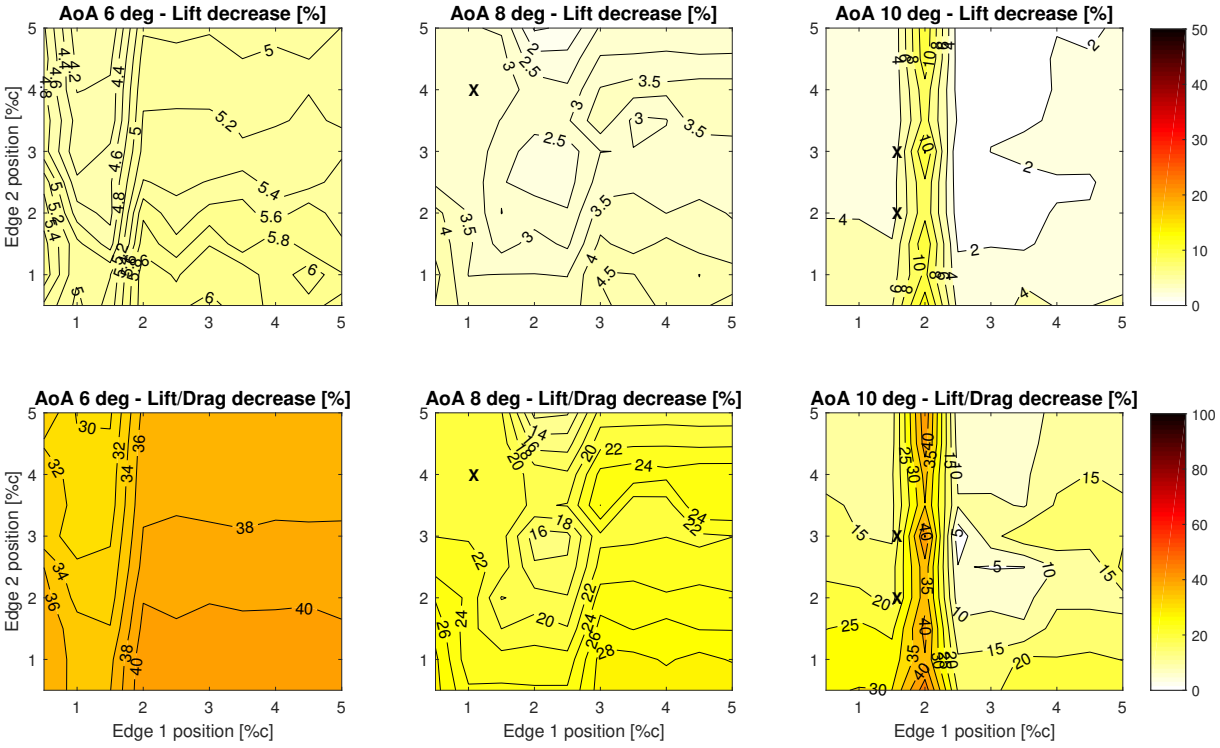

Figure 12. Results for variation in leading edge cavity position for Edge 1 and 2.

Significant reductions in lift and lift/drag are seen with up to 10% loss in lift and 40% loss in lift/drag. However, for AoA 6 and 8 deg the losses in lift and lift/drag seems to be quite constant despite of the position of Edge 1 and 2 for 6 and 8 degrees AoA. The drag is lower when Edge 1 is positioned upstream of the stagnation point. For 10 degrees AoA, the penalty is high when Edge 1 is located at the stagnation point. All three AoAs shows that the penalty is higher, the closer Edge 2 is to the leading edge. Note that the three values marked with X have been omitted due to an unsatisfied convergence criteria.

4.5. Wide symmetric cavities with variations of depth covering the leading edge

The last parameter that has been investigated is the depth/height. It is impossible to combine height and depth in the same simulation. A LER with a height of 1 %c starts to look more like ice accretion, which is outside the scope of this work. Based on this, it was chosen to show the results for depth of LER as one parameter and a combination of Edge 1 and 2 position as the other parameter. Table 5 shows the inputs with the results plotted in Figure 13. Note that Edge 1 and 2 have the same chordwise positions, there is no cross combination of these.

Table 5. Input values for variation in leading edge cavity position for Edge 1 and 2 combined with a depth change.

Figure 13 Total: 100	**Edge 1 Position**	**Edge 2 Position**	**Edge 1 Slope**	**Edge 2 Slope**	**Depth (-) Height (+)**
	1 %c p.s.	1 %c s.s.	85°	85°	-0.1 %c
	2 %c p.s.	2 %c s.s.			-0.2 %c
	⋮	⋮			⋮
	10 %c p.s.	10 %c s.s.			-1 %c

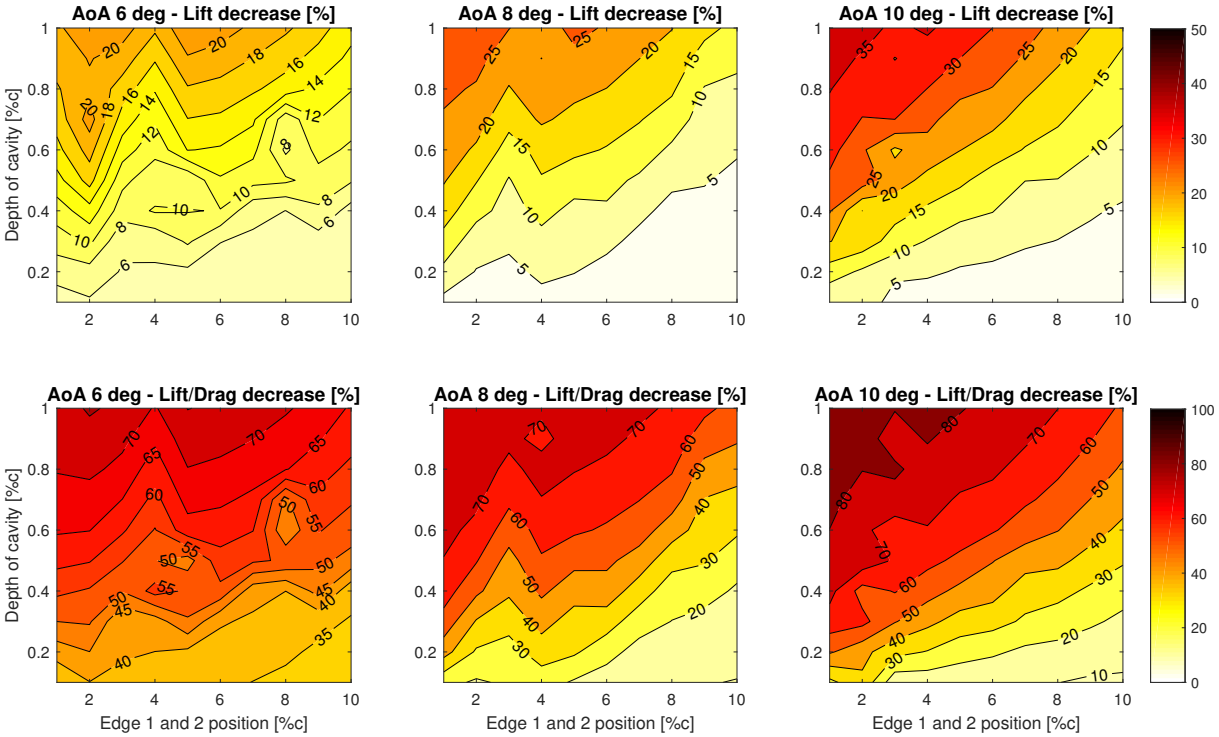

Figure 13. Results for variation in in leading edge cavity position for Edge 1 and 2 and combined with a depth change.

The aerodynamic properties for LER seem to depend strongly on the depth of the LER for all three AoAs. The lift drops between 5% for 0.1 %c depth and up to 35% for 1 %c depth. The lift/drag is strongly degraded when the depth exceeds 0.3-0.4 %c. A reduction of up to 90% in lift/drag at 12 degrees AoA makes the depth the most critical parameter in this study. A stronger correspondence between edge positions and lift reduction is seen when the depth is

increased. Having Edge 2 close to the leading edge is much worse than having the LER extended back to 10%c.

5. Conclusion

This parametric study was conducted on simplified disturbances on a NACA 63_3-418 airfoil, at a Reynolds Number of 3 million. The simplified disturbance was described by two steps forming either a bump or a cavity. The major shape descriptors was position of two edges, the angle of these and the depth or height of the disturbance. In general, the results depends on whether the disturbance is constructed as covering the leading edge or as a disturbance on either the suction- or pressure side. The conclusion sums up the governing tendencies.

1) The slopes within a range of 45-90 degrees of Edge 1, i.e. the edge first encountered when moving clockwise around the airfoil from the trailing edge, had negligible impact on the aerodynamic performance of the airfoil of less than $\pm 0.5\%$ on lift and $\pm 1\%$ on lift/drag.

2) The slopes within a range of 45-90 degrees of Edge 2, i.e. the edge first encountered when moving counter clockwise around the airfoil from the trailing edge, had an impact on the aerodynamic performance of the airfoil of less than $\pm 1\%$ on lift and $\pm 2.5\%$ on lift/drag.

3) The position of Edge 1 was tested in various positions in the frontal 10%c of the airfoil. An edge position in the stagnation point generally results in high performance loss. The position of Edge 1 has the most impact on performance in low AoAs if it is located elsewhere of the stagnation point. The variation in Edge 1 position may account for up to 10% on lift and 20% on lift/drag.

4) The position of Edge 2 follows the structure of Edge 1 positions. An Edge 2 location close to leading edge gives the most performance penalty. If Edge 1 and Edge 2 are both located upstream of the stagnation point, the location of Edge 2 has less impact when simulating a bump. The variation in Edge 2 position may account for up to 5% on lift and 10% on lift/drag, highly depending on Edge 1 location.

5) The depth/height parameter was tested for a range of 0.1 to 1%c. Changes in bump height has severe impact on the performance. A leading edge with added material is out of the scope for this study, as it would be closer to an ice accretion analysis. Analysis of missing material on the leading edge (cavities) shows that the depth plays a significant role. Even with the same location of Edge 1 and 2, the depth in the specified range is seen to account for up to 30% on lift and 80% on lift/drag.

The governing conclusion is that the most important parameters to estimate or measure when analyzing the performance loss of a NACA 63_3-418 airfoil is the position/extension and depth/height of a disturbance whereas a detailed shape of the disturbance is of less importance.

Acknowledgements

The authors want to acknowledge the Danish Energy Agency for the support and funding of this project, the *"Leading Edge Roughness on Wind Turbine Blades", 64015-0046. The acknowledgement also goes to the Technical University of Denmark and Power Curve ApS.*

References

[1] Sareen A, Sapre C A and Selig M S 2014 Effects of leading edge erosion on wind turbine blade performance *Wind Energy, 17:15311542* 17:15311542

[2] Ehrmann R S, Wilcox B, White E B and Maniaci D C 2017 Effect of Surface Roughness on Wind Turbine Performance *Sandia National Laboratories*

[3] Jacobs E N 1932 Airfoil Section Characteristics as Affected by Protuberances *National Advisory Committee for Aeronautics* URL `https://ntrs.nasa.gov/search.jsp?R=19930091520`

[4] Kerho M F and Bragg M B 1997 Airfoil Boundary-Layer Development and Transition with Large Leadge-Edge Roughness *AIAA Vol. 35, No. 1*

[5] Mortensen K 2008 CFD simulations of an airfoil with leading edge ice accretion *Department of Mechanical Engineering* 117
[6] Broeren A P, Addy H E, Bragg M B, Busch G T, Guffond D and Montreuil E 2011 Aerodynamic Simulation of Ice Accretion on Airfoils *National Advisory Committee for Aeronautics*
[7] Cebeci T 1987 Effect of Intercycle Ice Accretions on Airfoil Performance *California State University (NASA)*
[8] Broeren A P, Bragg M B and Addy H E 2004 Effects of Environmentally Imposed Roughness on Airfoil Performance *Journal of Aircraft Vol. 41*
[9] Turkia V, Huttunen S and Wallenius T 2013 Method for estimating wind turbine production losses due to icing *VTT Technology)*
[10] Sermeus K and Yang H 2015 CFD Simulation of Aircraft Icing Effects using Roughness Modeling *62nd CASI Aeronautics Conference*
[11] Bak C, Gaunaa M, Olsen A S and Kruse E K 2016 What is the critical height of leading edge roughness for aerodynamics? *Journal of Physics: Conference Series* **753**
[12] van Rooij R and Timmer W A 2003 Roughness Sensitivity Considerations for Thick Rotor Blade Airfoils *Journal of Solar Energy Engineering-transactions of the ASME* **125** 468–478
[13] White E B, Kutz D, Freels J, Hidore J P, Grife R, Sun Y and Chao D 2011 Leading-Edge Roughness Effects on 63_3-418 Airfoil Performance *49th AIAA Aerospace Sciences*
[14] Ehrmann R S, White E B, Maniaci D C, Chow R, Langel C M and van Dam C P 2013 Realistic Leading-Edge Roughness Effects on Airfoil Performance *31st AIAA Applied Aerodynamics Conference*
[15] Standish K, Rimmington P, Laursen J and Paulsen H N 2010 Computational Prediction of Airfoil Roughness Sensitivity *48th AIAA Aerospace Sciences Meeting and Exhibit*
[16] Langel C M, Chow R, Hurley O F, van Dam C P, Ehrmann R S and White E B 2015 Analysis of the Impact of Leading Edge Surface Degradation on Wind Turbine Performance *33rd Wind Energy Symposium* URL `https://doi.org/10.2514/6.2015-0489`
[17] Bak C, Fuglsang P, Johansen J and Antoniou I 2000 Wind Tunnel Tests of the NACA 63-415 and a Modified NACA 63-415 Airfoil *Risø National Laboratory*
[18] Gaudern N 2014 A practical study of the aerodynamic impact of wind turbine blade leading edge erosion *The Science of Making Torque from Wind 2014 (TORQUE 2014), Journal of Physics: Conference Series 524 (2014) 012031*
[19] Krog Kruse E, Sørensen N and Bak C 2018 Predicting the Influence of Surface Protuberance on the Aerodynamic Characteristics of a NACA 63_3-418 *Journal of Physics: Conference Series, 1037(2), 2018 [022008]* URL `https://doi.org/10.1088/1742-6596/1037/2/022008`
[20] Sørensen N N 1998 HypGrid2D, a 2-D Mest Generator *Risø National Laboratory*
[21] Michelsen J 1992 Basis3D - a Platform for Development of Multiblock PDE Solvers *Technical Report AFM 92-05, Technical University of Denmark, Department of Fluid Mechanics*
[22] Michelsen J 1994 Block structured Multigrid solution of 2D and 3D elliptic PDE's *Technical Report AFM 94-06, Technical University of Denmark, Department of Fluid Mechanics*
[23] Sørensen N 1995 General Purpose Flow Solver Applied to Flow over Hills *Risø National Laboratory*
[24] Leonard B P 1979 A stable and accurate convective modelling procedure based on quadratic upstream interpolation *Comput. Meths. Appl. Mech. Eng, 19:59–98* 19:59–98
[25] Menter F R 1993 Zonal Two Equation k-ω Turbulence Models for Aerodynamic Flows *AIAA 1993-2906*
[26] Drela M and Giles M B 1987 Viscous-Inviscid Analysis of Transonic and Low Reynolds Number Airfoils *AIAA 25(10):1347-1355, Vol. 25 NO. 10*

APPENDIX F

Article 4: Wind Tunnel Experiments on a NACA 63_3-418 Airfoil with Different Types of Leading Edge Roughness

Wind Tunnel Experiments on a NACA 63_3-418 Airfoil with Different Types of Leading Edge Roughness

Emil Krog Kruse[1,2], Christian Bak[2] and Anders Smærup Olsen[2]

[1]Power Curve ApS, Stationsmestervej 81, DK-9200 Aalborg SV, Denmark
[2]Technical University of Denmark, Department of Wind Energy, Frederiksborgvej 399, DK-4000 Roskilde, Denmark

E-mail: ekk@powercurve.dk

Abstract. The NACA 63_3-418 airfoil has been tested in the new Poul la Cour Wind Tunnel at the Technical University of Denmark, Risø campus, to expand the publicly available data of airfoils with leading edge roughness. The airfoil was constructed with an exchangeable leading edge. The clean airfoil showed good agreement with results from other high quality wind tunnels. The airfoil was equipped with three heights of zigzag tape, a trip strip, three sandpaper types and leading edge cavities with different modifications. In general increasing zigzag tape heights reduce the maximum lift, whereas the increase in drag is less affected by the zigzag tape height. Almost the same reduction in maximum lift is seen for the different sandpaper types. However, the drag increases with the coarseness of the sandpaper. The highest zigzag tape and coarsest sandpaper resulted in most penalty on the aerodynamics. The experiments indicated that zigzag tape could be substituted by ordinary 2 dimensional tape strips with a similar height and hence reduce the complexity of simulating the setup. A combination of sandpaper and cavities showed the largest reduction in maximum lift and the highest increase in drag.

1. Introduction

In recent years there has been an increased focus on leading edge roughness (LER) on wind turbine blades because of the observation of unforeseen energy losses from wind turbines. There can be several explanations to why the energy losses are observed, but wind turbine owners have seen how the leading edges of the blades has been either 1) contaminated by e.g. bugs, dust or mud, 2) eroded by e.g. the rain or 3) damaged by e.g. structural fatigue after some years in operation. Even though the blades of wind turbines often are designed for operation in a harsh environment, the reduction in the power can be bigger than expected. Examples of surface damages observed by a wind turbine owner that potentially could have an effect on the aerodynamic performance is seen in Figure 1. The surface deviations can be very diverse, but in the figure three different types of roughness are seen. To the left a damage at the leading edge (LE) resembling sandpaper (SP) is seen. This type is often seen on the outmost part of the blade because of e.g. rain hitting the LE at high speed. In the middle is seen a void at the LE that can be due to a fatigue damage. Here particles have hit the surface for some time (see the top part of the photo), but then the top layer was peeling off, which was accelerated by stresses in the surface caused by e.g. blade bending. To the right a void downstream of

the LE is seen. This is probably not caused by particles hitting the surface, but more likely stresses in the surface caused by blade bending. These photos are shown to set the background for investigating the airfoil performance with many types of LER.

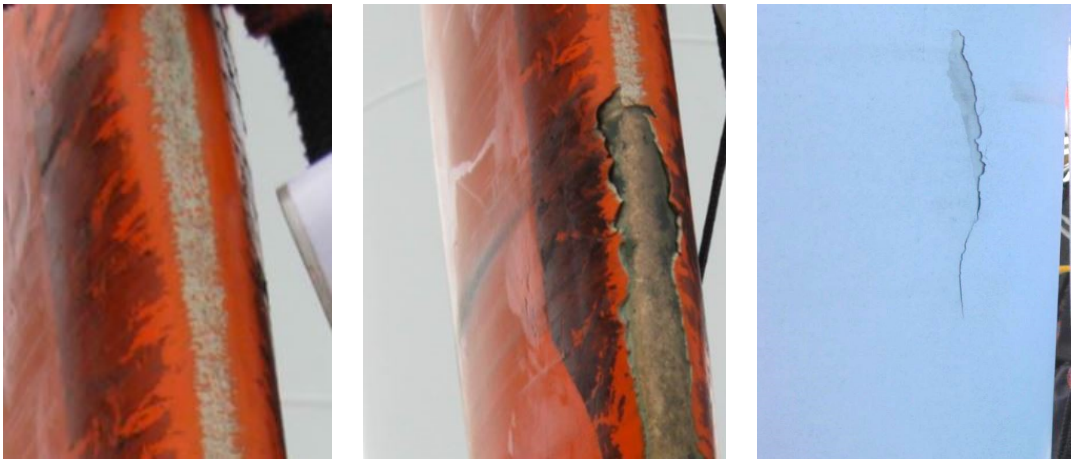

Figure 1. Examples of damages close to the leading edge of a wind turbine blade. Left: SP-like damage at the leading edge. Middle: Void at the leading edge. Right: Void downstream of the leading edge.

The reduction in performance is often taken into account already in the design phase of the wind turbine because it is known that the blade sections cannot maintain a perfectly clean surface throughout the lifetime of the wind turbine. Thus, when predicting the performance of a wind turbine an aeroelastic code is used, and here the performance of several blade sections, e.g. five radial sections, are needed for the entire blade from root to tip. Between the blade sections an interpolation is made. Often the performance data of each blade section is present both for a clean surface and for a surface with LER. Data for airfoils with LER is often obtained in wind tunnels, where the LER is simulated by mounting a tape either at the LE or very close to the LE.

LER on wing sections is not a new discovery, but was observed already in the early stages of the aviation industry, see [1, 2, 3, 4]. Even though LER has attracted much attention in recent years, this phenomenon has been known in the wind turbine industry for decades and that is why airfoils have been tested with LER for a long time, see e.g. [5, 6, 7]. This was often done with a standard zigzag tape (ZZ) close to the LE of the airfoils.

LER as observed on wind turbine blades has also been investigated. An early investigation was made in 1996, where a pattern corresponding to bugs was investigated [8]. In the early years of the wind turbine industry the tip speed was not very high (around 60 m/s), but in later years the tip speed has increased up to around 90 m/s. Thus, in recent years the performance of wind turbines with LER has been investigated in more detail. Examples of such investigations are found in work by Sareen et al. [9], Gaudern [10], Ehrmann et al. [11] and Langel et al. [12].

In this paper different LER configurations are investigated: The SP type as shown to the left in Figure 1 and the LE void type as shown in the middle of the same figure. This is done in wind tunnel tests of a NACA 63_3-418 airfoil. These configurations are compared to the more de facto standard way of testing airfoils with ZZ. Because LER is a rather diverse phenomenon, where

many types of damages are seen, the authors expect that a mapping of the effects of LER will take several years to establish. Thus, this paper is intended as a contribution to this mapping.

2. Methods

2.1. Wind Tunnel Facility and Airfoil Model

The NACA63_3-418 airfoil was tested in the closed loop low turbulence wind tunnel, the Danish Aerodynamic and Aeroacoustic Wind Tunnel, the Poul la Cour Tunnel (PLCT) at the Technical University of Denmark (DTU) Wind Energy, Risø Campus. The test section is rectangular, with dimensions W x H x L = 3.00 m x 2.00 m x 9.00 m. The model had a chord of c = 1.00 m and vertically spanned the height of the test section of 2.00 m, giving an aspect ratio of 2.00. The airfoil was connected to turntables in both ends with only a very small gap below 0.5 mm between the airfoil and the turntable. The turntable can rotate the airfoil with readings of the position with a precision of 1/100 degrees. A traversable wake rake for assessing the total drag was positioned about two chords downstream of the airfoil trailing edge. The airfoil was tested at many Reynolds numbers, but mainly at Re = 3 million and 5 million corresponding to Mach numbers of 0.13 and 0.22. The wind tunnel showed turbulence intensities of around 0.1%. At maximum lift coefficients ($C_{l,max}$) the model blockage was around 8%. Models can be tested in PLCT in two configurations: One configuration with hard walls and pressure taps for test of pure aerodynamics and one configuration with Kevlar walls for test of aeroacoustics. The hard walls with pressure taps was used in the tests presented in this paper.

The airfoil was designed with an exchangeable LE. The airfoil is shown as a CAD drawing in Figure 2, where the pressure side (PS) is seen. The LEs had a length in chordwise direction of 15%c and is shown in the drawing as the light blue part. Even though the LEs had a tight fit to the main model it turned out that air could flow through the small gaps at the connections. That was the reason for mounting 0.05 mm thick aluminum tape over the gaps. This sealed the flow, but there was a risk that the tape moved slightly because of pressure differences between the internal of the airfoil and the surface pressure. The green area at the mid part of the surface is a hatch into the interior of the model, so that the LE can be fixated to the main part of the airfoil. This hatch had a tight fit, but also here there was a small gap between the main part of the airfoil and the hatch.

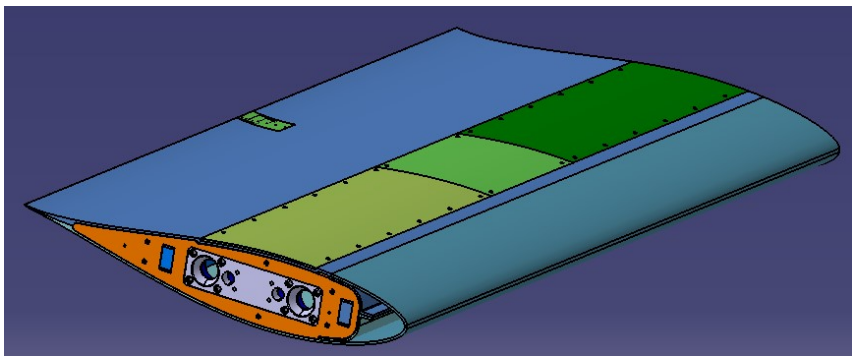

Figure 2. A CAD drawing of the airfoil model. The PS of the airfoil is shown.

Three exchangeable LEs were designed where two of them were utilized in this work. One LE had pressure taps included. With this one pressure distributions could be measured and also standard tests could be carried out with ZZ and other types of LER emulations. Examples are shown in Figure 3 with SP P40 around the LE to the left and with ZZ with height 0.4 mm at

10%c at the pressure side (PS) (that is seen in the photo) and at 2%c at the suction side (SS) (on the other side of the airfoil in the photo).

Another LE was manufactured with a cavity at the LE extending from 3%c at the PS all the way around LE to 3%c at the SS. This is shown in Figure 4 where the airfoil is seen from PS with P40 SP mounted in the cavity. The edges that form a forward facing step has a depth of 3 mm and the angles of the steps are 90 degrees to the surface. This can simulate the geometry of an airfoil that has experienced severe erosion similar to the photo mid Figure 1. To the left in Figure 4, the entire model is seen and to the right a close up of the LE is seen.

Figure 3. The NACA 63_3-418 airfoil in the PLCT test section. Left: The airfoil mounted with SP P40 at LE. Right: The airfoil mounted with ZZ of height 0.4 mm at 10%c at PS and 2%c at SS.

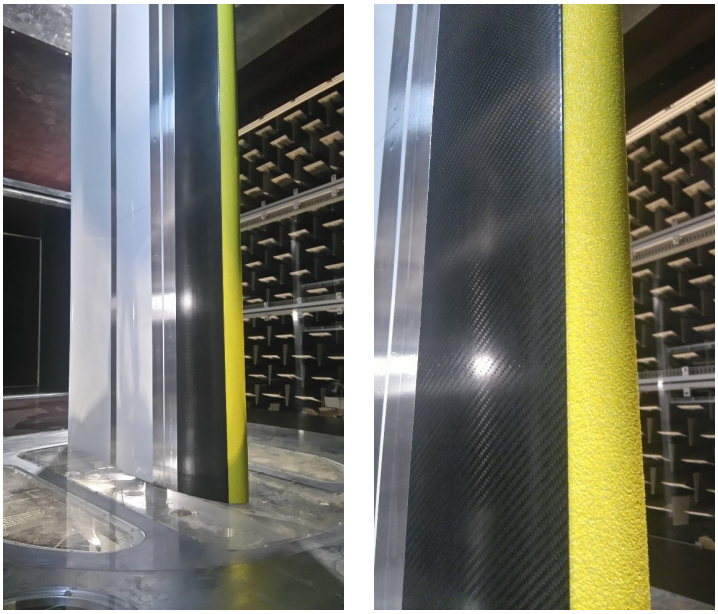

Figure 4. The NACA 63_3-418 airfoil in the PLCT test section with the LE that includes a cavity, but no pressure taps. Left: The airfoil mounted with SP P40 at LE in the bottom of the cavity. Right: A close-up of the same configuration.

Many types of roughness were applied. Three different types of ZZ are presented in this work with height 0.2 mm, 0.4 mm and 0.8 mm. Also, a rectangular rail with a height of almost 1 mm is used and positioned to form a protuberance at the SS surface. The SPs are denoted with the common term P and then the number of grains per square inch. In this case we have used P40, that is a coarse SP, P120 that is a fine SP and P400 that is an extra fine SP. The details of the roughness add-ons are described in Table 1. Here also the roughness heights for the SPs are shown and these roughness heights were found in reference [13].

Table 1. Description of the roughness add-ons used in the tests.

Roughness type	Mean height [mm]	Width [mm]	Spanwise angle [deg]	Eq. Roughness height, k_r [mm]
ZZ				
ZZ0.2	0.205	12	60	-
ZZ0.4	0.400	12	60	-
ZZ0.8	0.790	12	60	-
Protuberance				
P1	0.962	20	-	-
SP [14]				
P40	0.2	115	-	1.637
P120	0.2	115	-	0.357
P400	0.2	93	-	0.098

Figure 5 shows the different configurations. a) shows the clean case. b) shows the LE cavity ranging from 3%c PS to 3%c SS with a depth of 3%c. c) Shows the LE cavity with SP. d) Shows the extension of the SP. e) Shows the position of ZZ and P1 in 2%c and f) shows the ZZ in 2%c SS and 10%c PS.

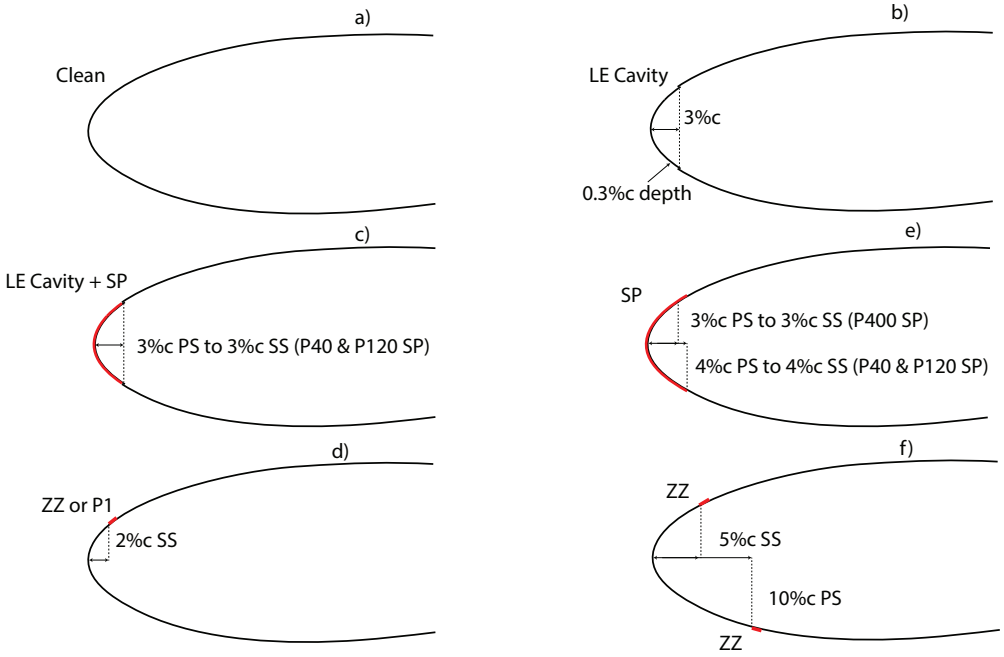

Figure 5. Different configurations of LER with the a) Clean case, b) LE cavity ranging from 3%c PS to 3%c SS with a depth of 3%c, c) LE cavity with SP, d) extension of the SP, e) position of ZZ and P1 in 2%c and f) ZZ in 2%c SS and 10%c PS.

2.2. Instrumentation and Data Acquisition

The airfoil was equipped with 100 pressure taps distributed over the surface with higher density close to the LE and the trailing edge (TE). The walls were also equipped with pressure taps. 48 taps on each wall spaced over 6 times the chord length with a 0.35 of the chord offset from the center line of the test section. The pressure taps were more densely spaced at the center where the airfoil is mounted. Approximately 2 times the chord downstream of the TE a wake rake with a width of 0.7 of the chord length, was positioned with 96 stagnation pressure tubes and 6 static pressure tubes. Pressures from the airfoil surface, the walls and the wake rake were sampled with 100 Hz by six ScaniValve Miniature Pressure Scanners (MPS4264) each with 64 pressure sensors. The flow speed in the test section was determined from correlation of measured flow speed in an empty test section and measured pressure difference in the upstream contraction. Furthermore, temperature, humidity and the angular position of the turntable were measured.

2.3. Analyzing Data

Each measurement point was measured for 60 seconds and averaged before it was corrected according to the methods described by Allen and Vincenti [15] and with a second order correction of the blockage described by Garner et al. [16]. The lift was determined in two different ways: One way was to integrate the airfoil surface pressures and another way was to integrate the wall surface pressures. Since many tests were carried out with the LE covered by SP or with the LE that included the cavity, but had no pressure taps included, the lift shown in this work is only determined by integration of the wall surface pressures. The drag was determined by integration of the velocity deficit in the wake measured by the wake rake by the method of B. M. Jones [17]. In some tests, the wake was wider than the wake rake. In these cases the velocity deficit was measured over two tests, positioning the wake rake so the entire deficit could be captured under the assumption that the wake was steady.

3. Results

In this section results from the wind tunnel tests are presented. First, data for the clean airfoil and the airfoil with ZZ is compared to data from other wind tunnels. Then data from different configurations of the airfoil with ZZ is shown, followed by data from different configurations with SP. Then special configurations with voids in the surface are shown. In the end selected data with the different configurations are compared to be able to conclude on the quality of the different ways to represent roughness.

3.1. The Clean Airfoil Compared to Other Measurements

PLCT was inaugurated in April 2018, but required some further development of instruments, turntables etc. before it was able to carry out measurements on airfoils. In the beginning of 2019 the tunnel was ready for the first measurements and to validate the tunnel it was important to investigate how PLCT compared to other high quality wind tunnels. In Figure 6 a polar from PLCT for the NACA 63_3-418 airfoil with a clean surface at a Reynolds number Re = 3 million is compared to polars from Langley LTPT (NASA) [4], Delft and LM LSWT [18] and Stuttgart [19]. Even though the tests are not all carried out on the exact same model the agreement with the other wind tunnels is good. Both for the lift coefficient (C_l) and the drag coefficient (C_d) there are only small deviations. The most important difference is for C_l for angles of attack (AoA) greater than 12 deg and the slightly higher C_d at low AoAs. Concerning C_l for AoAs greater than 12 degrees NASA, Stuttgart and PLCT show higher C_l than Delft and LM. A likely reason to this is that C_l is measured at the walls in NASA, Stuttgart and PLCT, whereas C_l is measured on the airfoil surface in Delft and LM. This is confirmed by the measurements in PLCT, where C_l is lower after maximum C_l when it is measured at the airfoil surface. This is an important input to future measurements, but the general comparison to other wind tunnels is very good. Concerning C_d this is in the upper end at low AoAs up to 3 degrees compared to the wind tunnel measurements in other wind tunnels. Above AoAs of 3 degrees the performance is on top of the other data. The reason for this could be that the edge in the surface between the exchangeable LE and the main model is disturbing the boundary layer and force earlier transition from laminar to turbulent flow. When transition moves towards the LE for increasing AoAs and upstream of the edge, it has no influence on C_l and C_d. This is confirmed by XFOIL computations [20] where computations under the assumption of free transition with the e^N model (N=7) show that the transition point is at 51%c for 0 degrees AoA and moves upstream of 20%c, where the edge of the exchangeable LE is, between 5 and 6 degrees AoA.

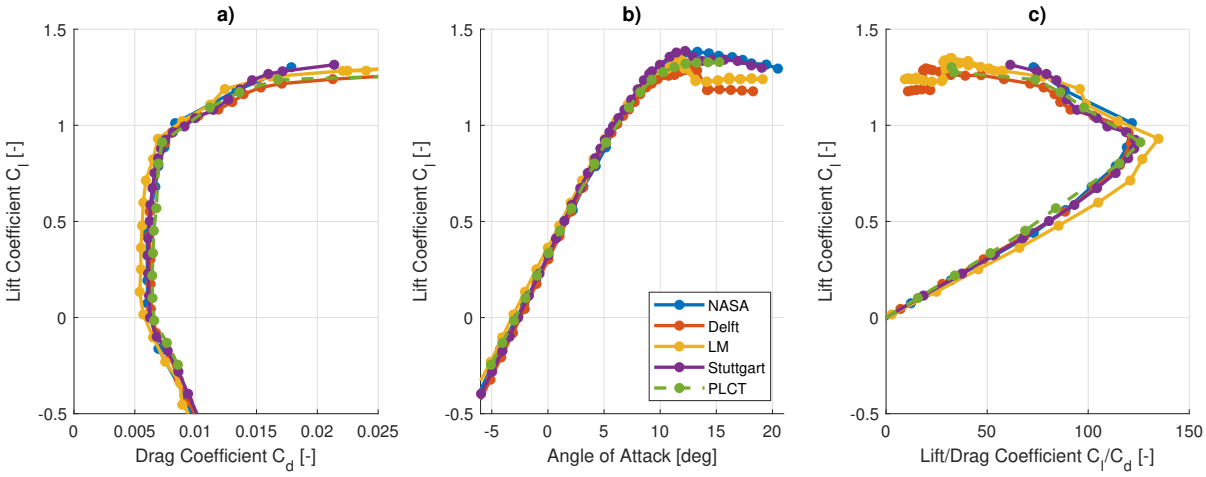

Figure 6. a) Comparisons of C_l as a function of C_d, b) C_l as a function of AoA and c) C_l as a function of C_l/C_d for the NACA 63_3-418 with clean surface at Re = 3 million tested in the Langley LTPT (NASA), in the Delft LTT, in the LM wind tunnel, in the Stuttgart Laminar Wind Tunnel and in the PLCT.

3.2. Zigzag Tape Compared to Other Measurements

Tests on the NACA 63_3-418 airfoil with 0.4 mm high ZZ at 2%c at the SS and 10%c at the PS is shown in Figure 7, where the polars from PLCT is compared to polars from Delft, LM and Stuttgart. These polars are compared to the clean configuration in PLCT. It is clear that data compares well with the LM and that C_d is somewhat higher at low AoAs in Delft and Stuttgart tunnel. When analyzing the data, this is as expected because the ZZ relative to the chord length is relatively higher in the Delft and the Stuttgart tunnel (67% higher) whereas it is only slightly higher in the LM (11% higher). This is because the ZZ height is the same in all tunnels, whereas the airfoil chords are 0.6 m, 0.6 m, 0.9 m and 1.0 m in the Delft, Stuttgart, LM and PLCT, respectively. Thus, the comparison between the different tunnels highlight the importance of scaling LER correctly.

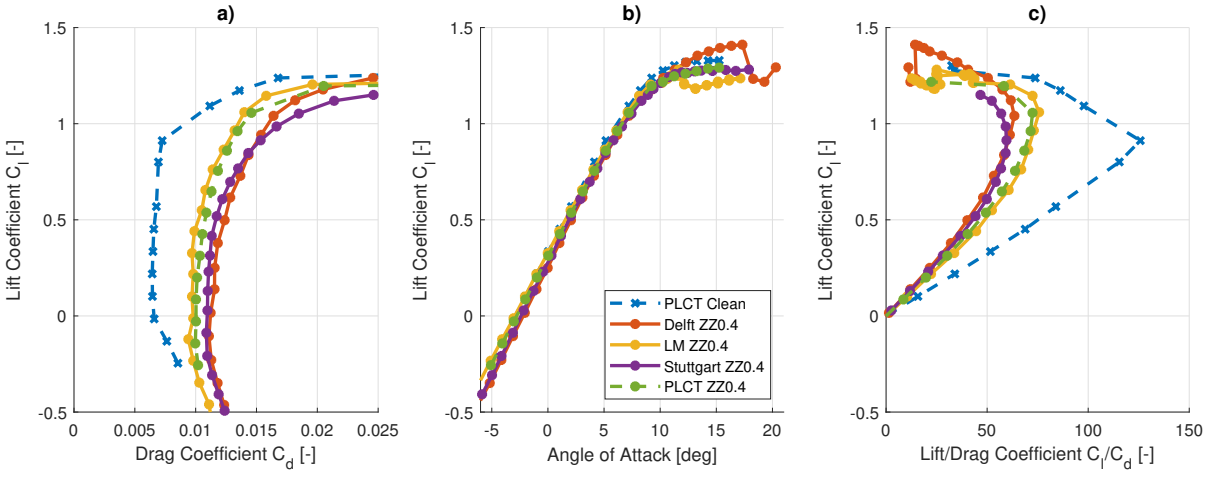

Figure 7. a) Comparisons of C_l as a function of C_d, b) C_l as a function of AoA and c) C_l as a function of C_l/C_d for the NACA 63_3-418 with ZZ at Re = 3 million tested in the PLCT. ZZ with a height of 0.4 mm is mounted at the SS 2%c and the PS 10%c.

3.3. Zigzag Tape

LER was simulated by mounting ZZ at 2%c at the SS. The ZZ has three different heights: 0.2 mm, 0.4 mm and 0.8 mm. Results are shown for Re = 5 million in Figure 8 and compared to the clean configuration. It is clear that the higher the ZZ is, the lower $C_{l,max}$ becomes and the higher C_d becomes. For these heights of ZZ it seems that $C_{l,max}$ is reduced almost linearly with tape height, but this is not the case for C_d. Here, the increase in C_d is almost identical at low AoAs, i.e. below approximately 2 degrees AoA.

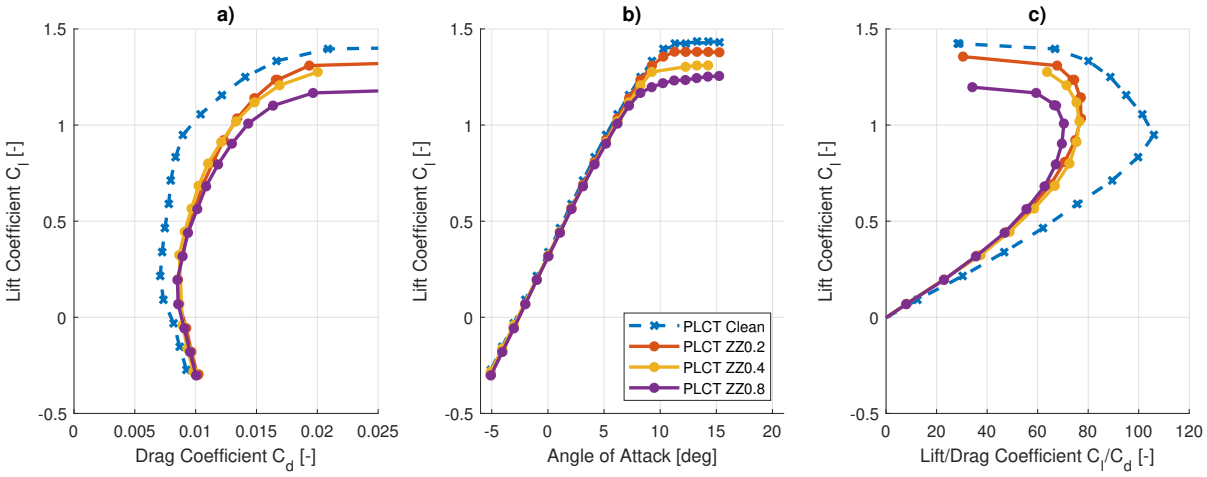

Figure 8. a) Comparisons of C_l as a function of C_d, b) C_l as a function of AoA and c) C_l as a function of C_l/C_d for the NACA 63_3-418 with ZZ at Re = 5 million tested in the PLCT. The ZZ is located only in SS = 2%c. Three different heights of ZZ are shown and compared to the clean case.

3.4. Protuberance

As an alternative to ZZ a rectangular bump in form of an extruded strip with a height of 0.962 mm and a width of 20 mm at 2%c at the SS was tested. The result is shown in Figure 9 and compared to the test with 0.8 mm ZZ and the clean case. The protuberance shows only marginally lower $C_{l,max}$ and slightly greater C_d compared to ZZ0.8. The difference is probably due to the slightly higher thickness of the metal strip. With the small difference in performance between the ZZ tape and the metal strip it indicates that the ZZ 3D shape is of little importance. This corresponds well with the findings by Kruse et al. [21] that from a computational study conclude that *it is indeed possible to simulate small LER by direct implementation in the grid, and it is to some extent sufficient to do simulations in 2D rather than 3D*. This indicates that 2D shapes (extruded add-ons) to some extend can replace a 3D shape like ZZ. For simulation purpose this is an important information, because 2D computations are much less costly and complex than 3D computations.

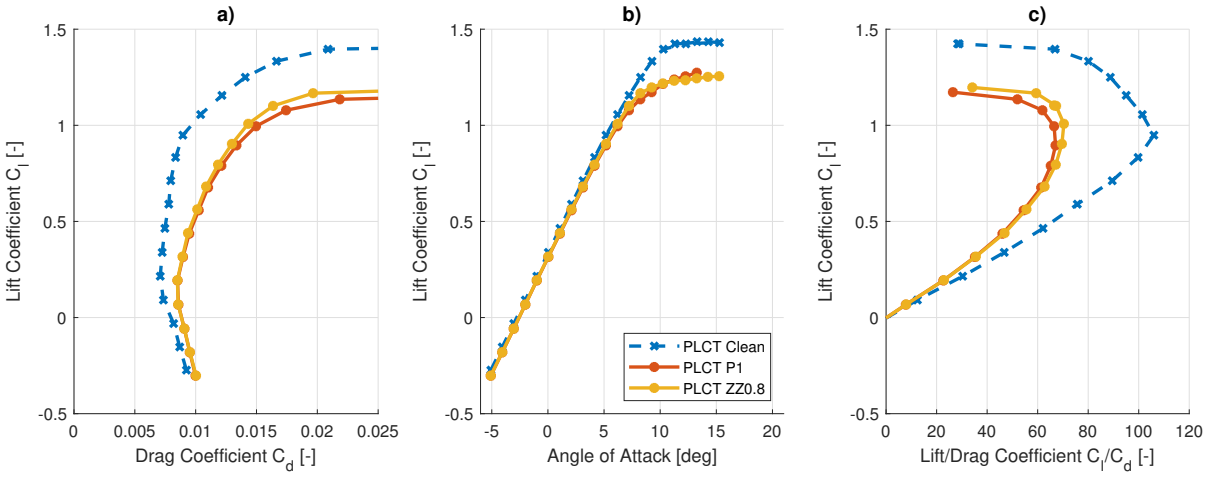

Figure 9. a) Comparisons of C_l as a function of C_d, b) C_l as a function of AoA and c) C_l as a function of C_l/C_d for the NACA 63_3-418 with a 0.962 mm height protuberance at the LE at 2%c at the SS at Re = 5 million tested in the PLCT compared to the clean and ZZ0.8 cases.

3.5. Sandpaper

LER was also simulated by mounting SP. This is because wind turbine blades can be eroded at the LE where the surface texture becomes SP like. Thus, the SP is not only different in terms of the surface texture compared to ZZ, but also because it is mounted around the LE. Results from these tests are shown in Figure 10. Three different types of SP were tested. They were ordinary SP types that in SP terms is denoted P400 (extra fine), P120 (fine) and P40 (coarse), where the numbers are inversely proportional to the grain size. The interesting outcome from these tests were that $C_{l,max}$ was reduced to almost the same level no matter the grain size. Here, the results show that $C_{l,max}$ is lowest for the fine sandpaper and slightly higher the more coarse the sandpaper becomes. This is according to the authors somewhat unexpected and the reason for this is unknown. However, C_d increased as expected as a function of roughness height, so the coarser SP the higher C_d.

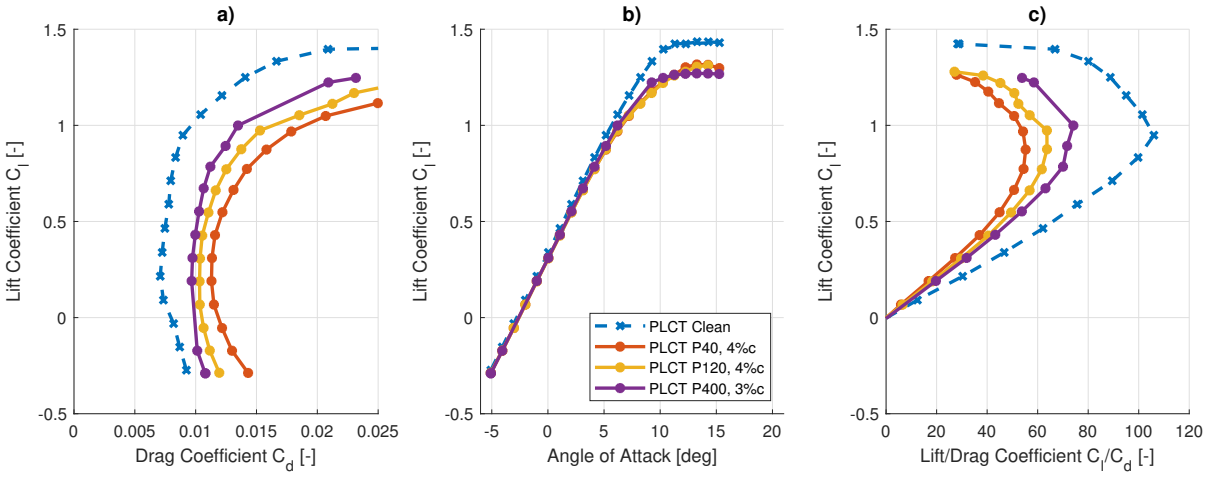

Figure 10. a) Comparisons of C_l as a function of C_d, b) C_l as a function of AoA and c) C_l as a function of C_l/C_d for the NACA 63_3-418 with SP at Re = 5 million tested in the PLCT. Three different types of SP are shown and compared to the clean case.

3.6. Cavity

Observations from inspections of full-scale wind turbine blades have shown that cavities in the surface might appear. Such cavities can be caused by delamination of the fiber structure, but also simply from an erosion process. Therefore, an airfoil with a big cavity was tested, where the cavity covered the entire LE from 3%c on the PS to 3%c on the SS. The cavity had a depth of 3 mm (0.3%c) and had relatively sharp edges with an angle of 90 degrees to the surface. Thus, this corresponds to a severely eroded LE. The results from the tests are shown in Figure 11. Four different cases were tested and compared to the clean configuration: 1) The LE cavity with no sandpaper in the cavity and with a smooth surface in the cavity as the rest of the airfoil. 2) LE cavity with the cavity covered by P120 SP. 3) LE cavity with the cavity covered by P40 SP. 4) The LE cavity with a smooth surface as the rest of the airfoil, but with tape at the edges forming a slope of the edges that were about 45 degrees to the surface. $C_{l,max}$ were very different in the four cases. The cavity with smooth bottom and 90 degree edges showed a reduction in $C_{l,max}$, whereas this became much worse if SP was mounted in the cavity. Thus, the higher roughness height in the bottom of the cavity the lower $C_{l,max}$. However, smoothening the edges with tapes and creating 45 degree edges resulted in almost no reduction in $C_{l,max}$ compared to the clean case. However, in the linear lift region, the difference in C_l between the 45 degree and 90 degree edges is just 0.01 (1%) at 8 degrees AoA, which agree well with the findings based on Computational Fluid Dynamics (CFD) and shown in [22]. Furthermore, the penalty on C_d compared to the clean case was on the other hand severe no matter how the bottom and the edges of the cavity were shaped and C_d at low AoAs more than doubled. The tests also showed that the higher the roughness in the cavity, the higher C_d became especially for AoAs greater than 5 degrees.

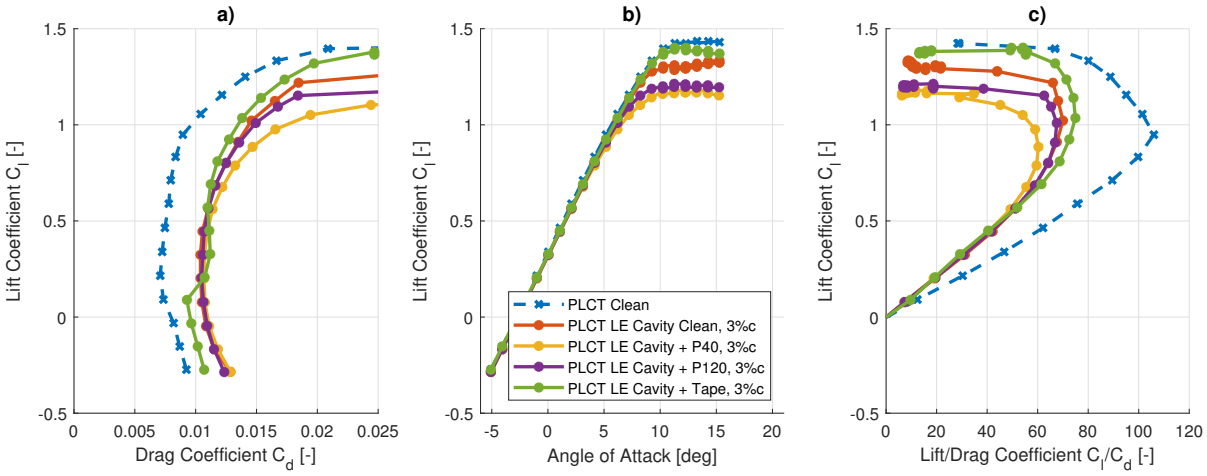

Figure 11. a) Comparisons of C_l as a function of C_d, b) C_l as a function of AoA and c) C_l as a function of C_l/C_d for the NACA 63_3-418 with a cavity at the LE (LE Cavity) from 3%c at the PS to 3%c at the SS with and without SP in the cavity at Re = 5 million tested in the PLCT. Two different types of SP are shown and compared to the clean case, the case with no SP in the cavity and with no SP in the cavity and tape reducing the slopes at the edges of the cavity.

3.7. Comparison of Different Roughness Types

To summarize the different LER types and to compare how much the different types of roughness affect the airfoil performance, selected configurations are compared. This is done in Figure 12 where the clean airfoil is seen together with the de facto standard way of testing roughness for airfoils used for wind turbines: ZZ0.4 at 2%c SS and ZZ0.4 at 10%c PS, the LE cavity with SP P40 in the cavity, SP P40 added directly to the surface and ZZ0.8 at 2%c SS.

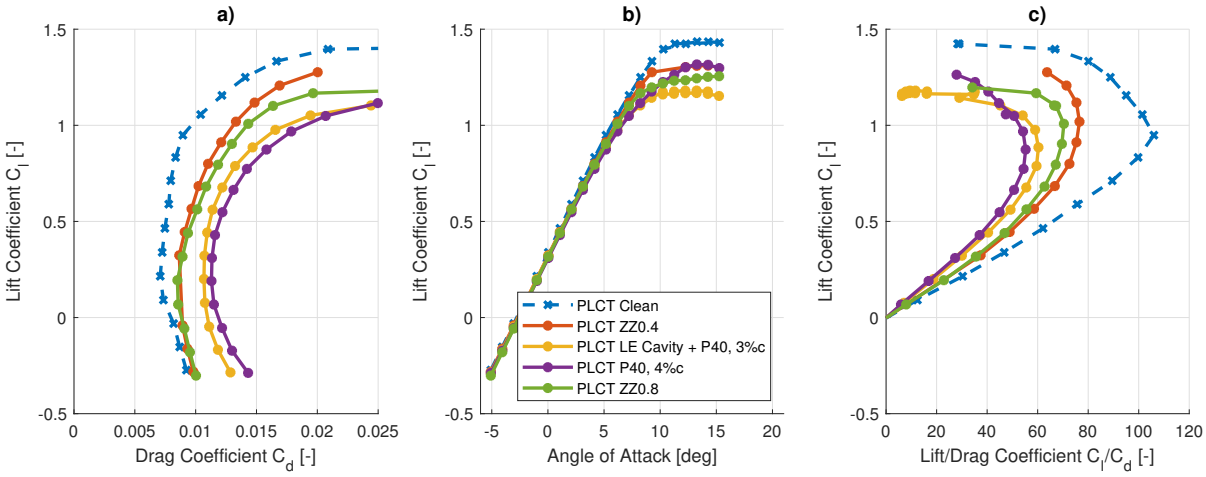

Figure 12. a) Comparisons of C_l as a function of C_d, b) C_l as a function of AoA and c) C_l as a function of C_l/C_d for the NACA 63_3-418 with different types of LE roughness at Re = 5 million tested in PLCT. The roughness types are ZZ 0.4mm tape at 2% SS 10% PS, ZZ 0.8 mm at 2%c, SP P40 from 3%c PS to 3%c SS and LE cavity with SP P40 in the cavity.

From the comparisons it is seen that C_l/C_d as a result of the ZZ as expected is lower than the clean case, but somewhat higher than the cases with SP. On the other hand the loss in $C_{l,max}$ shows big variations with the LE cavity showing the biggest loss. To find a pattern in the changes two key parameters were analyzed: The loss in C_l at AoA = 13.3 degrees and the loss in C_l/C_d at 5.2 degrees. These AoAs correspond to $C_{l,max}$ and max(C_l/C_d) for the clean case and they are plotted in Figure 13.

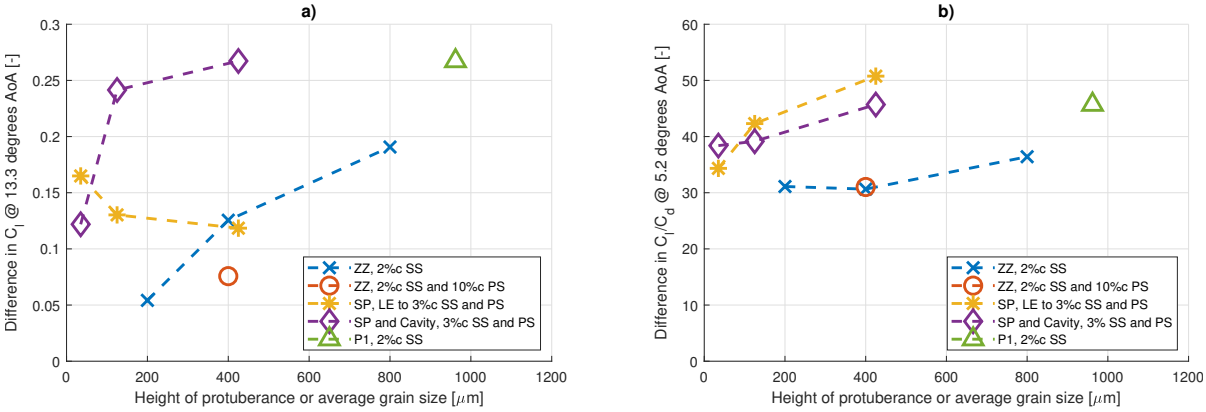

Figure 13. a) Loss in C_l. b) Loss in C_l/C_d ratio. For configurations with ZZ at 2%c at the SS, SP at the very LE and a cavity in the LE with different kinds of SP in the cavity. These configurations are compared to the standard way of simulating LER, i.e. ZZ at 2%c at the SS and at 10%c at the PS and compared to a protuberance at 2%c at the SS.

All data in the results section are shown in Figure 13. For ZZ at 2%c the plotted values show that there is a loss in C_l of about 0.025 every time the height is increased with 0.1 mm. The increase in loss of C_l/C_d is not as clear, but there is a loss between 31 and 36 with the lower heights showing smaller losses. SP at the LE showed an unexpected decrease in C_l for increasing roughness height. Whether this was a coincidence due to small differences in mounting the SP,

or this is due to a fundamental flow mechanism is unknown. However, the losses in $C_{l,max}$ were big and the variation between the roughness height was moderate, between 0.12 and 0.16. The losses in C_l/C_d were significant and increasing for increasing roughness height, between 34 and 51. These losses were significantly higher than for ZZ. Finally, for the cavity at LE the losses in C_l were significant. An increasing roughness height at the bottom of the cavity showed an increasing loss in C_l, between 0.12 and 0.27. The loss in C_l/C_d was also significant, but the increase as a function of roughness height was moderate, between 38 and 46.

These roughness configurations were compared to the de facto standard configuration, ZZ0.4 at 2%c SS and 10%c PS. The loss in C_l and C_l/C_d as a result of this configuration is in the lower end of the other configurations and especially the loss in C_l is small. Therefore, if only this configuration is used to evaluate the roughness sensitivity of the airfoil there is a risk that the airfoil performance is overestimated. The consequence of estimating C_l/C_d to 75 instead of e.g. 65 is an overestimation of power. Using the relation shown by Bak [23], $P_{loss} = 1.5 \cdot \lambda_{loc}/(C_l/C_d)$, shows that if the local speed ratio, λ_{loc}, was 7 and C_l/C_d was 75 the loss compared to operation at infinitely high Reynolds numbers, inviscid flow, would be 14.0%. This should be compared to the situation of C_l/C_d was 65 and here the loss would be 16.2%. Thereby the power would be estimated 2.2 percentage point higher with $C_l/C_d = 75$ instead of $C_l/C_d = 65$. More challenging is it to estimate the power losses due to a reduction in $C_{l,max}$. This depends on the controller design of the wind turbine, but in general power losses will be observed because of losses in $C_{l,max}$ due to a lower slope of the power curve close to the shoulder of the power curve, i.e. close to rated power. Here, significant power losses, i.e. several percentage in power, can per experience be seen in case of significant losses in $C_{l,max}$.

4. Conclusion

Measurements were carried out on the NACA 63_3-418 in the Poul la Cour Tunnel (PLCT) with and without leading edge roughness (LER). The clean configuration measured at Re = 3 million corresponded well with measurements in the high quality wind tunnels NASA, Delft, LM and Stuttgart. The maximum lift is predicted higher in NASA, Stuttgart and PLCT than Delft and LM, probably because the lift in Delft and LM is measured by pressure taps on the airfoil surface where the lift in the other three are measured by wall pressure taps. Differences between Delft, LM, Stuttgart and PLCT were seen on the NACA 63_3-418 equipped with 0.4 mm zigzag tape. The difference was probably due to different chord lengths of the test airfoils resulting in a relatively higher zigzag tape on smaller chords. Therefore, an absolute comparison is difficult, but the results showed the same trends.

The airfoil as measured in the PLCT was equipped with zigzag tapes of 0.2, 0.4 and 0.8 mm height. The changes in lift in the linear lift region were minor whereas a significant drop in maximum lift was observed between the zigzag tape heights, resulting in the highest drop for the thickest tape. The drag increase was similar in the linear lift region for all zigzag tapes. In the stall region, the 0.8 mm zigzag tape showed higher drag whereas the 0.2 and 0.4 mm were close to the same drag values. Also, a 2 dimensional step was tested with a height of 0.962 mm, resembling the results for 0.8 mm zigzag tape. A key conclusion of the study is that it supports the use of 2 dimensional protuberances as LER in wind tunnel tests, which are less complex and computational heavy to simulate in e.g. CFD simulations.

The airfoil was also equipped with P40, P120 and P400 SP, where the lowest number defines the coarser SP. Opposite to the zigzag tape conclusions, all three SP types gives a similar lift penalty but different drag penalties. The coarser SP gives the highest drag, with almost a factor of 2 compared to the finest SP, for most angles of attack.

A special leading edge was exchanged with the leading edge that had the original shape. It was mounted at the airfoil body at 20%c at the suction side and 20%c at the pressure side. Furthermore, it had a cavity with a depth of 0.3%c spanning from 3%c on the suction side to 3%c on the pressure side. A clean case and two cases where P40 and P120 SP were applied inside the cavity were made. The edges of the cavity were 90 degrees in these three tests. One additional test was made with a clean surface of the cavity, but with tapes on the edges that changed the angle of the edges from 90 degrees to 45 degrees. The impact on maximum lift varied with the configuration, where the clean cavity with 45 degrees edges had the least impact, followed by the clean 90 degree case. The SP reduced the lift even further, with the P40 giving the highest penalty. The drag penalty was not changed much in the linear lift region, but the SP case gave higher drag in the stall region. For this configuration, the drag is probably dominated by the edges from the cavity.

Comparing the different types of roughness showed very different performance. The two key numbers, loss of maximum lift and loss of lift-drag ratio, showed to be rather different whether zigzag tape, sandpaper or cavity were tested. Thus, using zigzag tape showed an almost continuous reduction in maximum lift as a function of tape height. This was not the case for the lift-drag ratio. An almost opposite picture was seen for sandpaper, where a continuous increase in the drag was seen for increasing roughness height. However, here the maximum lift was almost constant. Having a cavity with a forward facing step increased the drag significantly, but the loss in maximum lift was very dependent on the surface texture of the cavity. Since leading edge roughness can appear in many different ways it is important to be aware of the most common deviations of the surface quality and test these deviations because the losses in maximum lift and lift-drag ratio are very different depending on the type of leading edge roughness.

Acknowledgements
The authors acknowledgement goes to the Technical University of Denmark, Power Curve ApS and the Danish Energy Agency for the support and funding of this project, the *"Leading Edge Roughness on Wind Turbine Blades", 64015-0046.* The authors also want to thank Jimmie Beckerlee for an invaluable support during the wind tunnel tests.

References

[1] Eastman J N and Sherman A 1932 Wing Characteristics as affected by protuberances of short span *National Advisory Committee for Aeronautics* URL `https://ntrs.nasa.gov/search.jsp?R=19930091523`
[2] Jacobs E N 1932 Airfoil Section Characteristics as Affected by Protuberances *National Advisory Committee for Aeronautics* URL `https://ntrs.nasa.gov/search.jsp?R=19930091520`
[3] Hooker R W 1933 The aerodynamic characteristics of airfoils as affected by surface roughness *NACA-TN-457 Langley Memorial Aeronautical Laboratory* 468–478
[4] Abbott I and Von Doenhoff A 1959 Theory of wing sections, including a summary of airfoil data *Dover Publications*
[5] van Rooij R and Timmer W A 2003 Roughness Sensitivity Considerations for Thick Rotor Blade Airfoils *Journal of Solar Energy Engineering-transactions of the ASME* **125** 468–478
[6] Fuglsang P, Antoniou I and S Dahl K 1998 Wind tunnel tests of the FFA-W3-241, FFA-W3-301 and NACA 63-430 airfoils *Risø National Laboratory*
[7] Bak C, Fuglsang P, Johansen J and Antoniou I 2000 Wind Tunnel Tests of the NACA 63-415 and a Modified NACA 63-415 Airfoil *Risø National Laboratory*
[8] Janiszewska J, Ramsay R, Hoffmann M and Gregorek G 1996 Effects of grit roughness and pitch oscillations on the S814 airfoil *National Renewable Energy Laboratory* URL `https://doi.org/10.2172/273772`
[9] Sareen A, Sapre C A and Selig M S 2014 Effects of leading edge erosion on wind turbine blade performance *Wind Energy, 17:15311542* 17:15311542
[10] Gaudern N 2014 A practical study of the aerodynamic impact of wind turbine blade leading edge erosion

The Science of Making Torque from Wind 2014 (TORQUE 2014), Journal of Physics: Conference Series 524 (2014) 012031

[11] Ehrmann R S, White E B, Maniaci D C, Chow R, Langel C M and van Dam C P 2013 Realistic Leading-Edge Roughness Effects on Airfoil Performance *31st AIAA Applied Aerodynamics Conference*

[12] Langel C M, Chow R, Hurley O F, van Dam C P, Ehrmann R S and White E B 2015 Analysis of the Impact of Leading Edge Surface Degradation on Wind Turbine Performance *33rd Wind Energy Symposium* URL https://doi.org/10.2514/6.2015-0489

[13] Mylon P, Buckley-Johnstone L, Lewis R, Carr M and Martin N 2014 Factors influencing the perception of roughness in manual exploration: Do medical gloves reduce cutaneous sensibility? *Proceedings of the Institution of Mechanical Engineers, Part J: Journal of Engineering Tribology* **229** URL https://journals.sagepub.com/doi/10.1177/1350650113517111

[14] Kruse E K, Bak C and Olsen A S 2019 Wind Tunnel Tests on a NACA 63_3-418 Airfoil with Different Types of Leading Edge Roughness *Submitted to Wileys Wind Energy*

[15] L Runyan H and E Watkins C 1951 Considerations on the Effect of Wind-Tunnel Walls on Oscillating Air Forces for Two-Dimensional Subsonic Compressible Flow *National Advisory Committee for Aeronautics* 20

[16] Garner H C, Rogers E W, Acum W E and Maskell E C 1966 Subsonic Wind Tunnel Wall Corrections *AGARDograph 109* AD0657092 URL https://doi.org/10.1016/0167-6105(94)00119-X

[17] Jones B 1936 Measurement of profile drag by the Pitot-Traverse method *H.M. Stationery Office*

[18] Bak C, Aagaard Madsen H, Gaunaa M, Schmidt Paulsen U, Fuglsang P, Romblad J, Olesen N, Enevoldsen P, Laursen J and Jensen L 2010 DAN-AERO MW: Comparisons of airfoil characteristics for two airfoils tested in three different wind tunnels *Torque 2010* 59–70

[19] Bak C, Skrzypiński W, Fischer A, Gaunaa M, Brønnum N F and Kruse E K 2018 Wind tunnel tests of an airfoil with 18% relative thickness equipped with vortex generators *Journal of Physics: Conference Series* **1037(2)** 022044 URL https://doi.org/10.1088/1742-6596/1037/2/022044

[20] Drela M and Giles M B 1987 Viscous-Inviscid Analysis of Transonic and Low Reynolds Number Airfoils *AIAA 25(10):1347-1355, Vol. 25 NO. 10*

[21] Krog Kruse E, Sørensen N and Bak C 2018 Predicting the Influence of Surface Protuberance on the Aerodynamic Characteristics of a NACA 63_3-418 *Journal of Physics: Conference Series, 1037(2), 2018 [022008]* URL https://doi.org/10.1088/1742-6596/1037/2/022008

[22] Krog Kruse E, Sørensen N and Bak C 2019 A 2-Dimension Quantitative Parametric Investigation of Simplified Surface Imperfections on the Aerodynamic Characteristics of a NACA 63_3-418 *Submitted to Wileys Wind Energy*

[23] Bak C 2013 Aerodynamic design of wind turbine rotors *In P. Brønsted and R. Nijssens "Advances in wind turbine blade design and materials", Woodhead Publishing Series in Energy; No. 47*

APPENDIX G

Article 5: The influence of surface texture on Structure-from-Motion reconstructions

The influence of surface texture on Structure-from-Motion reconstructions

Mikkel Schou Nielsen[a,*], Ivan Nikolov[b], Emil Krog Kruse[c], Jørgen Garnæs[a], Claus Madsen[b]

[a] *Kogle Allé 5, DK-2970, Hørsholm*
[b] *Rendsburggade 14, DK-9000, Aalborg*
[c] *Stationsmestervej 81, DK-9200, Aalborg*

Abstract

In general, optical methods for geometrical measurements are influenced by the surface properties of the examined object. In Structure from Motion (SfM), local variations in surface color or topography are necessary for detecting feature points for the point-cloud triangulation. Thus the level of contrast or texture is important for an accurate reconstruction. However, quantitative studies of the influence of surface texture on the geometrical reconstruction are largely missing.

This study investigates the influence of the object texture level on the reconstruction accuracy using a set of reference artefacts. The artefacts are designed with well-defined surface geometries, and quantitative metrics are introduced to evaluate the lateral resolution, vertical geometric variation and spatial-frequency information of the reconstructions. The influence of texture level is compared to variations in capturing range. For the SfM measurements, a state of the art commercial SfM software solution and a top tier DSLR camera are used. The findings are compared to results using calibrated optical microscopes.

The results show that the proposed pipeline can be used for investigating the influence of texture on SfM reconstructions. The introduced metrics allow for a quantitative comparison of the reconstructions at varying texture level and range. Both range and texture level are seen to affect the reconstructed geometries although in different ways.

*Corresponding author
Email address: msn@dfm.dk (Mikkel Schou Nielsen)

While an increase in range at fixed focal length reduces the spatial resolution, an insufficient texture level causes an increased noise level and may introduce errors in the reconstruction.
Keywords: Structure from Motion, Vision Metrology, 3D reconstruction, Surface topography, Surface texture

1. Introduction

In recent years, Structure from Motion (SfM) has received increased interest. Aided by a rapid development of software solutions [1], SfM offer reconstructions of 3D geometric models in great detail with simple, fast and low-cost acquisition [2, 3, 4]. As a result, potential applications of SfM for quantitative geometric measurements have been considered within a broader range of fields such as cultural heritage [5, 6, 1], geoscience [2, 3, 4, 7, 8, 9], construction site monitoring [10, 11, 12] and infrastructure inspection [13, 14, 15, 16, 17]. Common for these fields are the need for accurate geometric models to allow reliable quantitative analyses. Since the applications cover large differences in object surfaces and capturing conditions, many factors may influence the SfM reconstructions. Among these are the local variations in surface color or topography of the object surface. Both of these properties are often referred to as the 'texture' of the surface. However, although a level of texture is necessary for a successful SfM reconstruction, quantitative studies of the influence of texture on the reconstruction accuracy are missing.

In SfM, objects and surfaces are reproduced in 3D by using a number of image acquisitions from different distances and angles. The algorithms utilize image feature correspondences, sparse point cloud triangulation and point interpolation to create dense point clouds and 3D meshes from the imaged objects and surfaces [18, 19]. As the creation of the dense point cloud applies multi-view stereo algoritms, the full SfM pipeline can sometimes be refered to as SfM-MVS [19]. SfM has many advantages compared to more conventional 3D reconstruction methods [20]. As it requires only conventional hardware like a DSLR camera, SfM has relatively lower overhead costs

compared to laser scanning, LiDAR scanning, etc. Additionally it can be used both indoor and outdoor [21] unlike structured light [22] and time of flight [23] scanners which tend to fail when direct sunlight is present. Finally it is capable of creating much more detailed reconstructions than most 3D-from-stereo systems. On the software side, a number of commercial SfM solutions are available. The work by [5] focuses on the low-cost and free solutions, while the work by [3, 1, 24] covers the newer free and paid software packages.

The accuracy of SfM reconstructions is influenced by a number of factors related to both the acquisition system and the surface properties of the object. Since SfM depends on triangulation of feature points, the angular coverage of the acquired images affects the reconstruction accuracy. Thus, an increase in number of images can improve the accuracy when additional angles and poses are added [4, 25]. The range, i.e. the capturing distance from camera to object, is a limiting factor of the resolution of the SfM reconstruction [19]. As the spatial resolution of the acquired photos scales with range, the reconstruction accuracy scales accordingly [26, 27, 19]. Furthermore, the accuracy depends on the used optics and imaging equipment [28], the lighting conditions [29] as well as the surface properties of the captured objects. In SfM, the object surfaces ideally should not be glossy or transparent, and in the absence of outside contrast sources, like structured light, a level of texture on the surface is needed. This texture can either originate from a local variation in surface coloring or a local height variation of the surface topography, e.g. roughness. A sufficient texture level is required for enough distinct features on the object surface to be tracked from image to image [4, 9]. Low texture regions may result in empty regions of the point cloud [30] and could require increased overlap of images [3]. However, although low texture regions impact the SfM reconstruction accuracy, little research has been published on this.

Several approaches have been applied to evaluate the accurracy of SfM reconstructions. In [31], an approach from vision metrology was incorporated by using well-defined scan settings and reference targets to document the geometric accuracy by SfM. More often, approaches rely on a comparison to other optical techniques such as a LiDAR, laser scanner or total station. In the case of reference point clouds as with LiDAR or laser scanner, direct point-to-point comparison with the SfM point cloud

can be carried out [4, 5, 32, 8]. Similarly when digital elevation models (DEM) are produced, a direct raster-to-raster comparison is possible [32, 33]. Conversely, a comparison can be made between a point cloud and reference target points obtained with e.g. a total station [2, 30]. Either way, the comparison is influenced by the reference technique from e.g. the measurement uncertainty of the reference points [33] or the alignment of point clouds. As an alternative to reference measurements, the use of 3D printed objects allow for direct comparison of the measured geometries to the design geometry of the used CAD model [34].

Common metrics for evaluating SfM reconstructions are the standard deviation (SD) [2, 5, 1] or root mean squared (RMS) deviation [32, 30, 27] between SfM reconstructions and reference points. The SD and RMS metrics have usually been reported as overall global statistics. An advantage of the SD and RMS metrics is that negative and positive deviations will not cancel each other out as with the sometimes reported mean deviation or mean error [19]. As the accuracy might vary locally with the object surface geometry, metrics with spatial information or across multiple length scales are of interest when evaluating SfM reconstructions. One way to obtain additional spatial information is by estimating a SD value for each point on the DEM or point cloud [35, 33]. This can be used to study e.g. the effect of local surface height on the reconstruction accuracy. In addition, some studies have compared geometric measures on the object such as distances or angles [6, 36] to the SfM point clouds. Notwithstanding, more systematic approaches for studying the accuracy dependence on local topography are needed.

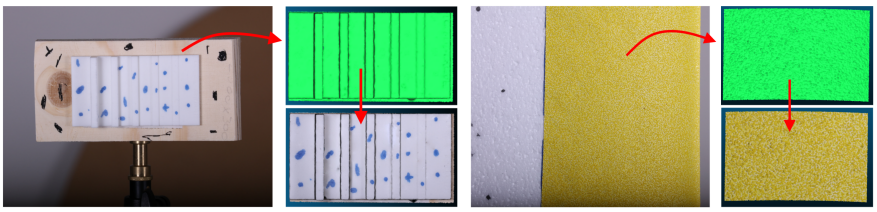

Figure 1: Step-height and sandpaper artefacts used in the paper, as well as the reconstructed meshes and color textures

In this study, we introduce a pipeline for investigating the influence of surface tex-

ture on SfM reconstructions. The pipeline was evaluated by SfM measurements on two sets of reference artefacts as shown in Figure 1. To study the effect of varying color contrast, a 3D-printed step-height artefact was prepared with different color patterns applied to the surface. The effect of local height variations was studied using a set of artefacts with industrial sandpaper of varying grit size covering the surface. The artefacts were chosen to provide quantitative reference values, i.e. the nominal height of the steps and the sandpaper grain size distributions in accordance with ISO 6344 [37]. In addition, the use of a 3D-printed artefact allows for direct comparison to the design geometry. The influence of texture was compared to the effect of the camera-to-object range on the reconstruction.

The SfM reconstructions were based on high-resolution images taken with a DSLR camera with a focal length of 260 mm and at a close range between 1.5 m - 2.2 m. This close zoom on the surface allowed for comparing the SfM reconstructions to topography maps measured using calibrated confocal (CM) and focus variation microscopes (FVM). In addition, this high-resolution setup was required to capture the surface topography of the sandpaper artefact.

To quantify the texture influence, a number of parameters and metrics are introduced to describe the reconstructed topography across multiple scales. These parameters include RMSE values, heights of surface structures, surface roughness values as well as power spectral density (PSD) analysis.

2. Methodology

2.1. Preparation of Artefacts

Two types of samples were used; a 3D printed step-height artefact with various coloring added and a set of artefacts consisting of foam pieces covered with sandpaper of grit sizes from P40 to P240. The former type represented an ordered height-variation on the macro-level while the latter represented randomly distributed height-variations on the micro-level.

The step-height artefact of 50 mm in width and 95 mm in length consisted of five symmetric steps of nominal heights 0.63 mm, 1.25 mm, 2.5 mm, 5 mm and 10 mm

(a) (b)

Figure 2: Artefacts for validating reconstructions of the surface topography from macro and micro height variations. Subfigure 2a shows the 3D printed step artefact with nominal heights - 0.63 mm, 1.25 mm, 2.5 mm, 5 mm and 10 mm. Subfigure 2b shows an example of a foam artefact with the P40 sandpaper attached to it.

and nominal width of 5 mm. The artefact, seen in Figure 2a, was 3D printed using strong PLA material with a subsequent polishing for an additional smoothing of the surface. The removal of material by the polishing procedure is estimated to be of the order of 0.01 mm, which would not change the geometry significantly. In addition to the monochrome surface, two types of coloring were added to study the influence of color-contrast on the SfM reconstructions. The types of coloring were: no coloring, a projected light pattern and a marked pattern painted on the surface of the artefact.

For the sandpaper artefact, industrial sandpapers of varying grit size from P40 to P240 were attached to curved foam surfaces that were cut using a CnC foam cutter as shown in Figure 2b. The grit-size range was chosen to study the influence of surface roughness on the SfM reconstruction. As the sandpaper follows the standards proposed by [38], the grain size and hence the roughness is well-defined. Furthermore sandpaper is readily available and can be easily added to different surface shapes and sizes. The the average particle diameters of the used grit sizes are shown in Table 1.

Table 1: Sandpaper grit size and the nominal average particle diameter in μm [38]

Grit size	P40	P60	P80	P100	P120	P180	P240
Nom. av. diam. (μm)	425	269	201	162	125	82	58.5

2.2. SfM Capturing Conditions

An indoor environment was chosen for image acquisition for both types of artefacts. A Canon 5Ds DSLR camera with a Canon 70-300 f/4-5.6L IS USM zoom lens was used and the captured images had a size of 8688x5792 pixels. The sensor pixel size was $4.14\,\mu m$ and a focal length of 260 mm was used. The lighting was provided by two Elinchrom 4RX flash lights. The exposure time was set to 1/200 sec. so problems of blurring caused by vibrations were prevented and a F-stop of f/20, so all the surface of the imaged artefacts was in focus.

The range, i.e. the sample-to-camera distance, was 1.5 m for the three texture levels of the step-height artefact and 1.7 m for the seven grit sizes of the sandpaper artefact. To investigate the influence of distance, the range was varied for a sub-set of the artefacts; at 1.5 m and 2.0 m for the step-height artefact colored with a marked pattern and at 1.5 m, 1.7 m, 2.0 m and 2.2 m for the P40 sandpaper artefact. The 1.5 m was chosen as a lower limit on the range, since the chosen lens had difficulties focusing at closer distances. The upper limit was restricted to 2.2 m by the size of the indoor location. The range settings are summarized in table 2.

For a fixed focal length, the range determines the ground sampling distance (GSD), i.e. the spatial size on the object that each pixel in a captured image covers. Using a pinhole camera model, the GSD can be calculated as the sensor pixel size multiplied by the ratio of the focal length to the range. With the used settings in the study, the GSD varied between $24\,\mu m$ and $35\,\mu m$ for ranges 1.5 m to 2.2 m, as shown in table 2.

To capture all surface details of the two types of artefacts, images were acquired at every 10 degrees along a semi-circular path from 0 to 180 degrees around the artefact. This was repeated for three different heights with the camera facing towards the artefact at all times resulting in a total of 54 images. As the same number of images was used regardless of the range, the overlap of individual images will vary in these

Table 2: Summary of the range and focal length used for sample scans and the corresponding GSD at the sample. P## = sandpaper artefact of grit P##, SH = step-height artefact, c = clean, p = projected light pattern, m = marked pattern.

Scans	SHc, SHp, SHm, P40	P40,...,P240	SHm, P40	P40
Focal length	260 mm	260 mm	260 mm	260 mm
Range	1.5 m	1.7 m	2.0 m	2.2 m
GSD	$24\,\mu m$	$27\,\mu m$	$32\,\mu m$	$35\,\mu m$

reconstructions.

2.3. From Point Cloud to topographic map

The reconstruction software used was ContextCapture by [39]. It was selected as it provides one of the highest accuracies compared to other state of the art solutions, although it suffers from degradation in performance in sub-optimal conditions [24]. The pipeline from input images, 3D reconstruction and extraction of a depth map patch is visualized in Figure 3. An overview of the process is given below.

The captured images 3a were imported to ContextCapture and a triangulation, feature extraction and matching step was performed to find the camera positions and key feature points from the input images 3b. From these positions and feature points, a sparse point cloud was formed. Next in the reconstruction process a dense point cloud was created and meshed into a triangle mesh 3c. Finally a (color) texture is build from the visual data from the input images 3d. To establish the absolute scale in the reconstruction, reference lengths on the artefacts were used. For the foam artefacts, the scale was fixed using the distance between a set of feature points on the surface. For the step-height artefact, the length and width of the artefact were used to fix to an absolute scale.

Prior to the data analysis, a DEM was created from each reconstruction using the following pipeline. First, the reconstructed meshes were transferred to CloudCompare [40]. The reconstructed sandpaper samples were registered to each other so a patch can be extracted from each from an approximately the same place. The registration was

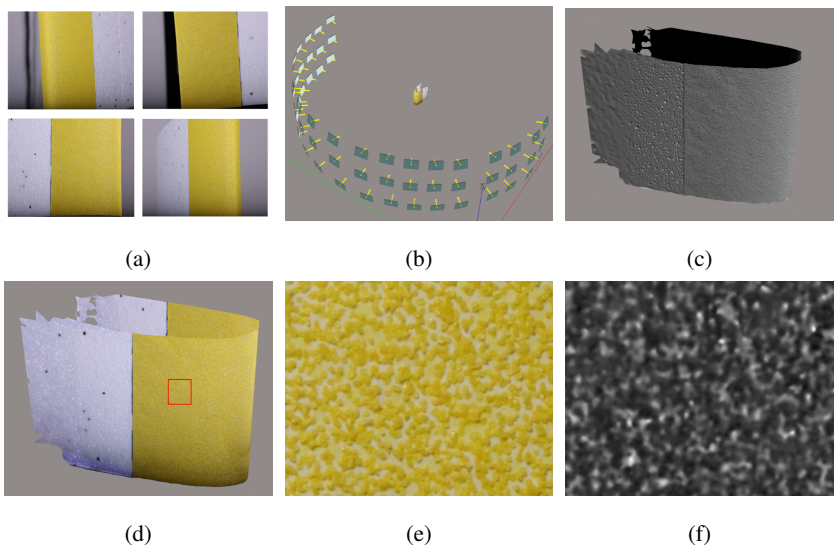

(a) (b) (c)

(d) (e) (f)

Figure 3: Pipeline for 3D reconstruction using SfM. 3a) Initially, images were acquired at every 10 degrees of a halfcircle around the object at three different heights and tilt angles. 3b The camera pose of the images and points on the object surface were then calculated. 3c and 3d Example of a reconstructed surface geometry without and with color. See 3e for an extracted patch from the reconstruction. See 3f for resulting depth map.

done by minimizing the distance between them using an iterative closest point (ICP) algorithm, and a patch was extracted from each reconstruction 3e. For the sandpaper artefacts, the patches were roughly 50 mm x 50mm in size while the full 50 mm x 95 mm area of the step-height artefact was extracted. The patches were oriented with the Z axis perpendicular to the mesh surface, and was rasterized into a topographic map 3f. This was done by an interpolation of the point-cloud points to a map with equidistant point spacing and using the average z-value of each grid space.

2.4. Microscopy Measurements

For the microscopy reference measurements of the step-height artefact, the 3D surface geometry was acquired through focus-variation microscopy (FVM) using a calibrated Hirox RH-2000 microscope [41]. A region-of-interest topographic map was measured across each step. The 0.63 mm, 1.25 mm and 2.5 mm steps were measured using the MXB-5000REZ mid-range objective with x140 magnification, a pixel size of 2.18 μm and a 22.5 μm vertical step size. The MXB-2016Z objective with x100 magnification, a pixel size of 1.69 μm and a 150 μm vertical step size were used for the 5 mm and 10 mm steps. For the 3D surface reconstruction, the custom Hirox software was used. The FVM microscope was calibrated in the vertical direction to a set of gauge blocks with traceability through a laser interferometry calibration. The relative uncertainty was 2% in the vertical direction.

As reference measurements for the sandpaper artefacts, confocal microscopy (CM) measurements were carried out on sandpaper samples of the sandpaper used for the foam artefacts. A calibrated PLU NEOX confocal microscope by Sensofar [42] with x5 magnification was used. The spatial pixel size was 3.32 μm, and the vertical step size was 12 μm. The 3D surface reconstruction was performed using the custom Sensofar software. Two sets of measurements were conducted; one with a square FoV of around 10 mm x 10 mm and one with a rectangular FoV of 40 mm x 2 mm. The former was used for particle size analysis and the latter for power spectral density analysis. The sensitivity of the CM microscope in the vertical direction was calibrated using a set of step height transfer standards. Traceability was ensured through calibration of the standards by e.g. an AFM equipped with laser interferometers. The relative uncertainty

was 3% in the vertical direction.

3. Data Analysis

The main software programs used for the data analysis were the Scanning Probe Image Processor (SPIP) [43] as well as custom scripts in MATLAB. SPIP is an image processing program with special tools for accurate characterization of image structures. A number of characterization parameters were calculated to analyze the surface properties as explained below.

3.1. Height of Steps

The step height was calculated from the DEMs using the "ISO 5436 Step Height" [44] analysis tool of the SPIP application software. In turn, each step of the artefact was selected and cropped with the step aligned along the up-down direction. A leveling was made using ground level on both sides of the step, and an "ISO 5436 Step Height" analysis was performed on each line across the step. The result was a mean value as well as a SD for the height of each step.

3.2. Edge resolution

As a measure of the spatial resolution of the step-height artefact, the edge resolution (ER) was used. Each step of the artefact was divided into sections. For each section, the ER was found as the width between the 10% and 90% height level. Thus, the ER is zero for a 90 degree side wall angle and grows when the angle decreases. The mean value and standard deviation of the ER were calculated for each step.

3.3. Particle Analysis

Ideally, the individual grains of the sandpaper samples would appear in the SfM and CM reconstructions as separable particles. Thus, by analyzing the particle size a comparison to the nominal average grain size should be possible. Therefore, to evaluate the SfM reconstruction of the sandpaper, an image segmentation was carried out on the SfM DEMs and CM topographic maps to label individual particles.

The initial image segmentation was conducted in four steps. First the topographic map was filtered to remove low-frequency components. A Gaussian filter with a 5 mm cut-off wavelength was applied using the SPIP software. Secondly, an adaptive thresholding segmentation of height structures and background was performed using the MATLAB image processing toolbox. For each pixel, the segmentation finds a threshold level from a local neighborhood analysis. Thirdly, a modified watershed algorithm for irregular features from the Biovoxxel toolbox [45] in ImageJ was applied to label individual particles in a label map. For the algorithm, a convexity level of 0.95 was used. Lastly using the label map, each individual particle could be selected from the topographic map. In Figure 4, the segmentation process is illustrated.

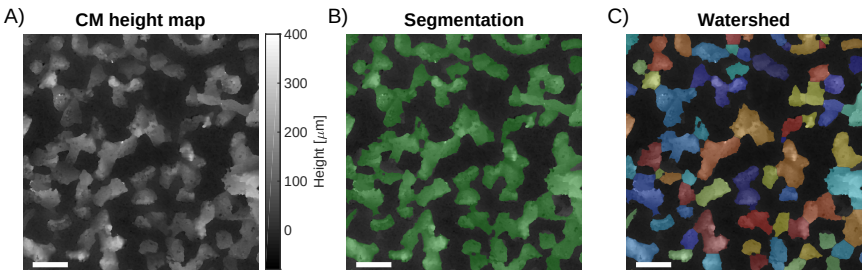

Figure 4: Illustration of the image segmentation of a P80 sandpaper. A) The topographic map after filtering to remove low-frequency variations. B) The segmentation result after the adaptive thresholding is shown in green overlayed on the topographic map. C) The coloring shows the labeling of the individual particles after applying the modified watershed algorithm to the segmentation. The width of the scale bar is 0.5 mm

From the image segmentation, the height of each labeled particle was calculated using MATLAB. The height was found as the distance from the highest point on the individual particle to the background reference plane. The background reference plane was found as the global mean height level of the background in the topographic map. A particle density value was calculated as the ratio of the number of labeled particles to the measured surface area.

3.4. Roughness Analysis

The root mean square area roughness parameter S_q was chosen as a measure of the overall height variations of a DEM. The S_q parameter of the DEM was calculated using

the "Roughness Analysis" tool of the SPIP application software. At first, the surface was leveled. Then, an area roughness analysis was carried out using a S-filter of $10\,\mu m$ and a L-filter of $5\,mm$ as described in [46].

3.5. Power Spectral Density Analysis

To investigate the wavelength dependence of the SfM reconstructions, a power spectral density (PSD) analysis was conducted on the sandpaper-artefacts measurements. When used on measurements of surface topography, the PSD is the Fourier transform of the surface height autocorrelation function. More in-depth introductions to the use and calculation of PSD of surface topography measurements can be found in [47, 48]. A PSD analysis was carried out on both CM and SfM measurements of the sandpaper artefacts and the SfM topographic maps of both step-height and sandpaper artefacts for the different capturing conditions, i.e. object texture and imaging range. As output of the PSD analysis, an average of one-sided 1D PSD curves from the lines in the topographic maps was calculated. The software used was the "Average X-PSD" tool of the "FFT/PSD analysis" toolbox in SPIP.

4. Results

4.1. Step-height Artefact

The variation in color contrast on the step-height artefact had a clear impact on the SfM reconstructions. For the smooth monochrome surface, the measurement at 1.5 m resulted in not enough feature points being extracted and ContextCapture SfM software could not produce neither a point cloud nor a mesh. This was improved somewhat by projecting a random dot pattern perpendicularly on the surface using a light projector. As seen in Figure 5c, a reconstruction of the artefact was possible although it suffered from a few holes and variation in the side-wall widths. An even better improvement was achieved when the horizontal and vertical faces of the surface were marked with a pattern of spots and lines. Figure 5a and Figure 5b show the reconstructions of the marked pattern condition at a range of 1.5 m and 2 m, respectively.

Qualitatively, the influence of the color contrast is visible in the middle and bottom rows of Figure 5. A much larger variation in width is observed with the projected

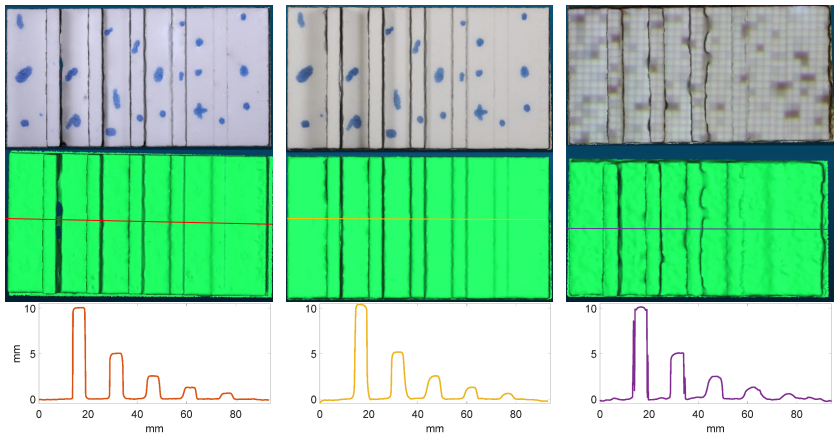

(a) (b) (c)

Figure 5: The reconstructed step-height artefact. The reconstructions in 5a at 1.5 m and in 5b at 2.0 m range are of the manually marked artifact. In 5c, the reconstruction using a projected pattern over the artefact is shown. The top and middle row shows the reconstruction with and without color texture. In the bottom row, a line profile is shown across the artefact with position indicated by the line in the middle row.

light pattern of Figure 5c (middle panel) than for the marked pattern in Figure 5a. In addition, while the line profile of the marked pattern reconstruction in Figure 5a (bottom panel) shows almost rectangular side-walls and step corners, the side-wall and corner angles are reduced in the line profile of the projected pattern in Figure 5c. This indicates a loss in resolution and accuracy of the reconstruction. A somewhat similar effect is seen by increasing the range from 1.5 m to 2 m as seen by comparing Figure 5a and 5b.

Quantitative results are shown in Table 3 and Table 4. Since no successful SfM reconstruction was obtained from the monochrome smooth surface, too little color contrast clearly affects the measurement of height values. However, for all successful SfM reconstructions and FVM measurements the mean height values were comparable regardless of the variation in color contrast and imaging range as shown in Table 3. In contrast, the capturing conditions did influence the SD of the measured height values which is further illustrated in Figure 6A. The use of a projected light color contrast at a 1.5 m range gave a significantly larger SD compared to the marked pattern measure-

Table 3: Parameters from the step-height artefact measurements using FVM and SfM. SfM was conducted for marked pattern artefact at 1.5 m (SM1.5) and 2.0 m (SM2) and for artefact with projected light pattern at 1.5 m (SP1.5). Listed are mean height and ER values for each step. The standard deviations are shown in parenthesis.

Step	Height				Edge resolution (ER)			
	FVM	SM1.5	SM2	SP1.5	FVM	SM1.5	SM2	SP1.5
[mm]	[mm]	[mm]	[mm]	[mm]	[mm]	[mm]	[mm]	[mm]
0.63	0.620	0.629	0.588	0.61	0.472	1.58	2.18	2.88
	(0.0055)	(0.027)	(0.044)	(0.064)	(0.062)	(0.27)	(0.52)	(0.57)
1.25	1.225	1.253	1.21	1.183	0.365	1.12	1.82	2.58
	(0.0087)	(0.026)	(0.053)	(0.032)	(0.047)	(0.36)	(0.24)	(0.53)
2.5	2.468	2.519	2.523	2.45	0.335	0.84	1.91	1.48
	(0.0060)	(0.028)	(0.042)	(0.094)	(0.043)	(0.18)	(0.29)	(0.66)
5	4.959	5.042	5.095	4.81	0.334	0.492	1.10	0.78
	(0.016)	(0.033)	(0.039)	(0.45)	(0.042)	(0.087)	(0.46)	(0.25)
10	9.887	9.99	10.32	9.2	0.387	0.41	1.17	1.27
	(0.041)	(0.32)	(0.35)	(1.5)	(0.071)	(0.15)	(0.53)	(0.30)

ment. On average for all steps, an increase of a factor of 5 was observed. In addition, moving the marked pattern artefact to a range at 2 m also increased the SD values with a factor of 1.5 on average. The RMSE value between the full SfM reconstruction and design geometry of the artefact showed a similar behaviour as seen from Table 4. The RMSE was 1.8 times larger for the projected pattern and 1.2 times larger for the marked pattern at 2 m compared to the marked pattern at 1.5 m range. While in general the SD values for the smaller steps were relatively constant within each measurement, a significant increase was seen especially for the 10 mm step. For the projected light pattern, the 10 mm step SD value had to be cropped at 0.5 mm in Figure 6A to allow for visual comparison of the other results.

The lateral spatial resolution was also influenced by the capturing condition as illustrated by the edge resolution (ER) in Figure 6B. As recalled from section 3.2, the ER is the lateral width between the 10% and 90% height of the step. Both the use

Table 4: Raster-to-raster RMSE between SfM and design geometry. Marked pattern artefact at 1.5 m (SM1.5) and 2.0 m (SM2) and projected light pattern artefact at 1.5 m (SP1.5).

Scan	SM1.5	SM2	SP1.5
RMSE	0.57 mm	0.70 mm	1.04 mm

of the projected light pattern and increasing the range with the marked pattern from 1.5 m to 2 m resulted in a reduced resolution as seen from the larger ER. In both cases the ER across all steps was on average a factor of two larger compared to the 1.5 m marked pattern measurement. While the 10 mm step had the largest SD height value, the ER values were largest for the 0.63 mm step and in general decreased with the height. Thus, both low and high aspect ratios of the steps can pose a challenge for the accuracy of the reconstructed geometries by SfM.

How the capturing conditions affected the reconstructions can be seen in more detail from the PSD analysis in Figure 6C. The dotted (blue) line shows a simulated PSD curve using the nominal artefact geometry. The full (red), dashed (yellow) and dot-dashed (purple) lines are from the SfM measurements using projected pattern at 1.5 m, marked at 1.5 m and 2 m, respectively. For the long-wavelength components at frequencies from 0.01 mm^{-1} to 0.1 mm^{-1}, the SfM curves follow the nominal PSD. Thus, all reconstructions are able to reconstruct the large-scale geometry of the step-height artefact.

However, from 0.3 mm^{-1} and depending on the capturing conditions the SfM curves start to deviate from the nominal. The marked pattern reconstruction at 1.5 m follows the closest path to the nominal curve. The distinct peaks at high frequencies in the nominal curve can also be found in the SfM curve up to around 3 mm^{-1}. Increasing the SfM range to 2 m is seen to cause a reduction in the PSD intensity from 0.3 mm^{-1} and above compared to the 1.5 m curve. In addition, the distinct peaks are only visible up to 2 mm^{-1}. This indicates that an increased range decreases the sensitivity of the reconstruction across a range of frequencies and reduces the resolution limit.

For the projected light pattern reconstruction, a different behaviour is seen. From 0.3 mm^{-1} the peak-to-valley amplitude of the curve oscillations decreases rapidly, and

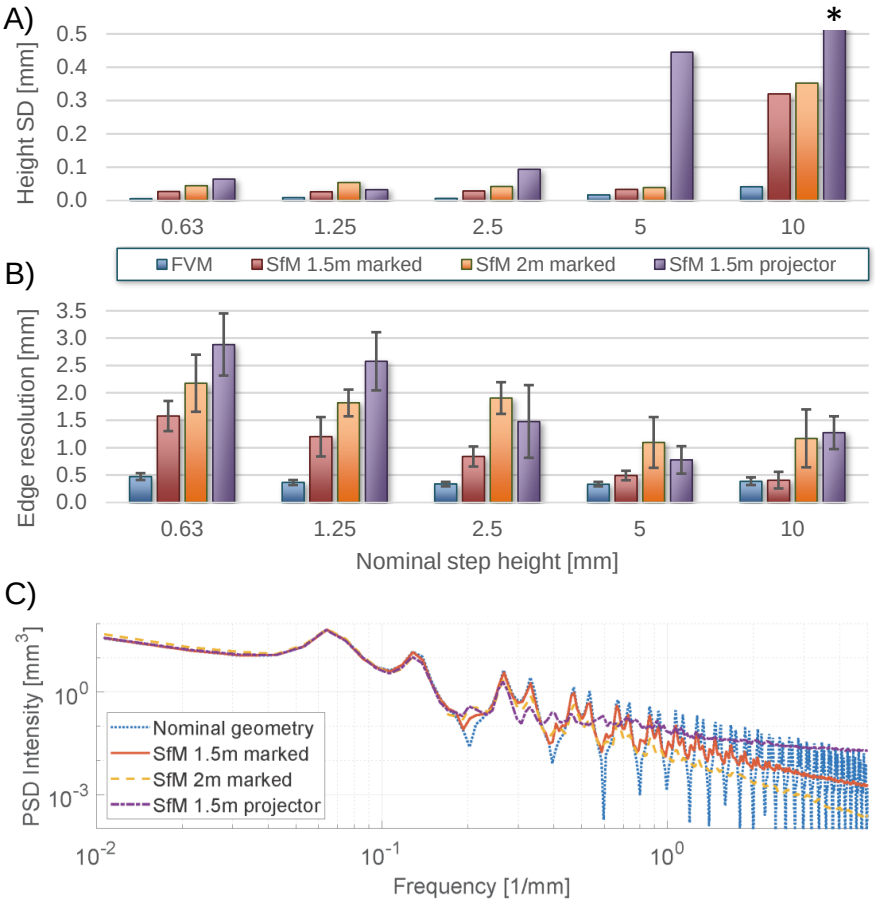

Figure 6: Step height artefact parameters from FVM, SfM marked pattern at 1.5 m and 2.0 and SfM projected pattern at 1.5 m. A) SD of measured step height. Note that the SD of the 10 mm step of the SfM projected pattern was cropped off at 0.5 mm for better visual comparison. B) measured ER with the SD as errorbar. C) Power spectral density (PSD) analysis of the full reconstructed step-height artefact. Both intensity and frequency are shown on a log-scale. SfM measurements are compared to a nominal PSD based on the design geometry.

from around 1.2 mm^{-1} the curve flattens. Furthermore, the intensity level lies above the marked pattern curve from 1 mm^{-1} and even the nominal curve from 4 mm^{-1}. This larger intensity could indicate an increased noise level. According to [48] the presence of white noise introduces a flat region at high frequencies of a PSD curve with an intensity propotional to the strength of the noise. Thus, an interpretation could

be that a degradation in color contrast leads to an increased noise in the reconstruction which was not seen when changing the range.

4.2. Sandpaper Artefacts

The influence of the topography texture on the SfM reconstructions could be seen in both the reconstructed color and geometry. In Figure 7, the color contrast of the SfM reconstructions from P40 to P240 at 1.7 m range are shown. While the color contrast of P40, P60, P80 and P100 reconstructions appears uniform across the patches, darker areas are visible on the P120, P180, P240. These artefacts could be caused by too few detected feature points due to the reduced topography texture.

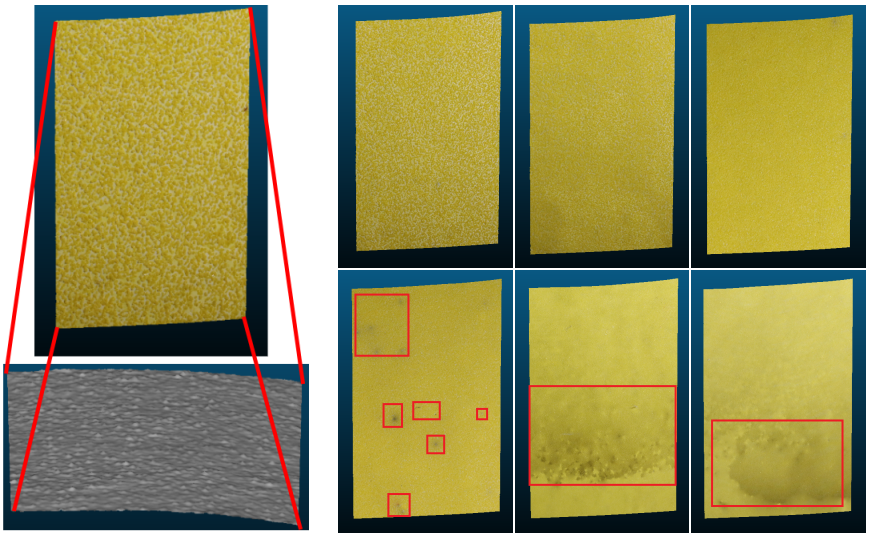

Figure 7: SfM reconstructions of the seven grit sizes at 1.7 m range. (Leftmost) P40 with close up of the geometry. (Top row) P60, P80, P100 and (bottom row) P120, P180, P240. The P120, P180 and P240 reconstructions show darker areas with erroneous color texture. These areas are marked with red.

The reconstructed SfM topography can be studied more closely in Figure 8. Figure 8D through 8F show a zoom-in of the SfM DEM of grit sizes P40, P80 and P180, respectively. The corresponding CM topographies are shown in Figure 8A through 8C. The image width has been scaled down with a factor of two between each column to mimic the decreasing grain diameter as from Table 1.

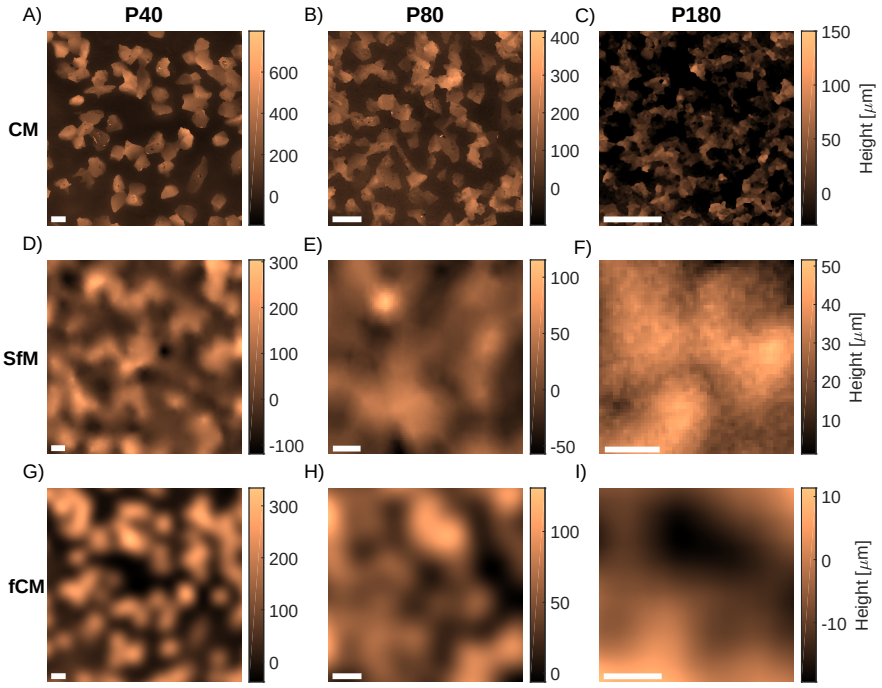

Figure 8: Topographic maps of sandpaper artefacts with grits P40, P80 and P180. CM (top row), SfM (middle row) at 1.7 m range and fCM (bottom row) after Gaussian filtering with σ = 0.21 mm. A), D), G) P40. B), E), H) P80. C), F), I) P180. The width of the scale bar is 0.5 mm in all panels. Note that CM and SfM have been measured at different sample locations.

As seen from the figure, the SfM reconstructions suffer from a much poorer spatial resolution compared to the CM measurements. While the lateral resolution of the CM measurement was limited by the pixel spacing of 0.03 mm, the SfM resolution from the ER analysis in section 4.1 was found at best to be 0.5 mm. Accordingly, a direct comparison of SfM and CM would be difficult. To compare the two topographies with very different resolutions, an alternative approach inspired by [49, 50] was employed. By applying a Gaussian low-pass filter to the CM topographies of Figure 8A through 8C, a set of topographic data with spatial resolution resembling the SfM DEM can be modelled. The filter width was determined by applying a range of Gaussian filters to synthetic data of an ideal edge to find the relation between the values of the ER and σ. An ER value of 0.5 mm was chosen which gave σ = 0.21 mm. The resulting

topographies after applying the Gaussian filter are shown in Figure 8G through 8I. Especially for the P40 and P80 grits, the filtered CM (fCM) topographies have a similar appearance and height range as the SfM topographies. For the P180 grit, however, the SfM DEM of Figure 8F shows a larger height range as well as a higher level of high frequency noise than the fCM of Figure 8I.

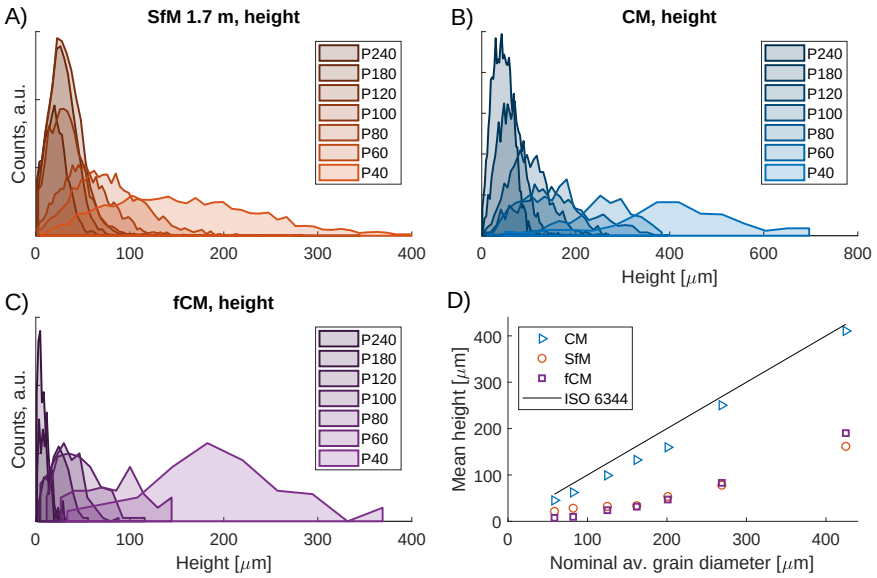

Figure 9: A-C) Height distributions for SfM, CM and fCM particle analysis. A) SfM, B) CM, C) fCM, D) Mean measured height values versus the nominal grain diameter. The SfM range was 1.7 m.

For the particle analysis, the limited spatial resolution of the SfM DEMs meant that the grains could not be resolved individually. Instead groups of neighbouring particles were observed as illustrated by comparing fCM topographies in Figure 8G through 8I to CM in 8A trough 8C. In addition, the resolution was also found to affect the measured heights. While the CM particle size distributions in Figure 9B range from 0 to 600 μm, both the SfM of Figure 9A and fCM distributions of Figure 9C lie in the range from 0 to 400 μm. Nonetheless, the particle analysis demonstrated that the fCM data also quantitatively gave a better description of the SfM topographies. Figure 9D shows that the mean particle heights are also fairly comparable for fCM and SfM albeit some discrepancies for grits P40, P180 and P240. Since the CM values were in

good correspondence with the nominal grain sizes, this supports that the smaller height values found by the SfM were due to the limited lateral resolution.

Table 5: Parameters from CM, SfM at a range of 1.7 m and filtered CM (fCM). Values shown are the average particle height, the particle surface density and the S_q roughness parameter

Grit size	Av. height			Density			S_q		
	CM	SfM	fCM	CM	SfM	fCM	CM	SfM	fCM
	$[\mu m]$	$[\mu m]$	$[\mu m]$	$[mm^{-2}]$	$[mm^{-2}]$	$[mm^{-2}]$	$[\mu m]$	$[\mu m]$	$[\mu m]$
P40	411	162	190	1.4	0.59	0.56	138.2	64.1	75.2
P60	250	78	83	3.5	0.88	0.84	86.7	32.0	35.1
P80	160	54	47	6.9	1.04	1.09	61.0	25.0	20.9
P100	132	34	32	9.7	1.08	1.26	51.4	18.5	16.6
P120	99	32	24	16.2	1.16	1.28	40.1	16.7	11.4
P180	62	28	10	32.4	1.23	2.92	25.2	16.3	7.8
P240	45	22	8	58.5	1.04	4.83	19.9	14.1	7.1

Table 5 summarizes the mean height and particle density from the particle analysis as well as the S_q parameter from the area roughness analysis. The particle density values for SfM reflect how the reduced lateral resolution limits the detection of individual grains. While the CM density is seen to be around 2.5 times larger than the SfM value for P40, this difference increases to a factor of around 50 for the P240 grit. The RMS roughness S_q provides an alternative measure of the overall height variations compared to the particle analysis. Nonetheless, the S_q values from both CM, SfM and fCM data followed the same trend as the average particle height. In fact, the correlation coefficient between the mean height from the particle analysis and S_q was 0.99. As with the mean height, the S_q values for SfM and fCM were comparable despite some discrepancies for grits P40, P180 and P240.

The PSD analysis of Figure 10 offers a look at the frequency dependency of the CM, SfM and fCM topographies. The figure shows the PSD intensity in the frequency interval 0.1 mm^{-1} to 10 mm^{-1}, which corresponds to wavelengths from 10 mm and down to 0.1 mm, respectively. For the CM curves, a flat region is seen at low frequencies in the interval 0.1 mm^{-1} to 1.0 mm^{-1}, which is a common feature of PSD

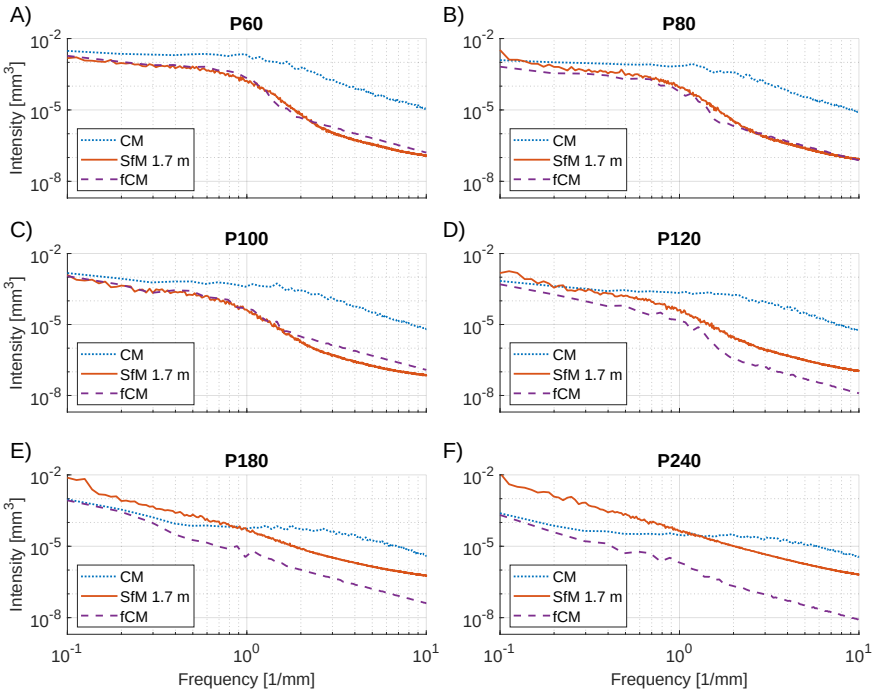

Figure 10: PSD analysis of CM (dotted line), SfM at 1.7 m range (full line), and fCM (dashed line) topographies of sandpaper artefacts of grit sizes P60-P240. The average of 1D PSD curves for each line in the DEM is shown on a log-log scale. A) P60. B) P80. C) P100. D) P120. E) P180. F) P240.

curves of engineered surfaces [47, 48]. The frequency where the curve begins to decrease, called the roll-off wave vector, is related to the largest structures of the surface [47, 48]. As seen by comparing Figure 10A through 10F, the roll-off of the CM curves moves to higher frequencies which corresponds to the smaller grain size of the finer grits.

The same feature is not observed in the fCM curves. The reduced resolution due to filtering is seen to lower the PSD intensity of the fCM curves and especially at the higher frequencies. Consequently, no roll-off wave vector is observed for the fCM curves. A similar behaviour is seen for the SfM curves which overlap with the fCM curves for P60 to P100 as seen from Figure 10A through 10C. However, at P120 and finer grit sizes, the PSD intensities of the SfM reconstructions increase above the fCM intensities, as seen in Figure 10D through 10F. This increase reflects the presence of

Table 6: Parameters of sandpaper P40 artefact from SfM measurements at a varying range and fCM data of a varying filter width. Values shown are the average particle height, particle area density as well as the S_q roughness parameter.

Range	Av. height		Density		Sq	
	SfM [μm]	fCM [μm]	SfM [mm^{-2}]	fCM [mm^{-2}]	SfM [μm]	fCM [μm]
1.5 m	172	207	0.64	0.91	67.0	81.9
1.7 m	166	195	0.60	0.54	66.5	75.2
2.0 m	138	164	0.57	0.50	54.6	66.1
2.2 m	109	150	0.50	0.45	46.2	60.9

topography variations in the SfM reconstructions that cannot be fully explained by the model of reduced resolution. One explanation could be that the texture level becomes too low at P120 for the SfM reconstructions to function properly. As an effect, an increased amount of noise appears in the reconstructed topography which was also observed in Figure 8F. The presence of an increased noise could also explain the SfM discrepancies in particle height and S_q for the P180 and P240 grit sizes.

For the P40 sandpaper artefact, SfM measurements at four different distances were conducted at ranges of 1.5 m, 1.7 m, 2.0 m and 2.2 m. As the range is increased, a proportionally larger spatial resolution should be observed. To include this effect in the modelled fCM data, the P40 CM measurement was filtered using Gaussian low-pass filters of increasing filter size. Thus, a value of σ proportional to the range was applied giving a σ of 0.19 mm, 0.21 mm, 0.25 mm and 0.27 mm.

The quantitative parameters from the range study are summarized in Table 6. With increasing range, a smaller average height, particle density and S_q roughness were observed for the SfM data. A similar decrease of parameter values was seen with increasing filter size of the fCM data. As was also observed for the 1.7 m data in Table 5, the SfM height and S_q values of Table 6 are seen to be smaller than the fCM values for all ranges. These differences indicate that the modelled fCM data does not give a full description of the SfM reconstruction of the P40 grit.

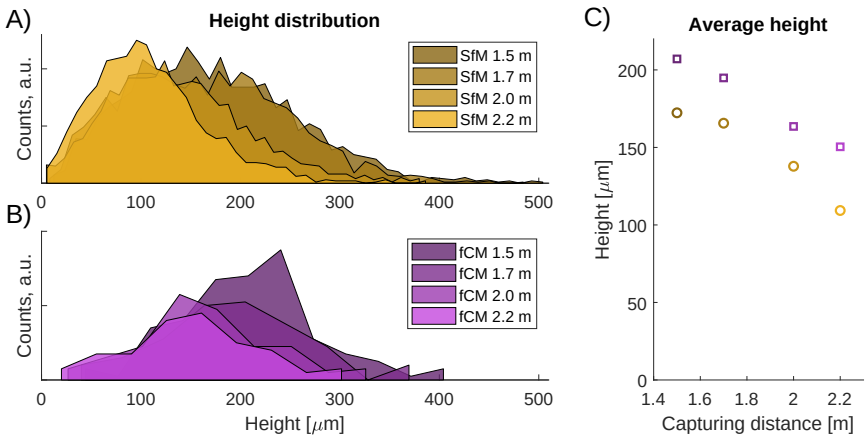

Figure 11: Particle height for P40 artefact at varying capture distance. A) SfM distributions. B) fCM distributions. C) Mean height vs range.

Figure 11 shows the height distributions from the particle analysis of the P40 grit. In Figure 11A, the SfM height distributions at varying range are shown while Figure 11B shows the height distributions of the modelled fCM data. With increasing range, the height distributions are seen to shift towards lower height values. A similar behaviour can also be seen for the increasing filter width. However, although the same trend is observed, the fCM mean height values are larger than the SfM values as shown in Figure 11C.

The spatial frequency information of the PSD analysis also shows a dependence on the range. As seen from Figure 12, an increase in range causes a reduction of the PSD intensity of the SfM curves in the frequency interval 0.5 mm^{-1} to 2.0 mm^{-1}. As an example, the 1.5 m range SfM curve has an intensity close to $10^{-3}\,\mathrm{mm}^3$ at a frequency of $1.0\,\mathrm{mm}^{-1}$ while the intensity for the 2.2 m curve has decreased to just above $10^{-2}\,\mathrm{mm}^3$. The changing filter size of the fCM curves are seen to result in a similar behaviour. Nonetheless, the overlap between fCM and SfM is not seen to be perfect. While the PSD intensity for the fCM curves is smaller between 1.0 mm^{-1} and 2.0 mm^{-1}, a larger intensity is observed for frequencies between 0.2 mm^{-1} and 1.0 mm^{-1}.

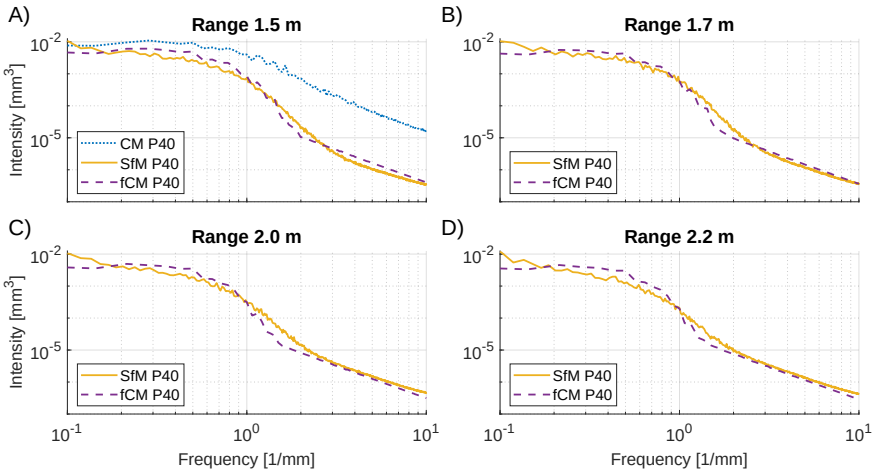

Figure 12: PSD analysis of P40 grit size at varying range or filtering level. CM (dotted line), SfM (full line), and fCM (dashed line). The average of 1D PSD curves for each line in the DEM is shown on a log-log scale. A) 1.5 m. B) 1.7 m. C) 2.0 m. D) 2.2 m.

5. Discussion

In general, some level of texture is required in SfM reconstructions. This was illustrated by the scan of the monochrome step-height artefact where the reconstruction failed altogether. In addition, this study demonstrates that the surface texture also heavily influences the reconstructed surface topography of SfM DEMs. In comparison to the marked pattern step-height, the low-level color-contrast of the projected light pattern resulted in a lower precision of the measured height as well as a reduced lateral resolution. However, whereas [31] found that a projected light pattern decreased the accuracy compared to no pattern, the projected light in this study did aid in the SfM reconstruction. At low roughness-levels of the sandpaper artefact, reconstruction errors in the color texture were observed.

Furthermore, the PSD analysis of both artefact types indicated an increase in noise at low texture levels. This was observed as a larger PSD intensity at high spatial frequencies for the projected light pattern of the step-height artefact and for finer grits sizes of the sandpaper artefact. In this way, the PSD analysis indicated when the texture level became a significant source of high-frequency noise. In the case of the sandpaper

artefacts, a transition was seen between P100 and P120. Thus the roughness texture became insufficient for a nominal average grain size between 125 μm and 160 μm corresponding to 5-6 times the GSD. Interestingly, this transition level was below the lateral spatial resolution as found from the step-height artefact.

The importance of texture level pose a challenge when evaluating the quality of SfM reconstructions. Commercial software may produce a reconstruction even at low levels of texture. As seen in this study, these reconstructions could introduce erroneous texture features and increased geometrical variations. Although such deviations may be possible to detect when measuring known surfaces, the effect of low texture could lead to false interpretations when inspecting unknown surfaces. Thus, the level of texture on the object surface should be taken into account when applying SfM for geometrical measurements.

A variation in range was introduced to influence the spatial resolution of the SfM reconstructions. Since the focal length was kept constant, an increase in range from 1.5 m to 2.2 m increased the GSD from $24\,\mu m$ to $35\,\mu m$. An effect of the range was observed on several parameters. At a larger range, the SfM reconstructions of the sandpaper artefact resulted in smaller particle-height and S_q values. For the marked pattern step-height artefact an increase in range from 1.5 m to 2.0 m resulted in larger height SD, RMSE and ER values. The absolute RMSE values of 0.57 mm at 1.5 m and 0.70 mm at 2.0 mm are comparable to previously reported values for comparison of DEMs [27]. However, the influence of low texture of the projected light pattern led to a larger RMSE of 1.04 mm at 1.5 m range. For the PSD analysis, an increase in range led to smaller PSD intensities at high spatial frequencies for both artefact types. This was in contrast to the observations at low texture levels where increased intensities were observed. Thus, the PSD analysis might indicate whether a SfM measurement was limited by insufficient spatial resolution or surface texture.

The proposed quantitative metrics in the study allowed for a diverse description of the reconstructed topographies. Although all parameters were affected by the texture level and range, the conclusions drawn from each varied. For the vertical dimension, a number of parameters were introduced. For the step-height artefact, the height of each step and RMSE of the full geometry were used. For the sandpaper artefacts, the

mean particle height and S_q roughness parameter were calculated. While these parameters could validate the overall dimensions of the reconstruction through comparison to nominal values and reference microscopy measurements, they provided limited information on the influence of texture. For the step-height artefact, the lateral spatial resolution described by the edge widths of the steps in combination with the SD of the height of the steps offered additional insights. While the height SD saw the greatest effect of a lower color contrast on the 10 mm step, the worst lateral resolution was observed on the 0.63 mm step. Thus, these parameters indicate that variations in the geometry may lead to locally reduced resolutions of the SfM reconstruction. Finally, the PSD analysis offered a multi-scale description of the frequency-dependence of the reconstructed topographies. In case of the step-height artefact, the PSD analysis was used to compare the measured topographies to the design geometry. While at low spatial frequencies the PSD intensities were similar, discrepancies appeared at a higher frequency depending on the range or texture level. For the sandpaper artefact, the PSD analysis could be used to validate the modelled fCM data that used filtering to describe the spatial resolution of the SfM reconstructions.

As a future study, the influence of color texture could be investigated more thoroughly using a range of color patterns of varying areal coverage, size and shape. This might determine whether a transition level of insufficient color contrast exists. The type of patterns should preferably be marked directly on the surface rather than projected using a light projector. . In addition, other state of the art SfM software solutions could be investigated to determine whether the influence of texture depends on the software or is a fundamental property of SfM.

6. Acknowledgements

The authors would like to thank Morten Hannibal Madsen for fruitful discussions on the design of reference artefacts. This work has received funding by the Energy Technology Development and Demonstration Program (project number 64015-0046) under the Danish Energy Agency. MSN and JG were also supported by funds from the Danish Agency for Institutions and Educational Grants. The funding bodies had no

involvement in the research work or preparation of the manuscript.

References

[1] J. Schöning, G. Heidemann, Evaluation of multi-view 3d reconstruction software, in: International Conference on Computer Analysis of Images and Patterns, Springer, 2015, pp. 450–461.

[2] M. Sturzenegger, D. Stead, Close-range terrestrial digital photogrammetry and terrestrial laser scanning for discontinuity characterization on rock cuts, Engineering Geology 106 (3) (2009) 163–182.

[3] M. Westoby, J. Brasington, N. Glasser, M. Hambrey, J. Reynolds, 'structure-from-motion'photogrammetry: A low-cost, effective tool for geoscience applications, Geomorphology 179 (2012) 300–314.

[4] M. Favalli, A. Fornaciai, I. Isola, S. Tarquini, L. Nannipieri, Multiview 3D reconstruction in geosciences, Computers & Geosciences 44 (2012) 168–176. doi:https://doi.org/10.1016/j.cageo.2011.09.012.
URL http://www.sciencedirect.com/science/article/pii/S0098300411003128

[5] T. P. Kersten, M. Lindstaedt, Image-based low-cost systems for automatic 3d recording and modelling of archaeological finds and objects, in: Euro-Mediterranean Conference, Springer, 2012, pp. 1–10.

[6] A. Koutsoudis, B. Vidmar, G. Ioannakis, F. Arnaoutoglou, G. Pavlidis, C. Chamzas, Multi-image 3d reconstruction data evaluation, Journal of Cultural Heritage 15 (1) (2014) 73–79.

[7] L. Javernick, J. Brasington, B. Caruso, Modeling the topography of shallow braided rivers using Structure-from-Motion photogrammetry, Geomorphology 213 (2014) 166–182. doi:10.1016/j.geomorph.2014.01.006.
URL http://dx.doi.org/10.1016/j.geomorph.2014.01.006

[8] K. Thoeni, A. Giacomini, R. Murtagh, E. Kniest, A comparison of multi-view 3D reconstruction of a rock wall using several cameras and a Laser scanner, International Archives of the Photogrammetry, Remote Sensing and Spatial Information Sciences - ISPRS Archives 40 (5) (2014) 573–580. doi:10.5194/isprsarchives-XL-5-573-2014.

[9] N. Micheletti, J. H. Chandler, S. N. Lane, Structure from Motion (SfM) Photogrammetry, in: Geomorphological Techniques, online ed. Edition, British Society for Geomorphology Geomorphological Techniques, 2015, Ch. 2.2, pp. 1–12.
URL http://geomorphology.org.uk/sites/default/files/chapters/2.2.2{_}SfM.pdf

[10] S. Siebert, J. Teizer, Mobile 3d mapping for surveying earthwork projects using an unmanned aerial vehicle (uav) system, Automation in Construction 41 (2014) 1–14.

[11] K. K. Han, M. Golparvar-Fard, Appearance-based material classification for monitoring of operation-level construction progress using 4D BIM and site photologs, Automation in Construction 53 (2015) 44–57. doi:10.1016/J.AUTCON.2015.02.007.
URL https://www.sciencedirect.com/science/article/pii/S0926580515000266

[12] S. Tuttas, A. Braun, A. Borrmann, U. Stilla, Acquisition and consecutive registration of photogrammetric point clouds for construction progress monitoring using a 4d bim, PFG–Journal of Photogrammetry, Remote Sensing and Geoinformation Science 85 (1) (2017) 3–15.

[13] M. R. Jahanshahi, S. F. Masri, C. W. Padgett, G. S. Sukhatme, An innovative methodology for detection and quantification of cracks through incorporation of depth perception, Machine vision and applications (2013) 1–15.

[14] K. Chaiyasarn, T.-K. Kim, F. Viola, R. Cipolla, K. Soga, Distortion-Free Image Mosaicing for Tunnel Inspection Based on Robust Cylindrical Surface Estimation

through Structure from Motion, Journal of Computing in Civil Engineering 30 (3) (2016) 4015045. doi:10.1061/(ASCE)CP.1943-5487.0000516.

[15] S. Stent, R. Gherardi, B. Stenger, K. Soga, R. Cipolla, Visual change detection on tunnel linings, Machine Vision and Applications 27 (3) (2016) 319–330.

[16] J. E. N. Masson, M. R. Petry, Comparison of mesh generation algorithms for railroad reconstruction, in: Autonomous Robot Systems and Competitions (ICARSC), 2017 IEEE International Conference on, IEEE, 2017, pp. 266–271.

[17] A. Khaloo, D. Lattanzi, Hierarchical Dense Structure-from-Motion Reconstructions for Infrastructure Condition Assessment, Journal of Computing in Civil Engineering 31 (1) (2017) 04016047. doi:10.1061/(ASCE)CP.1943-5487.0000616.
URL http://ascelibrary.org/doi/10.1061/{%}28ASCE{%}29CP.1943-5487.0000616

[18] C. Wu, Towards linear-time incremental structure from motion, in: 3DTV-Conference, 2013 International Conference on, IEEE, 2013, pp. 127–134.

[19] M. W. Smith, J. L. Carrivick, D. J. Quincey, Structure from motion photogrammetry in physical geography, Progress in Physical Geography: Earth and Environment 40 (2) (2016) 247–275. doi:10.1177/0309133315615805.
URL https://doi.org/10.1177/0309133315615805

[20] L. Gomes, O. R. P. Bellon, L. Silva, 3d reconstruction methods for digital preservation of cultural heritage: A survey, Pattern Recognition Letters 50 (2014) 3–14.

[21] T. Schöps, J. L. Schönberger, S. Galliani, T. Sattler, K. Schindler, M. Pollefeys, A. Geiger, A multi-view stereo benchmark with high-resolution images and multi-camera videos, in: Proc. CVPR, 2017.

[22] J. Schöning, G. Heidemann, Taxonomy of 3d sensors-a survey of state-of-the-art consumer 3d-reconstruction sensors and their field of applications., in: VISIGRAPP (3: VISAPP), 2016, pp. 194–199.

[23] J. R. Rosell-Polo, E. Gregorio, J. Gené, J. Llorens, X. Torrent, J. Arno, A. Escola, Kinect v2 sensor-based mobile terrestrial laser scanner for agricultural outdoor applications, IEEE/ASME Transactions on Mechatronics.

[24] I. Nikolov, C. Madsen, Benchmarking close-range structure from motion 3d reconstruction software under varying capturing conditions, in: Euro-Mediterranean Conference, Springer, 2016, pp. 15–26.

[25] N. D'Amico, T. Yu, Accuracy analysis of point cloud modeling for evaluating concrete specimens, in: SPIE Smart Structures and Materials+ Nondestructive Evaluation and Health Monitoring, International Society for Optics and Photonics, 2017, pp. 101691D–101691D.

[26] N. Micheletti, J. H. Chandler, S. N. Lane, Investigating the geomorphological potential of freely available and accessible structure-from-motion photogrammetry using a smartphone, Earth Surface Processes and Landforms 40 (4) (2015) 473–486. doi:10.1002/esp.3648.
URL https://onlinelibrary.wiley.com/doi/abs/10.1002/esp.3648

[27] M. W. Smith, D. Vericat, From experimental plots to experimental landscapes: topography, erosion and deposition in sub-humid badlands from Structure-from-Motion photogrammetry, Earth Surface Processes and Landforms 40 (12) (2015) 1656–1671. doi:10.1002/esp.3747.
URL http://doi.wiley.com/10.1002/esp.3747

[28] T. P. Kersten, D. Omelanowsky, M. Lindstaedt, Investigations of low-cost systems for 3d reconstruction of small objects, in: Euro-Mediterranean Conference, Springer, 2016, pp. 521–532.

[29] Li Zhang, Curless, Hertzmann, Seitz, Shape and motion under varying illumination: unifying structure from motion, photometric stereo, and multiview stereo, in: Proceedings Ninth IEEE International Conference on Computer Vision, IEEE, 2003, pp. 618–625 vol.1. doi:10.1109/ICCV.2003.1238405.
URL http://ieeexplore.ieee.org/document/1238405/

[30] S. Harwin, A. Lucieer, Assessing the accuracy of georeferenced point clouds produced via multi-view stereopsis from unmanned aerial vehicle (uav) imagery, Remote Sensing 4 (6) (2012) 1573–1599. doi:10.3390/rs4061573.
URL http://www.mdpi.com/2072-4292/4/6/1573

[31] I. Toschi, E. Nocerino, M. Hess, F. Menna, B. Sargeant, L. MacDonald, F. Remondino, S. Robson, Improving automated 3D reconstruction methods via vision metrology, Vol. 9528, International Society for Optics and Photonics, 2015, p. 95280H. doi:10.1117/12.2184974.
URL http://proceedings.spiedigitallibrary.org/proceeding.aspx?doi=10.1117/12.2184974

[32] M. R. James, S. Robson, Straightforward reconstruction of 3D surfaces and topography with a camera: Accuracy and geoscience application, Journal of Geophysical Research: Earth Surface 117 (F3). doi:10.1029/2011JF002289.
URL https://agupubs.onlinelibrary.wiley.com/doi/abs/10.1029/2011JF002289

[33] J. Goetz, A. Brenning, M. Marcer, X. Bodin, Modeling the precision of structure-from-motion multi-view stereo digital elevation models from repeated close-range aerial surveys, Remote Sensing of Environment 210 (2018) 208–216. doi:10.1016/J.RSE.2018.03.013.
URL https://www.sciencedirect.com/science/article/pii/S0034425718301068

[34] M. Slavcheva, W. Kehl, N. Navab, S. Ilic, Sdf-2-sdf: Highly accurate 3d object reconstruction, in: European Conference on Computer Vision, Springer, 2016, pp. 680–696.

[35] M. R. James, S. Robson, M. W. Smith, 3-D uncertainty-based topographic change detection with structure-from-motion photogrammetry: precision maps for ground control and directly georeferenced surveys, Earth Surface Processes and Landforms 42 (12) (2017) 1769–1788. doi:10.1002/esp.4125.
URL http://doi.wiley.com/10.1002/esp.4125

[36] P. Ingwer, F. Gassen, S. Püst, M. Duhn, M. Schälicke, K. Müller, H. Ruhm, J. Rettig, E. Hasche, A. Fischer, R. Creutzburg, Practical usefulness of structure from motion (SfM) point clouds obtained from different consumer cameras, in: Proceedings Volume 9411, Mobile Devices and Multimedia: Enabling Technologies, Algorithms, and Applications, no. March, 2015, p. 941102. doi:10.1117/12.2074892.
URL http://proceedings.spiedigitallibrary.org/proceeding.aspx?doi=10.1117/12.2074892

[37] Iso 6344(1998) coated abrasives — grain size analysis parts 1-3, https://www.iso.org/standard/12643.html, accessed: 2018-04-24.

[38] Fepa - federation of european producers of abrasives, https://www.fepa-abrasives.com/abrasive-products/grains, accessed: 2017-10-10.

[39] Bentley: Contextcapture, https://www.bentley.com/en/products/brands/contextcapture, accessed: 2017-10-12.

[40] D. Girardeau-Montaut, Cloudcompare, http://www.cloudcompare.org/, accessed: 2017-10-12.

[41] Hirox rh-2000 microscope, http://www.hirox-europe.com/products/microscope/RH-2000-digital-microscope.php/, accessed: 2017-10-12.

[42] Plu neox confocal microscope, http://www.sensofar.com/, accessed: 2017-10-12.

[43] Scanning probe image processor (spip), http://www.nanoscience.com/products/afm/scanning-probe-image-processor/, accessed: 2017-10-12.

[44] Iso 5436, https://www.iso.org/obp/ui/#iso:std:61261:en, accessed: 2017-10-05.

[45] Biovoxxel, http://www.biovoxxel.de/, accessed: 2017-10-05.

[46] Iso 25178-3(2012) geometrical product specifications (gps) – surface texture: Areal – part 3: Specification operators, https://www.iso.org/standard/42895.html, accessed: 2017-10-13.

[47] B. N. J. Persson, O. Albohr, U. Tartaglino, A. I. Volokitin, E. Tosatti, On the nature of surface roughness with application to contact mechanics, sealing, rubber friction and adhesion, Journal of Physics: Condensed Matter 17 (1) (2005) R1–R62. doi:10.1088/0953-8984/17/1/R01.
URL http://stacks.iop.org/0953-8984/17/i=1/a=R01?key=crossref.7463e9973eaa58c09e5bdac3d1940d9d

[48] T. Jacobs, T. Junge, L. Pastewka, Quantitative characterization of surface topography using spectral analysis, Surface Topography: Metrology and Properties 5 (1) (2017) 013001. doi:10.1088/2051-672X/aa51f8.
URL http://stacks.iop.org/2051-672X/5/i=1/a=013001?key=crossref.50ac6ffd35a5b856f00ad7f32699d646

[49] J. Garnaes, N. Kofod, A. Kühle, C. Nielsen, K. Dirscherl, L. Blunt, Calibration of step heights and roughness measurements with atomic force microscopes, Precision Engineering 27 (1) (2003) 91–98. doi:10.1016/S0141-6359(02)00184-8.
URL https://www.sciencedirect.com/science/article/pii/S0141635902001848

[50] A. Kuhle, B.-G. Rosen, J. Garnaes, Comparison of roughness measurement with atomic force microscopy and interference microscopy, in: A. Duparre, B. Singh (Eds.), Advanced Characterization Techniques for Optics, Semiconductors, and Nanotechnologies, Vol. 5188, International Society for Optics and Photonics, 2003, p. 154. doi:10.1117/12.521309.
URL http://proceedings.spiedigitallibrary.org/proceeding.aspx?doi=10.1117/12.521309

Bibliography

[1] Emil Krog Kruse, Niels N. Sørensen, and Christian Bak. "Predicting the Influence of Surface Protuberance on the Aerodynamic Characteristics of a NACA 63_3-418". In: *Journal of Physics: Conference Series, 1037(2), 2018 [022008]* (2018). URL: https://doi.org/10.1088/1742-6596/1037/2/022008.

[2] Emil Krog Kruse et al. "CFD Simulations and Validation of a Wall Roughness Model Applied on a NACA 63_3-418 Airfoil". In: *Submitted to Wileys Wind Energy* (2019).

[3] Emil Krog Kruse, Niels N. Sørensen, and Christian Bak. "A 2-Dimension Quantitative Parametric Investigation of Simplified Surface Imperfections on the Aerodynamic Characteristics of a NACA 63_3-418 Airfoil". In: *Submitted to Wileys Wind Energy* (2019).

[4] Emil Krog Kruse, Christian Bak, and Anders Smærup Olsen. "Wind Tunnel Tests on a NACA 63_3-418 Airfoil with Different Types of Leading Edge Roughness". In: *Submitted to Wileys Wind Energy* (2019).

[5] Christian Bak et al. "What is the critical height of leading edge roughness for aerodynamics?" In: *Journal of Physics: Conference Series* 753 (2016). URL: https://doi.org/10.1088/1742-6596/753/2/022023.

[6] *Paris Agreement*. https://unfccc.int/. page 3, Article 2, 1 (a). 2015.

[7] Jt. Houghton et al. "Climate Change 2001: The Scientific Basis". In: *Foreign Affairs* 81.1 (2002), page 208.

[8] *Global Wind Report, Annual Market Update 2017*. www.gwec.net. Accessed: 2018-12-29. 2017.

[9] *In Situ LER Example from Renewable Advice*. http://www.renewableadvice.com/. 2014.

[10] *In Situ LER Example from Deutsche Windtechnik*. https://www.deutsche-windtechnik.com/. 2015.

[11] Enrique Cortés et al. "On the Material Characterisation of Wind Turbine Blade Coatings: The Effect of Interphase Coating–Laminate Adhesion on Rain Erosion Performance". In: *Materials* 10.10 (2017). ISSN: 1996-1944. DOI: 10.3390/ma10101146. URL: http://www.mdpi.com/1996-1944/10/10/1146.

[12] *SkySpecs*. www.skyspecs.com. Accessed: 2018-10-25.

[13] *Force Technology*. https://forcetechnology.com/en/services/drone-inspection-of-wind-turbines-onshore-and-offshore. Accessed: 2018-10-25.

[14] Hazim Shakhatreh et al. “Unmanned Aerial Vehicles: A Survey on Civil Applications and Key Research Challenges”. In: *CoRR* abs/1805.00881 (2018).

[15] Nicola D’Apuzzo. “Overview of 3D surface digitization technologies in Europe”. In: *Proc.SPIE* (2006). DOI: 10.1117/12.650123. URL: https://doi.org/10.1117/12.650123.

[16] Mostafa Abdel-Bary Ebrahim. “3D Laser Scanners’Techniques Overview”. In: *International Journal of Science and Research (IJSR)* 4, Issue 10 (2015), pages 323–331.

[17] *Scanning Concept Video*. www.powercurve.dk/LER-drone-inspection/. Accessed: 2018-12-28. 2015.

[18] George Rennie. “XXIII. On the friction and resistance of fluids”. In: *Philosophical Transactions of the Royal Society of London* 121 (1831), pages 423–442. DOI: 10.1098/rstl.1831.0024. URL: https://royalsocietypublishing.org/doi/abs/10.1098/rstl.1831.0024.

[19] J. N. Eastman and A. Sherman. “Wing Characteristics as affected by protuberances of short span”. In: *National Advisory Committee for Aeronautics* (1932). URL: https://ntrs.nasa.gov/search.jsp?R=19930091523.

[20] Eastman N. Jacobs. “Airfoil Section Characteristics as Affected by Protuberances”. In: *National Advisory Committee for Aeronautics* (1932). URL: https://ntrs.nasa.gov/search.jsp?R=19930091520.

[21] R. W. Hooker. “The aerodynamic characteristics of airfoils as affected by surface roughness”. In: *NACA-TN-457 Langley Memorial Aeronautical Laboratory* (1933), pages 468–478.

[22] Johann Nikuradse. “Strömungsgesetze in rauhen Rohren”. In: *VDI-Verl.* (1933).

[23] J. Nikuradse. “Laws of flow in rough pipes”. In: *VDI Forschungsheft* (1933).

[24] I.H. Abbott and A.E. Von Doenhoff. “Theory of wing sections, including a summary of airfoil data”. In: *Dover Publications*. Dover books on physics and chemistry (1959).

[25] K. Sermeus and H. Yang. “CFD Simulation of Aircraft Icing Effects using Roughness Modeling”. In: *62nd CASI Aeronautics Conference* (2015).

[26] M. B. Bragg, G. M. Gregorek, and J. D. Lee. “Airfoil aerodynamics in icing conditions”. In: *Journal of Aircraft* 23.1 (1986), pages 76–81. DOI: 10.2514/3.45269. URL: https://doi.org/10.2514/3.45269.

[27] A. P. Broeren et al. “Aerodynamic Simulation of Ice Accretion on Airfoils”. In: *National Advisory Committee for Aeronautics* (2011).

[28] A. P. Broeren, M. B. Bragg, and H. E. Addy. “Effects of Environmentally Imposed Roughness on Airfoil Performance”. In: *Journal of Aircraft Vol. 41* (2004).

[29] Michael Bragg et al. “Airfoil ice-accretion aerodynamic simulation”. In: *45th AIAA Aerospace Sciences Meeting and Exhibit* (2007), page 85.

[30] T. Cebeci. “Effect of Intercycle Ice Accretions on Airfoil Performance”. In: *California State University (NASA)* (1987).

[31] Lasse Makkonen et al. “Modelling and Prevention of Ice Accretion on Wind Turbines”. In: *Wind Engineering* 25.1 (2001), pages 3–21. DOI: 10.1260/0309524011495791. URL: https://doi.org/10.1260/0309524011495791.

[32] K. Mortensen. “CFD simulations of an airfoil with leading edge ice accretion”. In: *Department of Mechanical Engineering* (2008), page 117.

[33] E. Sagol. “Three dimensional numerical prediction of icing related power and energy losses on a wind turbine”. PhD thesis. Ecole Polytechnique, Montreal (Canada), 2014.

[34] V. Turkia, S. Huttunen, and T. Wallenius. “Method for estimating wind turbine production losses due to icing”. In: *VTT Technology)* (2013).

[35] Peter Blasco, Jose Palacios, and Sven Schmitz. “Investigation of Wind Turbine Power Generation During Atmospheric Icing by Multi-Disciplinary Experimentation”. In: (). DOI: 10.2514/6.2015-0496. URL: https://doi.org/10.2514/6.2015-0496.

[36] Marie Cecilie Pedersen and Chungen Yin. “Preliminary Modelling Study of Ice Accretion on Wind Turbines”. In: *Energy Procedia* 61 (2014). International Conference on Applied Energy, ICAE2014, pages 258–261. ISSN: 1876-6102. URL: http://www.sciencedirect.com/science/article/pii/S1876610214029324.

[37] Marie Cecilie Pedersen and Henrik Sørensen. “Towards a CFD Model for Prediction of Wind Turbine Power Losses due to Icing in Cold Climate”. English. In: Conference date: 10-04-2016 Through 15-04-2016. April 2016. URL: http://isromac-isimet.univ-lille1.fr/index.php?rubrique=home.

[38] M. Etemaddar, Martin Otto Laver Hansen, and T. Moan. “Wind turbine aerodynamic response under atmospheric icing conditions”. English. In: *JohnWiley & Sons Ltd.* 17.2 (2014), pages 241–265. ISSN: 1095-4244. DOI: 10.1002/we.1573. URL: https://doi.org/10.1002/we.1573.

[39] Peter Fuglsang, Ioannis Antoniou, and Kristian S. Dahl. “Wind tunnel tests of the FFA-W3-241, FFA-W3-301 and NACA 63-430 airfoils”. In: *Risø National Laboratory* (January 1998).

[40] C. Bak et al. “Wind Tunnel Tests of the NACA 63-415 and a Modified NACA 63-415 Airfoil”. In: *Risø National Laboratory* (2000).

[41] W Timmer and R.P.J.O.M. Rooij. “Summary of the Delft University Wind Turbine Dedicated Airfoils”. In: *Journal of Solar Energy Engineering-transactions of The Asme - J SOL ENERGY ENG* 125 (January 2003). DOI: 10.1115/1.1626129. URL: https://doi.org/10.1115/1.1626129.

[42] R. van Rooij and W. A. Timmer. “Roughness Sensitivity Considerations for Thick Rotor Blade Airfoils”. In: *Journal of Solar Energy Engineering-transactions of the ASME* 125 (2003), pages 468–478.

[43] W. A. Timmer. "An Overview of NACA 6-Digit Airfoil Series Characteristics with Reference to Airfoils for Large Wind Turbine Blades". In: *47th AIAA Aerospace Sciences* (2009).

[44] N. Gaudern. "A practical study of the aerodynamic impact of wind turbine blade leading edge erosion". In: *The Science of Making Torque from Wind 2014 (TORQUE 2014), Journal of Physics: Conference Series 524 (2014) 012031* (2014).

[45] E. B. White et al. "Leading-Edge Roughness Effects on 63_3-418 Airfoil Performance". In: *49th AIAA Aerospace Sciences* (2011).

[46] M. F. Kerho and M. B. Bragg. "Airfoil Boundary-Layer Development and Transition with Large Leadge-Edge Roughness". In: *AIAA Vol. 35, No. 1* (1997).

[47] Mark Drela. "XFOIL: An Analysis and Design System for Low Reynolds Number Airfoils". In: volume 54. June 1989. DOI: 10.1007/978-3-642-84010-4-1. URL: https://doi.org/10.1007/978-3-642-84010-4-1.

[48] R.P.J.O.M. Van Rooij. *Modification of the boundary layer calculation in RFOIL for improved airfoil stall prediction*. September 1996.

[49] F. R. Menter. "Zonal Two Equation k-ω Turbulence Models for Aerodynamic Flows". In: *AIAA 1993-2906* (1993).

[50] David C. Wilcox. "Turbulence Modeling for CFD, 3^{rd} Edition". In: *DWC Industries* (2006).

[51] Tobias Knopp, Bernhard Eisfeld, and Javier Bartolome Calvo. "A new extension for the k-ω turbulence models to account for wall roughness". In: *International Journal of Heat and Fluid Flow* (2008).

[52] Bernhard Eisfeld, Tobias Knopp, and Javier Bartolome Calvo. "Application of a New Roughness Extension for k—ω Turbulence Models". In: *Springer Berlin Heidelberg* (2010). Edited by Andreas Dillmann et al., pages 43–50.

[53] R. S. Ehrmann et al. "Realistic Leading-Edge Roughness Effects on Airfoil Performance". In: *31st AIAA Applied Aerodynamics Conference* (2013).

[54] C. M. Langel, R. Chow, and C. P. van Dam. "Further Developments to a Local Correlation Based Roughness Model for Boundary Layer Transition Prediction". In: *American Institute of Aeronautics and Astronautics* (2015).

[55] C. M. Langel et al. "A Computational Approach to Simulating the Effects of Realistic Surface Roughness on Boundary Layer Transition". In: *American Institute of Aeronautics and Astronautics* (2014).

[56] C. M. Langel et al. "Analysis of the Impact of Leading Edge Surface Degradation on Wind Turbine Performance". In: *33rd Wind Energy Symposium* (2015). DOI: 10.2514/6.2015-0489. URL: https://doi.org/10.2514/6.2015-0489.

[57] David C. Maniaci et al. "Experimental Measurement and CFD Model Development of Thick Wind Turbine Airfoils with Leading Edge Erosion". In: *IOP Publishing* 753 (September 2016), page 022013. DOI: 10.1088/1742-6596/753/2/022013. URL: https://doi.org/10.1088/1742-6596/753/2/022013.

[58] C. M. Langel, R. Chow, and C. P. van Dam. "RANS Based Methodology for Predicting the Influence of Leading Edge Erosion on Airfoil Performance". In: *Sandia National Laboratories* (2017).

[59] R. S. Ehrmann et al. "Effect of Surface Roughness on Wind Turbine Performance". In: *Sandia National Laboratories* (2017).

[60] A. Sareen, C. A. Sapre, and M. S. Selig. "Effects of leading edge erosion on wind turbine blade performance". In: *Wind Energy, 17:1531–1542* (2014), 17:1531–1542.

[61] K. Standish et al. "Computational Prediction of Airfoil Roughness Sensitivity". In: *48th AIAA Aerospace Sciences Meeting and Exhibit* (2010).

[62] Marijn Leendert Willy Veraart. "Deterioration in aerodynamic performance due to leading edge rain erosion". Master's thesis. Wind Energy Research Group Faculty of Aerospace Engineering Delft University of Technology, 2017.

[63] Onur Özyesil et al. "A Survey on Structure from Motion". In: *ArXiv* abs/1701.08493 (2017).

[64] Agisoft. *Metashape*. Access: 8th Aug 2019. URL: https://www.agisoft.com/.

[65] Bentley. *ContextCapture*. Access: 8th Aug 2019. URL: https://www.bentley.com/en/products/brands/contextcapture/.

[66] Ivan Adriyanov Nikolov and Claus Brøndgaard Madsen. "Performance Characterization of Absolute Scale Computation for 3D Structure from Motion Reconstruction". English. In: SCITEPRESS Digital Library, February 2019. DOI: 10.5220/0007444208840891. URL: https://doi.org/10.5220/0007444208840891.

[67] Ivan Adriyanov Nikolov and Claus Brøndgaard Madsen. "Benchmarking Close-range Structure from Motion 3D Reconstruction Software under Varying Capturing Conditions". English. In: volume 10058 2016. Germany: Springer, October 2016. ISBN: 978-3-319-48495-2. DOI: 10.1007/978-3-319-48496-9-2. URL: https://doi.org/10.1007/978-3-319-48496-9-2.

[68] ISO. *6344-1:1998 Coated abrasives — Grain size analysis — Part 1: Grain size distribution test*. 1998.

[69] Ivan Adriyanov Nikolov and Claus Brøndgaard Madsen. "Interactive Environment for Testing SfM Image Capture Configurations". English. In: SCITEPRESS Digital Library, February 2019. DOI: 10.5220/0007566703170322. URL: https://doi.org/10.5220/0007566703170322.

[70] Ivan Adriyanov Nikolov and Claus Brøndgaard Madsen. "LiDAR-based 2D Localization and Mapping System using Elliptical Distance Correction Models for UAV Wind Turbine Blade Inspection". English. In: SCITEPRESS Digital Library, 2017. ISBN: 978-989-758-227-1. DOI: 10.5220/0006124304180425. URL: https://doi.org/10.5220/0006124304180425.

[71] M. Drela and M. B. Giles. "Viscous-Inviscid Analysis of Transonic and Low Reynolds Number Airfoils". In: *AIAA 25(10):1347-1355, Vol. 25 NO. 10* (1987).

[72] J.A. Michelsen. “Basis3D - a Platform for Development of Multiblock PDE Solvers”. In: *Technical Report AFM 92-05, Technical University of Denmark, Department of Fluid Mechanics* (1992).

[73] J.A. Michelsen. “Block structured Multigrid solution of 2D and 3D elliptic PDE’s”. In: *Technical Report AFM 94-06, Technical University of Denmark, Department of Fluid Mechanics* (1994).

[74] N.N. Sørensen. “General Purpose Flow Solver Applied to Flow over Hills”. In: *Risø National Laboratory* (1995).

[75] N. N. Sørensen. “HypGrid2D, a 2-D Mest Generator”. In: *Risø National Laboratory* (1998).

[76] Christian Bak. “Aerodynamic design of wind turbine rotors”. In: *In P. Brønsted and R. Nijssens "Advances in wind turbine blade design and materials", Woodhead Publishing Series in Energy; No. 47* (2013).

[77] E. L. Lawler and D. E. Wood. “Branch-and-Bound Methods: A Survey”. In: *Oper. Res.* 14.4 (August 1966), pages 699–719. ISSN: 0030-364X. DOI: 10.1287/opre.14.4.699. URL: http://dx.doi.org/10.1287/opre.14.4.699.